



Fátima Alexandra Meira Machado **Dextrin: a platform for the development of drug delivery systems**

UMinho | 2022



Universidade do Minho
Escola de Engenharia

Fátima Alexandra Meira Machado

**Dextrin: a platform for the
development of drug delivery
systems**

October 2022



Universidade do Minho
Escola de Engenharia

Fátima Alexandra Meira Machado

**Dextrin: a platform for the
development of drug delivery systems**

Doctoral Thesis
Doctorate in Biomedical Engineering

Work developed under the supervision of:
Francisco Miguel Portela da Gama, PhD
José Alberto Ribeiro Martins, PhD
José Eduardo Pereira, PhD

October 2022

DIREITOS DE AUTOR E CONDIÇÕES DE UTILIZAÇÃO DO TRABALHO POR TERCEIROS

Este é um trabalho académico que pode ser utilizado por terceiros desde que respeitadas as regras e boas práticas internacionalmente aceites, no que concerne aos direitos de autor e direitos conexos.

Assim, o presente trabalho pode ser utilizado nos termos previstos na licença abaixo indicada.

Caso o utilizador necessite de permissão para poder fazer um uso do trabalho em condições não previstas no licenciamento indicado, deverá contactar o autor, através do RepositóriUM da Universidade do Minho.

Licença concedida aos utilizadores deste trabalho



Atribuição-NãoComercial-SemDerivações
CC BY-NC-ND

<https://creativecommons.org/licenses/by-nc-nd/4.0/>

AGRADECIMENTOS / ACKNOWLEDGEMENTS

Finda esta etapa, não posso deixar de lembrar e agradecer a todas as pessoas que contribuíram para a sua concretização. Ao meu orientador, o professor Miguel Gama, pela confiança depositada para a realização deste trabalho, por me criar toda a estrutura necessária, pelas oportunidades e experiências proporcionadas, pelos ensinamentos e pelo esforço que tornaram possível terminar esta etapa com sucesso. Ao professor José Alberto, pelo otimismo e motivação nos momentos difíceis. Acima de tudo pela permanente disponibilidade e qualidade no suporte teórico e prático, que foram cruciais para a resolução de problemas e para o sucesso dos trabalhos. Ao professor José Eduardo, pelos ensinamentos, trabalho árduo com animais, e a toda a sua equipa. Por todo o suporte no planeamento dos trabalhos, pelas críticas construtivas e pelos conselhos úteis na supervisão dos trabalhos. Às professoras de histologia, Justina Oliveira e Isabel Pires, pelo carinho, simpatia e suporte imprescindível numa área que não a da minha formação. À Vanessa Silva, e professora Patrícia Poeta, pela receção amável e grande suporte na execução dos trabalhos de microbiologia. Foi um prazer trabalhar convosco! Agradeço também à professora Ana Colette e sua equipa, ao professor José Domingos dos Santos e Ana Brandão pela colaboração ao longo deste trabalho. Ao Dr. Nuno Cruz, do Hospital da Luz, pela amável receção, transferência de conhecimentos e apoio na concretização do estudo clínico.

A todos os que passaram pelo LTEB, agradeço a ajuda, boa disposição, companheirismo. Um agradecimento especial à Isabel Pereira que supervisionou com rigor várias tarefas desta tese. Obrigado a todos os meus amigos (vocês sabem quem são), que viveram comigo o pior, e o melhor, que esta etapa me fez passar. Por último, e mais importante, um obrigado à minha família e ao meu namorado, que foram incansáveis e imprescindíveis, para que tudo isto fosse possível. E à bimbi, a minha “sombra”, que sorte tenho de a ter.

Agradeço à Fundação para a Ciência e Tecnologia (FCT) o financiamento através do projeto nº 003262 titulado “iBONE therapies: advanced solutions for bone regeneration”, e das bolsas SFRH/BD/132000/2017 e COVID/BD/152430/2022, no âmbito do financiamento estratégico UIDB/04469/2020; COMPETE 2020 (POCI-01-0145-FEDER-006684) e BioTecNorte (NORTE-01-0145-FEDER-000004) financiado pelo Fundo Europeu de Desenvolvimento Regional no âmbito do Programa Operacional Regional do Norte - Norte2020.



STATEMENT OF INTEGRITY

I hereby declare having conducted this academic work with integrity. I confirm that I have not used plagiarism or any form of undue use of information or falsification of results along the process leading to its elaboration.

I further declare that I have fully acknowledged the Code of Ethical Conduct of the University of Minho.

Dextrino: uma plataforma para o desenvolvimento de sistemas de entrega de fármacos

RESUMO

O osso possui uma capacidade regenerativa limitada. Para complicar, as infecções ósseas associadas a biomateriais são um sério problema devido à rápida evolução da resistência microbiana aos antibióticos. O dextrino é um polímero natural seguro, com grande potencial como sistema de libertação de fármacos, contudo, ainda pouco frequente na prática clínica. Este trabalho faz uso do dextrino como componente principal de formulações de hidrogel (HG) e micelares, para a entrega de componentes antimicrobianos e regeneradores de osso.

Combinámos um péptido antimicrobiano, LLKKK18 (LL18), e um antibiótico comumente usado, cloridrato de vancomicina (VH), incorporados num HG à base de dextrino oxidado (ODEX), a fim de encontrar um equilíbrio adequado entre (elevados) efeitos microbicidas e (reduzida) toxicidade contra tecidos do hospedeiro, para o tratamento da osteomielite. Doses de VH de 10, 24 e 483 μM , combinadas com LL18 a 300 μM , suprimiram a infecção *in vivo* em 10 %, 30 % e 70 % dos indivíduos, respetivamente, com dano reduzido para os tecidos. Desenvolvemos depois um sistema micelar por conjugação de dextrino com vitamina D3, ao qual o LL18 catiónico foi adsorvido electrostaticamente. As micelas de ~ 150 nm com LL18 incorporado melhoraram a biocompatibilidade do péptido, promoveram o fecho de feridas ($\leq 0,125$ mg/mL), e exibiram uma parceria sinérgica com um perfil antimicrobiano altamente melhorado, atingindo-se 100 % de morte bacteriana com 0,175 mg/mL:17,5 $\mu\text{g/mL}$ (micela:péptido). As micelas melhoraram bastante o desempenho do LL18.

Uma formulação de Bonelike® Poro (BL®P) e células estaminais de polpa dentária humana (hDPSCs), incorporadas no HG de ODEX, foi testada para o tratamento de defeitos ósseos de tamanho crítico num modelo ovino. Os resultados confirmaram um manuseio mais fácil do BL®P e melhor preenchimento do defeito ósseo, sem comprometer o crescimento de osso novo. No entanto, a adição de hDPSCs não mostrou benefícios. Num estudo clínico, Bonelike by Biosskin® (BL®) associado ao HG de ODEX, foi implantado no alvéolo imediatamente após a exodontia. Após 6 meses de tratamento, os resultados mostraram uma boa osteointegração sem sinais de reação adversa, um aumento da reabsorção de grânulos ($p = 0,029$) e uma tendência para maior crescimento de osso novo em relação ao grupo BL®, tendo ainda sido benéfico para a estabilidade primária do implante dentário ($p = 0,017$). Esta validação clínica pode encorajar a inclusão de outros materiais à base de dextrino na clínica.

Palavras-chave: dextrino, hidrogel, LLKKK18, micelas, vitamina D3.

Dextrin: a platform for the development of drug delivery systems

ABSTRACT

Bone has a limited regenerative capacity. To complicate, biomaterial-associated infections are a serious burden due to rapidly evolving microbe resistance to antibiotics. Dextrin is a safe natural polymer with great potential as a platform for drug delivery systems, yet still uncommon in clinics. This work makes use of dextrin as a main component in hydrogel (HG) and micellar formulations, for the delivery of antimicrobial and bone regenerative components.

We combined an antimicrobial peptide, LLKKK18 (LL18), and a commonly used antibiotic, vancomycin hydrochloride (VH), loaded into oxidized-dextrin (ODEX)-based HG, attempting to find a suitable balance between (high) microbicide effects and (low) host tissue toxicity, for osteomyelitis treatment. VH doses of 10, 24, and 483 μM , combined with LL18 at 300 μM , suppressed *in vivo* infection in 10 %, 30 %, and 70 % of the individuals, respectively, with reduced tissue damage. We then developed a micellar system by conjugation of dextrin to vitamin D3, to which cationic LL18 was adsorbed electrostatically. LL18-loaded micelles of ~ 150 nm showed improved peptide biocompatibility, promoted wound healing (≤ 0.125 mg/mL), and exhibited a synergistic partnership with a highly improved antimicrobial profile, reaching 100 % bacteria killing at 0.175 mg/mL:17.5 $\mu\text{g}/\text{mL}$ (micelle:peptide). Micelles greatly improved LL18 performance.

A formulation of Bonelike® Poro (BL®P) and human dental pulp stem cells (hDPSCs), embedded within ODEX HG, was tested for the management of critical-sized defects in an ovine model. Results confirmed the easier handling of BL®P and better defect filling, without compromising new bone ingrowth. However, addition of hDPSCs showed no benefits. In a clinical study, Bonelike by Biosskin® (BL®) associated with ODEX HG, was implanted into the alveolar socket immediately after exodonty. After 6 months of treatment, results showed good osseointegration with no signs of adverse reaction, increased granules resorption ($p = 0.029$), and a tendency for more new bone ingrowth compared to BL® group, being even beneficial for the implant primary stability ($p = 0.017$). This clinical validation may encourage the clinical translation of other dextrin-based materials.

Keywords: dextrin, hydrogel, LLKKK18, micelle, vitamin D3.

LIST OF CONTENTS

AGRADECIMENTOS / ACKNOWLEDGEMENTS	iii
RESUMO	v
ABSTRACT	vi
LIST OF FIGURES	xiii
LIST OF TABLES	xxii
LIST OF ABBREVIATIONS AND ACRONYMS	xxiv
CHAPTER 1	27
MOTIVATION AND OUTLINE	27
1.1. Context and Motivation	28
1.1 Aims and Outline	29
1.2 Scientific Output	31
1.3 References	33
CHAPTER 2	35
LITERATURE REVIEW	35
2.1 Bone	36
2.1.1 Bone Anatomy and Composition	36
2.1.2 Bone Histology	38
2.1.3 Bone Remodeling	39
2.1.4 Bone Repair	40
2.1.5 Injectable Bone Substitutes	42
2.1.5.1 The Case of DEXGEL Bone	44
2.2 The Challenge of Osteomyelitis	45
2.2.1 Pathophysiology / Pathogenic Mechanism of Infection	47
2.2.2 <i>Staphylococcus aureus</i> as the Primary Pathogen in Osteomyelitis	48
2.3 Human Cathelicidin and LLKKK18 Derivative	51

2.3.1 Encapsulation Mechanisms	55
2.4 Vitamin D3	56
2.4.1 Antimicrobial Action	58
2.4.2 Benefits for Bone Healing	60
2.4.3 Vitamin D3-conjugated Nanocarriers	62
2.5 Dextrin	63
2.5.1 Smart Option for Therapy Design	64
2.5.2 Dextrin-based Drug Delivery Systems	66
2.5.3 Dextrin-based Hydrogels for Tissue Engineering	72
2.5.4 Benefits for Bone Healing	74
2.6 References	76
CHAPTER 3	86
INJECTABLE HYDROGEL AS A CARRIER OF VANCOMYCIN AND A CATHELICIDIN-DERIVED PEPTIDE FOR OSTEOMYELITIS TREATMENT	86
3.1 Introduction	87
3.2 Materials and Methods	89
3.2.1 Materials	89
3.2.2 Dextrin Oxidation and Hydrogel Preparation	90
3.2.3 <i>In vitro</i> Biocompatibility	90
3.2.3.1 Cell Culture	90
3.2.3.2 Cell Viability Assay	91
3.2.3.3 Hemolysis Assay	92
3.2.3.4 pH Monitoring Upon Hydrogel Degradation	93
3.2.4 Hydrogel Degradation and LL18 Release	93
3.2.5 Bacteria and Antibacterial Assays	94
3.2.5.1 Bacterial Susceptibility Testing	94
3.2.6 Animal Model and <i>In vivo</i> General Procedures	95
3.2.6.1 Sacrifice and Microbiological Evaluation	97

3.2.6.2	Bone Histology	98
3.2.7	Statistical Analysis	99
3.3	Results and Discussion	99
3.3.1	<i>In vitro</i> Biocompatibility	99
3.3.1.1	Cytotoxicity and Hemolysis	99
3.3.2	Hydrogel Degradation and pH Changes	102
3.3.3	Hydrogel Degradation and LL18 Release	103
3.3.4	Antibacterial Activity	104
3.3.5	<i>In vivo</i> Study	105
3.3.5.1	Osteomyelitis Model and Bacterial Load	105
3.3.5.2	Histopathological Analysis	107
3.4	Conclusion	111
3.5	References	111
CHAPTER 4		116
THERAPEUTIC PARTNERSHIP OF LLKKK18 AND VITAMIN D3 LOADED INTO DEXTRIN-BASED MICELLES TAILORED FOR BONE INFECTIONS		116
4.1	Introduction	117
4.2	Materials and Methods	119
4.2.1	Materials and Reagents	119
4.2.2	Production of Micelles	120
4.2.2.1	Succinylation of Vitamin D3	120
4.2.2.2	Synthesis of Conjugates	120
4.2.3	Peptide Loading	122
4.2.4	Characterization of Conjugates and Micelles	122
4.2.4.1	Infrared Spectroscopy	122
4.2.4.2	Thermogravimetric Analysis	123
4.2.4.3	Differential Scanning Calorimetry	123
4.2.4.4	Critical Micellar Concentration	123

4.2.4.5	Size and Zeta Potential	124
4.2.4.6	Morphology	124
4.2.5	Biocompatibility	124
4.2.5.1	Cell Culture Conditions	124
4.2.5.2	Cell Viability Assay	125
4.2.5.3	Hemolysis Assay	126
4.2.6	Cell Internalization	126
4.2.6.1	Fluorescently labeled Conjugates	126
4.2.6.2	Subcellular Localization and Cell Uptake	127
4.2.7	Functionality	127
4.2.7.1	Bacterial Susceptibility Test	127
4.2.7.2	Inhibition of Albumin Denaturation	128
4.2.7.3	Migration Assay	128
4.2.8	Statistical Analysis	129
4.3	Results and Discussion	129
4.3.1	Characterization of Vitamin D3-Dextrin Conjugates	129
4.3.2	LL18 Association Efficiency	133
4.3.3	Morphology and Stability	135
4.3.4	Cytotoxicity and Hemolysis	136
4.3.5	Fluorescently Labeled Micelles	139
4.3.6	Subcellular Localization and Cell Uptake	140
4.3.7	Functionality	145
4.4	Conclusion	150
4.5	References	150
CHAPTER 5		155
DEXTRIN HYDROGEL LOADED WITH A MACROPOROUS BONELIKE® SCAFFOLD AND		
DENTAL PULP STEM CELLS FOR CRITICAL-SIZED DEFECT REPAIR		155
5.1. Introduction		156

5.2. Materials and Methods	158
5.2.1. Materials and Reagents	158
5.2.2. Preparation of Dextrin-based Hydrogel	158
5.2.3. Preparation of Bonelike® Poro	159
5.2.4. Bonelike® Poro Dissolution Behaviour	159
5.2.5. Mechanical Test	160
5.2.6. Scanning Electron Microscopy	160
5.2.7. Human Dental Pulp Stem Cells Culture and Characterization	160
5.2.8. Preparation of Formulations for <i>In vivo</i> Implantation	161
5.2.9. Surgical Procedure	162
5.2.10. Micro-computed Tomography Analysis	163
5.2.11. Histological Analysis	164
5.2.12. Statistical Analysis	164
5.3 Results	164
5.3.1 Human Dental Pulp Stem Cells Characterization	164
5.3.2 Dissolution Rate, Morphology and Mechanical Behaviour	165
5.3.3 Surgical Analysis	168
5.3.4 Bone Regeneration of Critical-sized Defects	169
5.3.4.1 Micro-computed Tomography Analysis	169
5.3.4.2 Histological Analysis	171
5.4 Discussion	172
5.5 Conclusion	174
5.6 References	174
CHAPTER 6	178
RANDOMIZED CLINICAL STUDY OF INJECTABLE DEXTRIN-BASED HYDROGEL AS A CARRIER OF A SYNTHETIC BONE SUBSTITUTE	178
6.1 Introduction	179
6.2 Materials and methods	180

6.2.1	Study Design and Overall Clinical Procedures	180
6.2.2	Recruitment	182
6.2.3	Materials	184
6.2.4.	Preparation of DEXGEL	184
6.2.5.	Preparation of BL® Granules	184
6.2.6.	DEXGEL Bone kit	185
6.2.7.	Ethical Considerations	187
6.2.8.	Surgical Procedure	187
6.2.8.1.	Tooth Extraction and Biomaterial Implantation	187
6.2.8.2.	Sample Collection and Implant Placement	188
6.2.9.	Histological Analysis	189
6.2.10.	Computed Tomography	189
6.2.11.	Implant Stability Quotient	189
6.2.12.	Statistical Analysis	190
6.3	Results	190
6.3.1	Clinical Analysis	191
6.3.2	Histological and Histomorphometric Analysis	192
6.3.3	Bone Density and Volume	193
6.3.4	Primary Stability of the Implant	195
6.4	Discussion	197
6.5	Conclusion	201
6.6	References	202
CHAPTER 7		206
FINAL REMARKS		206
7.1	General Conclusions	207
7.2	Suggestions for Future Work	209
7.3	References	210

APPENDIX A	211
APPENDIX B	213
APPENDIX C	214

LIST OF FIGURES

Figure 2.1 – Schematic representation of an adult femur.....	37
Figure 2.2 – Differentiation of bone cells from mesenchymal stem cells and hematopoietic stem cells.	38
Figure 2.3 – Schematic representation of the different stages of a fracture healing: haematoma formation and local inflammation; then, angiogenesis is upregulated, cartilaginous callus is formed formation, blood vessels penetrate and endochondral ossification gives place to primitive woven bone; and finally remodeling replaces the woven for lamellar bone. FGF, fibroblast growth factors; TNF, tumor necrosis factor; PDGF, platelet-derived growth factors; BFGF, basic fibroblast growth factor; VEGF, Vascular endothelial growth factor; IL, interleukin; MSCs, mesenchymal stem cells.....	42
Figure 2.4 – Treatment-related complications of a bone infection.....	46
Figure 2.5 – <i>Staphylococcus aureus</i> (<i>S. aureus</i>) mechanism for persistent infection and subsequent osteoblast damage: microbial surface components recognizing adhesive matrix molecules (MSCRAMMs) and protein A (SpA), interact with osteoblasts surface following internalization; intracellularly they can i) damage lysosome membrane, avoiding degradation and escaping to cytosol, ii) form small colony variants (SCV) highly resistant to antibiotics and immune system, iii) produce deoxyribonucleic acid (DNA)-damaging reactive oxygen species (ROS), iv) induce osteoclast differentiation via receptor activator of nuclear factor kappa-B (RANKL) stimulation, v) induce cell apoptosis through tumor necrosis factor-related apoptosis-inducing ligand (TRAIL) stimulation and subsequent recognition by cell surface receptors, vi) produce cell membrane-damaging components, inducing cell death, and escape to infect other cells.	50
Figure 2.6 – Mechanisms of LL37 antimicrobial actions.	52
Figure 2.7 – Immunomodulatory actions of LL37 ⁶⁹	53
Figure 2.8 – (A) Amino acid sequence projections for LL37 and its LLKKK18 (LL18) peptide derivative, N-terminal (left) to C-terminal (right). To increase cationicity, Q22, D26, and N30 in LL37 were replaced by K22, K26, and K30 LL18. (B) α -helical peptide structures N-terminal (bottom) to C-terminal (up): LL37 has 37.8 % hydrophobic amino acids and a net charge of +6 at pH 7, whereas LL18 has 44.4 % and +8, respectively. At left, hydrophobic residues are shown in red, hydrophilic residues are shown in white, at right positive charges are highlighted in blue and negative charges in red (PyMOL software).	54
Figure 2.9 – Vitamin D3 metabolism.	57

Figure 2.10 – Classic signaling pathway of vitamin D3 metabolites. Serum 25-hydroxyvitamin D3 (25[OH]D3) is converted to 1 α ,25-dihydroxyvitamin D3 (1,25[OH]2D3) by mitochondrial 1 α -hydroxylase, initiating the signaling cascade by binding to vitamin D3 receptor (VDR), which dimers with retinoid X receptor (RXR), and binds to specific deoxyribonucleic acid (DNA) sequences, vitamin D3 response elements (VDRE), regulating the transcription of several genes. 1,25(OH)2D3-VDR-RXR complex then synthesizes cathelicidin as an inactive pro-peptide (hCAP18) which is cleaved upon release of the active LL37 by proteases ¹²³	59
Figure 2.11 – Vitamin D3, VD3, (-OH) succinylation reaction with succinic anhydride (-C(=O)OH), resulting in a succinylated VD3 with a carboxyl group end, suitable for covalent conjugation of other components (designed in ChemDraw software).	63
Figure 2.12 – Structure of dextrin (designed in ACD/ChemSketch software).	64
Figure 2.13 – Schematic representation of (A) dextrin oxidation with sodium periodate and (B) subsequent crosslinking reaction with adipic dihydrazide, resulting in hydrogel formation (designed in ACD/ChemSketch software).	73
Figure 3.1 – (A) Amino acid sequence projections for LL37 and its LL18 peptide derivative (N terminal to C terminal). To increase cationicity, Q22, D26, and N30 in LL37 were replaced by K22, K26, and K30 LL18. Positively charged residues are marked with “+” and negatively charged residues are marked with “-”. Hydrophobic residues are shown in red, hydrophilic residues are shown in white. Whereas LL37 has 37.8 % hydrophobic amino acids and a net charge of +6 at pH 7, LL18 has 44.4 % and +8, respectively. (B) α -helical structure of LL18 (PyMOL software).	88
Figure 3.2 – Surgical procedure in rat tibia defects: (A) exposed tibia; (B) bone drilling; (C) bone defect completed; (D) application of inoculum and (E) defect filled with hydrogel formulations.	96
Figure 3.3 – MC3T3-E1 cell viability assessed by the MTT assay: (A) Dose-dependent effect of HG _{dil} and its isolated components - ODEX and ADH - and non-oxidized dextrin; (B) Dose-dependent effect of LL18. Cells were exposed to different concentrations for 24 h. Results were calculated as percentage of the negative control and data are presented as mean \pm SD (n = 3), * <i>p</i> < 0.05, ** <i>p</i> < 0.01, *** <i>p</i> < 0.001 vs HG _{dil} . ADH, adipic acid dihydrazide; HG _{dil} , diluted hydrogel; ODEX, oxidized dextrin. HG _{dil} refers to the sum of ODEX and ADH concentrations. The concentrations of the pure components, which are the same as in HG _{dil} , can be found in Table 3.1	100

Figure 3.4 – Dose-response (cell viability) curves of MC3T3-E1 cells exposed for 24 h to different concentrations of: **(A)** diluted dextrin-based hydrogel (HG_{dil}); **(B)** oxidized dextrin (ODEX); and **(C)** LLKKK18 (LL18), assessed by the MTT reduction assay, for 50 % cytotoxic concentration (CC₅₀) calculation. Data are presented as mean ± SD (n = 3)..... 100

Figure 3.5 – Percentage of hemolysis caused by the hydrogel (HG) and its degradation products at equivalent concentrations, upon their interaction with dog red blood cells for 1 hour: **(A)** empty HG and **(B)** HG loaded with 429 µM of LL18, both 5-fold and 10-fold diluted. Data are expressed as percentage relative to the control and presented as mean ± SD (n=3). Diluted hydrogel (HG_{dil}) refers to the sum of oxidized dextrin (ODEX) and adipic dihydrazide (ADH) concentrations. Tested concentrations refer to HG_{dil}; the concentrations of the pure components can be found in **Table 3.3**. 102

Figure 3.6 – pH changes of the dextrin-based hydrogel until complete degradation in phosphate-buffered saline buffer, pH 7.4. Results expressed as mean ± SD (n = 3). 103

Figure 3.7 – Cumulative release profile of LLKKK18 (LL18)-loaded hydrogel (HG; lines) and HG wet weight loss (bars) calculated in specified time-points within 192 hours, performed at pH 7.4 (grey) and 5.8 (black) at 37 °C. Data are presented as mean ± SD (n=6)..... 104

Figure 3.8 – Bone defects of rat tibias after sacrifice, 7 days post-treatment, representative of: **(A)** an infected bone and **(B)** a non-infected bone..... 105

Figure 3.9 – Mean bacterial counts in colony forming units (CFU)/g bone from implanted-site after a 7-day treatment of MRSA-induced osteomyelitis with: **(A)** increasing concentrations of LLKKK18 (LL18), including empty hydrogel (HG) and a vancomycin (VH)-loaded formulation; and **(B)** increasing concentrations of VH-loaded formulations in combination with a fixed LL18 concentration. Results are presented as mean ± SD (n=10), (**p* < 0.05, ***p* < 0.01, ****p* < 0.001). C1, C2, C3 and C4 correspond to 86; 215; 300 and 429 µM of LL18, respectively. VH1, VH2 and VH3 correspond to 10; 24 and 483 µM..... 107

Figure 3.10 – Haematoxylin- and eosin-stained histological sections of the left and right tibias of rats 7 days after surgery (scale bars=500 µm). Periosteal inflammation (asterisk), intraosseous acute inflammation (black arrow), bone necrosis (black arrowhead) and bacteria (dashed arrow). C1, C2, C3 and C4 correspond to 86; 215; 300 and 429 µM of LL18, respectively. VH1, VH2 and VH3 correspond to 10; 24 and 483 µM..... 108

Figure 3.11 – Haematoxylin- and eosin-stained histological sections of tibias, displayed by the four histopathological parameters analyzed. Histological signs described in the scoring system are evidenced with high magnification (scale bars = 50 μm or 100 μm). IAI, Intraosseous acute inflammation; ICI, intraosseous chronic inflammation; PI, periosteal inflammation; BN, bone necrosis; C1, C2, C3 and C4 correspond to 86; 215; 300 and 429 μM of LL18, respectively. VH1, VH2 and VH3 correspond to 10; 24 and 483 μM 109

Figure 3.12 – Histopathological scores of: **(A)** increasing concentrations of LLKKK18 (LL18), including empty hydrogel (HG) and a vancomycin hydrochloride (VH)-loaded formulation; and **(B)** increasing concentrations of VH-loaded formulations in combination with a fixed LL18 concentration. Results are presented as mean \pm SD (n=10), (* p < 0.05, ** p < 0.01, *** p < 0.001). Black, green and orange * were compared to HG + LL18 C4, No treatment, and HG **(A)** or HG + LL18 C3 **(B)** conditions, respectively. IAI, intraosseous acute inflammation; ICI, intraosseous chronic inflammation; PI, periosteal inflammation; BN, bone necrosis. 110

Figure 4.1 – Synthesis of vitamin D3-Dextrin (VD3-Dex) conjugates. **(A)** Vitamin D3 (VD3) was succinylated (SucVD3) by reaction with succinic anhydride in pyridine solvent using a catalytic amount of dimethylaminopyridine (DMAP) as nucleophilic catalyst. **(B)** VD3-Dex was prepared by a two-step procedure: first, SucVD3 was conjugated to dextrin polymer via ester bonding under carbodiimide (EDC) activation in the presence of DMAP catalyst, in dimethyl sulfoxide (DMSO) as solvent; next **(C)** the SucVD3-dextrin conjugate was allowed to react *in situ* with succinic anhydride under DMAP catalysis; the final conjugate was purified by dialysis against water and freeze-dried, then unreacted SucVD3 was eliminated by ethanol extraction..... 121

Figure 4.2 – **(A)** ATR-Fourier-transform infrared spectroscopy (ATR-FTIR) studies; **(B)** Differential scanning calorimetry (DSC) thermograms; **(C)** thermogravimetric analysis (TGA) curves; **(D)** excitation spectra of pyrene as a function of VD3-Dex concentration and **(E)** plot of intensity peak ratios (I_{391}/I_{372}) versus log C, to determine critical micellar concentration (CMC). VD3, Vitamin D3; SucVD3, succinylated vitamin D3, VD3-Dex, vitamin D3-dextrin conjugate..... 132

Figure 4.3 – Influence of negative surface charge, VD3:dextrin preparation ratio, and freeze-drying process in the association efficiency (AE) of LL18 with micelles: **(A)** 1:4 vs 1:8 molar ratio of succinylated VD3-Dex vs 1:4 non-succinylated micelles, and **(B)**: before and after freeze-dry for 1:4 ratio succinylated VD3-Dex micelles. Micelles were prepared at 1 mg/mL in LL18-dissolved PBS solution. Results presented as mean \pm SD, n=3, (* p < 0.05, ** p < 0.01, *** p < 0.001)..... 134

Figure 4.4 – **(A)** Representative Cryo-SEM microphotographs of unloaded and LL18-loaded VD3-Dex micelles before and after a four-month storage in phosphate-buffered saline solution at 4 °C (magnification of 50,000x, scale bars = 1 μm). **(B)** Stability studies: dynamic light scattering measurements performed each month, from day 0 to 4 months. Formulation of 100μg:1mg peptide:micelle ratio, dissolved at 1 mg/mL of micelle..... 135

Figure 4.5 – Dose-dependent effect assessed by the MTT assay in **(A and C)** MC3T3-E1 and **(B and D)** BMMΦ. Cells were exposed to different concentrations for 24 h. Results calculated as percentage of the negative control and presented as mean ± SD, n = 3, (**p* < 0.05, ***p* < 0.01, ****p* < 0.001). Formulation of 100μg:1mg peptide:micelle ratio. 137

Figure 4.6 – Dose-response (cell viability) curves of cells exposed for 24 h to different concentrations of LLKKK18 (LL18) and loaded-LL18 (left), micelles and LL18-loaded micelles (right) in: **(A)** MC3T3-E1 and **(B)** BMMΦ. Results assessed by the cytotoxicity assay, for 50 % cytotoxic concentration (CC₅₀) calculation (n = 3)..... 137

Figure 4.7 – Percentage of hemolysis upon 5h incubation. Data are expressed as percentage relative to the control and presented as mean ± SD, n = 3, (**p* < 0.05, ***p* < 0.01, ****p* < 0.001)..... 138

Figure 4.8 – Representative scanning electron cryo-microscopy microphotographs of **(A)** FITC-VD3-Dex (1:40 mass ratio) and **(B)** LL18 (100 μg/mL)-loaded FITC-VD3-Dex, in phosphate-buffered saline solution at 1 mg/mL (magnification of 50,000×. Scale bars = 1 μm). 139

Figure 4.9 – Subcellular localization analysis by a confocal laser scanning microscope (CLSM) of unloaded and LL18-loaded FITC-VD3-Dex, after 1 h incubation, in MC3T3-E1 (60x magnification) and BMMΦ (100x magnification). Formulation of 25 μg:1 mg peptide:micelle ratio, incubated at 0.5 mg/mL. Green signal refers to FITC, and red signal to the lysosome probe. 142

Figure 4.10 – Subcellular localization analysis using a confocal laser scanning microscope (CLSM) of free and micelle-loaded LL18-TAMRA after 1 h incubation MC3T3-E1 (60x magnification) and BMMΦ (100x magnification). Formulation of 25 μg:1 mg peptide:micelle ratio, incubated at 0.5 mg/mL. Green signal refers to lysosome probe, red signal to TAMRA..... 143

Figure 4.11 – Subcellular localization analysis using a confocal laser scanning microscope (CLSM) of: (left) LL18-TAMRA-loaded FITC-VD3-Dex micelles after a 24 h incubation; and (right) free LL18-TAMRA and empty FITC-VD3-Dex micelles after 1 h incubation each, separately, in MC3T3-E1 (60x magnification)

and BMM Φ (100x magnification). Formulation of 25 μg :1 mg peptide:micelle ratio, incubated at 0.5 mg/mL. Lysosomes are not marked, green signal refers to FITC, red signal to TAMRA..... 144

Figure 4.12 – Concentration dependence of the intracellular uptake of FITC-VD3-Dex and LL18-loaded FITC-VD3-Dex by BMM Φ cells, after 1 h incubation: **(A)** electronic microscope observation (20x magnification), and **(B)** uptake quantification. Results presented as mean \pm SD, n = 3, (* p < 0.05, ** p < 0.01, *** p < 0.001). Formulation of 100 μg :1 mg peptide:micelle ratio..... 145

Figure 4.13 – **(A)** Albumin (1 % w/v) denaturation after 3h at 70 $^{\circ}\text{C}$ (n=3), **(B)** quantification (%) of open wound area in MC3T3-E1 cells after 24 h (n=6), and **(C)** antimicrobial activity against *S. aureus* after 24 h (n=4). Results presented as mean \pm SD (* p < 0.05, ** p < 0.01, *** p < 0.001). Formulation of 100 μg :1 mg peptide:micelle ratio. 148

Figure 4.14 – Dose ($\mu\text{g}/\text{mL}$)-response results for MC3T3-E1 cells exposed up to 72 h to different concentrations of mitomycin C, assessed by the MTT reduction assay. Results are expressed in absorbance values. Data are presented as mean \pm SD (n = 3)..... 149

Figure 5.1 – Sequence of events demonstrating preparation and handling of hydrogel formulations, accompanying the surgical procedure time length. BL $\text{\textcircled{R}}$ P, Bonelike $\text{\textcircled{R}}$ Poro; ODEX, oxidized-dextrin; ADH, adipic dihydrazide; hDPSCs, human dental pulp stem cells. 163

Figure 5.2 – Micro-computed tomography protocol visually exemplified. ROI, region of interest..... 164

Figure 5.3 – Human dental pulp stem cells (hDPSCs) cultured at passage 3, with a \sim 90% confluency, prior to trypsinization, cell viability assessment by the Trypan Blue TM exclusion assay, and dosage preparation..... 165

Figure 5.4 – Dissolution of Bonelike $\text{\textcircled{R}}$ Poro, expressed as the amount of calcium ions (Ca^{2+}) release as a function of time in oxidized-dextrin (ODEX) solution pH 5.2, and phosphate-buffered saline (PBS) buffer pH 7.2, up to day 15. Data are presented as mean \pm SD (n=5). 166

Figure 5.5 – SEM images of (A and D) Bonelike $\text{\textcircled{R}}$ Poro (BL $\text{\textcircled{R}}$ P) granules before immersion, (B and E) BL $\text{\textcircled{R}}$ P after 15 days of immersion in phosphate-buffered saline (PBS) solution and (C and F) in oxidized-dextrin (ODEX) solution. Macropores of BL $\text{\textcircled{R}}$ P are indicated by green arrows (A to C: 500 \times magnification, scale bars=100 μm , E to G: 4500 \times magnification, scale bars=10 μm). 166

Figure 5.6 – Compressive test: preparation of (A) disc-form HG + BL®P material in 12-diameter molds before (B) positioned under the probe, and (C) stress–strain curves for HG and HG + BL®P formulations. Data are presented as mean ± SD (n=3). HG, hydrogel; BL®P, Bonelike® Poro. 167

Figure 5.7 – **(A)** Frontal bone critical-sized defects performed in sheep, fulfilled with formulations: control (left-bottom); BL®P mixed with autologous blood (right-bottom); dextrin-based hydrogel (HG) + BL®P + hDPSCs (left-upper) and HG + BL®P (right-upper). **(B)** Harvested frontal bone after fixation. BL®P, Bonelike® Poro; HG, hydrogel; hDPSCs, human dental pulp stem cells. 168

Figure 5.8 – Representative micro-computed tomography (CT) slice images of the implantation sites after 3 and 6 weeks of treatment with different formulations. BL®P, Bonelike® Poro; HG, hydrogel; hDPSCs, human dental pulp stem cells. 170

Figure 5.9 – Quantification of the new bone (A), total bone (B) and granules (C) volumes in implanted sites after 3 and 6 weeks of treatment. Total bone refers to the sum of new bone with granules. Statistical analysis was performed within each time-point using one-way analysis of variance (ANOVA) followed by the post-hoc Tukey test (** $p < 0.01$ and *** $p < 0.001$). Results are shown as mean values ± SD (n = 5). BL®P, Bonelike® Poro; HG, hydrogel; hDPSCs, human dental pulp stem cells. 170

Figure 5.10 – Haematoxylin- and eosin-stained histological sections from implanted sites after 3 and 6 weeks of treatment. HG, hydrogel; hDPSCs, human dental pulp stem cells; BL®P, Bonelike® Poro granules; CT, connective tissue; NB, new bone; V, vessel; Ob, osteoblasts; Ocy, osteocytes; MB, mature bone; Mg, macrophage. Scale bar 500 µm (larger images) and 100 µm (smaller images). 171

Figure 5.11 – Masson's trichrome-stained histological sections from implanted sites after 3 and 6 weeks of treatment. HG, hydrogel; hDPSCs, human dental pulp stem cells; BL®P, Bonelike® Poro granules; CT, connective tissue; NB, new bone; V, vessel; Ob, osteoblasts; Oc, osteoclasts; Ocy, osteocytes; MB, mature bone. Scale bar 500 µm (larger images) and 100 µm (smaller images). 172

Figure 6.1 – Study designed for a two-tailed analysis with Student's t-test or Wilcoxon signed rank test (depending on the normality of the results), with a confidence interval (statistical power) of 95% (1-β=0.95). G*Power 3.1.9.2 software was used to define sample size. 181

Figure 6.2 – DEXGEL Bone preparation procedure. 186

Figure 6.3 – Time-line for DEXGEL Bone preparation and handling. 187

Figure 6.4 – Clinical images illustrating the procedures sequentially ordered from tooth extraction to dental implant placement. 188

Figure 6.5 – CONSORT flow diagram of this study. 191

Figure 6.6 – Toluidine blue-stained representative photomicrographs of the grafted site 6 months post-implantation: **(a)** DEXGEL Bone group and **(b)** BL® group. New bone (NB), BL® remains (BL) and connective tissue (CT). Magnification from left to right: **(a)** 1x, 3x and 10x; **(b)** 1x, 3x and 20x. 192

Figure 6.7 – Quantitative histomorphometric results of DEXGEL Bone and Bonelike by Biosskin® (BL®) conditions: total bone **(a)**, new bone formation **(b)**, reminiscent BL® granules **(c)**, and connective tissue **(d)** 6 months after implantation. Statistical analysis was performed using Student's t-test ($*p < 0.05$). Results are shown as mean percentages \pm SD (n = 6). Total bone refers to the sum of new bone with granules. 193

Figure 6.8 – Quantitative bone volume results (cm³) obtained from computer tomography (CT) analysis, at the implantation time and after 6 months. Results are shown as mean percentages \pm SD (n = 6). The differences in bone volume and time-point between DEXGEL Bone (test) and Bonelike by Biosskin®, BL®, (control) groups were analyzed using Student's t-test ($*p < 0.05$)..... 195

Figure 6.9 – Implant Stability Quotient (ISQ) results of DEXGEL Bone and Bonelike® (BL®) groups, upon dental implant placement. Statistical analysis was performed using Student's t-test ($*p < 0.05$). Results are shown as mean values \pm SD (n = 6)..... 196

LIST OF TABLES

Table 2.1 – Summary of the outcomes influenced by three different LL37 loading mechanisms ⁹⁸	56
Table 2.2 – Summary of constructs making use of dextrin versatility to create novel constructs/systems for biomedical purposes.	69
Table 3.1 – Concentrations of HG _{dil} , oxidized dextrin (ODEX) and adipic dihydrazide (ADH) solutions tested on the cytotoxicity assay. HG _{dil} , diluted dextrin-based hydrogel, refers to the sum of ODEX and ADH concentrations, diluted by a factor in the range of 28 to 443.	91
Table 3.2 – Concentrations of the HG _{dil} , oxidized-dextrin (ODEX) and LLKKK18 (LL18) tested in the cytotoxicity assay and used for CC ₅₀ calculation. HG _{dil} , diluted dextrin-based hydrogel, refers to the sum of ODEX and ADH concentrations	92
Table 3.3 – Concentrations of the HG _{dil} , oxidized dextrin (ODEX), adipic acid dihydrazide (ADH), dextrin and LL18 tested on hemolysis assay. HG _{dil} , diluted dextrin-based hydrogel, refers to the sum of ODEX and ADH concentrations, diluted by a factor of 5 and 10.	93
Table 3.4 – Concentrations of the HG _{dil} and correspondent concentrations of ODEX and ADH tested for antimicrobial activity. ADH, adipic acid dihydrazide; HG _{dil} , diluted dextrin-based hydrogel; ODEX, oxidized dextrin.	95
Table 3.5 – Concentration of LLKKK18 (LL18) and vancomycin hydrochloride (VH) tested <i>in vivo</i> : (A) increasing concentrations of LL18, including empty hydrogel (HG) and a VH-loaded formulation; and (B) increasing concentrations of VH-loaded formulations in combination with a fixed LL18.	97
Table 3.6 – Microscopic histological parameters and scoring system. Adapted from Fukushima <i>et al.</i> ⁴⁶	98
Table 3.7 – Minimal, and half-minimal, inhibitory concentrations, MIC and MIC ₅₀ , values of vancomycin hydrochloride (VH), LLKKK18 (LL18), diluted hydrogel (HG _{dil}) and its isolated components, oxidized-dextrin (ODEX) and adipic dihydrazide (ADH).	105
Table 4.1 – Drug loading (DL) efficiency % for different formulations with initial peptide concentration varying from 25 to 150 µg/mL.	134
Table 4.2 – Dynamic light scattering measurements of unlabeled and FITC-VD3-Dex micelles, dissolved in phosphate-buffered saline solution at a constant concentration of 1 mg/mL, and quantification of	

conjugated FITC by fluorescence spectroscopy ($\lambda_{ex}477/\lambda_{em}517$). Results for LL18 or LL18-TAMRA-loaded micelles are also shown. Results are expressed as mean \pm SD (n=3)..... 140

Table 4.3 – Summary balance of cytotoxicity and antimicrobial activity..... 149

Table 5.1 – Composition and properties of BL®P. 159

Table 5.2 – Composition of formulations applied *in vivo*. 161

Table 5.3 – Compressive modulus, stress (at 70 % strain) for HG and HG + BL®P formulations. Data are presented as mean \pm SD (n=3). 167

Table 6.1 – Overall study procedures listed by order of accomplishment. 182

Table 6.2 – Inclusion and exclusion criteria. 183

Table 6.3 – List of participants. 183

Table 6.4 – Composition of BL®. 185

Table 6.5 – Gelation time of HG upon mixture of ODEX and ADH, expressed in seconds (n = 3). After production and sterilization, ODEX (30 % w/v) and ADH (3.76 % w/v) solutions were separately kept at 4 °C and a gelling test was performed at different time-points by mixing both in a proportion of 7:3 volume, respectively. Freshly prepared ADH was also used for crosslinking in each time-point with the ODEX stored over time..... 190

Table 6.6 – Bone density classification by Misch ³⁷. 194

Table 6.7 – Bone density (HU) of DEXGEL Bone and BL® groups, for clinician interpretation. Results are shown as mean \pm SD (n = 6). The differences in bone volume and time-point between DEXGEL Bone (test) and Bonelike by Biosckin®, BL®, (control) groups were analyzed using Student’s t-test ($p < 0.05$). 194

Table 6.8 – Summary of mean and p value results, assessing the effect size of each outcome by Hedges's g calculations. 197

LIST OF ABBREVIATIONS AND ACRONYMS

A

- ADH** – Adipic dihydrazide;
AE – Association efficiency;
ALP – Alkaline phosphatase;
AMP(s) – Antimicrobial peptides(s);
ANOVA – One-way analysis of variance;
ATP – Adenosine triphosphate;
ATR-FTIR – Attenuated total reflectance Fourier transform infrared spectroscopy;

B

- BFGF** – Basic fibroblast growth factor;
BHI – Brain heart infusion;
BL® – Bonelike by Biosskin®;
BL®P – Bonelike® Poro;
BMMΦ – Bone marrow-derived macrophages;
BMP – Bone morphogenetic protein;

C

- Ca** – Calcium;
Ca/P – Calcium/phosphate;
CAMP – cathelicidin antimicrobial peptide;
CC₅₀ – 50 % cytotoxic concentration
CE – *Conformité Européene*
CEIC – National Ethics Commission for Clinical Research;
CFU – Colony forming units;
CI – Confidence interval;
CLSM – Confocal laser scanning microscope;
CMC – Critical micellar concentration;

CNPD – National Commission for the Protection of Data;

COVID-19 – Coronavirus disease 2019;

Cryo-SEM – Scanning electron cryo-microscopy

CT – Computed tomography;

D

- DBP** – Vitamin D3-binding protein;
DCM – Dichloromethane;
DGAV – Direção-Geral de Alimentação e Veterinária;
DGS – Direção-Geral da Saúde
dH₂O – Distilled water;
DL – Drug loading;
DLS – Dynamic light scattering;
DMAP – Dimethylaminopyridine;
DMEM – Dulbecco's Modified Eagle Medium;
DMSO – Dimethyl sulfoxide;
DNA – Deoxyribonucleic acid;
DPBS – Dulbecco's phosphate-buffered saline;
DSC – Differential scanning calorimetry;
DSPE-PEG – 1,2-distearoyl-sn-glycero-3-phosphoethanolamine-Poly(ethylene glycol)
E
ECM – Extracellular matrix;
EDC – 1-ethyl-3-(3-dimethylaminopropyl) carbodiimide hydrochloride;
EE – Encapsulation efficiency;

EUDAMED – European Databank on Medical Devices;

F

FBS – Fetal bovine serum;

FDA – Food and Drug Administration;

FGF – Fibroblast growth factors;

FITC – Fluorescein isothiocyanate;

G

GRAS – Generally recognized as safe;

H

H&E – Haematoxylin and eosin;

HA – Hydroxyapatite;

HCl – hydrochloric acid;

hDPSCs – Human dental pulp stem cells;

HG(s) – Hydrogel(s);

HG_{dil} – Diluted dextrin-based hydrogel;

HLA-DR – Human leucocyte antigen – DR isotype;

HSCs – Hematopoietic stem cells;

HU – Hounsfield units;

ICP-OES – Inductively coupled plasma optical emission spectroscopy;

I

IL – Interleukin;

INFARMED – National Authority of Medicines and Health Products I.P.;

ISQ – Implant Stability Quotient;

L

LL18 – LLKKK18;

LPS – Lipopolysaccharide;

M

MD(s) – Medical device(s)

MIC – Minimal inhibitory concentration

MIC₅₀ – Half-minimal inhibitory concentration

mRNA – Messenger ribonucleic acid;

MRSA – Methicillin-resistant *Staphylococcus aureus*;

MSCRAMMs – Microbial surface components recognizing adhesive matrix molecules;

MSCs – Mesenchymal stem cells;

MTT – 3-[4,5-Dimethylthiazole-2-yl]-2,5-diphenyl tetrazolium bromide;

N

NPs – Nanoparticles;

O

ODEX – Oxidized dextrin;

OM – Osteomyelitis;

P

p – p-value;

PBS – Phosphate-buffered saline;

PDGF – Platelet-derived growth factors;

PEG – Poly(ethylene glycol)

PLGA – Poly(lactic-co-glycolic acid)

PMMA – polymethylmethacrylate;

PMN – peripheral multinucleated cells;

PVA – Poly(vinyl alcohol);

R

RANKL – Receptor activator of nuclear factor kappa-B ligand;

RBCs – Red blood cells;

RFA – Resonance Frequency Analysis;

RGD – Arginine-glycine-aspartic acid;

rhEGF – Recombinant human epidermal growth factor;

RNA – Ribonucleic acid

RNEC – Registo Nacional de Estudos Clínicos; TCP, Tricalcium phosphate.

ROI – Circular Region of Interest;

ROS – Reactive oxygen species;

RT-PCR – Real-time polymerase chain reaction;

RXR – Dimerization with retinoid X receptor;

S

S. aureus – *Staphylococcus aureus*;

SBM – Starch binding module;

SCV – Small colony variants;

SD – Standard deviation;

SEM – Scanning Electron Microscope;

SI – Selectivity index;

siRNA – Small interfering ribonucleic acid;

SpA –protein A

SucVD3 – Succinylated vitamin D3;

T

TAMRA – carboxytetramethyl-rhodamine;

TCP – Tricalcium phosphate

TGA – Thermogravimetric analysis;

TGF- β – Transforming growth factor-beta;

TLR – Toll-like receptor;

TNF- α – Tumor necrosis factor-alpha;

TRAIL – Tumor necrosis factor-related apoptosis-inducing ligand;

U

UV – Ultraviolet;

V

V-ATPase – Vacuolar-type ATPase;

VD2 – Vitamin D2;

VD3 – Vitamin D3;

VDR – Vitamin D3 receptor;

VDRE – Vitamin D3 response elements;

VEGF – Vascular endothelial growth factor;

VH – Vancomycin hydrochloride;

VOI – Volume of interest;

W

Wnt – Wingless/integrase-1;

1,25(OH)2D3 – 1 α ,25-dihydroxyvitamin D3;

25(OH)D3 – 25-hydroxyvitamin D3

CHAPTER 1

1. MOTIVATION AND OUTLINE

This chapter describes the context and motivation driving this work. The objectives, the outline of the thesis, and the scientific output are also listed.

1.1. Context and Motivation

Dextrin has become a resourceful tool that partakes in a variety of constructs, exerting diverse roles to meet specific therapeutic demands ¹. However, despite its extensive use for human consumption as a nutraceutical or excipient, drug-delivery pharmaceutical technologies are uncommon in clinical practice. Major advantages include cost, abundant natural source, biocompatibility, biodegradability, solubility, and resourcefulness for a variety of modification strategies. Regarding bone healing, dextrin has been reported to stimulate the proliferation and differentiation of osteoblasts ², revealing a beneficial adjuvant role rather than simply providing a vehicle for pharmaceuticals. Overall, dextrin displays an interesting combination of advantages for drug delivery purposes, from development-stage processes to therapeutic efficacy, that may outperform other well-established carriers.

Hard-to-treat bone infections are still a common and serious burden, even in developed countries. There is a dual challenge compromising patient recovery: rapidly evolving microbe resistance to antibiotics and impaired bone healing ^{3,4}. In this sense, this work intends to develop a novel formulation featuring both antimicrobial and bone repair properties. Antimicrobial peptides emerge as an alternative to conventional antibiotics for their high spectrum of antimicrobial ability and a low tendency for microbe resistance ⁵. Cathelicidin is proposed as a smart option for bone infections therapy for reasons such as: i) potent anti-staphylococcal activity ^{6,7}, the most causative species in bone infections ⁸⁻¹¹, ii) inhibition of biofilm formation ^{6,12} and lipopolysaccharide activity ¹³; iii) pro-angiogenic activity ¹⁴⁻¹⁶; iv) promotes wound healing ^{15,16}; v) enhances bone regeneration ^{17,18}; and vi) clinical safety and remarkable healing rates as demonstrated in the treatment of chronic leg ulcers by topical treatment ¹⁹. LLKKK18 (LL18) is an 18-length amino acid peptide designed from LL37 – and therefore cheaper to produce – displaying improved features, such as higher cationicity and hydrophobicity. LL18 has been reported to: i) be three-fold more effective in the killing of mycobacteria than LL37 ²⁰, ii) display higher chemoattractant activity, decreased toxicity, and binding to plasma protein ²¹, and iii) improve burn wound healing in a rat model, advocating its angiogenic and chemoattractant potential ²². Nevertheless, LL18 is mostly unexplored and may bear a variety of beneficial tissue healing functions, beyond the antimicrobial activity.

Vitamin D3 (VD3) has been drawing attention for its role in fighting infections. The reason relies on the active metabolite, $1\alpha,25$ -dihydroxyvitamin D3, $1,25(\text{OH})_2\text{D}_3$, that acts by interacting with a nuclear vitamin D receptor (VDR), a ligand-activated transcription factor that controls gene expression through activation of gene transcription at specific deoxyribonucleic acid (DNA) sequences, the vitamin D3 response elements (VDRE) ²³. Cathelicidin can be up-regulated by a VD3-dependent mechanism, through

VDR, acting as a secondary messenger driving VD3-mediated host response to infection^{24,25}. As the VDR has been found in most cell types, VD3 is itself a pleiotropic, repair and maintenance agent acting across a wide variety of tissues. VD3 was reported to be locally activated in osteoblasts and exerted similar effects on cell differentiation as the biologically active form²⁶. The presence of activation machinery at a cellular level endows VD3 with the capability of acting in an autocrine manner in the local environment, supporting the rationale behind the use of this safer and affordable form via local administration. Enhanced levels of angiogenesis, vascularization, osteogenesis and bone structure differentiation were achieved using a VD3 enriched delivery system, successfully reconstructing artificial bone defects in the rat mandible²⁷. Clinically, antibiotic-associated VD3 granules have been topically applied to treat infected open wounds²⁸, including diabetic foot ulcer with osteomyelitis (OM), with successful results and minimum systemic side effects²⁹. Overall, VD3 is simultaneously evolving into a booster of immunity and inexpensive tissue healing adjuvant for bone infection therapy. Bioavailability is limited by low solubility due to its hydrophobic nature which, together with its cytotoxicity profile, could be diminished by a sustained delivery platform. In this sense, dextrin was used in this work to solubilize and shield LL18 and VD3 towards the development of a novel formulation with antimicrobial and bone repairing properties. This nano-scaled system is intended for intralesional administration, the preferable form of administration in bone infections. Taking advantage of an injectable oxidized dextrin (ODEX)-based hydrogel (HG) previously developed by our group, conditions are gathered to develop (in future work) a minimally invasive delivery system, that could retain the nano-construct at the lesion site for a longer period. For this reason, in this thesis, this HG is intended to be submitted to an *in vivo* rat model of OM. Parallely, the same HG is applied in a clinical study for the first time, providing the ultimate safety validation of (oxidized) dextrin-derived delivery platform for bone regeneration therapies. This step is set to improve medical confidence and encourage the translation into clinics of other dextrin-derived biomaterials.

1.1 Aims and Outline

This work aims at exploring dextrin as a platform for drug delivery, particularly tailored for bone infections. Non-antibiotic LL18 and VD3, combining antimicrobial and bone healing properties, are loaded into a dextrin-based nanocarrier, with the purpose of improving their solubility, toxicity and degradation profiles, and, subsequently, their biological effect. Parallely, an OM rat model was, for the first time, used to show dextrin HG suitability for the delivery of antimicrobials in a bone-infected context. Importantly, this trial also provides the first insight into (free) LL18 performance in the treatment of OM *in vivo*. Having that

said, the aforementioned nano-construct aims at enhancing LL18 biological activity in the future, by means of a shielding effect, further added by VD3 presence and culminating in a water-soluble dual-delivery nano-system suitable for incorporation into dextrin HG. This work also comprises the final stage of the project titled “iBONE therapies: advanced solutions for bone regeneration” (n° 003262), including a pre-clinical test and a clinical study of ODEX HG, previously developed by our group. The HG serves as a carrier for bioactive compounds and is evaluated in terms of handling, defect filling, and safety validation.

In summary, the aims of this thesis included: i) providing insight into cathelicidin-derived LL18 performance and ODEX-based HG suitability in the development of an effective formulation to treat OM; ii) exploring dextrin as a solubility- and shield-provider nanocarrier for LL18 and VD3; iii) perform a pre-clinical assessment of the HG as a carrier of hDPSCs and BL®P in the management of critical-sized bone defects; and iv) report the first-in-human clinical study of the HG as a carrier of BL® in the management of the alveolar socket. This thesis is structured in chapters that cover the research aims stated above, as indicated below.

Chapter 1 comprises the context and motivation driving this work, the aims and outline of this thesis, and the resulting scientific output.

Chapter 2 presents a description of the state-of-the-art, covering the subjects relevant to the outcomes, as follows: i) Bone physiology and remodeling, ii) OM and *staphylococcus aureus* (*S. aureus*) as the primary pathogen, iii) Cathelicidin and its LL18 derivative, iv) VD3 as an antimicrobial and bone repairing agent; and v) Dextrin as a platform for drug delivery and benefits for bone healing.

Chapter 3 reports ODEX HG use as a minimally invasive microbicide delivery system for OM treatment in a rat model, and the balance between antimicrobial effects and host cellular toxicity provided by LL18 and vancomycin hydrochloride. We show that combined doses of both can be optimized as to exert a potent antimicrobial effect with minimal tissue damage, culminating in a formulation with the potential to treat *S.aureus*-infected bone. This work also served as the first insight into ODEX HG and LL18 performance *in vivo*, in a bone infection context.

Chapter 4 aimed at developing an innovative construct for OM treatment, combining antimicrobial and bone healing properties. For this, dextrin was explored as a nanocarrier for VD3 and LL18 simultaneously, with the expectation of enhancing the performance of free LL18 described in the previous chapter. This chapter provides a thorough biophysical and functional characterization of LL18-loaded dextrin-VD3 micelles tailored for bone infections.

Chapter 5 describes a pre-clinical study of dextrin-based HG as a carrier of micro and macroporous Bonelike® Poro and human dental pulp stem cells in ovine critical-sized calvaria defects. Bone samples were collected after 3 and 6 weeks of treatment for histological and micro-computed tomography analysis.

Chapter 6 reports the first-in-human study of dextrin-based HG as a carrier of Bonelike by Bioskin® in the management of alveolar ridge preservation following tooth extraction, culminating in dental implant placement 6-months post-treatment. Results included histological and histomorphometric analysis, bone volume and density, and primary stability of the implant. The HG was evaluated for the purpose of providing easier granules handling and better defect filling, without compromising bone regeneration, and receiving safety validation for human use. This work was conducted at Hospital da Luz, Coimbra.

Chapter 7 summarizes the main achievements and conclusions of this work, and highlights future perspectives.

1.2 Scientific Output

Papers in International Peer-Reviewed Journals

- I. Chapter 2: Cristelo C, **Machado A**, Sarmiento B, Gama M. The roles of vitamin D and cathelicidin in type 1 diabetes susceptibility. *Endocrine Connections*, 10(1):R1-R12 (2021).
- II. Chapter 3: **Machado A**, Pereira L, Silva V, Pires I, Prada J, Poeta P, Maltez L, Pereira JE, Gama M. Injectable Hydrogel as a Carrier of Vancomycin and a Cathelicidin-derived Peptide for Osteomyelitis Treatment. *Journal of Biomedical Materials Research – Part A*, 110(11): 1786-1800 (2022).
- III. Chapter 4: **Machado A**, Martins JA, Gama M. Therapeutic partnership of cathelicidin-derived LLKKK18 loaded into vitamin D-dextrin micelles tailored for bone infections. (Submitted to *Journal of Controlled Release*).
- IV. Chapter 5: **Machado A**, Pereira L, Pereira JE, Maltez L, Brandão A, Alvites R, Sousa AC, Branquinho M, Caseiro AR, Pedrosa SS, Maurício AC, Pires I, Prada J, Santos JD, Gama M. Dextrin Hydrogel Loaded with a Macroporous Bone-like Scaffold and Dental Pulp Stem Cells for Critical-sized Defect Repair. (Submitted to *Materialia*)
- V. Chapter 6: **Machado A**, Pereira I, Costa F, Brandão A. Pereira JE, Maurício AC, Santos JD, Amaro I, Falacho R, Coelho R, Cruz N, Gama M. Randomized Clinical Study of Injectable Dextrin-based Hydrogel as a Carrier of a Synthetic Bone Substitute. *Clinical Oral Investigations*. (Accepted).

Oral presentations at international conferences

I. **Machado A**, Pereira I, Costa L, Silva V, Pires I, Prada J, Poeta P, Pereira JE, Gama M. Local delivery of LLKKK18 antimicrobial peptide released from oxidized dextrin hydrogel to treat osteomyelitis. 30th Conference of the European Society for Biomaterials (ESB) – Dresden, Germany. 9 – 13th (September 2019).

Poster presentations at international conferences

I. **Machado A**, Gama M, Martins J. Therapeutic partnership of cathelicidin-derived LLKKK18 loaded into vitamin D-dextrin micelles tailored for bone infections. 16th European Symposium on Controlled Drug Delivery – Egmond aan Zee, The Netherlands. 12 – 15th (April 2022).

II. **Machado A**, Martins J, Pereira JE, Gama M. Dextrin: a platform for the development of Drug Delivery Systems. 13th International Chemical and Biological Engineering Conference 2018 Conference – Aveiro, Portugal. 2 – 4th (October 2018).

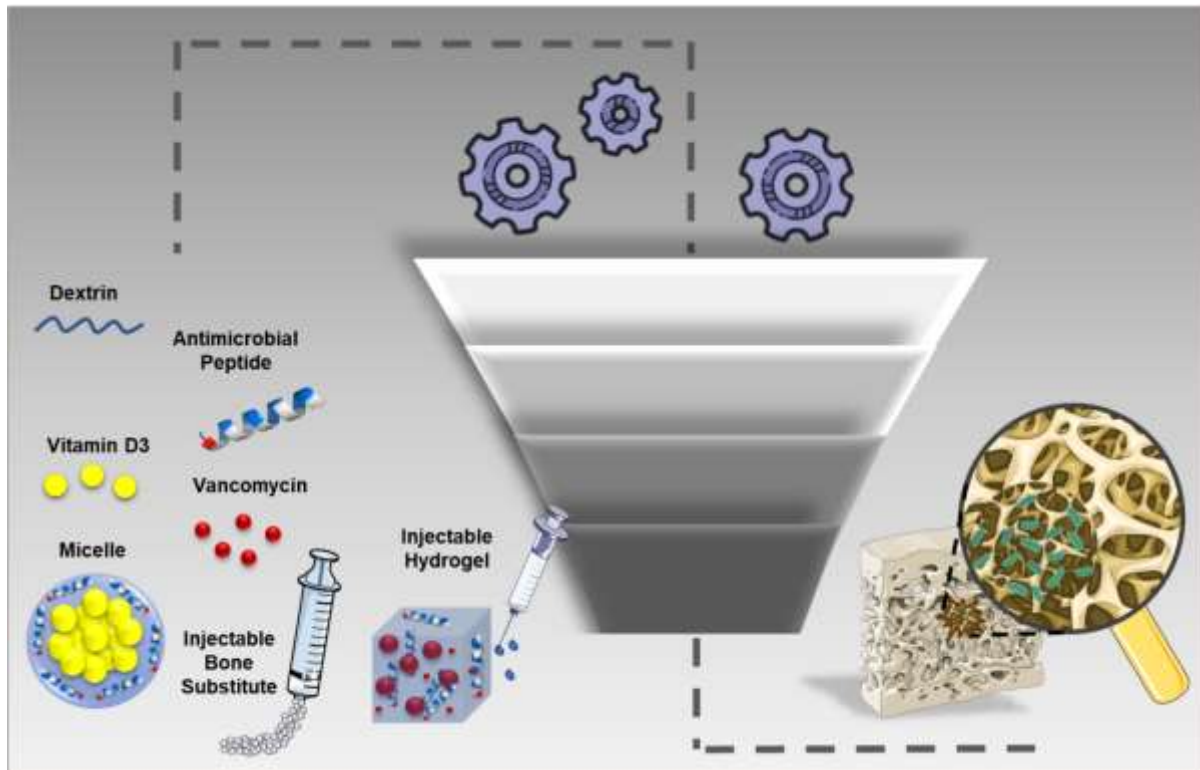
1.3 References

1. Gonçalves, C., Moreira, S. M., Carvalho, V., Silva, D. M. & Gama, M. Dextrin. in Encyclopedia of Biomedical Polymers and Polymeric Biomaterials (ed. Mishra, M.) 2634–2649 (CRC Press, 2016).
2. Asai, T. *et al.* Dextrin Promotes Proliferation of Cultured MC3T3-E1 Mouse Osteoblast-like Cells and Their Alkaline Phosphatase Activity: Implications for Potential Application of Dextrin as a Binder of Bone Filling Material. *J. Hard Tissue Biol.* 27, 65–68 (2018).
3. Gimza, B. D. & Cassat, J. E. Mechanisms of Antibiotic Failure During Staphylococcus aureus Osteomyelitis. *Front. Immunol.* 0, 303 (2021).
4. Li, B. & Webster, T. J. Bacteria antibiotic resistance: New challenges and opportunities for implant-associated orthopedic infections. *J. Orthop. Res.* 36, 22–32 (2018).
5. Spohn, R. *et al.* Integrated evolutionary analysis reveals antimicrobial peptides with limited resistance. *Nat. Commun.* 10, 1–13 (2019).
6. Boix-Lemonche, G., Guillem-Marti, J., D'Este, F., Manero, J. M. & Skerlavaj, B. Covalent grafting of titanium with a cathelicidin peptide produces an osteoblast compatible surface with antistaphylococcal activity. *Colloids Surfaces B Biointerfaces* 185, 110586 (2020).
7. Noore, J., Noore, A. & Li, B. Cationic antimicrobial peptide LL-37 is effective against both extra- and intracellular Staphylococcus aureus. *Antimicrob. Agents Chemother.* 57, 1283–90 (2013).
8. Zhang, X., Lu, Q., Liu, T., Li, Z. & Cai, W. Bacterial resistance trends among intraoperative bone culture of chronic osteomyelitis in an affiliated hospital of South China for twelve years. *BMC Infect. Dis.* 2019 191 19, 1–8 (2019).
9. Kavanagh, N. *et al.* Staphylococcal Osteomyelitis: Disease Progression, Treatment Challenges, and Future Directions. *Clin. Microbiol. Rev.* 31, e00084-17 (2018).
10. Pozo, E. G. del, Collazos, J., Carton, J. A., Camporro, D. & Asensi, V. Factors predictive of relapse in adult bacterial osteomyelitis of long bones. *BMC Infect. Dis.* 18, 1–11 (2018).
11. Tawfik, G. M. *et al.* Concordance of bone and non-bone specimens in microbiological diagnosis of osteomyelitis: A systematic review and meta-analysis. *J. Infect. Public Health* 13, 1682–1693 (2020).
12. Kang, J., Dietz, M. J. & Li, B. Antimicrobial peptide LL-37 is bactericidal against Staphylococcus aureus biofilms. *PLoS One* 14, e0216676 (2019).
13. Yu, X. *et al.* LL-37 inhibits LPS-induced inflammation and stimulates the osteogenic differentiation of BMSCs via P2X7 receptor and MAPK signaling pathway. *Exp. Cell Res.* 372, 178–187 (2018).
14. Kocuzulla, R. *et al.* An angiogenic role for the human peptide antibiotic LL-37/hCAP-18. *J. Clin. Invest.* 111, 1665–1672 (2003).
15. Yang, X. *et al.* Chitosan hydrogel encapsulated with LL-37 peptide promotes deep tissue injury healing in a mouse model. *Mil. Med. Res.* 7, 1–10 (2020).
16. Garcia-Orue, I. *et al.* LL37 loaded nanostructured lipid carriers (NLC): A new strategy for the topical treatment of chronic wounds. *Eur. J. Pharm. Biopharm.* 108, 310–316 (2016).
17. Kittaka, M. *et al.* The antimicrobial peptide LL37 promotes bone regeneration in a rat calvarial bone defect. *Peptides* 46, 136–142 (2013).
18. Li, L. *et al.* Cathelicidin LL37 Promotes Osteogenic Differentiation in vitro and Bone Regeneration in vivo. *Front. Bioeng. Biotechnol.* 9, 347 (2021).
19. Grönberg, A., Mahlapuu, M., Stähle, M., Whately-Smith, C. & Rollman, O. Treatment with LL-37 is safe and effective in enhancing healing of hard-to-heal venous leg ulcers: a randomized, placebo-controlled clinical trial. *Wound Repair Regen.* 22, 613–621 (2014).
20. Sonawane, A. *et al.* Cathelicidin is involved in the intracellular killing of mycobacteria in macrophages. *Cell Microbiol* 13, 1601–17 (2011).

21. Ciornei, C. D., Sigurdardóttir, T., Schmidtchen, A. & Bodelsson, M. Antimicrobial and chemoattractant activity, lipopolysaccharide neutralization, cytotoxicity, and inhibition by serum of analogs of human cathelicidin LL-37. *Antimicrob. Agents Chemother.* 49, 2845–50 (2005).
22. Silva, J. P. *et al.* Improved burn wound healing by the antimicrobial peptide LLKKK18 released from conjugates with dextrin embedded in a carbopol gel. *Acta Biomater.* 26, 249–262 (2015).
23. Essen, M. R. von & Geisler, C. VDR, the Vitamin D Receptor. *Encycl. Signal. Mol.* 5907–5914 (2018).
24. Chung, C., Silwal, P., Kim, I., Modlin, R. L. & Jo, E.-K. Vitamin D-Cathelicidin Axis: at the Crossroads between Protective Immunity and Pathological Inflammation during *Infection*. *Immune Netw.* 20, (2020).
25. Gombart, A. F., Borregaard, N. & Koeffler, H. P. Human cathelicidin antimicrobial peptide (CAMP) gene is a direct target of the vitamin D receptor and is strongly up-regulated in myeloid cells by 1,25-dihydroxyvitamin D3. *FASEB J.* 19, 1067–1077 (2005).
26. Mason, S. S., Kohles, S. S., Winn, S. R. & Zelick, R. D. Extrahepatic 25-Hydroxylation of Vitamin D3 in an Engineered Osteoblast Precursor Cell Line Exploring the Influence on Cellular Proliferation and Matrix Maturation during Bone Development. *ISRN Biomed. Eng.* 2013, 956362 (2013).
27. Ignjatović, N., Uskoković, V., Ajduković, Z. & Uskoković, D. Multifunctional hydroxyapatite and poly(D,L-lactide-co-glycolide) nanoparticles for the local delivery of cholecalciferol. *Mater. Sci. Eng. C. Mater. Biol. Appl.* 33, 943–50 (2013).
28. Shekhar, C. An Innovative Technique in Local Antibiotic Delivery Method in Open Infected Wounds of the Musculoskeletal System. *Int. J. Low. Extrem. Wounds* 18, 153–160 (2019).
29. Shekhar, C. *et al.* Role of topical cholecalciferol granules for antimicrobial drug delivery in diabetic foot ulcers. *Indian J. Orthop. Surg.* 5, 165–167 (2019).

CHAPTER 2

2. LITERATURE REVIEW



Bone is a living and dynamic tissue with self-regeneration and self-remodeling capacity. Understanding its structure, composition and cell function, is essential in the design of bone healing therapies. Bone healing constructs are designed to mimic bone composition and provide pro-healing actions, such as anti-inflammatory, angiogenic or osteogenic. However, bone repair comprises a tightly organized interplay of biomechanical and biological factors, spatially and temporally synchronized. Therapies should be designed not only as to provide bioactive agents, but, importantly, in the right moment and in the right level. Bone infections add another level of complexity. Treatment is still a challenge due to rapidly evolving microbe resistance to antibiotics. Cathelicidin and vitamin D3 partnership holds promise as a non-antibiotic strategy in pathogen fighting and tissue healing. Dextrin is an inexpensive natural polymer, displaying several advantageous features for bone applications, and is a multifunctional tool for the design of drug delivery systems.

Adapted from: *Endocrine Connections*, 10(1):R1-R12 (2021).

2.1 Bone

2.1.1 Bone Anatomy and Composition

Macroscopically, bone is divided into two main types: cortical (80 %) in the outer layer, and trabecular or cancellous (20 %) in the inner and spongy layer. Cortical bone is denser, and thereby harder, with a low 5 % to 10 % porosity, whereas trabecular bone exhibits 50 % to 90 %, resembling a honeycomb structure ¹. They are organized as to provide a proper balance. High mineralization content would promote strength, although impairing fracture resistance. The tendency to fracture depends on the content of mineralized bone (size and density), which varies with age, disease and therapies ².

According to shape, bones can be classified as long (e.g. tibia or femur), short (e.g. tarsal and carpal), flat (e.g. cranium, ribs, scapula and pelvis) and irregular (e.g. vertebrae, sacrum and coccyx) ³. As depicted in **Figure 2.1**, long bones are divided into: epiphysis, in both extremities; diaphysis, of tube-like shape in between them; and metaphysis, located between epiphysis and diaphysis. Epiphysis and metaphysis are divided by the epiphysial line, and are made of made of trabecular bone filled with red bone marrow. Diaphysis is made of dense and compact bone, possesses an inner medullary cavity filled with yellow marrow covered by an inner membrane, endosteum, and an outer fibrous membrane, named periosteum. Periosteum covers the entire bone up to the articular surfaces, is highly vascularized and holds a rich neural network ³.

Cortical bone has osteocytes-rich central canals, named osteons, through which blood vessels and nerves pass and interconnect with vessels on the surface of bone ¹. Cortical osteons are longitudinally oriented, cylindrical branching networks, called Haversian canals. These vascular tunnels deliver nutrients to osteocytes and remove waste, playing a critical role in bone mechanics and turnover ⁴. Instead, trabecular bone is differently rearranged in a network of trabeculae that connect to the adjacent cavities, and contains osteocytes in lacunae which are nourished by penetrating blood vessels from the periosteum.

At the microscopic scale, there are two forms of cortical and trabecular bone: woven (or primary) and lamellar (or mature) bone ¹. Woven bone forms quickly. For this reason, it displays less and random three-dimensional orientation of collagen fibers, thereby being mechanically weaker. During early stages of fracture healing, bone starts to grow as woven, later being replaced by lamellar bone. It also occurs in fetal bones. On the other hand, lamellar is made of a series of sheets, displaying an organized parallel arrangement of thicker collagen fibers, and is mineralized, thereby, showing higher stiffness.

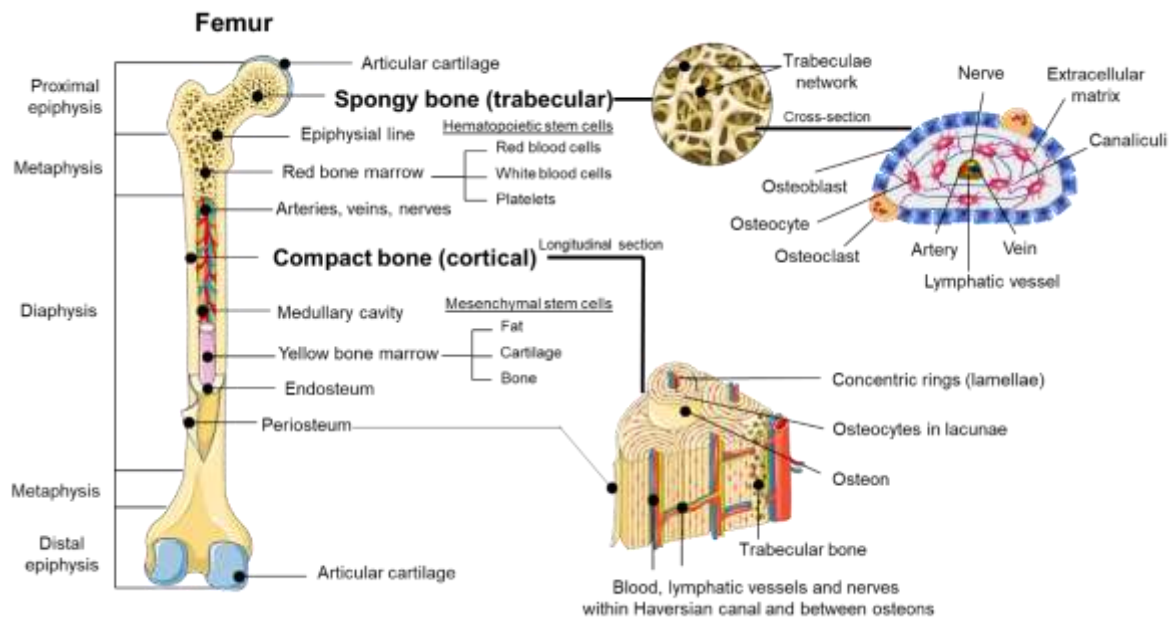


Figure 2.1 – Schematic representation of an adult femur.

With respect to the chemical composition, bone is a porous material consisting of water (~5%), mineral (~70%), and organic (~25%) phases. The inorganic phase is mainly composed of hydroxyapatite (HA), $\text{Ca}_{10}(\text{PO}_4)_6(\text{OH})_2$, which is composed of phosphate and calcium, but also bicarbonate, sodium, potassium, citrate, magnesium, carbonate, fluorite, zinc, barium and strontium¹. HA is widely used in the design of bone substitute implants, given its similarity with native bone, biocompatibility and osteoconductivity.

The organic phase consists of approximately 90% type I collagen and non-collagenous proteins, mostly being proteoglycans, and glycoproteins (e.g. alkaline phosphatase [ALP])⁵. Collagen proteins provide mechanical support and act as a scaffold for bone cells. Proteins in the extracellular matrix (ECM) control the development and the ultimate functional properties of bone. They are involved in various structural, enzymatic or signalling processes, regulating cell adhesion and responses to growth factors, for instance. They also regulate HA deposition, control the development, function, and homeostasis of tissues and organs. For this reason, ECM (or its components) is also used in the design of biomaterials to mimic natural environment⁵.

The organic phase provides flexibility, whereas the inorganic phase provides the necessary rigidity for resistance to mechanical stress. Together they provide a framework for the support of softer tissues, protection of vital organs, support for locomotion and muscular contraction.

2.1.2 Bone Histology

Bone tissue consists of a mineralized organic matrix in continuous remodeling. Three main bone cells control bone remodeling: osteoblasts, osteocytes, and osteoclasts. They arise from two cell lineages found in bone marrow: mesenchymal stem cells (MSCs) and hematopoietic stem cells (HSCs), as depicted in **Figure 2.2**. MSCs are multipotent stromal cells that can differentiate into osteoblasts, osteocytes, bone-lining cells (bone) and chondrocytes (cartilage), but also in myocytes (muscle) and adipocytes (fat). HSCs are stem cells from which derive monocytes, macrophages, or platelets (blood cells), but also osteoclasts (bone).

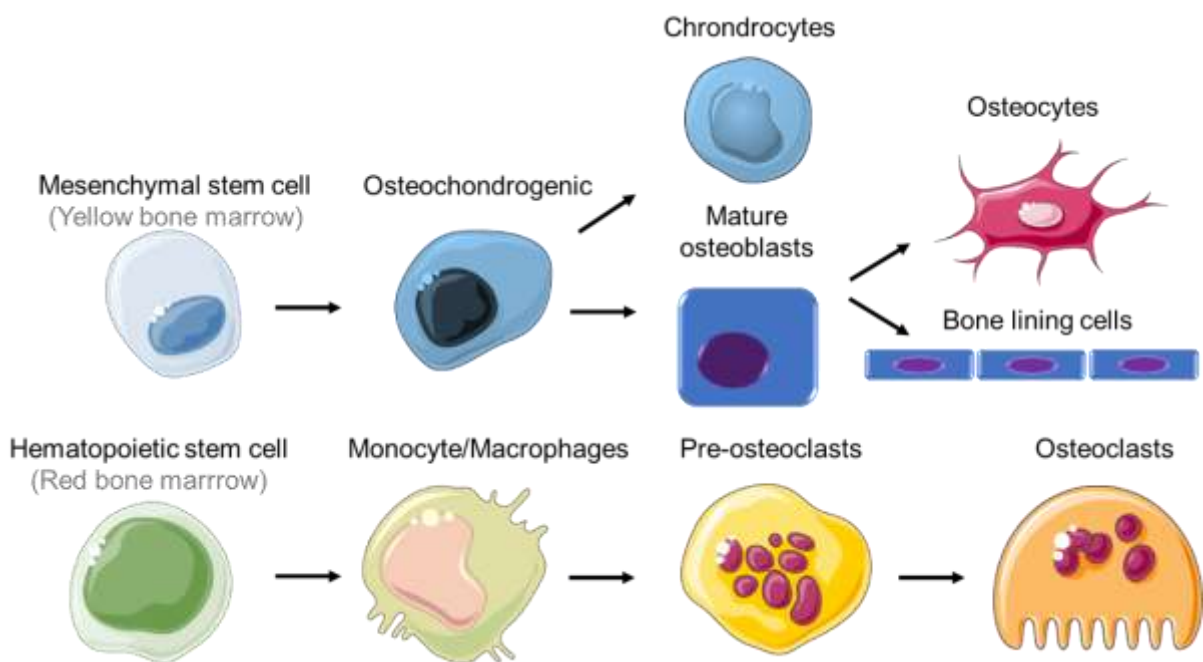


Figure 2.2 – Differentiation of bone cells from mesenchymal stem cells and hematopoietic stem cells.

Osteoblasts are cuboid-shaped bone-forming cells responsible for the synthesis, regulation of the deposition, and mineralization of the main organic ECM. This is a network of extracellular macromolecules, such as collagen, enzymes, and glycoproteins – produced by osteoblasts – that provide structural and biochemical support to surrounding cells, mainly responsible for cell adhesion, cell-to-cell communication and differentiation ⁶. The fate of an osteoblast may include either remaining on the surface of the bone, as bone lining cells, differentiating into osteocytes, or undergoing apoptosis ⁷. Bone lining cells, also known as resting or inactive osteoblasts, are quiescent flat cells covering the bone surfaces that are not undergoing remodeling. Although not completely understood, some functions have been associated with involvement in osteoclast differentiation in bone resorption sites ⁸. Osteoblasts

differentiate into osteocytes, which feature a specific key-marker, protein E11. Osteocytes are, star-shaped, highly active multifunctional bone cells that are surrounded by mineralized bone matrix, comprising 90–95% of the adult skeleton bone cells. They are involved in directing the bone remodeling process, through the regulation of osteoblast and osteoclast activities. They are localized in the mineral lacuna (**Figure 2.1**), surrounded by the bone fluid in equilibrium with the plasma, being exposed to hormones and signals coming for instance from the bloodstream, such as inorganic phosphorous or vitamin D3 (VD3). Osteocytes extend their action through tiny tunnels originated from the lacuna, canaliculi, forming a connection to neighboring osteocytes, osteoblasts and bone lining cells, osteoclasts, bone marrow cells and also the blood vessels. They possess gap junctions acting as channels to the passage of small molecules (calcium, adenosine triphosphate [ATP]) towards other bone cells, enabling direct cell–cell communication. Thereby, osteocytes, present throughout the entire bone, interconnect among them and with the other bone cells, can participate in the regulation of bone formation and resorption, and act as source of plasma calcium ⁹. Although not well understood, osteocytes also act as mechanosensors, involving ion channels, ECM adhesion molecules and the cytoskeleton ⁹.

Osteoclasts are bone-resorbing cells located within lacunae surrounded by mineralized bone matrix, which operate by decalcifying HA and degrading organic ECM. On the surface of the bone, they secrete organic matrix-digesting enzymes, matrix metalloproteinases, such as collagenases and cathepsin K, and promote acidification ($\text{pH} \sim 4$) by secreting protons (H^+), resulting in the solubilization of the mineral phase ¹⁰. They derive from the fusion of precursors of the monocyte-macrophage lineage, giving rise to multinucleated osteoclasts, typically holding three to twenty nuclei. They work in a synchronized manner in the formation, maintenance and destruction of bone tissue, to retain bone remodeling homeostasis. An imbalance in this activity can result in altered bone morphology and pathological bone ¹¹.

Osteoblasts, osteocytes, bone lining cells and osteoclasts, can sense and respond to mechanical stimuli, recently having been found to occur through the MSC-macrophage interaction. Mechanical stretch induces macrophage polarization to M2 phenotype following yes-associated protein activation and nuclear translocation, subsequently regulating downstream bone morphogenetic protein (BMP) 2 expression to favor MSCs osteogenesis¹².

2.1.3 Bone Remodeling

Healthy bone is in continuous remodeling, substituting old bone by new one through a continuous exchange of information and connected events. The remodeling cycle comprises five coordinated and overlapping steps: quiescence, activation, resorption, reversal and formation/mineralization ¹³. The

quiescent or resting phase refers to inactive bone, in which osteocyte expression of the wingless/integrase-1 (*Wnt*) inhibitors, Sclerostin and Dickkopf-1, prevents further bone formation¹⁴. Then, activation phase begins, as a result of any event such as microfracture, low calcium, or a deficient diet, by processes still unknown. In this phase, osteoclast precursors are recruited from the circulation and activated; then the lining cells separate from underlying bone, exposing the surface to be resorbed; multiple mononuclear cells fuse and form pre-osteoclasts that bind bone matrix, sealing and restraining the site under resorption from the surroundings, giving rise to the resorption phase. In this phase, osteoclasts pump protons into the resorbing site (acidification) and release proteolytic enzymes (e.g. cathepsin K), both resulting in degradation of the organic and mineral matrix¹⁰. Then, programmed osteoclast cell death ensures bone resorption is terminated. Resorption by osteoclasts create a shallow resorption cavity, called Howship's lacunae; destruction of matrix triggers the release of growth factors and cytokines, inducing the conversion of osteoprogenitor cells into osteoblasts, that fill the resorption cavities created by osteoclasts, to create new bone matrix.

In the subsequent phase, bone resorption reverts to bone formation. Although not completely understood, macrophages clear away the debris resulting from resorption, and then deposit a non-collagenous mineralized matrix cement-like substance to enhance osteoblastic adherence. Osteoblast precursors are recruited to initiate the new bone formation.

In the last phase, formation, osteoblasts synthesize and secrete a type I collagen-rich osteoid matrix, and take part in regulating osteoid mineralization. During this process, osteoblasts may either undergo osteocytogenesis, apoptosis or become bone lining cells. In the end, mineralization is complete and osteoblasts may undergo apoptosis, change into bone lining cells, or differentiate into osteocytes within the bone matrix. The formed osteocytes re-express *Wnt* inhibitors, resulting in the termination of bone formation and returning to resting/quiescent phase.

2.1.4 Bone Repair

Upon injury, restoring the functionality of the traumatized bone occurs through exchange between many different cell types. Their spatial and temporal distribution is fundamental for the repairing process. Bone repair occurs through three main biological stages: inflammation, formation of callus and remodeling, as depicted in **Figure 2.3**¹⁵. In the first stage, blood vessels disrupt (oxygen and nutrient restriction), causing the formation of a blood clot, haematoma, and local inflammation, resulting in cell activation and migration. Arriving platelets, neutrophils and macrophages release a cascade of signals of growth factors and cytokines: fibroblast growth factors (FGF), tumor necrosis factor (TNF- α), platelet-derived growth

factors (PDGF), basic fibroblast growth factor (BFGF), transforming growth factor (TGF- β) and cytokines, such as interleukin (IL) IL-1 and IL-6. Vascular endothelial growth factor (VEGF) is also stimulated, paving the way for revascularization. Subsequently, a cascade of signals (e.g., release of cytokines such as IL-1, IL-6 or TNF α) triggers the activation and recruitment (chemotaxis) of several immune cells to the damaged site, such as peripheral multinucleated cells (PMN), T- and B-cells, monocytes and MSCs. Finally, MSCs are stimulated to differentiate into osteochondrogenic lineage. This stage typically lasts 1–5 days in humans, 1–3 in mice.

The second phase, also called repair phase, is characterized by angiogenesis and callus formation. Pro-angiogenic cytokines such as VEGF, PDGF and IL-8 stimulate vascularization, thereby restoring the supply of nutrients and oxygen. This is a critical event for the subsequent bone development. The osteochondrogenic lineage developed in the previous phase, now gives rise to chondroblasts that form cartilage, and to osteoblasts that form woven bone. This early fibrocartilaginous area produces a bridge-like structure that stabilizes the damaged site, following a mineralization process and subsequent blood vessels penetration. Here, the osteochondrogenic lineage generates woven bone by rapid deposition of minerals, a bone type that is characterized by an arbitrary organization of collagen fibers and low mineral density. Continuously developing blood vessels further supports the recruitment of MSCs. In a later stage of this repairing process, the fibrocartilaginous callus is substituted by a primitive bone tissue, a hard callus, by a process called endochondral ossification. This entire stage can last up to four weeks.

In the last remodeling phase, the primitive woven bone is substituted by new lamellar bone through the synchronized interplay of bone-forming cells, osteoblasts, and bone-resorbing cells, osteoclasts. Vascularization is also remodeled, culminating into a completely, regenerated, functional bone structure. This stage may last various months. Details of the remodeling process are mentioned in section 2.1.3.

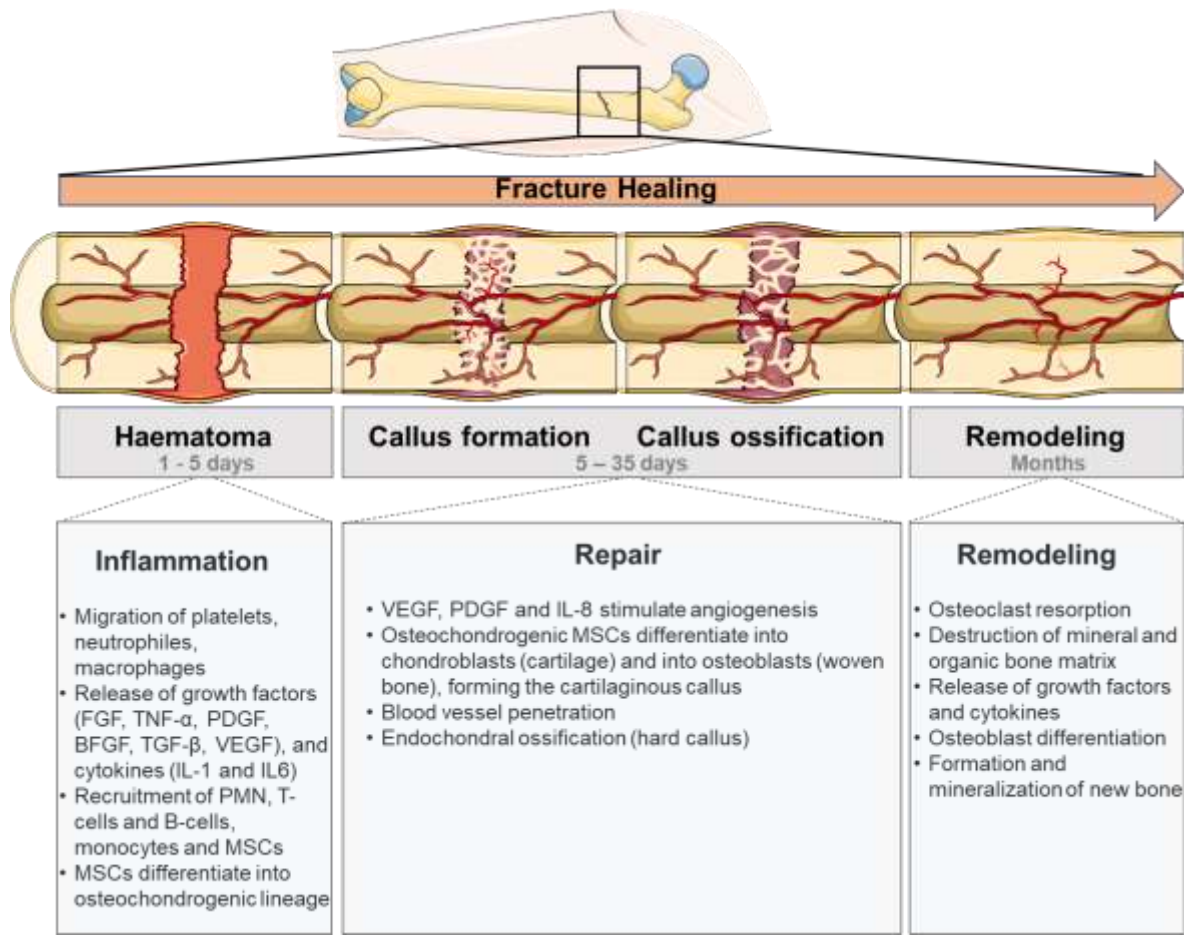


Figure 2.3 – Schematic representation of the different stages of a fracture healing: haematoma formation and local inflammation; then, angiogenesis is upregulated, cartilaginous callus is formed, blood vessels penetrate and endochondral ossification gives place to primitive woven bone; and finally remodeling replaces the woven for lamellar bone. FGF, fibroblast growth factors; TNF, tumor necrosis factor; PDGF, platelet-derived growth factors; BFGF, basic fibroblast growth factor; VEGF, Vascular endothelial growth factor; IL, interleukin; MSCs, mesenchymal stem cells.

2.1.5 Injectable Bone Substitutes

Technological advances, together with the growing need for bone regenerative therapies, have prompted the demand for bone grafts and substitutes. The need for bone grafts is a common event, given that they may arise from trauma, disease, surgery, infection, or malformations. A bone graft substitute is a living tissue – often containing a mineralized bone matrix – with enhanced bone regeneration ability, being transplanted into bone either alone or in combination with drugs or other materials. There are four types of bone grafts according to their source: allograft, from another individual, autograft, from the same individual, xenograft, from another species, and synthetic. Materials of natural origin may include HA, or

growth factors, and synthetic grafts can be based on calcium sulfate, tri-calcium phosphate ceramics, bioactive glasses, or polymers¹⁶. The ideal bone graft substitute should provide an osteoconductive matrix, osteoinductive factors, osteogenic cells, and structural integrity. Despite their success rates in clinical practice, autografts include donor site complications and the grafts are sometimes difficult to mold, and limited amount is available as well. Limitations of xenografts or allografts are mainly related to the risk of rejection or transmission of infectious diseases. Synthetic bone grafts can overcome these issues.

Grafts based on calcium phosphates display a bone-like composition, such as HA and tricalcium phosphate (TCP). They can be classified into ceramics, a porous and solid material derived from sintering, or cements, a form of paste that hardens upon application. HA is the main inorganic component of bones, is porous, osteoconductive, resorbable, biocompatible, shows good osseointegration, providing excellent conditions for tissue ingrowth, and has low resorption, thereby being more mechanically stable¹⁷. TCP displays faster reabsorption¹⁸, that is essentially cell-mediated^{19,20}. They are both biocompatible, bone-mimicking materials widely used in bone regeneration therapy.

Bone substitutes should provide mechanical stability and promote the healing process, ultimately being replaced by functional tissue through remodeling. However, the management of large defects, unsatisfactory vascularization, and shortcomings in reabsorption rates and biomechanical performances remain a challenge. The rate of resorption is of primordial importance as it dictates the duration of osteoconductive support essential for bone regeneration. Low resorption rates, such as those found in pure HA or bovine-seed bone substitutes (Bio-Oss®, Geistlich Biomaterials, Switzerland), can result in a number of complications, such as displacement of the graft materials, implant failure, foreign body reactions, chronic inflammation, soft tissue fenestrations and associated cysts, and lack of biodegradation requiring the removal of the bone graft material²¹. In this regard, new bone substitute materials associated with sodium alginate as a glue to fix the bone particles, Mega-TCP and Mega-oss, performed comparably to Bio-Oss® in terms osteoblast differentiation ability, though displaying higher resorption rates than those of Bio-Oss (24.4%, 15.3%, and 3.3%, respectively)²². Additionally, Mega-TCP has lower price and easier source, however, *in vivo* and clinical evidence is yet to be accomplished. On the other hand, synthetic TCP bone substitutes (e.g. Cerasorb®), with high resorption rates provide short-term mechanical stability, having been associated with longer healing times²³. Given that *de novo* bone formation is dependent on a time-dependent synchronized vascularization and bone formation, resorption rate becomes essential. Vascularization is also dependent on the porosity of the materials.

There has been a growing interest in delivering bone healing agents, such as MSCs, drugs, or growth factors. Thus, the development of innovative grafting materials should provide a proper environment for

their incorporation, and controlled release, which could be provided by HG matrices ²⁴. Additionally, unsatisfactory handling properties may also hinder the use of many available bone substitutes. From a commercial point-of-view handling is of particular importance to good injectability upon filter-pressing, to avoid the release or migration of particles, assess difficult sites, mold to the defect, and provide a reproducible mixing procedure. The optimal design of HGs-combined scaffolds should be clinically evidence-based. HGs matrices are expected not to impair the healing process, but they add another form of complexity to the product. Thus, biodegradation, biocompatibility, osseointegration and osteoconductive properties of the final formulations are crucial parameter to be examined. Indeed, HGs should act as a bio-inert scaffold suitable for cell adhesion, migration, proliferation and differentiation, and for the deposition of new bone along the graft surface while it degrades.

2.1.5.1 The Case of DEXGEL Bone

This thesis includes the first clinical study of DEXGEL Bone, an injectable, synthetic, porous, osteoconductive bone substitute indicated to fill small bone defects. It is composed (i) of a dextrin HG matrix (DEXGEL), which will be degraded and reabsorbed *in vivo* by hydrolysis (blood amylases) and undergo renal elimination; and (ii) Bonelike by Biosskin® (BL®), a granular bone substitute, consisting HA matrix, TCP and ionic species commonly found in human bone, i.e. magnesium, sodium and fluor. The addition of TCP phase confers a degradability character to the low-degradable HA. The specific combination of these two biomaterials endows DEXGEL Bone with a porous and interconnective three-dimensional structure, serving as favorable support for the bone tissue regeneration process. DEXGEL simultaneously promotes support, cohesion, and stabilization of granules, improved handling properties (injectability), and more effective filling of bone defects.

A medical device (MD) is any instrument, equipment, software, material, or article used alone or in combination, which the main effect is not achieved in the human body by pharmacological, immunological, or metabolic means, though may be supported by them (Dec. Law 145/2009). MDs differ from drugs by acting in a physical way rather than pharmacological, metabolic, or immunological actions. Before placing an MD on the European market, first, it must be CE (*Conformité Européene*) marked. This marking ensures that it complies with the regulatory criteria that applies to it. To obtain a CE mark, the MD must undergo a clinical evaluation. MDs are organized into different risk classes, from lower to higher risk: classe I for non-invasive (low risk), classe IIa for short-term invasive (moderate risk), classe IIb for long-term invasive (high risk), and classe III for long-term invasive (critical risk). According to Dec. Law 145/2009, DEXGEL Bone is a risk class III, for being a long-term implantable MD, for being

intended to be fully introduced into the body, through surgical intervention, and retained, after the intervention, for a period longer than 30 days (continuous use), and also for being intended to produce a biological effect, mimicking the effect of bone reconstruction and regeneration.

Bonelike by Bioskin® is a classe IIb synthetic bone substitute MD having already been commercially available, which fabrication process is patented by Bioskin, Molecular and Cell Therapies, SA. It is currently out of the market, having its CE marking withdrawn, though, still in compliance with the regulatory criteria. The clinical study here described, aimed at innovating this product by introducing injectability properties, in order to restore CE marking. With all the regulatory criteria approved, the resulting MD underwent fabrication and clinical evaluation. The first clinical study with MD intervention of DEXGEL Bone was performed in skeletally mature individuals in need of replacing a tooth with a dental implant, in the upper premolar areas (Hospital da Luz, Coimbra, Portugal).

Polysaccharides simulate the ECM of natural bone presenting excellent biocompatibility and have been widely used as the base-component of HGs ²⁴. Despite good outcomes *in vitro* and *in vivo*, complex preparation processes and high costs may limit clinical translation of many HGs. Dextrin, the base component of DEXGEL Bone, is an inexpensive raw material derived from starch, providing a simple and cost-effective preparation methodology solution.

DEXGEL Bone is expected to compete with other commercially available injectable bone graft substitutes. Some products come in the form of highly viscous gels, disfavoring the surgical process, or in the form of pastes with poor cohesive properties. Examples of the latest advancement in bone substitute technology include, for instance, Norian® (Synthes), chronOS® (Synthes), Hydroset™ (Stryker) and BoneSource® (Stryker), which are essentially calcium phosphate types of cement currently commercialized as injectable devices. Polymer-based substitutes include for instance, Healos® (DePuy), based on crosslinked collagen and HA, available in strips, or Cortoss® (Stryker), an injectable paste, though non-resorbable resin, with ceramic particles. However, we find in our HG-reinforced scaffold, with bioactive agent release capabilities, an innovative and more advanced product. Comparable devices (injectable, resorbable and osteoconductor), include In´Oss® (Biomatlante), based on an HG and bioactive ceramics, and K-iBS® (Ceramed) based on a chitosan matrix and bioactive ceramics.

2.2 The Challenge of Osteomyelitis

Osteomyelitis (OM) is an inflammation of the bone resulting from infection ²⁵. Being one of the oldest diseases recorded, remains a burden in modern society, accounting for numerous hospitalizations and considerable costs. Although epidemiology data available presents considerable disparities depending on

many factors, bone infections are recognized as a recurrent event. Indeed, OM may arise from i) pathogen spread through the bloodstream (hematogenous), ii) blood circulation associated diseases and iii) open wounds around bone, trauma or surgery, and can affect any bone at any age. For instance, incidence is reported as 16.7 and 21.8 cases per 100,000, per year, in Germany ²⁶ and in United States ²⁷, respectively, but is far more prevalent among susceptible patients, such as those with poor blood circulation conditions. OM was diagnosed in 50 % out of 482 patients with diabetic foot infections indicated for amputation ²⁸. Moreover, diabetics have shown a 32.1 % risk of limb loss secondary to OM compared to 8.6 % in non-diabetics ²⁹, and a mortality rate exceeding 50 % six to eight years post-amputation ³⁰. As a measure of the economic burden, treatment costs of fracture-related infections were estimated to be approximately 6.5-times more expensive than in non-infected patients ³¹.

Standard treatment is based on systemic antimicrobial therapy in combination, when required, with surgery. A dual challenge compromising patient recovery is evident: i) antibiotic failure and ii) impaired bone healing ^{32,33}. Rapidly evolving microbe resistance and the lack of new antibiotics greatly contribute to treatment failure. Subsequently, disease progresses into a severe status characterized by low blood supply and necrotic tissue, preventing systemic antibiotics as well as immune cells to reach the affected area, thus working as a favorable milieu for microorganisms and further impairing therapy success. At this stage, surgery is required to remove destructed tissue, resulting in a gap devoid of blood vessels, and providing an opportunity for another infection. Extensive debridement increases the area that requires bone healing, whereas limited debridement may leave residual infection (**Figure 2.4**), perpetuating treatment in repetitive cycles of surgery and antibiotics. Hard-to-treat infections take longer to treat and heal, sometimes culminating in amputation. This is the most challenging-to-treat stage of OM that must be targeted by the development of innovative treatments.

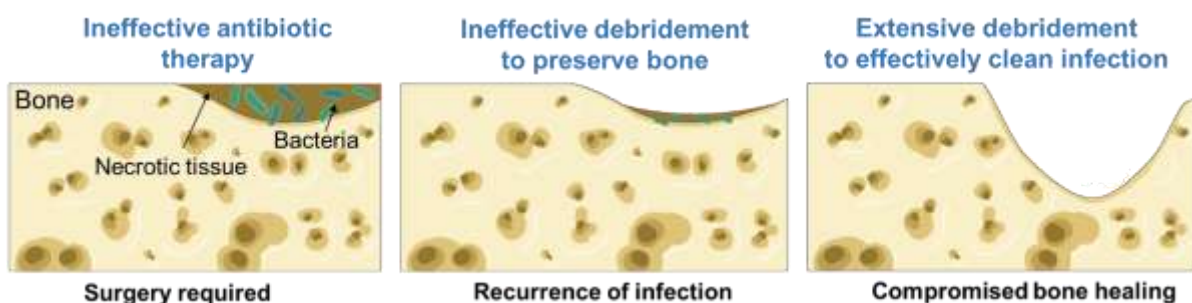


Figure 2.4 – Treatment-related complications of a bone infection.

That said, novel types of antimicrobials with reduced tendency for microbe resistance and additional tissue repairing properties have been designed to address an effective treatment ³⁴. Additionally, the local

administration has been favored over systemic, as the typically avascular affected sites require higher systemic antibiotic doses and frequency, prompting toxicity issues without a healing guarantee. Local or intralesional administration allows achieving high local antimicrobial concentration while keeping low the serum levels.

Since surgical debridement frequently leaves residual bacteria that serve as a nidus for persistent infection, continuously hindering bone growth, antibiotics-impregnated synthetic bone grafts have been locally applied for prolonged antibacterial therapy and bone healing. Antibiotic-impregnated polymethylmethacrylate (PMMA) has been the gold standard clinical treatment for many decades ³⁵. However, this non-degradable biomaterial has the main disadvantage of requiring a second surgery to be removed few weeks post-implantation, being ultimately replaced by a bone graft. This represents another opportunity for infection, more cycles of systemic antibiotics, hospitalization, more costs and discomfort to patients. Commonly preferred PMMA-loaded antibiotics include gentamycin, vancomycin and tobramycin ³⁵. PMMA is available in the form of bead-chains or spacers, with shortcomings varying from material dislocation, unsatisfactory mechanical behavior, and demand of invasive techniques. Recent vehicles for local treatment include HGs, cements, micro or nanoparticles (NPs), coatings/films, scaffolds and sponges, delivering a range of therapeutics such as antibiotics, bacteriophages, antimicrobial peptides (AMPs), enzymes and more ³⁶. Innovative treatment approaches have mainly focused on designing biomaterial coatings based on: i) silver ions or antibiotics (mostly gentamicin and vancomycin), ii) bioinspired nanopatterned surfaces of superhydrophobic nature resembling insect wings or lotus flower, taken as exhibiting bactericidal properties, iii) titanium nanotubes that, besides anti-bactericidal they also increase osteoblasts adhesion onto the surface, iv) chemical modification with zwitterionic surfaces, peculiarly able to form a hydration layer serving as a physical and energetic barrier against adsorption of nonspecific proteins or bacteria ³⁷. Overall, researchers pursue a one-step solution that: i) provides high and prolonged local antimicrobial concentration while ii) being safe to other tissues; iii) reduces the need for systemic antibiotics; iv) lacks susceptibility for mechanisms of microbe resistance; v) holds broad spectrum activity; vi) promotes bone healing; vii) is biodegradable; viii) requires less invasive techniques and ix) is cost-effective.

2.2.1 Pathophysiology / Pathogenic Mechanism of Infection

Chronic OM is a long-lasting infection of the bone and bone marrow, which can progress to bone necrosis and sequestrum formation. It may present as a recurrent or intermittent disease, with periods of quiescence of variable duration. These tend to relapse, after apparently successful therapy ³⁸. The

incidence of significant infection within three months after an open fracture, has been reported to be as high as 27 %³⁹.

Briefly, OM progression involves inflammation, bone loss, and spreading of bacterial infection to soft tissue. Within 10 days of infection onset an acute phase is established, which progresses to a sub-acute phase within two weeks to one month, and frequently evolves to a chronic phase that remains for several months, possibly becoming incurable. When a bone becomes infected, immune cells are attracted to the area and secrete enzymes that will elicit bacteria death. Bacteria are phagocytosed and toxic oxygen radicals and proteolytic enzymes released cause lysis of the adjacent tissue. In acute phase, inflammation of surrounding blood vessels leads to increased intraosseous pressure, reducing blood flow and oxygen delivery to the area inducing the formation of devitalized necrotic bone, named sequestrum. Sequestrum is dead bone with deteriorated connection with healthy bone and, thus, detached from nutrition sources as blood vessels or Haversian system, hindering the healing process. This is also a nidus of chronic infection, that needs to be surgically removed. Due to the decreased blood flow during inflammation and to the avascular nature of sequestrum in the chronic phase, both antibiotics and immune cells are difficult to reach the affected area.

2.2.2 *Staphylococcus aureus* as the Primary Pathogen in Osteomyelitis

Microbe resistance to antibiotics is a serious threat to human health⁴⁰, severely hampering the treatment of bone infections. OM can be triggered by bacteria or fungi, standing out *Staphylococcus aureus* (*S. aureus*) as the most causative species^{25,28,41}. Methicillin-resistant *Staphylococcus aureus* (MRSA) is particularly challenging, a high priority pathogen for World Health Organization to be targeted for the development of new antibiotics⁴⁰. In the last two decades, efforts have been made to understand the ability of this agent to colonize, persist in tissues and induce bone loss⁴².

First, osteoblasts were demonstrated to be capable of internalizing *S. aureus*⁴³, partially explained by a connection between fibronectin and binding proteins expressed on bacteria⁴⁴, showing the ability to mediate the apoptotic pathway⁴⁵. Later, interaction with osteoblasts were demonstrated even in the absence of fibronectin-binding proteins, highlighting the involvement of *S. aureus* protein A (SpA) binding to osteoblasts. This triggers a series of events culminating in increased expression of receptor activator of nuclear factor kappa-B ligand, RANKL, a key cytokine involved in osteoclast differentiation (i.e. initiating bone resorption), inhibition of cultured osteoblast mineralization and proliferation and induction of apoptosis⁴⁶. SpA and fibronectin-binding proteins are two among many other *S. aureus* microbial surface

components recognizing adhesive matrix molecules (MSCRAMMs) that mediate host-cells attachment, partially explaining the virulence success of this species ²⁵.

S. aureus can induce osteoblast necrosis via the release of cell membrane-damaging virulence factors (phenol-soluble modulins), and also apoptosis through release of tumor necrosis factor-related apoptosis-inducing ligand (TRAIL), which interacts with receptors on infected osteoblasts ^{47,48}, both resulting in the spread of intracellular bacteria capable of re-infecting other cells. The bacteria can also damage deoxyribonucleic acid (DNA), either directly or indirectly through the production of reactive oxygen species (ROS) ⁴⁹.

A study showing that bacteria could be internalized to lower extent although surviving more in osteoblasts, as compared to macrophages, suggests the absence of an effective defense/phagocytic mechanism to clear bacteria ⁵⁰. Hamza and colleagues provided *in vivo* evidence that intra-cellular *S. aureus* inoculation of as low as 10² colony forming units could induce severe bone infections ⁵¹. Their data suggested that intra-cellular *S. aureus* can hide in host cells during symptom-free periods and, under certain conditions, escape and lead to infection recurrence. Persistent infection caused by intracellular *S. aureus* can be explained by two main reasons: escape from vesicles or acquisition of a small colony variants (SCV) phenotype. *S. aureus* has been tracked in late endosomal/lysosomal of osteoblast compartments ⁵², avoiding the proteolytic activity by escaping from lysosomes to cytoplasm through membrane disruption promoted by membrane-damaging factors ⁵³. Alternatively, they can persist as SCV, a low-virulent, slow-growing and quiescent population with remarkable tolerance to antibiotics and immune system compared to wild-type ⁵⁴. Under favorable conditions, most of SCV variants can quickly revert to the highly virulent wild-type, resulting in repeated relapse of chronic OM patients ⁵⁵. SCV have shown to contribute to increased tolerance to antibiotics during chronic OM, some of them even having induced SCV formation ⁵⁶. Moreover, the membrane potential of SCV is reduced, limiting transportation of protons across the cell membrane. This feature has been correlated to the persistent character ⁵⁷ and reduced influx of antibiotics ⁵⁸, at least partially by diminishing the electrostatic interaction with positively charged compounds/antimicrobials. The ability to remain in necrotic tissue for long periods suggests that SCV have low nutrition requirements. **Figure 2.5** depicts a summary of *S. aureus* mechanisms for persistent infection in osteoblasts.

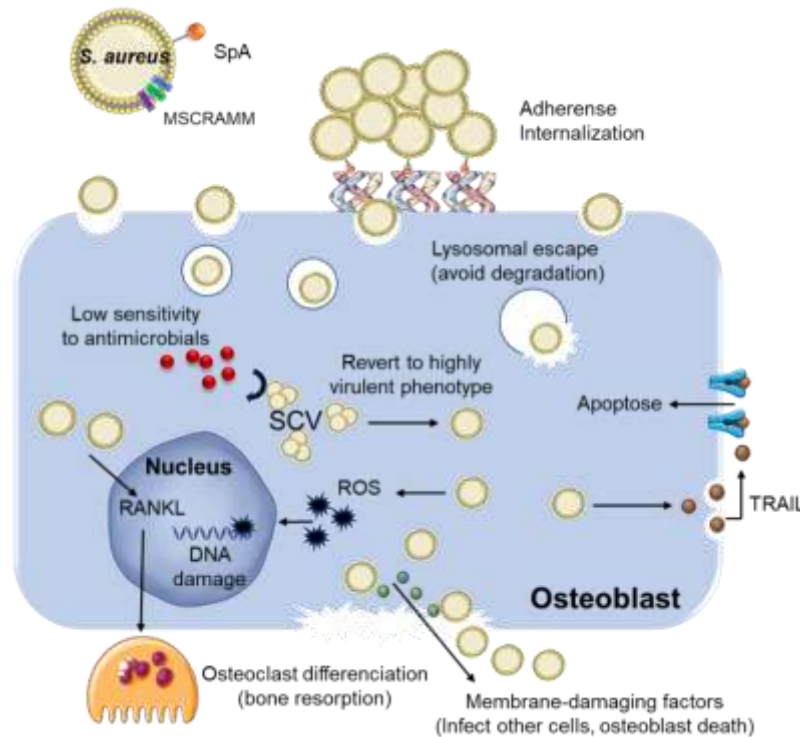


Figure 2.5 – *Staphylococcus aureus* (*S. aureus*) mechanism for persistent infection and subsequent osteoblast damage: microbial surface components recognizing adhesive matrix molecules (MSCRAMMs) and protein A (SpA), interact with osteoblasts surface following internalization; intracellularly they can i) damage lysosome membrane, avoiding degradation and escaping to cytosol, ii) form small colony variants (SCV) highly resistant to antibiotics and immune system, iii) produce deoxyribonucleic acid (DNA)-damaging reactive oxygen species (ROS), iv) induce osteoclast differentiation via receptor activator of nuclear factor kappa-B (RANKL) stimulation, v) induce cell apoptosis through tumor necrosis factor-related apoptosis-inducing ligand (TRAIL) stimulation and subsequent recognition by cell surface receptors, vi) produce cell membrane-damaging components, inducing cell death, and escape to infect other cells.

One mechanism against membrane-active cationic antibiotics relies on the up-regulation of *mprF* gene encoding for an enzyme responsible for linking lysine (+) to phosphatidylglycerol (-) ⁵⁹. Subsequently, the formed complex lysine-phosphatidylglycerol (+) is translocated to the outer portion of the membrane, consequently increasing the bacteria surface charge. Another defense strategy has been associated to ATP synthase, which inactivation resulted in higher antimicrobial activity by specific AMPs, including human cathelicidin, LL37 ⁶⁰.

2.3 Human Cathelicidin and LLKKK18 Derivative

AMPs are short, generally 10–50 amino acids, naturally occurring molecules holding a broad spectrum of antibacterial activities. They are used as the basis for the development of novel antimicrobials, with the advantage of retaining less propensity for multidrug-resistant mechanisms, compared to conventional antibiotics⁶¹. Additionally, they can be obtained from plenty of sources, for instance, from insects, microbes, algae and mammals. The identification of novel peptides continues to increase, contrasting with the lack of new antibiotics.

LL37 is a 37 amino acid cationic peptide of the human innate immune system, the C-terminal part derived from the single human cathelicidin protein identified to date, hCAP18. LL37 can electrostatically interact with cell wall molecules of pathogens and perforate cytoplasmic membranes, exerting antimicrobial activity through the creation of pores⁶². A secondary offensive role was proposed based on peptide fiber formation interacting with the structure of the alkyl chains, rather than the head groups of the membrane lipids, acting as a shield against bacterial attack⁶³.

The mechanism is complex, and novel information is arising from high-resolution technology to provide more detail. LL37 has been proposed to adopt fibril-like structures capable of enclosing lipids, as a form of mechanism to selectively extract bacterial lipids, thereby destabilizing the microbe membrane⁶⁴. The fibril-like architectures consist of dimers of anti-parallel helices and the formation of amphipathic surfaces. The peptide interacts with lipids through the hydrophobic sites at the dimer interface, subsequently remodeling and then engulfing the lipids. More detailed insight has demonstrated that LL37 displays various modes of oligomerization, peptide-peptide interactions are made through residues located in the peptide center from lysine 12 to phenylalanine 27, and peptide-detergent (membrane-mimics) interaction occurs primarily through the central part of the sequence⁶². The same study proposes the transmembrane channel architecture of the peptide. The roles of cathelicidin may be extended to interactions with lipopolysaccharide (LPS), peptidoglycan, cytoplasmic proteins, and DNA⁶⁵⁻⁶⁷, or via the production of ROS⁶⁸. **Figure 2.6** depicts the antimicrobial mechanism of LL37.

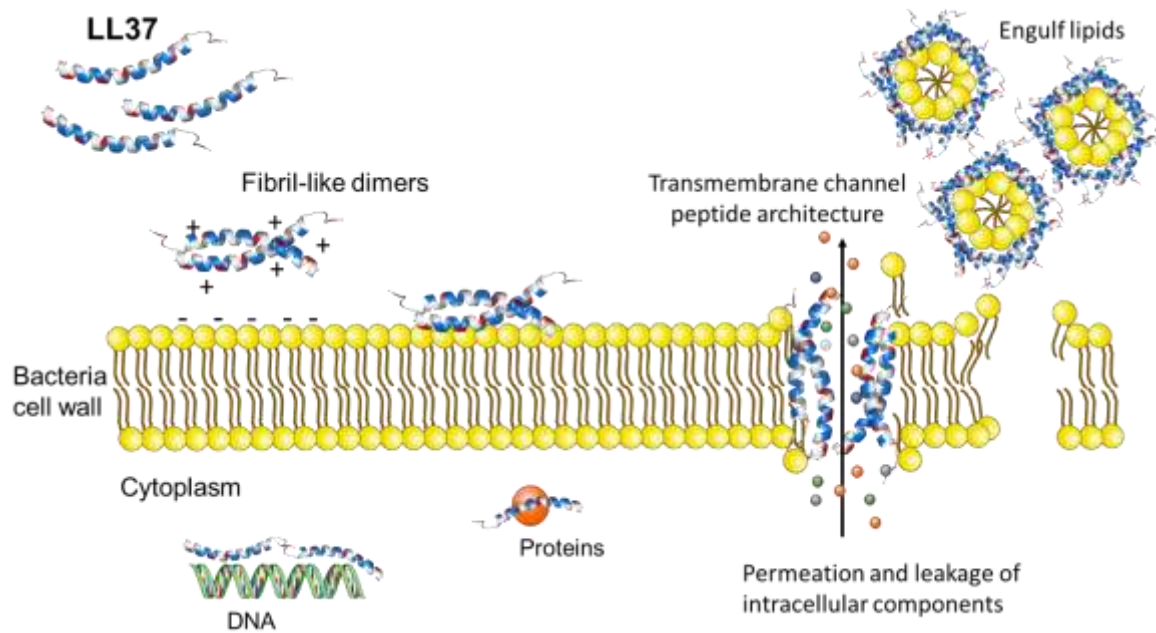


Figure 2.6 – Mechanisms of LL37 antimicrobial actions.

LL37 can also exert antimicrobial activity indirectly through immunomodulation (**Figure 2.7**), by acting as a chemoattractant of immune cells to the infected or damaged sites and influencing the production of inflammatory mediators ⁶⁹. Cathelicidin acts on, and is expressed by, several cell types, particularly epithelial and immune cells: neutrophils, epithelial, dendritic, monocytes and macrophages, mast cells, natural killer cells, MSCs, and even lymphocytes, acting as a bridge between the innate and adaptive immune systems ^{69,70}. The peptide can stimulate the differentiation of immune cells and the secretion of proinflammatory cytokines, chemokines, or costimulatory factors, synergizing with other active substances to promote immune responses. Both pro-inflammatory and anti-inflammatory responses may be stimulated, depending on the microenvironment. Although immunomodulation is not subject of study of this thesis work, it is a noteworthy rational basis for cathelicidin use in therapy design.

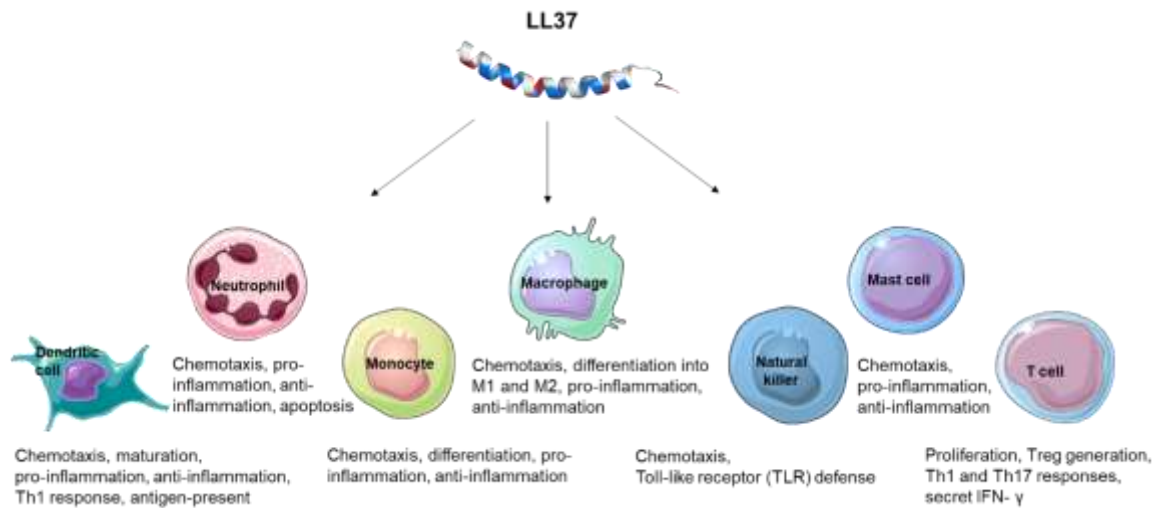


Figure 2.7 – Immunomodulatory actions of LL37 ⁶⁹.

Of note, although regarded as less prone to bacterial resistance than antibiotics, prolonged bacterial exposure to LL37 have shown to result in increased MRSA tolerance ⁷¹. However, more understanding is needed, and the use of cathelicidin in novel treatment approaches is worthwhile, given its superiority compared to other agents. Indeed, cathelicidin is proposed as a smart option for bone infections therapy for holding potent antistaphylococcal activity ^{72,73}, the most causative species in bone infections ^{25,74-76}, for inhibiting biofilm formation ^{72,77} and LPS activity ⁷⁸. The bactericidal effect of LL37 against both extra and intracellular *S. aureus* has been reported as being even superior to conventional antibiotics in eliminating intracellular bacteria ⁷³. Additionally, owing to a pro-angiogenic activity ⁷⁹⁻⁸¹, and stimulation of the migration of undifferentiated rat stem cells, the peptide has demonstrated to promote wound healing ^{80,81} and bone regeneration ^{82,83} *in vivo*.

The first-in-human trial using LL37 as a topical treatment for chronic leg ulcers demonstrated safety and markedly healing rates ⁸⁴. LL37 has entered phase II clinical studies for further investigation of its antimicrobial activity and its ability to modulate inflammation and healing of diabetic foot ulcers (NCT04098562). Moreover, a 24-aminoacid cathelicidin-derived AMP, OP-145 ⁸⁵, has successfully completed a safety and tolerability study in patients with chronic otitis media and has initiated phase II clinical trial in chronic middle ear infection (ISRCTN 84220089). Authors claim OP-145 offers benefits to antibiotic-unresponsive patients, opening a window of acceptance for novel peptide products designed with improved mechanism of action. LL37 has also been used as novel therapy for melanoma delivered as intratumorally injections (NCT02225366) ⁸⁶, and significantly improved symptoms of COVID-19 patients by oral administration of capsules bearing *Lactococcus lactis* genetically modified to produce

LL37⁸⁷. However, LL37 exogenous administration is discouraged by a costly long peptide length and early degradation, requiring higher doses and frequent administration.

LLKKK18 (LL18) is an 18-length amino acid peptide designed from LL37 displaying higher cationicity and hydrophobicity. This results in higher attachment to pathogen membrane (i.e. higher antimicrobial activity), being three-fold more effective in the killing of mycobacteria than LL37⁸⁸, exhibiting higher chemoattractant activity, decreased toxicity and binding to plasma protein⁸⁹. At neutral pH, LL37 is amphipathic and cationic with a net charge of +6 and 37.8 % hydrophobic amino acids, whereas LL18 has +8 and 44.4 %, respectively. In solution, they adopt α -helical structure (**Figure 2.8**). LL18 retains most of the LL37 residues involved in peptide–lipid (i.e. bacterial membrane) and in peptide–peptide interactions⁶⁴.

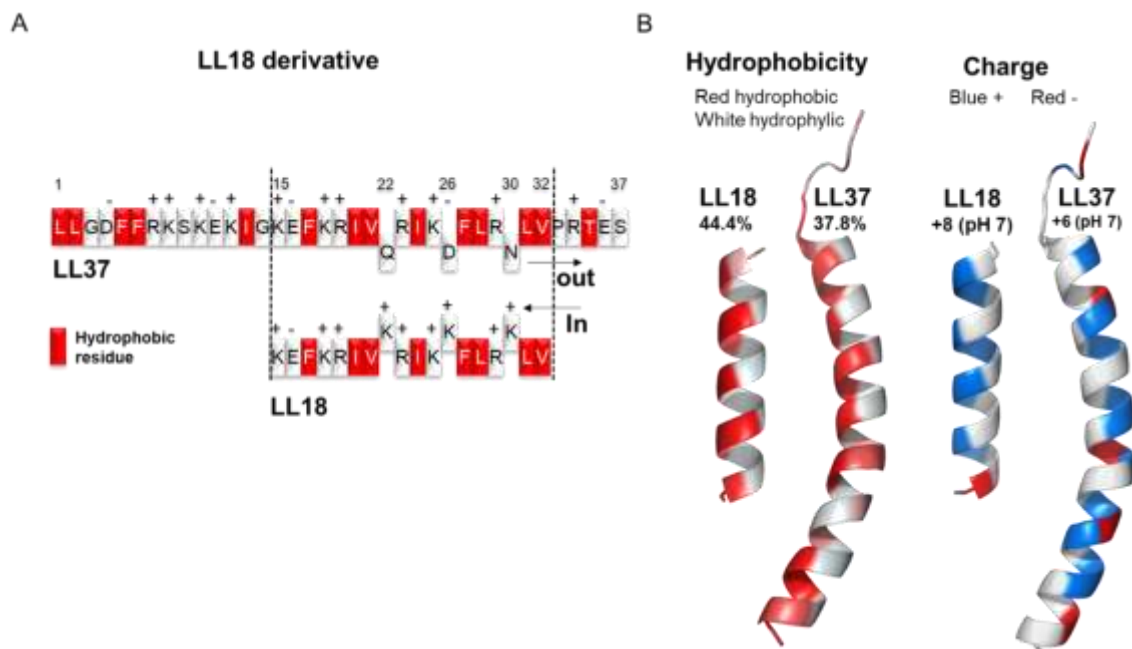


Figure 2.8 – (A) Amino acid sequence projections for LL37 and its LLKKK18 (LL18) peptide derivative, N-terminal (left) to C-terminal (right). To increase cationicity, Q22, D26, and N30 in LL37 were replaced by K22, K26, and K30 LL18. **(B)** α -helical peptide structures N-terminal (bottom) to C-terminal (up): LL37 has 37.8 % hydrophobic amino acids and a net charge of +6 at pH 7, whereas LL18 has 44.4 % and +8, respectively. At left, hydrophobic residues are shown in red, hydrophilic residues are shown in white, at right positive charges are highlighted in blue and negative charges in red (PyMOL software).

As an *in vivo* demonstration of the angiogenic and chemoattractant potential, LL18 has been reported to improve burn wound healing in a rat model, by topically applying a dose of 15 μ g of LL18 every 3 days during the first 9 days post-burn⁹⁰. Treatment with LL18 increased VEGF, and microvessel development,

reduced oxidative stress and inflammation, specifically, displaying low neutrophil and macrophage infiltration and pro-inflammatory cytokines levels, and induced more collagen deposition. However, the peptide showed no improvements in the regeneration of cranial defects in a goat model ⁹¹, which advocates the importance of more in-depth studies. Early degradation, a common limitation, may diminish its actions *in vivo*, particularly in the case of a single administration. LL18 also increased tissue damage as a function of concentration in an OM rat model ⁹², revealing another critical parameter. Nevertheless, LL18 is mostly unexplored. While manufacturing costs can be reduced by shorter derivatives, toxicity and early degradation may be circumvented by sustained delivery platforms.

2.3.1 Encapsulation Mechanisms

Numerous nanocarriers have been designed for the delivery of cathelicidin by a range of mechanisms, particularly tailored for antimicrobial and tissue healing applications. The outcomes may vary in encapsulation efficiency (EE) %, ease of preparation, peptide stabilization and prolonged release, all influencing the final peptide biological activity. LL37 was entrapped into chitosan NPs through strong hydrogen bonds with 86.9 % EE ⁹³. NPs were prepared by ionic gelation of chitosan cross-linked by multivalent anions (sodium tripolyphosphate), displaying 68 % biofilm formation inhibition compared to the free peptide. In another work, using the same approach, chitosan NPs had an EE of 78.52 %, enhanced stability under thermal, salts, and acidic pH, subsequently improving MRSA infection and wound healing in rats ⁹⁴. In another approach, LL37 was attached onto the surface of a covalently conjugated vancomycin-NPs formulation, with a loading efficiency of 66.5 % ⁹⁵. The peptide was adsorbed by blending with NPs, owing to their high surface area and suitable pore size, resulting in efficient anti-staphylococcal activity, and excellent wound healing in a mouse model. LL37 was incorporated in the inner water phase of poly(lactic-co-glycolic acid) acid (PLGA) NPs by W/O/W emulsion-solvent evaporation technique, with an EE of 70.2 % and drug loading (DL) of 1.02 (μg LL37/mg NP), showing a sustained *in vitro* release for 14 days ⁹⁶. Intradermal injection of LL37-PLGA-NPs displayed significant higher collagen deposition, re-epithelialized and neovascularized composition, resulting in complete wound closure after 13 days, unlike the free peptide condition. It increased angiogenesis, up-regulated IL-6 and VEGF expression, as well. In another approach, cationic LL37 was electrostatically attached to a negatively-charged lipid-based nanocarrier by simple mixing, with an EE of 60 % at pH 3.0 ⁹⁷. This pH-sensitive construct, could associate LL37 at $\text{pH} \leq 4.5$, but dissociated it at pH 6.0, which may hinder its application in certain scenarios. Other nanocarriers may retain LL37 at higher pH, and release it at acidic

pH, as convenient. Electrostatic attraction is a simple preparation method offering a pH-sensitive triggered release.

Chemical conjugation is another usually employed mechanism. Lipid nanocapsules were used to compare three different peptide incorporation strategies: peptide encapsulation, surface adsorption and covalent attachment ⁹⁸. Three AMPs were used as models, including LL37, and compared in terms of EE, peptide antimicrobial activity and protection against proteases. Adsorption onto the surface of carriers, implying predominantly electrostatic, but also Van der Waals or hydrophobic interactions, provided partial protection, resulting in a more potent antimicrobial activity. Encapsulation into reversed micelles by phase inversion process, provided higher stability and a higher EE that culminated in the preservation of peptide activity. Covalent conjugation by transacylation, linking the pegylated hydroxystearate from the carrier shell and the functional amino groups of peptides, exposing the peptide at the surface, resulted in peptide inactivation, despite a high EE. Although other nanosystems may behave differently, this study provides a useful insight on the critical influence of different LL37 loading mechanisms in functional biological outcomes (**Table 2.1**).

Table 2.1 – Summary of the outcomes influenced by three different LL37 loading mechanisms ⁹⁸.

Formulation	EE	General Antimicrobial activity	Stabilization against proteases	MIC <i>S. aureus</i> (µg/mL)	MIC MRSA (µg/mL)
Adsorption	+ (34.6 %)	+	+	8–16	4
Encapsulation	++ (99.4 %)	+	++	32	8
Conjugation	++ (82.5 %)	–	ND	>128	>128
Free LL37		*	*	8–16	8–16

EE, encapsulation efficiency; MIC, minimal inhibitory concentration; MRSA, methicillin-resistant *Staphylococcus aureus*; ND, not determined; (–) indicates absence; * a symbol (+/–) was not assigned by authors. LL37 MIC varied between 8 to 16, and displayed considerably lower stabilization against protease compared to all loaded LL37 formulations.

2.4 Vitamin D3

VD3, or cholecalciferol, is a liposoluble molecule precursor of human steroid hormones, physiologically obtained mostly through exposure to ultraviolet (UV)-B sunlight but also through diet ⁹⁹. This vitamin is

essential for human health and two major forms can be identified, one from vegetal origin, vitamin D2 (VD2), or ergocalciferol, and another from animal origin, VD3. Though, VD2 has been reported as being less potent and shorter acting than VD3, with respect to increasing the measurable metabolite blood levels^{100,101}. Sunlight VD3, obtained in the skin from 7-dehydrocholesterol, is biologically inactive and must undergo two enzymatic activation steps⁹⁹ (**Figure 2.9**). After production, it is partially stored in adipose tissues, while another part is converted to 25-hydroxyvitamin D3 (25[OH]D3) by the liver. 25(OH)D3 is further hydroxylated into the active form 1 α ,25-dihydroxyvitamin D3 (1,25[OH]2D3) in the kidneys, which then acts to maintain serum calcium levels and bone homeostasis.

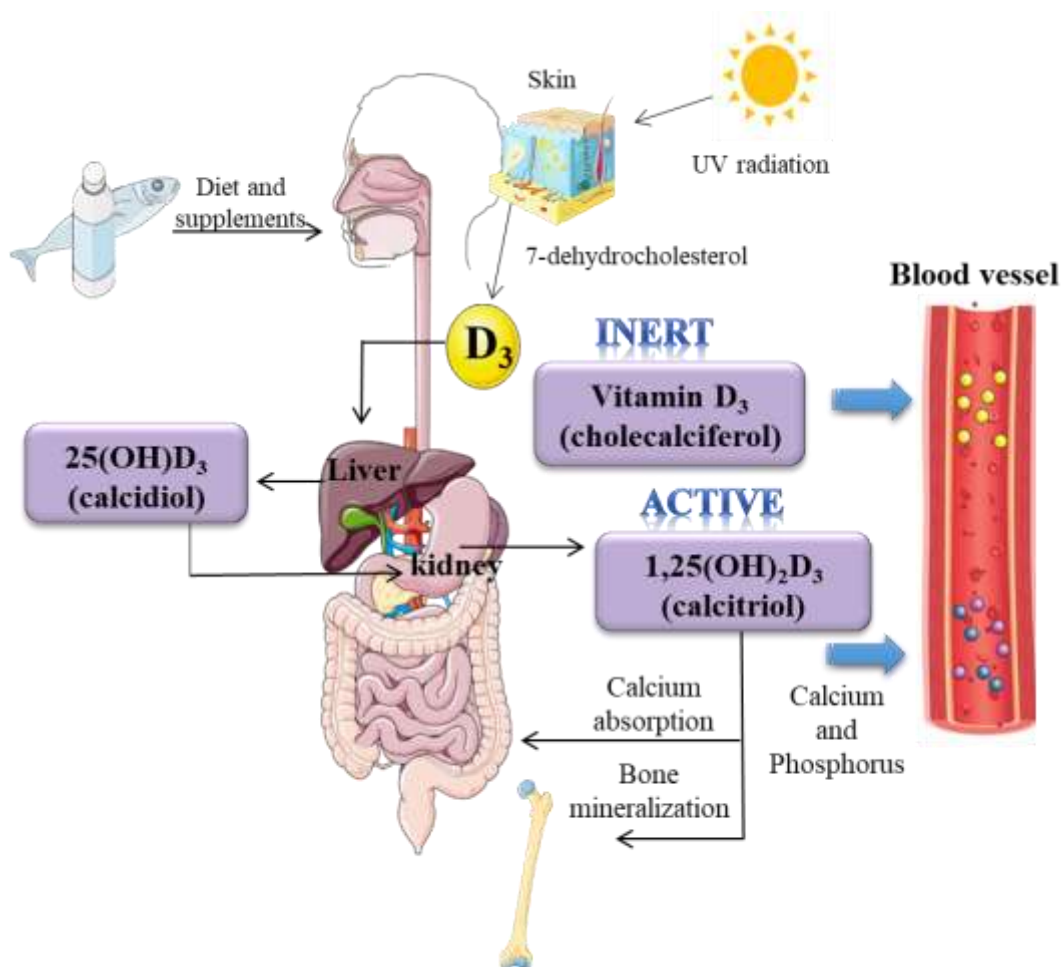


Figure 2.9 – Vitamin D3 metabolism.

VD3 actions go beyond a calcium, phosphorus and bone homeostasis regulator, expanding to antimicrobial¹⁰², immunomodulatory, anticancer or cardiovascular effects⁹⁹. Holding a rapid onset of action and short half-life (4 h to 8 h⁹⁹), the therapeutic use of 1,25(OH)2D3 is well-known associated with a propensity for hypercalcemia, a condition resulting from excessive reabsorption of calcium¹⁰³. Indeed, the exogenous administration of 1,25(OH)2D3 oversteps VD3 metabolism conversion stages, interfering

with the regulatory processes. The risk of hypercalcemia occurrence, though less concerning, must also be considered for VD3 overdosing intake ^{103,104}. Nevertheless, holding a slower onset of action and higher functional half-life (≤ 2 months ⁹⁹), inactive VD3 emerges as a generally safer, and more inexpensive, option for therapeutic design.

2.4.1 Antimicrobial Action

VD3 is currently in the spotlight for its role in fighting infections. The reason relies on the active metabolite, 1,25(OH)2D3, that acts by interacting with a nuclear vitamin D3 receptor (VDR), a ligand-activated transcription factor that functions to control gene expression through activation of gene transcription at specific DNA sequences, vitamin D3 response elements (VDRE) ¹⁰⁵. Cathelicidin can be up-regulated by a VD3-dependent mechanism, through VDR, acting as a secondary messenger driving VD3-mediated host response to infection ^{102,106} (**Figure 2.10**). Serum VD3 internalize cells, undergo enzymatic activation and subsequent binding to VDR. Dimerization with retinoid X receptor (RXR) induces gene transcription at VDRE sites.

Upregulation of cathelicidin via VD3 or its active metabolite has been reported in many cell types, for instance, monocytes/macrophages ¹⁰⁷, keratinocytes ¹⁰⁸, epithelial cells ¹⁰⁹. *In vitro*, VD3 metabolites-responsive cathelicidin resulted in boosted macrophage response against *Mycobacterium leprae* (25[OH]D3) ¹¹⁰, *Leishmania* (1,25[OH]2D3) ¹¹¹, and *Mycobacterium tuberculosis* (1,25[OH]2D3) ¹¹². Treatment with 1,25[OH]2D3 increased LL37 expression and improved antimicrobial activity of adult adipose-derived MSCs against *S. aureus* ¹¹³. After treatment with 1,25(OH)2D3-loaded nanofiber matrices, also bearing a 1,25(OH)2D3 inactivating enzyme inhibitor, engineered exosomes derived from monocytic cells displayed gene and protein expression levels around 500 times higher comparing to untreated and to CAMP (cathelicidin antimicrobial peptide) gene transfected cells ¹¹⁴. Subsequently, promoted high cell proliferation and migration, enhanced of endothelial tube formation, and antimicrobial activity. Conditions with free 1,25(OH)2D3 or 1,25(OH)2D3-loaded matrices, without inhibitory enzyme, had a drastically less pronounced effect. Although this advocates the critical regulator role of 1,25(OH)2D3 inactivating enzyme, it clearly reveals the potent effect of 1,25(OH)2D3 in stimulating cathelicidin.

In vivo proof-of-concept has recently been demonstrated by topical skin application of 1,25(OH)2D3, in a wound infection model of transgenic mice carrying the human cathelicidin gene ¹¹⁵. Cathelicidin gene expression was increased, subsequently improving *S. aureus* killing. *In vivo* demonstrations of antimicrobial VD3-cathelicidin partnership are scarce probably due to absence of suitable animal models, given that mice and other mammals lack the mechanism of cathelicidin induction via VD3. A clinical study

reported increased LL73 expression after intralesional injection of VD3 (Devarol-S of Memphis®, Egypt) in 20 patients with multiple verrucae vulgaris, a skin disease caused by human papillomavirus infection¹¹⁶. VD3 was administered every 2 weeks, in 4 sessions, and treatment was safe and effective. Given that exogenous administration of cathelicidin is usually hampered by a range of factors including toxicity, limited solubility and stability, VD3 may constitute a cost-effective non-antibiotic option to raise endogenous therapeutic levels of this AMP.

VDR has been found in most cell types, particularly immune cells, such as macrophages, dendritic cells, B-cells and T-cells¹¹⁷⁻¹¹⁹. For this reason, VD3 is a pleiotropic agent acting as a molecular switch targeting hundreds of human genes across a wide variety of tissues. Importantly, many cell types have been found to co-express VDR and VD3 or 25(OH)D3 activating enzymes, particularly immune cells¹²⁰. With all the necessary activation machinery at a cellular level, local administration of inactive VD3 becomes viable in the design of advanced therapeutic systems. Additional defense mechanisms VD3-associated include regulation of autophagy^{107,121}, pathways involved in oxidative stress¹²² and promotion of anti-inflammatory response¹²¹.

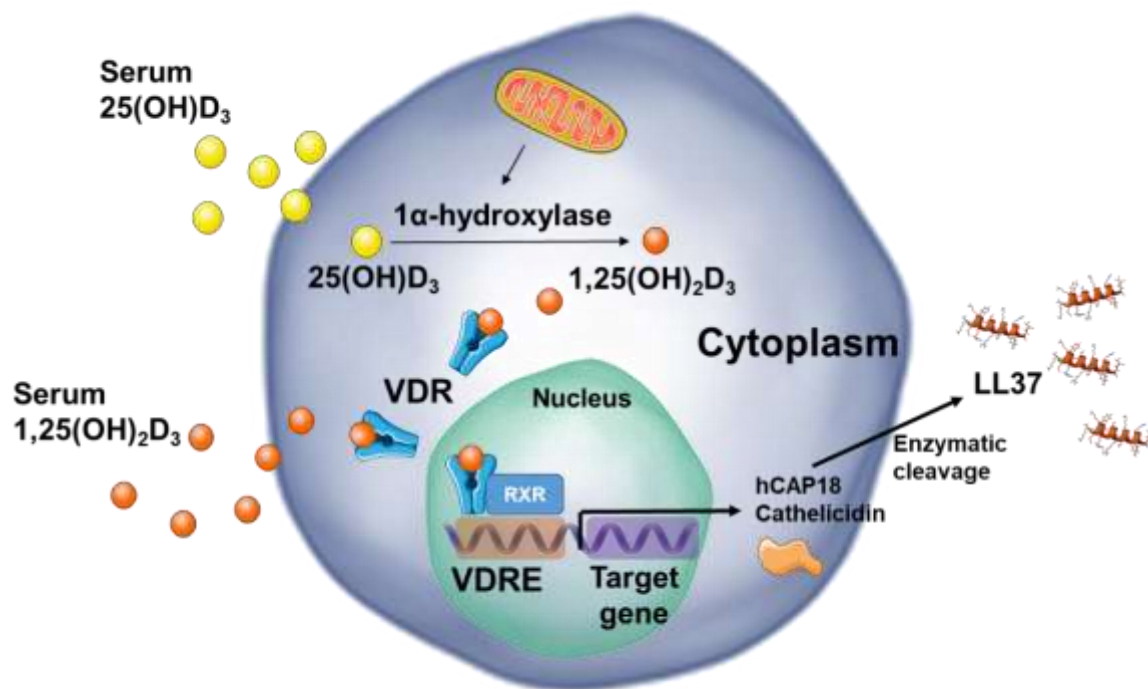


Figure 2.10 – Classic signaling pathway of vitamin D3 metabolites. Serum 25-hydroxyvitamin D3 (25[OH]D₃) is converted to 1α,25-dihydroxyvitamin D3 (1,25[OH]₂D₃) by mitochondrial 1α-hydroxylase, initiating the signaling cascade by binding to vitamin D3 receptor (VDR), which dimerizes with retinoid X receptor (RXR), and binds to specific deoxyribonucleic acid (DNA) sequences, vitamin D3 response elements (VDRE), regulating the transcription of several genes. 1,25(OH)₂D₃-VDR-RXR complex then

synthesizes cathelicidin as an inactive pro-peptide (hCAP18) which is cleaved upon release of the active LL37 by proteases ¹²³.

Hereupon, the antimicrobial action of VD3 appears to be indirect, mostly on the basis of stimulated expression of cathelicidin via VDR-VDRE gene activation ^{102,106}. Direct antimicrobial activity by itself is mostly unexplored, with most available studies reporting bactericidal improvements exclusively by concomitant administration with antibiotics ^{124,125}. Tintino and colleagues evaluated the inhibitory effect of VD3 on both sensitive and multidrug resistant *S. aureus* efflux pumps ¹²⁴. Both did not exhibit clinically relevant antibacterial activity, however, when associated with antibiotics against resistant strains carrying efflux pumps, VD3 increased antibiotic efficacy. The underlying mechanism is hypothesized to be related to the high degree of lipophilicity ^{124,126}, a key feature for the solubility in the bacterial membrane and binding to the efflux transporters before resistance mechanisms can occur. This can alter the structure of the bacterial lipoprotein membrane, resulting in the damage of essential components for the bacterial membrane integrity, thereby enhancing antibiotic uptake.

2.4.2 Benefits for Bone Healing

MC3T3-E1 from mouse calvaria is a widely used model to study the capability of compounds in stimulating osteoblastic bone formation. 1,25(OH)2D3 promoted cell differentiation at 10^{-10} , 10^{-12} , and 10^{-14} M, and induced early bone nodule formation at 10^{-12} M, in MC3T3-E1 ¹²⁷. Different concentration of VD3, 25(OH)D3 and 1,25(OH)2D3 were tested on the early and later differentiation, proliferation, and biomineralization of osteoblasts isolated from rat calvaria ¹²⁸. Results indicated that VD3 could not be directly metabolized by osteoblasts, since the respective activating enzymes of messenger ribonucleic acid (mRNA) were not significantly upregulated, and did not exert as much stimulation on the osteoblast differentiation and biomineralization as 25(OH)D3 and 1,25(OH)2D3, at the same concentration range 50–200 nM. However, in another study, VD3 was shown to be metabolized to 1,25(OH)2D3 in osteoblast precursor derived from human marrow (OPC1), for doses ($\geq 10^{-7}$ M) of 10 μ M for VD3 and 10 nM for 1,25(OH)2D3 ¹²⁹. VD3 also increased ALP activity, an indicator of osteoblast maturation, and calcium deposits in both OPC1 and MC3T3-E1, acting closely to the active form. Stem cells are attractive agents for bone regeneration therapy. Recently, VD3 enhanced osteogenic differentiation of dental tissue derived MSCs, thought only under specific conditions. Dental pulp-derived cells had the best osteogenic response to VD3 (2.5 nM) as gene expression but with the lowest mineralization rate ¹³⁰. Through gene array analysis, active 1,25(OH)2D3 displayed direct effect on a set of osteogenic and adipogenic genes required

for human MSCs differentiation, thus providing more insight on the effect of active metabolite in bone metabolism ¹³¹.

In vivo, submerging an intraosseous implant in a VD3 solution (10 % p/v) improved bone formation around implants and reduced the loss of crestal bone loss after 12 weeks osseointegration, in dog a mandibular model ¹³². Clinically, antibiotic (tobramycin or tobramycin and vancomycin)-impregnated VD3 granules (WO2020031083A1) have been topically applied to treat infected open wounds ¹³³, including in diabetic foot ulcer with OM, with successful results and minimum systemic side effects ¹³⁴. As a complement, *in vitro* studies showed that VD3 (0.01 nM) co-administrated with vancomycin could prevent the cytotoxic action of the antibiotic at 7500 µg/mL, in MC3T3-E1 ¹³⁵. Although more mechanistic insight is needed, reducing antibiotic toxicity to osteoblasts may have constituted another form of therapeutic action of clinically applied VD3 granules. Interestingly, as mentioned before, VD3 has been shown to exert antibacterial activity exclusively in combination with antibiotics ^{124,125}.

The roles and benefits of VD3 and 1,25(OH)2D3 have also been explored in *in vivo* bone models in association with delivery systems or scaffolds. The properties of HA NPs coated (by mixture) with VD3-loaded PLGA (50:50) NPs (HA/VD3/PLGA, 3:2:8 mass ratio) were compared to HA NPs coated with VD3 (HA/VD3, 2:8 mass ratio). The release of VD3 from HA/VD3 was fast and triggered necrosis of MC3T3-E1 *in vitro*, nevertheless improving the reconstruction of bone defects *in vivo*. HA/VD3/PLGA displayed a more sustained profile, resulting in the greatest levels of enhanced angiogenesis, vascularization, osteogenesis and bone structure differentiation, in artificial bone defects of the rat mandible ¹³⁶. A thiol-polyethylene glycol(PEG)-1,25(OH)2D3 conjugate was covalently bonded onto gold NPs through the thiol groups (-SH), and observed to enhance osteogenic differentiation of human adipose-derived stem cells *in vitro* ¹³⁷. Functionalized and non-functionalized NPs of 60 nm were prepared at 20 µM in colloidal solution states for analysis, though 1,25(OH)2D3 content is not clear. 1,25(OH)2D3 was loaded into a β-cyclodextrin grafted onto chitosan, a complex further co-loaded with calcitonin onto the surface of titanium-based implants capable of releasing those compounds in a sustained manner. *In vitro*, released 1,25(OH)2D3 upregulated the expression of calcium-binding protein and BMP2 in osteoblasts extracted from neonatal rat calvaria, as an indication of calcium deposition and differentiation stimulus. *In vivo*, bone remodeling was greatly enhanced under osteoporotic conditions and osseointegration was also improved ¹³⁸. As an example of a scaffold, 1,25(OH)2D3-loaded graphene oxide, with 36.87 ± 4.87 EE %, was incorporated into gelatin-HA at different 1,25(OH)2D3 concentrations ¹³⁹. All scaffolds degraded after one month of submersion into phosphate-buffered saline solution (PBS) and supported buccal fat pad-

derived stem cells adhesion. The scaffold enriched with 1 % of loaded 1,25(OH)₂D₃ had the best mechanical properties, 0.5 % displayed the best cell viability, and 2 % induced the best ALP activity.

Overall, reported conclusions regarding VD₃ osteogenic actions are highly dependent on concentration, and bioactive doses should not be comparable to the other metabolites. Inactive VD₃ is capable of stimulating biological functions of osteoblasts, although at generally higher (and non-toxic) concentration ranges than the active form. Thus, besides holding antimicrobial properties, extra-hepatic VD₃ has evolved to a booster of bone healing, with promising applicability as an inexpensive adjuvant for bone infection therapy. Though, bioavailability is limited by low solubility due to its hydrophobic nature which, together with its cytotoxicity profile, can be diminished by carrier platforms.

2.4.3 Vitamin D₃-conjugated Nanocarriers

Numerous delivery systems in the nanometer range have been developed to load fat-soluble VD₃, with the main purposes of achieving sustained release, increased solubilization and, thereby, bioavailability. Affinity to the hydrophobic moieties of nanocarriers is the typical base-mechanism. Excluding other metabolites and analogues, this section focuses only on chemically bounded VD₃, a not as widely employed approach.

As depicted in **Figure 2.11**, VD₃ holds one hydroxyl group suitable for covalent bonding. In this regard, some studies have used conjugated VD₃ as part of the delivery carrier, preferably together with PEG, for the main purpose of delivering anticancer drugs, mostly doxorubicin. Both succinic acid and glutarate are used to introduce a carboxyl group into VD₃, then acting as linkers.

Succinylated VD₃ was conjugated to PEG to produce self-assembled nanomicelles acting as emulsifiers for doxorubicin-loaded PLGA NPs¹⁴⁰. Stabilization with VD₃-PEG resulted in improved drug encapsulation and more sustained release from NPs. Another self-assembling VD₃-PEG conjugate was produced to encapsulate anticancer doxorubicin¹⁴¹. In this case, glutarate ester linker was selected instead of succinate ester for its longer carbon chain length, a feature presumably associated with increased esterase activity and intrinsic clearance increase. Glutarate is a five-carbon cyclic structure dicarboxylic anhydride, whereas succinate is a four-carbon. VD₃ was appointed as not only being useful as an excipient to encapsulate doxorubicin, but also as a chemosensitizer for enhancing therapeutic effect in a synergistic manner when in combination with the anticancer drug. Another glutarate VD₃-PEG conjugate-based micelles were used to load tacrolimus, for the treatment of ocular inflammation¹⁴². VD₃-PEG demonstrated therapeutic and synergistic action in combination with tacrolimus. However, similar to all the previously mentioned studies, chemically conjugated VD₃ content was not quantified. In a different approach, succinylated VD₃

was conjugated to three different anticancer drugs into 1,2-distearoyl-sn-glycero-3-phosphoethanolamine-Poly(ethylene glycol) (DSPE-PEG)-based NPs, a functionalized PEG conjugated lipid¹⁴³. VD3 was of interest to improve DL by means of hydrophobic interactions with DSPE-PEG. Overall, although some authors advocate therapeutic benefits, covalently bounded VD3 is mostly used with a purpose of a carrier adjuvant for the delivery of other bioactive drugs.

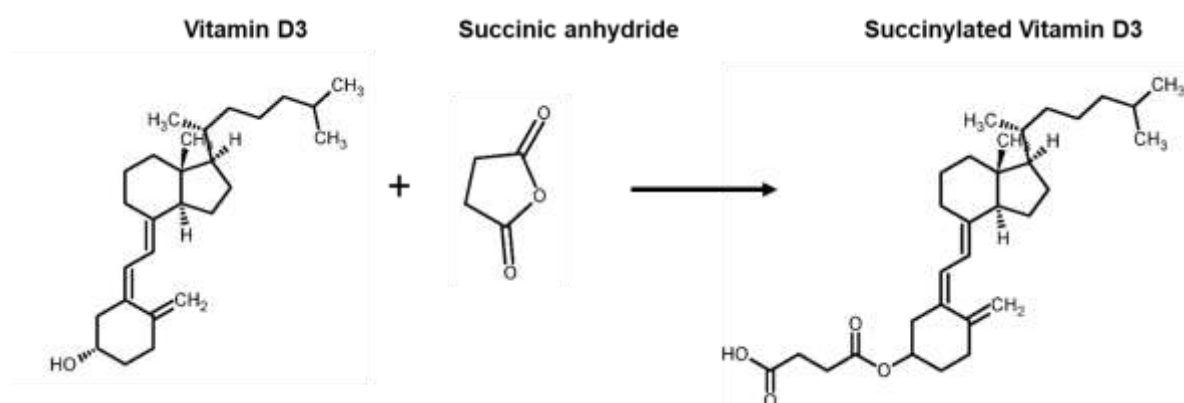


Figure 2.11 – Vitamin D3, VD3, (–OH) succinylation reaction with succinic anhydride (–C(=O)OH), resulting in a succinylated VD3 with a carboxyl group end, suitable for covalent conjugation of other components (designed in ChemDraw software).

2.5 Dextrin

Dextrin is continuously unveiling itself as a multifunctional tool for diverse reaction mechanisms in the development of modernistic (nano)biomaterials. This review intends to provide an understanding of how dextrin could work as a preferable platform for innovative therapies, particularly for bone or tissue healing, and encourage more research to disclose its role at a cellular level. Relevant dextrin-based drug delivery systems are hereby reviewed.

Dextrin ((C₆H₁₀O₅)_n) is a glucose polymer predominately composed of α-(1→4) glycosidic bonds, derived from starch partial hydrolysis achieved by applying dry heat under acidic conditions (pyrolysis or roasting) and enzymatic cleavage (amylases). Starches are a sugar-based source of energy mostly found in plants, such as potatoes, corn, wheat, or rice. Depending on the source and on how it is processed, it can exhibit different structures (linear, branched, or cyclic with different glycosidic bond types) and properties such as hygroscopicity, fermentability, sweetness, stability, gelation, solubility, bioavailability, viscosity, thereby being useful for multi-purposes, from food to adhesive or textile industries. Silva *et al.* have characterized the structure of several commercially available dextrans, which ranged from 6 to 17 glucose residues and

2 to 13 % branching degrees ¹⁴⁴. With respect to the biomedical field, we hereby focus on linear dextrin, a low molecular weight polymer displaying several hydroxyl groups suitable for bioconjugation (**Figure 2.12**). The practical work described in the next chapters of this thesis relates to Tackidex® (Roquette), a medical-grade dextrin derived from potato. Tackidex® displayed a heterogeneous polymerization degree mostly in the range of 4 to 7, up to a maximum of 16, and a convenient gelification rate for its use as an injectable device compared to other dextrans ¹⁴⁴. In this work, Tackidex® was always used after dialysis (< 1000 kDa).

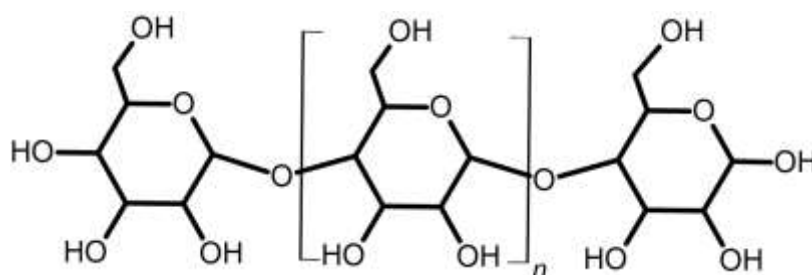


Figure 2.12 – Structure of dextrin (designed in ACD/ChemSketch software).

2.5.1 Smart Option for Therapy Design

As a result of inadequate clinical translation of therapeutic active compounds in their free form, alternative carriers emerged to overcome the hurdles associated with several features, such as systemic toxicity and side effects, early degradation, inadequate bioavailability, poor water solubility, low permeability or low stability. Biocompatibility, degradability and subsequent excretion mechanism, as well as the viability of the production method at industrial scale, have crucial implications for clinical translation. In this context, dextrin is a smart option for therapy design for several reasons:

- i)** non-toxic; available in medical grade, suitable for clinical practice; Food and Drug Administration (FDA) approved, accepted as a generally recognized as safe (GRAS) food ingredient ¹⁴⁵;
- ii)** Can be sterilized by gamma irradiation, one of the most preferable sterilization methods for medical devices, having shown not to change dextrin structure ¹⁴⁴;
- iii)** low molecular weight ¹⁴⁴ far below the renal filtration limit range (~30–50 kDa) ¹⁴⁶, avoiding tissue accumulation;
- iv)** biodegradable, as it can be enzymatically decomposed into glucose monosaccharides by blood α -amylases (E.C. 3.2.1.1) ¹⁴⁷, which then undergo renal elimination. This feature is of major importance

as it is connected to an enzymatic stimuli-responsive character, with implications on drug release profile or biomaterial degradation rate ¹⁴⁷;

- v)** holds multiple reactive primary and secondary hydroxyl groups, suitable for conjugations or grafting reactions. Additionally, the presence of two adjacent secondary hydroxyl groups in each monomer makes possible the rupture of C2–C3 bond by oxidation reaction, resulting in multiple functional aldehydes across the polymer chain. The degree of modifications can be precisely adjusted, with reproducibility ¹⁴⁸;
- vi)** after oxidation, dextrin is able to form pH-sensitive Schiff bonds with other components ^{149,150}; which denotes another stimuli-responsive opportunity, as to retain drugs at physiological conditions and triggering degradation in specific sites or cells;
- vii)** degradation rate can be controlled, i.e. delayed, as a function of chemical modification ^{147,151}, therefore useful to tailor the rate of a molecule liberation;
- viii)** conjugation does not diminish or modify protein activity, rather it provides a shielding effect. Upon enzymatic breakage of dextrin glycosidic bonds, drug activity is restored ^{90,152};
- ix)** low, and adjustable, viscosity, to improve quality of shape-filling materials ¹⁵³;
- x)** solubility in water and in certain polar aprotic solvents (where nucleophiles are more nucleophilic) such dimethyl sulfoxide (DMSO), very popular in bioconjugation for being chemically inert, and stable at high temperatures; solubility in DMSO makes possible co-dissolution of dextrin with certain water-insoluble drugs;
- xi)** optically active;
- xii)** derives from a natural, broadly available, renewable source – starch;
- xiii)** inexpensive.

It is fair to recognize the therapeutic success and future potential applicability of many other available well-known polymers in the drug delivery and tissue engineering fields, such as PEG, PLGA, chitosan, and many more, although some general disadvantages can be pointed out as opposed to dextrin. PEG is synthesized from non-renewable sources (petroleum), and has recently been linked to allergic responses to the mRNA coronavirus disease 2019 (COVID-19) vaccines ¹⁵⁴. Indeed, despite being recognized as a non-immunogenic synthetic polymer, PEG-related immune responses have come into light ¹⁵⁵. Dextran has been proposed as an alternative to PEG to serve as low protein-binding biomaterial coating and promote desired cell adhesion ¹⁵⁶. The presence of multiple reactive sites – equally present in dextrin – enabled the simultaneous grafting to a surface material and to cell adhesion peptides, culminating in the stimulation of endothelial, fibroblast, and smooth muscle cell attachment and spreading *in vitro*. Chitosan

use is hindered for displaying low solubility in neutral and alkaline pH water, requiring efforts to synthesize derivatives of enhanced solubility¹⁵⁷. PLGA NPs, for instance, require cryoprotectants to endure freeze-drying, and surfactants as stabilizing agents. The latter have shown to influence PLGA-PEG NPs fate within the brain, advocating its importance as a design parameter¹⁵⁸. A key-aspect for a successful scale-up and industrial production of a nanocarrier relies on the simplicity of the methodology.

There are plenty of different applications where each material may present better suitability. Since science is continuously evolving and there is still so much room for improvement with regards to each polymer, it is not fair to designate one single best option. For instance, not only intrinsic properties influence the fate, but also the production methods or drug–polymer interactions can determine the physicochemical characteristics of the resulting system and, therefore, its biological performance. The use of dextrin as a platform for drug delivery here presented advocate its potential to outperform well-established competitors in some applications, and intends to encourage more research.

2.5.2 Dextrin-based Drug Delivery Systems

Modern technological advances opened a window of opportunities for a diverse range of engineered constructs. **Table 2.2** lists a variety of mechanism by which dextrin can be customized to partake in several different constructs for drug delivery purposes, evidencing its versatility. Modifications such as succinylation, oxidation, crosslinking, hydrophobic or physical interactions, have been employed to produce polymer–drug conjugates, nanogels, NPs, other nanocomplexes and HGs.

Esterification is a very popular starch modification¹⁵⁹, being succinylation the most preferable method for the introduction of carboxyl groups ($-C(=O)OH$) along the backbone chain with precise tunability¹⁶⁰. The process includes the reaction of a carboxylic acid (succinic anhydride) with an alcohol (starch derivative), producing an ester. Succinic acid is a four-carbon cyclic structure dicarboxylic anhydride, highly reactive toward nucleophiles. Attack of a nucleophile at one carbonyl group opens the anhydride ring forming a covalent bond, whereas the second carbonyl group end results in a free carboxylic acid. For non-aqueous reactions, dimethylaminopyridine (DMAP) is regularly used as the organic catalyst (proton acceptor) to activate starch, making it nucleophilic, and to react with succinic anhydride to form a succinyl pyridinium intermediate, which then reacts with starch, finally culminating in starch succinate¹⁶¹. Then, a covalent link can be created between carboxylic acid ($-C(=O)OH$) and free amines ($-NH_2$) of bioactive molecules by carbodiimide chemistry. Dextrin-LL18 conjugates reduced free peptide antimicrobial activity from a 50 % cytotoxic concentration (CC_{50}) of $0.35 \pm 0.01 \mu M$ to $1.77 \pm 0.25 \mu M$, though restoring it to $0.48 \pm 0.03 \mu M$ after enzymatic breakage of the dextrin glycosidic bonds by α -amylase⁹⁰. This suggests an initial

shield effect, the peptide activity being restored upon release resulting from dextrin degradation. Consistently, this shield-and-restoring effect was also reported for dextrin conjugation to epidermal growth factor with potential for tissue repair therapy ^{152,162,163}, and colistin ^{164,165}.

Another strategy relies on grafting hydrophobic moieties in the dextrin backbone, resulting in self-assembled structures with hydrophobic cores suitable for the stabilization of other hydrophobic compounds. For instance, grafting vinyl acrylate groups in dextrin backbone by transesterification was used to prepare a nanocarrier for IL-10 ¹⁶⁶, superparamagnetic iron oxide NPs ¹⁶⁷, and for curcumin ¹⁶⁸ delivery.

Oxidation with sodium periodate has been the preferable method to introduce multiple aldehydes in dextrin, in which vicinal diols (in C2 and C3 position) can be cleaved by strong oxidants into its corresponding carbonyl compounds ¹⁵⁹ (**Figure 2.13**). These aldehydes are then suitable for dynamic Schiff base bonds, which confer a stimuli responsive feature as it disintegrates upon acid hydrolysis ^{149,150}, being mostly used in the development of pH sensitive HGs. The dialdehydes resulting sodium periodate oxidation can be crosslinked through amines ($-NH_2$) present in crosslinkers such as hydrazides ^{91,92,169-171}. Dialdehyde dextrin can be used itself as an alternative low toxicity crosslinker for other polymer-based HGs, binding to chitosan amines ($-NH_2$) for instance ¹⁷², or to gelatin amines ¹⁷³, crosslinking being further reinforced with hydrogen bonding with borax. Apart from HGs, one example is the use of oxidized dextrin (aldehydes) coated onto the surfaces of silica NPs (amines) via pH-sensitive Schiff bonds ¹⁵⁰. The functional NPs effectively prevented premature drug release under physiological conditions, but rapidly released the drug in the presence of (acidic) cancer environment.

Dextrin also offers plenty of strategies in its native form for the development of drug delivery systems, without requiring previous chemical modifications. Hydrophobic amphotericin B was solubilized in native hydrophilic dextrin by dissolution in alkaline borate buffer, followed by freeze-drying or nano spray-drying methods, resulting in self-assembled nanocomplexes with superior selectivity index compared to free drug ¹⁷⁴. Dextrin provided a simple and inexpensive nanocarrier for amphotericin B. The hydroxyl groups from dextrin and from naringin are able to react with aldehydes of glyoxal, a crosslinker dialdehyde, via the formation of acetal bonds ¹⁷⁵. This dextrin-based nanocarrier improved naringin's therapeutic action against carcinoma-isolated HepG2, by activating anti-inflammatory responses and inducing apoptosis. Once more as a platform for anticancer treatment, unmodified dextrin was used as a coating of halloysite nanotubes by physical adsorption, upon mixing, sonication and vacuum-facilitated deposition, conferring an enzyme-activated intracellular delivery action ¹⁷⁶. Unmodified dextrin is also useful for HGs development, making use of the binding affinity between carbohydrates and binding domains of starch-

biding modules ¹⁷⁷, or benefiting of a bond between dextrin hydroxyl groups (–OH) and isocyanate-terminated prepolymer (–NCO) ¹⁷⁸. In a different strategy, polypyrrole- and dextrin-based nanocomposites were synthesized by *in situ* polymerization of polypyrrole (–NH) in presence of dextrin (–OH) activated in acidic medium ¹⁷⁹. Dextrin provided inexpensive biodegradability and biocompatibility to a composite with a poor mechanical property and processability, though with antioxidant and antibacterial activities.

In the preparation of scaffolds or other bone filling agents, dextrin is of interest as a pore-inducing agent ^{180,181} and for mechanical adjustments (e.g. viscosity, homogeneity) ^{153,180-182}, having implications on cell anchorage and activity ¹⁸⁰. In these cases, dextrin is typically used in its native form.

Overall, dextrin can incorporate both hydrophilic and hydrophobic therapeutics by covalent bond or other non-covalent interactions, not necessarily requiring a previous chemical modification. Several constructs can be designed by a plethora of mechanisms on the basis of its functional groups. Degradation and drug release may be fine-tuned taking advantage of pH, enzymes or degree of modification.

Table 2.2 – Summary of constructs making use of dextrin versatility to create novel constructs/systems for biomedical purposes.

Construct/ System	Therapeutic of interest	Dextrin modification	Reaction mechanism	Utility
Conjugates <small>90,152,162-165</small>	Peptides (colistin, LL18); epidermal growth factor.	Introduction of carboxyl groups ($-\text{CH}=\text{O}$) by succinylation.	Covalent bond between carboxyl ($-\text{CH}=\text{O}$) from modified-dextrin and amine ($-\text{NH}_2$) from bioactive molecule, by carbodiimide chemistry.	Shield-and-restoring effect: sustained release by enzymatic activation.
Coating onto silica NPs (MSNs) <small>150</small>	Doxorubicin.	Oxidation ($-\text{CH}=\text{O}$) via sodium periodate	DAD was conjugated on the surface of MSNs as caps by reaction between DAD aldehydes ($-\text{C}(=\text{O})\text{OH}$) and amines ($-\text{NH}_2$) of MSNs through Schiff-base reaction.	Triggered release at specific site (pH-sensitive); control premature drug release.
	Curcumin; IL-10 and iron oxide NPs.	Grafting of hydrophobic vinyl acrylate domains, by transesterification, resulting in an amphiphilic, self-assemble, system.	Hydrophobic-hydrophobic interactions. Drug internally stabilized through the hydrophobic domains.	Solubilization of hydrophobic molecules within the hydrophobic core of self-assembled hydrophobized dextrin.
Nanogels <small>166-168,183</small>	siRNA.	Dextrin was succinylated ($-\text{C}(=\text{O})\text{OH}$), then firstly linked to cystamine, and secondly to arginine via carbodiimide chemistry (carboxyl-amine bonds), then finally thiolated with dithiothreitol.	siRNA entrapped by charge condensation with positive arginine residues of modified dextrin. Nanogels formed by disulfide crosslinking as well as the electrostatic adsorption effect with siRNA.	Bioreducible responsive behavior (accelerated siRNA release in a bioreducible intracellular environment, as in tumor cells, remaining stable under physiological conditions.

Conductive Nanocomposites	Polypyrrole.	No modification.	<i>In situ</i> polymerization of polypyrrole, in the presence of dextrin activated in acidic medium.	Confer (inexpensive) biodegradability to a conductive nanocomposite with antioxidant and antibacterial activities.
179				
Nanocomplexes¹	Amphotericin B.	No modification.	Physical interaction.	Solubilize hydrophobic drug, shield toxicity and increase therapeutic index. Simple method and inexpensive formulation.
74				
NPs	Naringin.	No modification.	Hydroxyl groups (-OH) from dextrin and from naringin react with glyoxal (crosslinker) aldehydes (-CH=O) via the formation of acetal bonds.	Effective carrier for long-term naringin delivery, providing higher anticancer potency compared to free naringin.
175				
Dextrin-clogged nanotubes	Triazole dye brilliant green.	No modification.	Physically-adsorbed dextrin layer on nanotubes, via vacuum-facilitated deposition.	Selective anticancer drug delivery; enzyme-responsive coating to clog the tube opening until the cell absorbs these nanocarriers and induce release only inside the cells.
176				
Hydrogels	Recombinant protein made of RGD and SB).	No modification.	Binding affinity between the binding domain of SMB and dextrin.	Adsorb the RGD sequence to the hydrogel surface; improved adhesion of fibroblasts (> 30 %) to the hydrogel.
91,92,169-173,177,178	Bone substitutes; proteins; stem cells; urinary bladder matrix, VH, LL18.	Oxidation with sodium periodate; crosslinking with adipic hydrazide agent.	Schiff-base reaction - hydrazone bonds – between DAD (-CH=O) and hydrazide (-NH ₂).	Injectability; moldability; drug administration; mechanical strength reinforcement.

	Oxidation with sodium periodate, then used as crosslinker itself for an agarose and chitosan-based hydrogel.	Schiff base reaction between dextrin ($-CH=O$) and chitosan ($-NH_2$), and physical interaction with agarose.	Low cytotoxic crosslinking agent; stiffness strongly influenced by the degree of oxidation; adjustment of physico-chemical and elastic properties, with implications on cell attachment and proliferation.
	Oxidation with sodium periodate; borax as crosslinker.	By means of (reversible) imide bonds between dextrin ($-CH=O$) and gelatin ($-NH_2$); hydrogen bonds between dextrin ($-OH$) and hydrolyzed borax ($-OH$);	Injectable and self-healing properties, degradability and blood compatibility.
Dexamethasone.	No modification.	Grafting of polyurethane on dextrin occurs through the chemical reaction between isocyanate-terminated prepolymer ($-NCO$) and the hydroxyl group ($-OH$) of dextrin forming a urethane linkage ($-NHCOO-$). Hydrophobic interaction between drug and hydrogel.	Different graft density to control the hydrophilic–hydrophobic balance for regulated drug delivery.

LL18, LLKKK18; DAD, dialdehyde dextrin; NPs, nanoparticles; MSNs, mesoporous silica nanoparticles, RGD, Arg-Gly-Asp peptide; SBM, starch-binding module; siRNA, small interfering ribonucleic acid (siRNA); VH, vancomycin hydrochloride.

2.5.3 Dextrin-based Hydrogels for Tissue Engineering

The use of biomaterials as bone fillers may be limited by poor cohesivity or injectability. The development of shape fitting HGs revolutionized handling and delivery of tissue healing components, exhibiting homogeneity, molding and self-healing properties, allow access to difficult sites, and avoid early evasion of particles. This section discloses dextrin purpose in the development of HGs for tissue engineering purposes. Aldehyde-hydrazide bond has been the most preferable synthesis mechanism of dextrin-based HGs. An injectable oxidized dextrin (ODEX)-based HG has been proposed by our group ¹⁴⁸, and its use was recently reported in goat critical-sized bone defects ⁹¹, tibial fractures ¹⁸⁴, and in a rat model of OM ⁹². Moreover, *in vitro* and *in vivo* biocompatibility has been thoroughly validated ^{92,148,169,184,185}. Dialdehydes introduced in dextrin backbone by oxidation (40 % mol) with sodium periodate, spontaneously form covalent bonds – hydrazone linkages – with the amines of adipic dihydrazide (ADH), upon contact ¹⁸⁶ (**Figure 2.13**). Major advantages include rapid and convenient gelling time, granule stabilization, handling properties, injectability, biocompatibility, long shelf-life and ease of manufacture. Importantly, gelation time may be adapted by changing polymer/reticulating agent ratio and can be prepared at room temperature ¹⁴⁸. Due to the reversible nature of hydrazones linkages in water ¹⁸⁷, ODEX works as a delivery platform with rapid degradation profile ¹⁴⁴, presumably excluding any kind of interference with prolonged biological events following administration, for instance, during later-stage bone ingrowth. However, although it has been useful as a carrier of nanogels ¹⁴⁸, urinary bladder matrix ¹⁶⁹, stem cells ^{91,169}, ceramics ^{91,169}, peptides ^{91,92} and antibiotics ⁹², release profile methodologies addressed *in vitro* cannot be extrapolated.

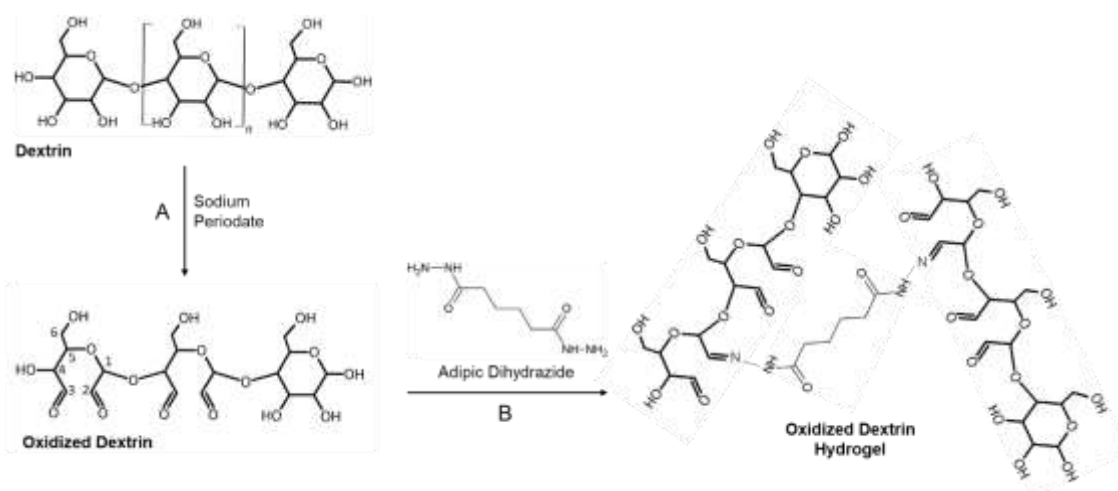


Figure 2.13 – Schematic representation of **(A)** dextrin oxidation with sodium periodate and **(B)** subsequent crosslinking reaction with adipic dihydrazide, resulting in hydrogel formation (designed in ACD/ChemSketch software).

While rapid degradation may be desired in certain cases, an irreversible deformation may restrain its use in others, for instance, due to low mechanical strength. Wang *et al.* proposed an injectable thermo-responsive HG, based on the *in situ* cross-linking between hydrazide-functionalized poly(N-isopropylacrylamide) and dialdehyde dextrin, with improved mechanical strength, elasticity and stability provided by reinforcement with hydrogen-bonding from poly(N-acryloyl glycinamide)¹⁷¹. Dialdehyde dextrin was produced by a $\sim 40\%$ (mol) oxidation with sodium periodate. Unlike ODEX that degrades within 24 h *in vitro*¹⁴⁴, drug release behavior could be studied for several days. Owing to the reinforcement provided by this new hydrazide-dialdehyde dextrin cross-linking, improved mechanical properties and delayed degradation endows suitability for tissue engineering with controlled delivery purposes. However, *in vivo* degradation behavior is not addressed yet, nor its toxicity profile, and a 30 min cure at 37 °C for the HG preparation may not be convenient in a surgery scenario.

In another study, HGs were prepared via aldehyde dextrin–functionalized hydrazide reaction, with starch NPs used as fillers for HG reinforcement of mechanical properties¹⁷⁰. HGs could be ready in 50 s at 37 °C, showed good injectability and stability in PBS, and displayed elasticity moduli generally 70 % higher than unreinforced samples. The HG showed good compatibility in L929 cells, however, the high 80.86 % dextrin oxidation degree may raise concerns, since no harmful effect was demonstrated only at low concentrations up to 400 $\mu\text{g}/\text{mL}$. A concentration-dependent toxic effect of aldehyde-bearing dextrin (40 %) has also been demonstrated in TK6 cell line¹⁸⁵.

Dialdehyde dextrin has also been proposed as a crosslinking agent alternative with reduced toxicity compared to commonly used crosslinkers, for instance glutaraldehyde¹⁷². HG network based on different ratios of agarose and chitosan were prepared by covalent bonding between oxidized dextrin ($-\text{COO}$) and

chitosan ($-NH_2$), via Schiff bases. A degree of 17.5 % dextrin oxidation positively influenced HG viscoelastic properties, homogeneity and network stability at pH 7.4, while exhibiting a low cytotoxicity profile. Cell adhesion and proliferation of human fibroblasts, epidermal keratinocytes and corneal epithelial cells were also generally better, compared to formulations with lower oxidation degree. Dextrin showed itself as a non-toxic tool to adjust physicochemical properties of HGs tailored for wound healing or soft tissue regeneration.

Another dialdehyde dextrin was used in association with gelatin and dialdehyde carboxymethyl cellulose to synthesize an HG, and borax and glutaraldehyde were used as binding agent and cross-linker, respectively, by means of (reversible) imide and hydrogen bonds ¹⁷³. The HG displayed injectable and self-healing properties, degradability and blood compatibility.

A dextrin-based HG functionalized with peptide Arg-Gly-Asp and starch binding module (RGD-SBM) recombinant protein worked as a platform for adhesion of fibroblasts ¹⁷⁷. Dextrin was of interest because of a specific affinity for the SBM element from the recombinant protein ¹⁸⁸, without resorting to complex chemistry or toxic elements. A superabsorbent and non-dissolvable HG film based on chemical crosslinking between dextrin-polyacrylamide and boric acid was synthesized using a free radical reaction mechanism, displaying viscoelastic and self-healing properties of injectable delivery and tissue engineering utility ¹⁸⁹. Self-healing reflects the ability of an HG to restore new bonds immediately after rupture. Dextrin was chosen for having functional groups for crosslinking, optical activity, low viscosity, and non-toxicity.

Overall, dextrin has been used in the preparation of HGs tailored for tissue engineering for its capability of improving stabilization, mechanical properties, biocompatibility and for serving as a safe alternative to toxic chemical intermediates in the fabrication method.

2.5.4 Benefits for Bone Healing

Owing to structural properties, dextrin has become a resourceful engineering tool to create improved products for biomedical applications. However, this glucose polymer may actually hold some therapy benefits by itself, particularly for tissue healing and infected conditions, rather than simply working as a biocompatible intermediate in biomaterial preparation and delivery. In an attempt to validate dextrin use as part of bone substitutes, *in vitro* effects were investigated in MC3T3-E1 mouse osteoblastic-like cells ¹⁹⁰. The polymer promoted proliferation and enhanced ALP activity at 0.1 and 1.0 mM, while from 10 mM up compromised cell viability, with a calculated CC_{50} of 41 mM. Correspondingly, a previous study had shown higher proliferating activity of fibroblastic L929 cells at the same 0.1 and 1.0 mM concentrations (CC_{50} 72 mM) ¹⁹¹.

Importantly, dextrin has recently unveiled itself as a source of energy used in hypoxic conditions by human osteoblast cell line hFOB 1.19¹⁹². Hypoxia conditions occur in depleted blood supply scenarios, for instance fractures¹⁹³, which compromises osteoblast function and bone formation, as well as increases bone resorption¹⁹⁴. Dextrin could therefore work as an adjuvant in bone repair as a source of energy to osteoblasts in oxygen depleted conditions (i.e. severely damaged bone). This supports dextrin could stand not only as a safe, but even beneficial compound for bone formation, yet also advocates the importance of a proper synthesis-dose and release rate *in vivo*. The polysaccharide also mimics the ECM of native bone, displaying good biocompatibility.

Degradation by blood α -amylase may constitute one of its most important advantages. The normal range for blood amylase is 25–85 units per liter (U/L)¹⁹⁵, but it may vary between different test measurements. Variations in total concentration are connected to some diseases. The levels of α -amylase measured in patient-derived acute (188 IU/L) and chronic (52 IU/L) wound fluids, were sufficient for recombinant human epidermal growth factor (rhEGF) efficient release from dextrin-rhEGF conjugates, providing proof-of-concept of polymer biodegradability in a close-to-clinical context¹⁵³. This supports that chemically conjugated drugs could be released from dextrin in acute or chronic bone wound scenarios.

In another work, dextran was proposed as an alternative to the commonly used PEG for surface modifications of implantable biomaterials for repelling undesired protein and cell binding, while enabling bioconjugation to specific bioactive molecules that promote adhesion of desired cells¹⁵⁶. The rationale to a better performance rely on the multiple reactive side groups along the polymer chain for grafting and conjugation to bioactive molecules (after dextrin oxidation) in sufficient amounts for stronger responses, compared to solely two reactive sites per molecule in PEG. Dextran is produced by bacteria and is mainly composed by α -1,6 glycosidic linkages, with α -1,3 branches (non-degradable by amylases) while dextrin derives from starch and is mostly composed of α -1,4 linkages. Although dextrin has not been tested for the same purpose, structural similarities with dextran show potential for controlling cellular interactions at the tissue–biomaterial interface, promoting implant integration.

Dextrin use should not be restricted to a non-toxic drug carrier. In a bone damage scenario, either arising by natural causes, disease or surgery, the occurrence of infections are common events hindering bone healing. Dextrin holds a lectin-mediated bacteria-carbohydrate binding ability. Indeed, carbohydrates have emerged as promising materials for antimicrobial targeted drug delivery, owing to carbohydrate-binding proteins – lectins. Lectins are present in animals, plants, lichens, bacteria, and higher fungi, and can selectively recognize carbohydrates and reversibly interact with them mainly through hydrogen bonds, van der Waals, and hydrophobic forces. A dextran(α -1,6-linked glucose polymer)-coated nanoparticle,

loading an antibiotic, demonstrated specific binding for lectins expressed by macrophages and a variety of pathogens *in vitro* ¹⁹⁶. The NPs significantly improved the antimicrobial efficacy against macrophage-infected intracellular *S. aureus* and *P. aeruginosa* in comparison with free antibiotic. Indeed, a previous study had reported a strong glucose-lectin affinity through affinity capillary electrophoresis, and both dextran and dextrin displayed an increase in lectin-interactions as a function of a decrease in the degree of polymerization ¹⁹⁷. The core structure was pointed as the major cause for the binding behavior, rather than the non-reducing-end sugar units.

Overall, dextrin shows benefits for bone repair: i) as a stimulator of proliferation and differentiation of osteoblasts and proliferation of fibroblasts; ii) as a source of energy in hypoxia conditions; iii) by confirmed susceptibility to amylase action (i.e. for drug release) in wound-derived human fluids; iv) for displaying potential as a low protein-binding implant coating, further providing multi-sites for grafting techniques that can confer selectivity for desired cell attachment, and v) for holding lectin binding-affinity, resulting in increased cell and bacteria uptake, thereby enhancing delivery of any entrapped-drugs. Nevertheless, much attention has been attributed to the structure versatility of dextrin to fabricate novel constructs, but little attention has been given to disclosing dextrin benefits at a cellular level. Although it may not work as a full-bodied treatment by itself, its adjuvant role may have been underrated so far and deserves more study.

2.6 References

1. Kahla, R. Ben & Barkaoui, A. Bone multiscale mechanics. in Bone Remodeling Process (eds. Kahla, R. Ben & Barkaoui, A.) 1–47 (Academic Press, 2021).
2. Boskey, A. L. Bone composition: relationship to bone fragility and antiosteoporotic drug effects. *Bonekey Rep.* 2, 447 (2013).
3. Clarke, B. Normal Bone Anatomy and Physiology. *Clin. J. Am. Soc. Nephrol.* 3, S131–S139 (2008).
4. Chang, B. & Liu, X. Osteon: Structure, Turnover, and Regeneration. *Tissue Eng. Part B. Rev.* 28, 261–278 (2022).
5. Lin, X., Patil, S., Gao, Y. G. & Qian, A. The Bone Extracellular Matrix in Bone Formation and Regeneration. *Front. Pharmacol.* 11, 757 (2020).
6. Theocharis, A. D., Skandalis, S. S., Gialeli, C. & Karamanos, N. K. Extracellular matrix structure. *Adv. Drug Deliv. Rev.* 97, 4–27 (2016).
7. Manolagas, S. C. Birth and death of bone cells: basic regulatory mechanisms and implications for the pathogenesis and treatment of osteoporosis. *Endocr. Rev.* 21, 115–137 (2000).
8. Perez-Amodio, S., Beertsen, W. & Everts, V. (Pre-)osteoclasts induce retraction of osteoblasts before their fusion to osteoclasts. *J. bone Miner. Res.* 19, 1722–1731 (2004).
9. Tresguerres, F. G. F. *et al.* The osteocyte: A multifunctional cell within the bone. *Ann. Anat.* 227, 151422 (2020).
10. Everts, V., Jansen, I. D. C. & de Vries, T. J. Mechanisms of bone resorption. *Bone* 163, 116499 (2022).

11. Nakamura, H. Morphology, Function, and Differentiation of Bone Cells. *J. Hard Tissue Biol.* 16, 15–22 (2007).
12. Dong, L. *et al.* Mechanical stretch induces osteogenesis through the alternative activation of macrophages. *J. Cell. Physiol.* 236, 6376–6390 (2021).
13. Kenkre, J. S. & Bassett, J. H. D. The bone remodelling cycle. *Ann. Clin. Biochem.* 55, 308–327 (2018).
14. Clevers, H. & Nusse, R. Wnt/ β -Catenin Signaling and Disease. *Cell* 149, 1192–1205 (2012).
15. Pfeiffenberger, M. *et al.* Fracture Healing Research—Shift towards In Vitro Modeling? *Biomedicines* 9, 748 (2021).
16. Fernandez de Grado, G. *et al.* Bone substitutes: a review of their characteristics, clinical use, and perspectives for large bone defects management. *J. Tissue Eng.* 9, (2018).
17. Fiume, E., Magnaterra, G., Rahdar, A., Verné, E. & Baino, F. Hydroxyapatite for Biomedical Applications: A Short Overview. *Ceramics* 4, 542–563 (2021).
18. Ishikawa, K. *et al.* Physical and histological comparison of hydroxyapatite, carbonate apatite, and β -tricalcium phosphate bone substitutes. *Materials (Basel)*. 11, 1993 (2018).
19. Böhner, M. Resorbable biomaterials as bone graft substitutes. *Mater. Today* 13, 24–30 (2010).
20. Sheikh, Z. *et al.* Mechanisms of in vivo degradation and resorption of calcium phosphate based biomaterials. *Materials (Basel)*. 8, 7913 (2015).
21. Rodriguez, A. E. & Nowzari, H. The long-term risks and complications of bovine-derived xenografts: A case series. *J. Indian Soc. Periodontol.* 23, 487 (2019).
22. Wang, T. Y., Xu, S. L., Wang, Z. P. & Guo, J. Y. Mega-oss and Mega-TCP versus Bio-Oss granules fixed by alginate gel for bone regeneration. *BDJ Open* 6, 1–8 (2020).
23. Kozakiewicz, M. & Wach, T. New Oral Surgery Materials for Bone Reconstruction—A Comparison of Five Bone Substitute Materials for Dentoalveolar Augmentation. *Materials (Basel)*. 13, (2020).
24. Xue, X., Hu, Y., Deng, Y. & Su, J. Recent Advances in Design of Functional Biocompatible Hydrogels for Bone Tissue Engineering. *Adv. Funct. Mater.* 31, 2009432 (2021).
25. Kavanagh, N. *et al.* Staphylococcal Osteomyelitis: Disease Progression, Treatment Challenges, and Future Directions. *Clin. Microbiol. Rev.* 31, e00084-17 (2018).
26. Walter, N., Baertl, S., Alt, V. & Rupp, M. What is the burden of osteomyelitis in Germany? An analysis of inpatient data from 2008 through 2018. *BMC Infect. Dis.* 2021 211 21, 1–8 (2021).
27. Kremers, H. M. *et al.* Trends in the Epidemiology of Osteomyelitis: A Population-Based Study, 1969 to 2009. *J. Bone Joint Surg. Am.* 97, 837 (2015).
28. Rossel, A. *et al.* Stopping antibiotics after surgical amputation in diabetic foot and ankle infections—A daily practice cohort. *Endocrinol. Diabetes Metab.* 2, e00059 (2019).
29. Keeney-Bonthrone, T. P., Hawes, A. M., Frydrych, L. M. & Delano, M. J. Long-Term Incidence of Amputation in Diabetic and Non-Diabetic Patients with Osteomyelitis. *J. Am. Coll. Surg.* 227, S105 (2018).
30. Yammine, K., Hayek, F. & Assi, C. A meta-analysis of mortality after minor amputation among patients with diabetes and/or peripheral vascular disease. *J. Vasc. Surg.* 72, 2197–2207 (2020).
31. Metsemakers, W. J., Smeets, B., Nijs, S. & Hoekstra, H. Infection after fracture fixation of the tibia: Analysis of healthcare utilization and related costs. *Injury* 48, 1204–1210 (2017).
32. Gimza, B. D. & Cassat, J. E. Mechanisms of Antibiotic Failure During Staphylococcus aureus Osteomyelitis. *Front. Immunol.* 0, 303 (2021).
33. Li, B. & Webster, T. J. Bacteria antibiotic resistance: New challenges and opportunities for implant-associated orthopedic infections. *J. Orthop. Res.* 36, 22–32 (2018).
34. Sadowska, J. M., Genoud, K. J., Kelly, D. J. & O'Brien, F. J. Bone biomaterials for overcoming antimicrobial resistance: Advances in non-antibiotic antimicrobial approaches for regeneration of infected osseous tissue. *Mater. Today* 46, 136–154 (2021).

35. van Vugt, T. A. G., Arts, J. J. & Geurts, J. A. P. Antibiotic-Loaded Polymethylmethacrylate Beads and Spacers in Treatment of Orthopedic Infections and the Role of Biofilm Formation. *Front. Microbiol.* 10, 1626 (2019).
36. Cobb, L. H., McCabe, E. M. & Priddy, L. B. Therapeutics and delivery vehicles for local treatment of osteomyelitis. *J. Orthop. Res.* 38, 2091–2103 (2020).
37. Vallet-Regí, M., Lozano, D., González, B. & Izquierdo-Barba, I. Biomaterials against Bone Infection. *Adv. Healthc. Mater.* 9, 2000310 (2020).
38. Haidar, R., Der Boghossian, A. & Atiyeh, B. Duration of post-surgical antibiotics in chronic osteomyelitis: empiric or evidence-based? *Int. J. Infect. Dis.* 14, e752-8 (2010).
39. Pollak, A. N. *et al.* The Relationship Between Time to Surgical Débridement and Incidence of Infection After Open High-Energy Lower Extremity Trauma. *J. Bone Jt. Surgery-American* 92, 7–15 (2010).
40. World Health Organization. Prioritization of pathogens to guide discovery, research and development of new antibiotics for drug-resistant bacterial infections, including tuberculosis. World Health Organization. Report <https://apps.who.int/iris/handle/10665/311820>. (2017).
41. Arshad, Z., Lau, E. J. S., Aslam, A., Thahir, A. & Krkovic, M. Management of chronic osteomyelitis of the femur and tibia: a scoping review. *EFORT open Rev.* 6, 704–715 (2021).
42. Josse, J., Velard, F. & Gangloff, S. C. Staphylococcus aureus vs. Osteoblast: Relationship and Consequences in Osteomyelitis. *Front. Cell. Infect. Microbiol.* 5, 85 (2015).
43. Hudson, M. C., Ramp, W. K., Nicholson, N. C., Williams, A. S. & Nousiainen, M. T. Internalization of Staphylococcus aureus by cultured osteoblasts. *Microb. Pathog.* 19, 409–419 (1995).
44. Ahmed, S. *et al.* Staphylococcus aureus fibronectin binding proteins are essential for internalization by osteoblasts but do not account for differences in intracellular levels of bacteria. *Infect. Immun.* 69, 2872–2877 (2001).
45. Tucker, K. A., Reilly, S. S., Leslie, C. S. & Hudson, M. C. Intracellular Staphylococcus aureus induces apoptosis in mouse osteoblasts. *FEMS Microbiol. Lett.* 186, 151–156 (2000).
46. Claro, T. *et al.* Staphylococcus aureus protein A binds to osteoblasts and triggers signals that weaken bone in osteomyelitis. *PLoS One* 6, (2011).
47. Young, A. B., Cooley, I. D., Chauhan, V. S. & Marriott, I. Causative agents of osteomyelitis induce death domain-containing TNF-related apoptosis-inducing ligand receptor expression on osteoblasts. *Bone* 48, 857–863 (2011).
48. Davido, B. *et al.* Phenol-Soluble Modulins Contribute to Early Sepsis Dissemination Not Late Local USA300-Osteomyelitis Severity in Rabbits. *PLoS One* 11, e0157133 (2016).
49. Deplanche, M. *et al.* Staphylococcus aureus induces DNA damage in host cell. *Sci. Rep.* 9, 1–13 (2019).
50. Hamza, T. & Li, B. Differential responses of osteoblasts and macrophages upon Staphylococcus aureus infection. *BMC Microbiol.* 14, 1–11 (2014).
51. Hamza, T. *et al.* Intra-cellular Staphylococcus aureus alone causes infection in vivo. *Eur. Cell. Mater.* 25, 341–50 (2013).
52. Jauregui, C. E., Mansell, J. P., Jepson, M. A. & Jenkinson, H. F. Differential interactions of Streptococcus gordonii and Staphylococcus aureus with cultured osteoblasts. *Mol. Oral Microbiol.* 28, 250–266 (2013).
53. Vandenesch, F., Lina, G. & Henry, T. Staphylococcus aureus hemolysins, bi-component leukocidins, and cytolytic peptides: a redundant arsenal of membrane-damaging virulence factors? *Front. Cell. Infect. Microbiol.* 2, 12 (2012).
54. Proctor, R. A. *et al.* Small colony variants: a pathogenic form of bacteria that facilitates persistent and recurrent infections. *Nat. Rev. Microbiol.* 4, 295–305 (2006).
55. Loss, G. *et al.* Staphylococcus aureus Small Colony Variants (SCVs): News From a Chronic Prosthetic Joint Infection. *Front. Cell. Infect. Microbiol.* 9, 363 (2019).

56. Tuchscher, L. *et al.* Staphylococcus aureus develops increased resistance to antibiotics by forming dynamic small colony variants during chronic osteomyelitis. *J. Antimicrob. Chemother.* 71, 438–448 (2016).
57. Wang, Y. *et al.* Inactivation of TCA cycle enhances Staphylococcus aureus persister cell formation in stationary phase. *Sci. Reports* 8, 1–13 (2018).
58. Qiao, J. *et al.* Properties and control of cold-induced small colony variants of Staphylococcus aureus. *Food Biosci.* 40, 100874 (2021).
59. Smitten, K. L. *et al.* Ruthenium based antimicrobial theranostics – using nanoscopy to identify therapeutic targets and resistance mechanisms in Staphylococcus aureus. *Chem. Sci.* 11, 70–79 (2019).
60. Liu, L. *et al.* Inhibition of the ATP synthase sensitizes Staphylococcus aureus towards human antimicrobial peptides. *Sci. Reports* 10, 1–9 (2020).
61. Spohn, R. *et al.* Integrated evolutionary analysis reveals antimicrobial peptides with limited resistance. *Nat. Commun.* 10, 1–13 (2019).
62. Sancho-Vaello, E. *et al.* The structure of the antimicrobial human cathelicidin LL-37 shows oligomerization and channel formation in the presence of membrane mimics. *Sci. Reports* 10, 1–16 (2020).
63. Shahmiri, M. *et al.* Membrane Core-Specific Antimicrobial Action of Cathelicidin LL-37 Peptide Switches between Pore and Nanofibre Formation. *Sci. Rep.* 6, 1–11 (2016).
64. Sancho-Vaello, E. *et al.* Structural remodeling and oligomerization of human cathelicidin on membranes suggest fibril-like structures as active species. *Sci. Reports* 7, 1–11 (2017).
65. Sochacki, K. A., Barns, K. J., Bucki, R. & Weisshaar, J. C. Real-time attack on single Escherichia coli cells by the human antimicrobial peptide LL-37. *Proc. Natl. Acad. Sci. U. S. A.* 108, E77-81 (2011).
66. Chung, M. C., Dean, S. N. & Van Hoek, M. L. Acyl carrier protein is a bacterial cytoplasmic target of cationic antimicrobial peptide LL-37. *Biochem. J.* 470, 243–253 (2015).
67. Zhu, Y., Mohapatra, S. & Weisshaar, J. C. Rigidification of the Escherichia coli cytoplasm by the human antimicrobial peptide LL-37 revealed by superresolution fluorescence microscopy. *Proc. Natl. Acad. Sci. U. S. A.* 116, 1017–1026 (2019).
68. Rowe-Magnus, D. A., Kao, A. Y., Prieto, A. C., Pu, M. & Kao, C. Cathelicidin peptides restrict bacterial growth via membrane perturbation and induction of reactive oxygen species. *MBio* 10, e02021-19 (2019).
69. Yang, B. *et al.* Significance of LL-37 on Immunomodulation and Disease Outcome. *Biomed Res. Int.* 2020, 8349712 (2020).
70. Bandurska, K., Berdowska, A., Barczyńska-Felusiak, R. & Krupa, P. Unique features of human cathelicidin LL-37. *BioFactors* 41, 289–300 (2015).
71. Kubicek-Sutherland, J. Z. *et al.* Antimicrobial peptide exposure selects for Staphylococcus aureus resistance to human defence peptides. *J. Antimicrob. Chemother.* 72, 115–127 (2017).
72. Boix-Lemonche, G., Guillem-Marti, J., D’Este, F., Manero, J. M. & Skerlavaj, B. Covalent grafting of titanium with a cathelicidin peptide produces an osteoblast compatible surface with antistaphylococcal activity. *Colloids Surfaces B Biointerfaces* 185, 110586 (2020).
73. Noore, J., Noore, A. & Li, B. Cationic antimicrobial peptide LL-37 is effective against both extra- and intracellular Staphylococcus aureus. *Antimicrob. Agents Chemother.* 57, 1283–90 (2013).
74. Zhang, X., Lu, Q., Liu, T., Li, Z. & Cai, W. Bacterial resistance trends among intraoperative bone culture of chronic osteomyelitis in an affiliated hospital of South China for twelve years. *BMC Infect. Dis.* 2019 191 19, 1–8 (2019).
75. Pozo, E. G. del, Collazos, J., Carton, J. A., Camporro, D. & Asensi, V. Factors predictive of relapse in adult bacterial osteomyelitis of long bones. *BMC Infect. Dis.* 18, 1–11 (2018).

76. Tawfik, G. M. *et al.* Concordance of bone and non-bone specimens in microbiological diagnosis of osteomyelitis: A systematic review and meta-analysis. *J. Infect. Public Health* 13, 1682–1693 (2020).
77. Kang, J., Dietz, M. J. & Li, B. Antimicrobial peptide LL-37 is bactericidal against *Staphylococcus aureus* biofilms. *PLoS One* 14, e0216676 (2019).
78. Yu, X. *et al.* LL-37 inhibits LPS-induced inflammation and stimulates the osteogenic differentiation of BMSCs via P2X7 receptor and MAPK signaling pathway. *Exp. Cell Res.* 372, 178–187 (2018).
79. Koczulla, R. *et al.* An angiogenic role for the human peptide antibiotic LL-37/hCAP-18. *J. Clin. Invest.* 111, 1665–1672 (2003).
80. Yang, X. *et al.* Chitosan hydrogel encapsulated with LL-37 peptide promotes deep tissue injury healing in a mouse model. *Mil. Med. Res.* 7, 1–10 (2020).
81. Garcia-Orue, I. *et al.* LL37 loaded nanostructured lipid carriers (NLC): A new strategy for the topical treatment of chronic wounds. *Eur. J. Pharm. Biopharm.* 108, 310–316 (2016).
82. Kittaka, M. *et al.* The antimicrobial peptide LL37 promotes bone regeneration in a rat calvarial bone defect. *Peptides* 46, 136–142 (2013).
83. Li, L. *et al.* Cathelicidin LL37 Promotes Osteogenic Differentiation in vitro and Bone Regeneration in vivo. *Front. Bioeng. Biotechnol.* 9, 347 (2021).
84. Grönberg, A., Mahlapuu, M., Stähle, M., Whately-Smith, C. & Rollman, O. Treatment with LL-37 is safe and effective in enhancing healing of hard-to-heal venous leg ulcers: a randomized, placebo-controlled clinical trial. *Wound Repair Regen.* 22, 613–621 (2014).
85. Malanovic, N. *et al.* Phospholipid-driven differences determine the action of the synthetic antimicrobial peptide OP-145 on Gram-positive bacterial and mammalian membrane model systems. *Biochim. Biophys. Acta - Biomembr.* 1848, 2437–2447 (2015).
86. Dolkar, T. *et al.* Dermatologic toxicity from novel therapy using antimicrobial peptide LL-37 in melanoma: A detailed examination of the clinicopathologic features. *J. Cutan. Pathol.* 45, 539–544 (2018).
87. Zhang, H. *et al.* Preliminary evaluation of the safety and efficacy of oral human antimicrobial peptide LL-37 in the treatment of patients of COVID-19, a small-scale, single-arm, exploratory safety study. *medRxiv preprint*, 2020.05.11.20064584 (2020)
88. Sonawane, A. *et al.* Cathelicidin is involved in the intracellular killing of mycobacteria in macrophages. *Cell Microbiol* 13, 1601–17 (2011).
89. Ciornei, C. D., Sigurdardóttir, T., Schmidtchen, A. & Bodelsson, M. Antimicrobial and chemoattractant activity, lipopolysaccharide neutralization, cytotoxicity, and inhibition by serum of analogs of human cathelicidin LL-37. *Antimicrob. Agents Chemother.* 49, 2845–50 (2005).
90. Silva, J. P. *et al.* Improved burn wound healing by the antimicrobial peptide LLKKK18 released from conjugates with dextrin embedded in a carbopol gel. *Acta Biomater.* 26, 249–262 (2015).
91. Pereira, I. *et al.* Regeneration of critical-sized defects, in a goat model, using a dextrin-based hydrogel associated with granular synthetic bone substitute. *Regen. Biomater.* 8, 1–10 (2021).
92. Machado, A. *et al.* Injectable hydrogel as a carrier of vancomycin and a cathelicidin-derived peptide for osteomyelitis treatment. *J. Biomed. Mater. Res. Part A* 110, 1786–1800 (2022).
93. Rashki, S. *et al.* Delivery LL37 by chitosan nanoparticles for enhanced antibacterial and antibiofilm efficacy. *Carbohydr. Polym.* 291, 119634 (2022).
94. Fahimirad, S., Ghaznavi-Rad, E., Abtahi, H. & Sarlak, N. Antimicrobial Activity, Stability and Wound Healing Performances of Chitosan Nanoparticles Loaded Recombinant LL37 Antimicrobial Peptide. *Int. J. Pept. Res. Ther.* 27, 2505–2515 (2021).
95. Lai, L. *et al.* Multifunctional MIL-101 nanoparticles with Fenton-like reactions to Co-deliver LL-37 peptide and Vancomycin for targeted NIR imaging and Drug-resistant bacteria treatment. *Chem. Eng. J.* 435, 135084 (2022).

96. Chereddy, K. K. *et al.* PLGA nanoparticles loaded with host defense peptide LL37 promote wound healing. *J. Control. Release* 194, 138–147 (2014).
97. Gontsarik, M., Mansour, A. Ben, Hong, L., Guizar-Sicairos, M. & Salentinig, S. pH-responsive aminolipid nanocarriers for antimicrobial peptide delivery. *J. Colloid Interface Sci.* 603, 398–407 (2021).
98. Matougui, N., Groo, A. C., Umerska, A., Cassisa, V. & Saulnier, P. A comparison of different strategies for antimicrobial peptides incorporation onto/into lipid nanocapsules. *Nanomedicine (Lond)*. 14, 1647–1662 (2019).
99. Dominguez, L. J., Farruggia, M., Veronese, N. & Barbagallo, M. Vitamin D Sources, Metabolism, and Deficiency: Available Compounds and Guidelines for Its Treatment. *Metabolites* 11, 255 (2021).
100. Armas, L. A. G., Hollis, B. W. & Heaney, R. P. Vitamin D2 is much less effective than vitamin D3 in humans. *J. Clin. Endocrinol. Metab.* 89, 5387–5391 (2004).
101. Balachandar, R., Pullakhandam, R., Kulkarni, B. & Sachdev, H. S. Relative Efficacy of Vitamin D2 and Vitamin D3 in Improving Vitamin D Status: Systematic Review and Meta-Analysis. *Nutrients* 13, 3328 (2021).
102. Chung, C., Silwal, P., Kim, I., Modlin, R. L. & Jo, E.-K. Vitamin D-Cathelicidin Axis: at the Crossroads between Protective Immunity and Pathological Inflammation during Infection. *Immune Netw.* 20, (2020).
103. Tebben, P. J., Singh, R. J. & Kumar, R. Vitamin D-Mediated Hypercalcemia: Mechanisms, Diagnosis, and Treatment. *Endocr. Rev.* 37, 521–547 (2016).
104. Rizzoli, R. Vitamin D supplementation: upper limit for safety revisited? *Aging Clin. Exp. Res.* 33, 19–24 (2020).
105. Essen, M. R. von & Geisler, C. VDR, the Vitamin D Receptor. in Choi S. *Encyclopedia of Signaling Molecules* 5907–5914 (Springer, Cham, 2018).
106. Gombart, A. F., Borregaard, N. & Koeffler, H. P. Human cathelicidin antimicrobial peptide (CAMP) gene is a direct target of the vitamin D receptor and is strongly up-regulated in myeloid cells by 1,25-dihydroxyvitamin D3. *FASEB J.* 19, 1067–1077 (2005).
107. Yuk, J.-M. *et al.* Vitamin D3 induces autophagy in human monocytes/macrophages via cathelicidin. *Cell Host Microbe* 6, 231–43 (2009).
108. Svensson, D., Nebel, D., Voss, U., Ekblad, E. & Nilsson, B. O. Vitamin D-induced up-regulation of human keratinocyte cathelicidin anti-microbial peptide expression involves retinoid X receptor α . *Cell Tissue Res.* 366, 353–362 (2016).
109. Schrupf, J. A., Sterkenburg, M. A. J. A. V., Verhoosel, R. M., Zuyderduyn, S. & Hiemstra, P. S. Interleukin 13 exposure enhances vitamin D-mediated expression of the human cathelicidin antimicrobial peptide 18/LL-37 in bronchial epithelial cells. *Infect. Immun.* 80, 4485–4494 (2012).
110. Kim, E. W., Teles, R. M. B., Haile, S., Liu, P. T. & Modlin, R. L. Vitamin D status contributes to the antimicrobial activity of macrophages against *Mycobacterium leprae*. *PLoS Negl. Trop. Dis.* 12, e0006608 (2018).
111. Crauwels, P. *et al.* Cathelicidin Contributes to the Restriction of *Leishmania* in Human Host Macrophages. *Front. Immunol.* 10, 2697 (2019).
112. Padhi, A. *et al.* *Mycobacterium tuberculosis* LprE Suppresses TLR2-Dependent Cathelicidin and Autophagy Expression to Enhance Bacterial Survival in Macrophages. *J. Immunol.* 203, 2665–2678 (2019).
113. Yagi, H. *et al.* Antimicrobial activity of mesenchymal stem cells against *Staphylococcus aureus*. *Stem Cell Res. Ther.* 11, 1–12 (2020).
114. Su, Y. *et al.* Engineered Exosomes Containing Cathelicidin/LL-37 Exhibit Multiple Biological Functions. *Adv. Healthc. Mater.* e2200849 (2022).

115. Lowry, M. B. *et al.* A mouse model for vitamin D-induced human cathelicidin antimicrobial peptide gene expression. *J. Steroid Biochem. Mol. Biol.* 198, 105552 (2020).
116. Sorour, N. E., Elesawy, F. M., Abdou, A. G., Abdelazeem, S. E. & Akl, E. M. Intralesional injection of vitamin D in verruca vulgaris increases cathelicidin (LL37) expression; therapeutic and immunohistochemical study. *J. Dermatolog. Treat.* 33, 291–296 (2022).
117. Heine, G. *et al.* 1,25-dihydroxyvitamin D(3) promotes IL-10 production in human B cells. *Eur. J. Immunol.* 38, 2210–2218 (2008).
118. Kongsbak, M., Levring, T. B., Geisler, C. & von Essen, M. R. The vitamin d receptor and T cell function. *Front. Immunol.* 4, 148 (2013).
119. Fiske, C. T. *et al.* Increased vitamin D receptor expression from macrophages after stimulation with M. tuberculosis among persons who have recovered from extrapulmonary tuberculosis. *BMC Infect. Dis.* 19, 366 (2019).
120. Bikle, D. D. Vitamin D metabolism, mechanism of action, and clinical applications. *Chem. Biol.* 21, 319–329 (2014).
121. Khare, D. *et al.* Calcitriol [1, 25(OH)₂ D₃] pre- and post-treatment suppresses inflammatory response to influenza A (H1N1) infection in human lung A549 epithelial cells. *Eur. J. Nutr.* 52, 1405–1415 (2013).
122. Ferreira, G. B. *et al.* Differential Protein Pathways in 1,25-Dihydroxyvitamin D₃ and Dexamethasone Modulated Tolerogenic Human Dendritic Cells. *J. Proteome Res.* 11, 941–971 (2012).
123. Cristelo, C., Machado, A., Sarmiento, B. & Gama, F. M. The roles of vitamin D and cathelicidin in type 1 diabetes susceptibility. *Endocr. Connect.* 10, R1 (2021).
124. Tintino, S. R. *et al.* Action of cholecalciferol and alpha-tocopherol on Staphylococcus aureus efflux pumps. *EXCLI J.* 15, 315–22 (2016).
125. Andrade, J. C. *et al.* Cholecalciferol, Ergosterol, and Cholesterol Enhance the Antibiotic Activity of Drugs. *Int. J. Vitam. Nutr. Res.* 88, 244–250 (2018).
126. Gibbons, S. Anti-staphylococcal plant natural products. *Nat. Prod. Rep.* 21, 263 (2004).
127. Kim, H. S. *et al.* Effects of 1,25-dihydroxyvitamin D₃ on the differentiation of MC3T3-E1 osteoblast-like cells. *J. Periodontal Implant Sci.* 48, 34–46 (2018).
128. Wang, D., Song, J. & Ma, H. An in vitro Experimental Insight into the Osteoblast Responses to Vitamin D₃ and Its Metabolites. *Pharmacology* 101, 225–235 (2018).
129. Mason, S. S., Kohles, S. S., Winn, S. R. & Zelick, R. D. Extrahepatic 25-Hydroxylation of Vitamin D₃ in an Engineered Osteoblast Precursor Cell Line Exploring the Influence on Cellular Proliferation and Matrix Maturation during Bone Development. *ISRN Biomed. Eng.* 2013, 956362 (2013).
130. Petrescu, N. B. *et al.* Cannabidiol and Vitamin D₃ Impact on Osteogenic Differentiation of Human Dental Mesenchymal Stem Cells. *Medicina (Kaunas).* 56, 1–23 (2020).
131. Al Saedi, A., Hayes, A., Kremer, R. & Duque, G. Elucidating the genetic effect of vitamin D on mesenchymal stem cell differentiation in vitro. *Res. Sq.* preprint, (2022).
132. Salomó-Coll, O. *et al.* Osseoinductive elements around immediate implants for better osteointegration: a pilot study in foxhound dogs. *Clin. Oral Implants Res.* 29, 1061–1069 (2018).
133. Shekhar, C. An Innovative Technique in Local Antibiotic Delivery Method in Open Infected Wounds of the Musculoskeletal System. *Int. J. Low. Extrem. Wounds* 18, 153–160 (2019).
134. Shekhar, C. *et al.* Role of topical cholecalciferol granules for antimicrobial drug delivery in diabetic foot ulcers. *Indian J. Orthop. Surg.* 5, 165–167 (2019).
135. Tsuji, K., Kimura, S., Tateda, K. & Takahashi, H. Does Vitamin D₃ Prevent the Inhibitory Effect of Vancomycin on Osteoblasts? *Clin. Orthop. Relat. Res.* 478, 420 (2020).
136. Ignjatović, N., Uskoković, V., Ajduković, Z. & Uskoković, D. Multifunctional hydroxyapatite and poly(D,L-lactide-co-glycolide) nanoparticles for the local delivery of cholecalciferol. *Mater. Sci. Eng. C. Mater. Biol. Appl.* 33, 943–50 (2013).

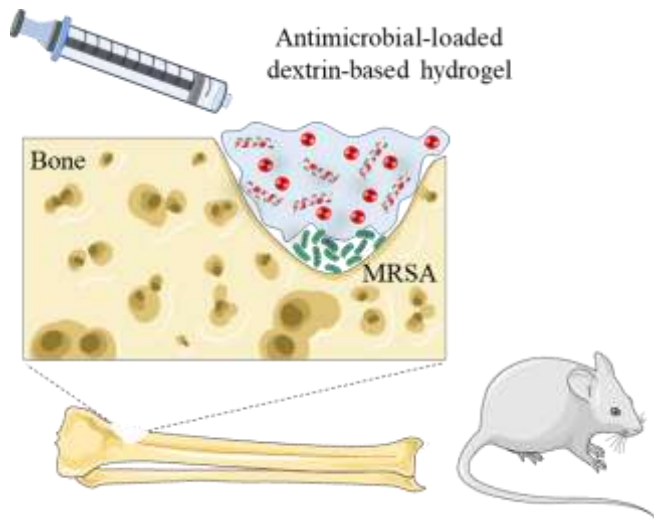
137. Nah, H. et al. Vitamin D-conjugated gold nanoparticles as functional carriers to enhancing osteogenic differentiation. *Sci. Technol. Adv. Mater.* 20, 826–836 (2019).
138. Chen, M. et al. Construction of multilayered molecular reservoirs on a titanium alloy implant for combinational drug delivery to promote osseointegration in osteoporotic conditions. *Acta Biomater.* 105, 304–318 (2020).
139. Mahdavi, R. et al. Bone tissue engineering gelatin-hydroxyapatite/graphene oxide scaffolds with the ability to release vitamin D: fabrication, characterization, and in vitro study. *J. Mater. Sci. Mater. Med.* 31, 97 (2020).
140. Zhao, H. Z., Tan, E. C. & Yung, L. Y. L. Potential use of cholecalciferol polyethylene glycol succinate as a novel pharmaceutical additive. *J. Biomed. Mater. Res. Part A* 84A, 954–964 (2008).
141. Kutlehria, S. et al. Cholecalciferol-PEG Conjugate Based Nanomicelles of Doxorubicin for Treatment of Triple-Negative Breast Cancer. *AAPS PharmSciTech* 19, 792–802 (2018).
142. Kutlehria, S. et al. Tacrolimus Loaded PEG-Cholecalciferol Based Micelles for Treatment of Ocular Inflammation. *Pharm. Res.* 35, 1–12 (2018).
143. Patil, S., Gawali, S., Patil, S. & Basu, S. Synthesis, characterization and in vitro evaluation of novel vitamin D3 nanoparticles as a versatile platform for drug delivery in cancer therapy. *J. Mater. Chem. B* 1, 5742–5750 (2013).
144. Silva, D. M. et al. Structural analysis of dextrans and characterization of dextrin-based biomedical hydrogels. *Carbohydr. Polym.* 114, 458–466 (2014).
145. “Food And Drugs.” Code of Federal Regulations, title 21 (2021), Chapter I, Subchapter B, Part 184, Subpart B §184.1277.
146. Kaneo, Y., Uemura, T., Tanaka, T. & Kanoh, S. Polysaccharides as drug carriers: biodisposition of fluorescein-labeled dextrans in mice. *Biol. Pharm. Bull.* 20, 181–187 (1997).
147. Hreczuk-Hirst, D., Chicco, D., German, L. & Duncan, R. Dextrans as potential carriers for drug targeting: tailored rates of dextrin degradation by introduction of pendant groups. *Int. J. Pharm.* 230, 57–66 (2001).
148. Molinos, M., Carvalho, V., Silva, D. M. & Gama, F. M. Development of a hybrid dextrin hydrogel encapsulating dextrin nanogel as protein delivery system. *Biomacromolecules* 13, 517–527 (2012).
149. Chen, H. et al. pH-Sensitive drug delivery system based on modified dextrin coated mesoporous silica nanoparticles. *Int. J. Biol. Macromol.* 85, 596–603 (2016).
150. Chen, C. et al. Functional polymeric dialdehyde dextrin network capped mesoporous silica nanoparticles for pH/GSH dual-controlled drug release. *RSC Adv.* 8, 20862–20871 (2018).
151. Ferguson, E., Thomas, D. & Walsh, T. Therapeutic Conjugates of a Dextrin Polymer and Colistin. Patent WO 2012/035310 (2013).
152. Harwicke, J. et al. Dextrin–rhEGF conjugates as bioresponsive nanomedicines for wound repair. *J. Control. Release* 130, 275–283 (2008).
153. Asai, T. & Kawai, T. Bone filling material comprising sintered titanium dioxide and dextrin and method for reconstructing bone defects using the same. Patent US20120064172A1 (2010).
154. McSweeney, M. D., Mohan, M., Commins, S. P. & Lai, S. K. Anaphylaxis to Pfizer/BioNTech mRNA COVID-19 Vaccine in a Patient With Clinically Confirmed PEG Allergy. *Front. Allergy* 0, 57 (2021).
155. Shiraishi, K. & Yokoyama, M. Toxicity and immunogenicity concerns related to PEGylated-micelle carrier systems: a review. *Sci. Technol. Adv. Mater.* 20, 324 (2019).
156. Massia, S. P. & Stark, J. Immobilized RGD peptides on surface-grafted dextran promote biospecific cell attachment. *J. Biomed. Mater. Res.* 56, 390–9 (2001).
157. Szymańska, E. & Winnicka, K. Stability of Chitosan—A Challenge for Pharmaceutical and Biomedical Applications. *Mar. Drugs* 13, 1819 (2015).
158. Joseph, A. et al. Surfactants influence polymer nanoparticle fate within the brain. *Biomaterials* 277, 121086 (2021).

159. Egharevba, H. O. Chemical Properties of Starch and Its Application in the Food Industry. in Chemical Properties of Starch (ed. Emeje, M. O.) (IntechOpen, 2019).
160. Hreczuk-Hirst, D., German, L. & Duncan, R. Dextrins as Carriers for Drug Targeting: Reproducible Succinylation as a Means to Introduce Pendant Groups. *J. Bioact. Compat. Polym.* 16, 353–365 (2001).
161. Ačkar, D. *et al.* Starch Modification by Organic Acids and Their Derivatives: A Review. *Mol.* 20, 19554–19570 (2015).
162. Hardwicke, J. *et al.* Bioresponsive Dextrin–rhEGF Conjugates: In Vitro Evaluation in Models Relevant to Its Proposed Use as a Treatment for Chronic Wounds. *Mol. Pharm.* 7, 699–707 (2010).
163. Ferguson, E. L. *et al.* Controlled release of dextrin-conjugated growth factors to support growth and differentiation of neural stem cells. *Stem Cell Res.* 33, 69–78 (2018).
164. Ferguson, E. L., Azzopardi, E., Roberts, J. L., Walsh, T. R. & Thomas, D. W. Dextrin–Colistin Conjugates as a Model Bioresponsive Treatment for Multidrug Resistant Bacterial Infections. *Mol. Pharm.* 11, 4437–4447 (2014).
165. Varache, M. *et al.* Polymer Masked–Unmasked Protein Therapy: Identification of the Active Species after Amylase Activation of Dextrin–Colistin Conjugates. *Mol. Pharm.* 16, 3199–3207 (2019).
166. Carvalho, V. *et al.* Self-assembled dextrin nanogel as protein carrier: controlled release and biological activity of IL-10. *Biotechnol. Bioeng.* 108, 1977–1986 (2011).
167. Gonçalves, C. *et al.* New dextrin nanomagnetogels as contrast agents for magnetic resonance imaging. *J. Mater. Chem. B* 1, 5853–5864 (2013).
168. Gonçalves, C. *et al.* Self-Assembled Dextrin Nanogel as Curcumin Delivery System. *J. Biomater. Nanobiotechnol.* 3, 178–184 (2012).
169. Silva, D. M. *et al.* Inflammatory response to dextrin-based hydrogel associated with human mesenchymal stem cells, urinary bladder matrix and Bonelike® granules in rat subcutaneous implants. *Biomed. Mater.* 11, 065004 (2016).
170. Li, S., Xia, Y., Qiu, Y., Chen, X. & Shi, S. Preparation and property of starch nanoparticles reinforced aldehyde–hydrazide covalently crosslinked PNIPAM hydrogels. *J. Appl. Polym. Sci.* 135, 45761 (2018).
171. Wang, D. *et al.* Hydrogen-Bonding Reinforced Injectable Hydrogels: Application As a Thermo-Triggered Drug Controlled-Release System. *ACS Appl. Polym. Mater.* 2, 1587–1596 (2020).
172. Gómez-Mascaraque, L. G., Méndez, J. A., Fernández-Gutiérrez, M., Vázquez, B. & San Román, J. Oxidized dextrins as alternative crosslinking agents for polysaccharides: Application to hydrogels of agarose–chitosan. *Acta Biomater.* 10, 798–811 (2014).
173. Sharma, A. K. *et al.* Borax mediated synthesis of a biocompatible self-healing hydrogel using dialdehyde carboxymethyl cellulose-dextrin and gelatin. *React. Funct. Polym.* 166, 104977 (2021).
174. Silva-Carvalho, R. *et al.* Development of dextrin-amphotericin B formulations for the treatment of Leishmaniasis. *Int. J. Biol. Macromol.* 153, 276–288 (2020).
175. Mohamed, E. E. *et al.* Anticancer activity of a novel naringin–dextrin nanoformula: Preparation, characterization, and in vitro induction of apoptosis in human hepatocellular carcinoma cells by inducing ROS generation, DNA fragmentation, and cell cycle arrest. *J. Drug Deliv. Sci. Technol.* 75, 103677 (2022).
176. Dzamukova, M. R., Naumenko, E. A., Lvov, Y. M. & Fakhrullin, R. F. Enzyme-activated intracellular drug delivery with tubule clay nanoformulation. *Sci. Reports* 2015 51 5, 1–11 (2015).
177. Moreira, S. M., Andrade, F. K., Domingues, L. & Gama, M. Development of a strategy to functionalize a dextrin-based hydrogel for animal cell cultures using a starch-binding module fused to RGD sequence. *BMC Biotechnol.* 8, 1–8 (2008).

178. Shukla, A., Singh, A. P. & Maiti, P. Injectable hydrogels of newly designed brush biopolymers as sustained drug-delivery vehicle for melanoma treatment. *Signal Transduct. Target. Ther.* 2021 61 6, 1–13 (2021).
179. Nazarzadeh Zare, E., Mansour Lakouraj, M. & Mohseni, M. Biodegradable polypyrrole/dextrin conductive nanocomposite: Synthesis, characterization, antioxidant and antibacterial activity. *Synth. Met.* 187, 9–16 (2014).
180. Gligor, I. *et al.* Porous c.p. Titanium Using Dextrin as Space Holder for Endosseous Implants. *Part. Sci. Technol.* 31, 357–365 (2013).
181. Dindelegan, G. C. *et al.* Multilayered Porous Titanium-Based 3rd Generation Biomaterial Designed for Endosseous Implants. *Mater. (Basel)* 14, 1727 (2021).
182. Mahmood, S. K. *et al.* Preparation and characterization of cockle shell aragonite nanocomposite porous 3D scaffolds for bone repair. *Biochem. Biophys. Reports* 10, 237–251 (2017).
183. Li, H. *et al.* A networked swellable dextrin nanogels loading Bcl2 siRNA for melanoma tumor therapy. *Nano Res.* 11, 4627–4642 (2018).
184. Pereira, I. *et al.* In vivo systemic toxicity assessment of an oxidized dextrin-based hydrogel and its effectiveness as a carrier and stabilizer of granular synthetic bone substitutes. *J. Biomed. Mater. Res. Part A* 107, 1678–1689 (2019).
185. Pereira, I., Fraga, S., Silva, S., Teixeira, J. P. & Gama, M. In vitro genotoxicity assessment of an oxidized dextrin-based hydrogel for biomedical applications. *J. Appl. Toxicol.* 39, 639–649 (2019).
186. Xu, J., Liu, Y. & Hsu, S. Hydrogels based on schiff base linkages for biomedical applications. *Molecules* 24, 3005 (2019).
187. Zhang, Z., He, C. & Chen, X. Hydrogels based on pH-responsive reversible carbon–nitrogen double-bond linkages for biomedical applications. *Mater. Chem. Front.* 2, 1765–1778 (2018).
188. Janeček, Š., Mareček, F., MacGregor, E. A. & Svensson, B. Starch-binding domains as CBM families—history, occurrence, structure, function and evolution. *Biotechnol. Adv.* 37, 107451 (2019).
189. Priya *et al.* Synthesis of dextrin-polyacrylamide and boric acid based tough and transparent, self-healing, superabsorbent film. *Int. J. Biol. Macromol.* 182, 712–721 (2021).
190. Asai, T. *et al.* Dextrin Promotes Proliferation of Cultured MC3T3-E1 Mouse Osteoblast-like Cells and Their Alkaline Phosphatase Activity: Implications for Potential Application of Dextrin as a Binder of Bone Filling Material. *J. Hard Tissue Biol.* 27, 65–68 (2018).
191. Asai, T. *et al.* In vitro biocompatibility of dextrin: the addition of a low concentration of dextrin in the medium promotes the cell activity of L929 mouse fibroblasts. *Cell Biol. Int.* 35, 645–648 (2011).
192. Cui, Y. C. *et al.* Metabolic utilization of human osteoblast cell line hFOB 1.19 under normoxic and hypoxic conditions: A phenotypic microarray analysis. *Exp. Biol. Med.* 246, 1177–1183 (2021).
193. Lu, C. *et al.* Tibial Fracture Decreases Oxygen Levels at the Site of Injury. *Iowa Orthop. J.* 28, 14 (2008).
194. Marenzana, M. & Arnett, T. R. The Key Role of the Blood Supply to Bone. *Bone Res.* 1, 203 (2013).
195. Springhouse. Diagnostic tests made incredibly easy! 448 (Lippincott Williams & Wilkins, 2008).
196. Ye, M. *et al.* A Dual-Responsive Antibiotic-Loaded Nanoparticle Specifically Binds Pathogens and Overcomes Antimicrobial-Resistant Infections. *Adv. Mater.* 33, e2006772 (2021).
197. Hong, M., Cassely, A., Mechref, Y. & Novotny, M. V. Sugar-lectin interactions investigated through affinity capillary electrophoresis. *J. Chromatogr. B. Biomed. Sci. Appl.* 752, 207–216 (2001).

CHAPTER 3

3. INJECTABLE HYDROGEL AS A CARRIER OF VANCOMYCIN AND A CATHELICIDIN-DERIVED PEPTIDE FOR OSTEOMYELITIS TREATMENT



A local drug delivery system that attempts to find a suitable balance between antimicrobial and regenerative actions was developed for osteomyelitis (OM) treatment. This system combines the angiogenic and immunomodulatory peptide LLKKK18 (LL18) and vancomycin hydrochloride (VH), loaded into an injectable oxidized dextrin (ODEX)-based hydrogel (HG).

In vitro cytotoxicity was analyzed in MC3T3-E1 pre-osteoblasts and erythrocytes. The kinetics of LL18 release was studied. Antimicrobial activity was assessed *in vitro* against a clinical Methicillin-resistant *Staphylococcus aureus* (MRSA). A rat model of acute OM was developed by direct inoculation into a tibia defect, concomitantly with the implantation of the drug-loaded HG. The local bioburden was quantified and damage in surrounding tissues was examined histologically. *In vitro*, ODEX-based HG displayed a safe hemolytic profile. Half of LL18 (53 %) is released during the swelling phase at physiological pH, then being gradually released until complete HG degradation. LL18-loaded HG at 300 μM was the most effective peptide formulation in decreasing *in vivo* infection among concentrations ranging from 86 to 429 μM . The histopathological scores observed *in vivo* varied with the LL18 concentration in a dose-dependent manner. VH at 28 mM completely eradicated bacteria, although with substantial tissue injury. We have found that sub-millimolar doses of VH combined with LL18 at 300 μM may suffice to eradicate the infection, with reduced tissue damage. We propose an easy-to-handle, shape-fitting HG formulation with the potential to treat MRSA-infected bone with low VH doses associated with LL18.

Adapted from: *J Biomed Mater Res Part A*, 110(11): 1786-1800 (2022).

3.1 Introduction

Osteomyelitis (OM) is an inflammation of the bone triggered by infection, which results in tissue destruction. OM accounts for numerous hospitalizations and costs, particularly among susceptible patients. In a study with 482 individuals, OM was diagnosed in 50 % of patients with diabetic foot infections indicated for amputation ¹. Moreover, treatment costs of fracture-related infections were estimated to be approximately 6.5-times more expensive than in non-infected patients ².

OM triggered by gram-positive bacteria, including Methicillin-resistant *Staphylococcus aureus* (MRSA), is usually treated with intravenous vancomycin ³. However, systemic administration of antibiotics is often ineffective and persistent infection continuously hinders bone healing. Particularly challenging is the treatment of MRSA-induced OM, a pathogen categorized as a high priority by the World Health Organization for the development of new treatments ⁴. To reduce systemic toxicity and improve outcomes, antibiotics-impregnated materials may be locally implanted for site-restricted and prolonged antibacterial therapy. Antibiotic-impregnated polymethylmethacrylate (PMMA) has been the standard local treatment for OM for many decades, with the main disadvantage of requiring a second surgery to remove the non-degradable material ⁵. Vancomycin is one of the preferred PMMA-loaded antibiotics to treat OM ⁵; however, doses above 2.5 wt% may compromise its load-bearing properties ⁶. Although intra-wound vancomycin can prevent *Staphylococcus aureus* (*S. aureus*) infection⁷, prolonged exposure and/or high doses further hampers tissue regeneration ⁸⁻¹⁰. Specific cut-off limits are, therefore, important to address.

Antimicrobial peptides (AMPs), a part of the primary host defense against microbial invasion, have a high spectrum of antimicrobial activity and low propensity for bacteria to develop resistance ¹¹. LL37, derived endogenously from the single human cathelicidin hCAP18, disrupts the membrane surface of pathogens through the creation of pores ¹². This is one of the few human bactericidal peptides with potent anti-staphylococcal activity ^{13,14}. *S. aureus*, the main etiological agent of OM ¹⁵, is a bone loss-inducing pathogen, not only able to invade but also to proliferate in osteoblasts ^{16,17}, where it can survive the effects of antibiotics and the host immune response¹⁸. The bactericidal effect of LL37 against both extra- and intracellular *S. aureus* has been reported, being even superior to conventional antibiotics in eliminating intracellular bacteria ¹⁹. LL37 also inhibits lipopolysaccharide (LPS) activity ^{20,21} and stimulates the migration of mesenchymal cells, which is important for bone repair²². Given its pro-angiogenic activity ²³, LL37 has been demonstrated to promote wound healing²⁴ and bone regeneration in a rat calvarial bone defect ^{25,26}. Importantly, LL37 also plays a central role in innate immunity and inflammation, as discussed elsewhere²⁷. It is a potent chemoattractant for mast cells, monocytes, T lymphocytes and neutrophils. By

recruiting immune cells to the site of infection, LL37 provide one additional mechanism to fight infections. This peptide also inhibits neutrophil apoptosis, increasing the number of viable cells during infection, and influences dendritic cells differentiation as to display up-regulated endocytic capacity, enhanced secretion of Th-1 inducing cytokines - that produce the proinflammatory responses to kill intracellular parasites -, and promotes Th-1 responses *in vitro*.

Although peptide-based drugs have been regarded as expensive, manufacturing costs have decreased dramatically with technological advances. Further efforts to reduce production costs include the synthesis of shorter peptides without compromising activity. LLKKK18 (LL18), an LL37 analog (**Figure 3.1**), has been engineered to enhance antimicrobial properties and decrease toxicity^{28,29}, being three-fold more effective in the killing of mycobacteria than LL37³⁰.

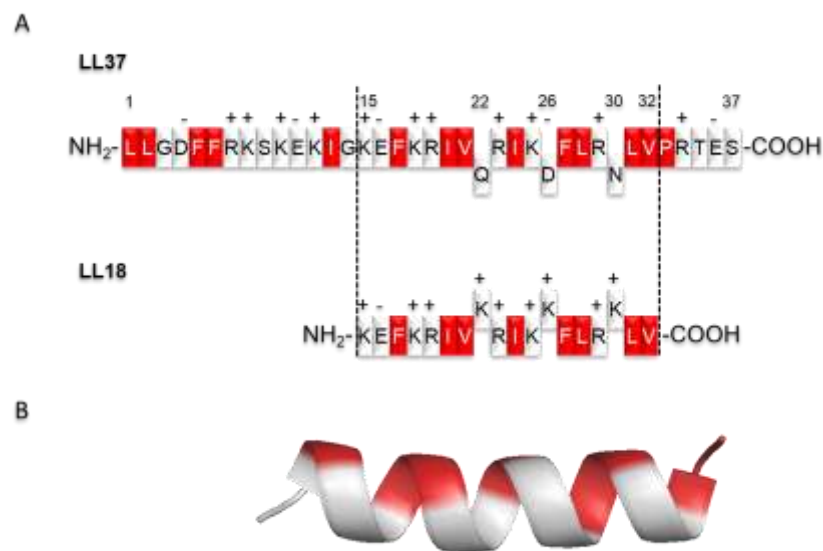


Figure 3.1 – (A) Amino acid sequence projections for LL37 and its LL18 peptide derivative (N terminal to C terminal). To increase cationicity, Q22, D26, and N30 in LL37 were replaced by K22, K26, and K30 LL18. Positively charged residues are marked with “+” and negatively charged residues are marked with “-”. Hydrophobic residues are shown in red, hydrophilic residues are shown in white. Whereas LL37 has 37.8 % hydrophobic amino acids and a net charge of +6 at pH 7, LL18 has 44.4 % and +8, respectively. **(B)** α -helical structure of LL18 (PyMOL software).

This 18-aminoacid length peptide displays higher hydrophobicity and cationicity than LL37, due to the substitution of polar uncharged residues glutamine and asparagine, and negatively charged aspartic acid by positively charged lysine residues.

This results in higher antimicrobial and chemoattractant activity, as previously described²⁸. LL18 has also been found to improve the healing process in rat burns through stimulated angiogenesis³¹.

Local drug delivery has become an attractive approach avoiding the side effects of high-dose systemic treatments while improving antimicrobial bone penetration. Hydrogels, particularly, *in situ* gelling hydrogels, allow the production of injectable formulations which may be administrated using minimally invasive procedures, perfectly fitting the irregularities of bone tissue defects while acting as drug delivery systems³². We have previously developed a fully resorbable and injectable dextrin-based hydrogel (HG) intended to perform as a multifunctional platform for the delivery of stem cells and other bioactive agents³³⁻³⁸. We have demonstrated its *in vitro* and *in vivo* biocompatibility and safety^{36,37}. This HG has been approved for an ongoing clinical study as a carrier of granular synthetic bone substitutes for alveolar bone repair (iBone Therapies: advanced solutions for bone regeneration; EUDAMED No.: CIV-15-09-013827), which brings it closer to real-life applications. Since its clinical use in the near future seems realistic, we developed a study to further investigate its suitability for bone infections that could ultimately target the antimicrobial and bone healing double-challenging OM.

Vancomycin-loaded hydrogels have been developed mainly for sustained delivery. Although bactericidal purposes may be achieved, specific cut-off concentrations *in vivo* are not addressed, with high concentrations being mostly used. Additionally, as far as we are aware, studies involving intralesional administration of exogenous cathelicidins in *in vivo* models of OM are lacking. We hypothesize the co-administration of vancomycin and LL18 may bear complementary antimicrobial and regenerative actions. Combating bacterial resistance using multiple bacterial targets by combination of antibiotics with AMPs has recently been regarded as a promising and cost-effective solution to control resistance escalation³⁹. It is also a way of introducing AMPs into clinical practice given that a sudden and complete replacement of antibiotics seems unlikely. Overall, we hereby developed a formulation combining low doses of vancomycin hydrochloride (VH) added to immunomodulatory LL18 peptide embedded in a clinical-staged HG platform. The endpoints of this study are: i) explore the balance between *in vivo* antimicrobial activity and tissue injury induced by VH, (ii) find a safe and effective formulation against severe MRSA bone infection combining low VH concentration with LL18, attempting to find a suitable balance between antimicrobial and regenerative actions and (iii) propose injectable dextrin-based HG as non-invasive mode of administration and a suitable antimicrobial carrier for OM therapy.

3.2 Materials and Methods

3.2.1 Materials

All reagents used were of the highest analytical grade available. Dextrin was from Tackidex B 167 (Batch E 1445), kindly provided by Roquette (Lestrem, France) and LL18 (H-KEFKRIVKRIKKFLRKLV-OH, MW =

2330 g/mol, > 95 % purity) was purchased from Schafer-N (Copenhagen, Denmark). Sodium m-periodate (CAS no. 7790-28-5), diethylene glycol (CAS no. 111-46-6), adipic acid dihydrazide (ADH; CAS no. 1071-93-8), VH (CAS no. 1404-93-9) and 3-[4,5-Dimethylthiazole-2-yl]-2,5-diphenyl tetrazolium bromide (MTT, CAS no 298-93-1) were purchased from Sigma-Aldrich (St. Louis, MO, USA). Fluorescamine (CAS no. 38183-12-9) was purchased from Acros Organics (Thermo Fisher Scientific, Geel, Belgium) and phosphate-buffered saline (PBS; CAS no. 10049-21-5) was supplied by Merck (Berlin, Germany).

3.2.2 Dextrin Oxidation and Hydrogel Preparation

Dextrin oxidation was performed as previously described by Pereira *et al.*⁴⁰. Briefly, aqueous solutions of dextrin (2 % w/v) were oxidized with sodium m-periodate, to yield the theoretical degree of oxidation of 40 %, at room temperature and with stirring, in the dark. The oxidation reaction was stopped after 20 hours by dropwise addition of an equimolar amount of diethylene glycol to reduce any unreacted periodate. Sodium *m*-periodate and diethylene glycol were removed by dialysis, using a membrane with a molecular weight cut-off 1000 Da (Merck Millipore, Billerica, MA, USA), and then freeze-dried. Oxidized dextrin (ODEX) was dissolved in phosphate-buffered saline (PBS) solution (30 % w/v) and the solution was sterilized by gamma irradiation (IONISOS, Dagneux, France), using a ⁶⁰Co source, at 20 kGy (2 kGy/h), at room temperature. ADH was also dissolved in PBS solution (3.76 % w/v) and sterilized by filtration, using a 0.22 µm pore filter membrane (Pall Corporation, Ann Arbor, MI, USA). For the crosslinking reaction, ODEX and ADH solutions were mixed in a 7:3 volume ratio, respectively.

3.2.3 *In vitro* Biocompatibility

3.2.3.1 Cell Culture

Mouse pre-osteoblast MC3T3-E1 was acquired from RIKEN BioResource Center Cell Bank (Tsukuba, Ibaraki, Japan) and maintained in Dulbecco's Modified Eagle Medium (DMEM) with 1,0 g/L glucose supplemented with 10 % (v/v) heat-inactivated fetal bovine serum (FBS) and 1 % (v/v) Penicillin (10,000 U/mL)-Streptomycin (10,000 µg/mL) at 37 °C and 5 % CO₂, all obtained from Merck Millipore (Massachusetts, USA). Triton X-100 and paraformaldehyde, were purchased from Sigma-Aldrich (St. Louis, MO, USA).

3.2.3.2 Cell Viability Assay

Cytotoxicity of the HG and its components was evaluated according to ISO 10993-5⁴¹. The HG components were mixed at diluted concentrations (HG_{dil}) as compared to the formulation described in section 2.2. Using the diluted conditions prevents the mixture of ingredients from jellifying, given the low concentration of the components and the excess of water. This way we attempt to detect toxicological synergistic effects of the two components and also to mimic the release of the HG components *in vivo*, as dilution occurs upon degradation. In addition to HG_{dil}, several concentrations of LL18, ADH and ODEX were tested. ODEX was sterilized by gamma irradiation and all other reagents by filtration with a 200 nm pore size filter. MC3T3-E1 cells were used for the MTT viability assay. Briefly, 1.5×10^4 cells in low glucose DMEM medium, supplemented with 10 % FBS and 1 % penicillin and streptomycin, were cultured in 96-well plates for 24 h at 37 °C with 5 % CO₂. Afterwards, the medium was replaced by solutions of the test samples previously dissolved in same culture medium. After 24 h incubation, test samples at different concentrations were replaced by 50 µL of MTT solution (1 mg/mL) and the plates were incubated at 37 °C for 2 h. The precipitated formazan was solubilized in isopropanol for 15 minutes and the absorbance of the supernatant measured spectrophotometrically at 570 nm (650 nm background subtracted). **Table 3.1** shows the different concentrations of HG and the corresponding doses of individual components (ODEX and ADH), including non-oxidized dextrin for comparison. Different concentrations were considered for proper adjustment of dose-response curves for 50 % cytotoxic concentration (CC₅₀) calculation (**Table 3.2**).

Table 3.1 – Concentrations of HG_{dil}, oxidized dextrin (ODEX) and adipic dihydrazide (ADH) solutions tested on the cytotoxicity assay. HG_{dil}, diluted dextrin-based hydrogel, refers to the sum of ODEX and ADH concentrations, diluted by a factor in the range of 28 to 443.

HG _{dil} (mg/mL)	ODEX (mg/mL)	ADH (mg/mL)	Dextrin (mg/mL)
0.50	0.47	0.03	0.47
1.00	0.95	0.05	0.95
1.50	1.42	0.08	1.42
2.00	1.90	0.10	1.90
3.00	2.85	0.15	2.85
4.00	3.80	0.20	3.80

6.00	5.69	0.31	5.69
7.00	6.64	0.36	6.64
8.00	7.59	0.41	7.59

Table 3.2 – Concentrations of the HG_{dil}, oxidized-dextrin (ODEX) and LLKKK18 (LL18) tested in the cytotoxicity assay and used for CC₅₀ calculation. HG_{dil}, diluted dextrin-based hydrogel, refers to the sum of ODEX and ADH concentrations

HG_{dil} (mg/mL)	ODEX (mg/mL)	LL18 (μM)
2.00	0.47	2.15
3.00	0.95	4.29
4.00	1.42	8.58
6.00	1.90	17.17
7.00	2.85	32.19
8.00	3.80	42.92
10.00		53.65
		214.59

3.2.3.3 Hemolysis Assay

Blood was obtained from a healthy dog after owners' agreement and collected to an EDTA tube. Hemolysis assay was performed according to ASTM International (F756–13)⁴². Whole blood was centrifuged (10 minutes at 1200 g, 4 °C) and the supernatant and buffy coat were discarded. Red blood cells (RBCs) were resuspended in isotonic PBS pH 7.4. The purified RBCs were counted using a Neubauer chamber and diluted to a concentration of 1×10^8 cells/mL. Afterwards, 450 μL of RBCs were placed in a 48-well plate containing 50 μL of test-samples dissolved in PBS buffer (**Table 3.3**). Plates were incubated for 1 h at 37 °C under agitation (150 rpm) after which solutions were collected to micro tubes and centrifuged (10 min at 1200 ×g, 4 °C). The supernatants were collected for analysis of the extent of hemolysis by measuring the absorption of the hemoglobin at 540 nm. Results were expressed as a percentage of hemolysis with respect to the amount of hemoglobin released in the presence of 1 % of triton X-100, which was taken as measure of complete (100 %) lysis: $\text{hemolysis (\%)} = [(\text{AbsS} - \text{AbsNC}) / (\text{AbsLys} -$

AbsNC)] × 100, where S, NC and Lys stands for the Sample, Non-treated Control and the completely lysed sample, respectively.

Table 3.3 – Concentrations of the HG_{all}, oxidized dextrin (ODEX), adipic acid dihydrazide (ADH), dextrin and LL18 tested on hemolysis assay. HG_{all}, diluted dextrin-based hydrogel, refers to the sum of ODEX and ADH concentrations, diluted by a factor of 5 and 10.

HG_{all} (mg/mL)	ODEX (mg/mL)	ADH (mg/mL)	Dextrin (mg/mL)	LL18 (μM)
22.13	21.00	1.13	21.00	43
44.26	42.00	2.26	42.00	86

3.2.3.4 pH Monitoring Upon Hydrogel Degradation

HG samples were molded into discs with a total volume of 4 mL (8 mm thickness × 24 mm diameter), and after setting of the crosslinking reaction, they were immersed in 50 mL PBS solution at 37 °C. PBS buffer (1×, 10 mM) is often employed for routine experiments since it is isotonic, mimics osmotic strength, pH and yields a buffer capacity similar to that of the biological fluids⁴³. The pH values of the PBS solution were measured at different time intervals until complete degradation: 10, 20, 30 minutes and 1, 2, 3, 4, 5, 6, 10 and 22 hours (n = 3).

3.2.4 Hydrogel Degradation and LL18 Release

These studies were performed in PBS buffer at both pH 7.4 and 5.8, with a total of six replicates of empty HG and 429 μM LL18-loaded HG. The hydrogels were prepared with 400 μL volume in acrylic molds with disk shape (4 mm thickness × 12 mm diameter) and allowed to crosslink for one hour, before weighing (Wi). Then, the hydrogels were immersed in 3 mL of buffer (diffusion medium), and incubated at 37 °C in a 12-well plate. The hydrogels were collected from the wells at regular intervals, wiped with filter paper, weighed (Wt) and returned to the wells. The percentage of mass loss was determined using the equation: mass loss (%) = 100 – [(Wt / Wi) × 100]. At the same time intervals, an aliquot was collected (the volume replaced) and LL18 was quantified using the fluorescamine assay. Briefly, 200 μL sample were transferred to a 96-well plate and mixed with 50 μL of a fluorescamine solution at 0.3 mg/mL in acetone. After 15 minutes of incubation the fluorescence emission was recorded at 480 nm at an excitation wavelength of 385 nm (Cytation™ 3 microplate reader, BioTek Instruments, Inc., VT, USA). For the

calibration curve, the emission intensities were plotted against LL18 concentrations ranging from 1.3 to 32.2 μM . The percentage of peptide cumulative release was then calculated using the equation: cumulative release (%) = (released compound / initial compound) \times 100.

3.2.5 Bacteria and Antibacterial Assays

The MRSA strain chosen for this study was isolated from a diabetic human patient displaying a foot ulcer with an OM infection, supplied by the University of Trás-os-Montes and Alto Douro collection. This strain displays phenotypic resistance to penicillin, ceftazidime, erythromycin, clindamycin, gentamycin and tobramycin. Resistance to penicillin is encoded by the *blaZ* gene. The isolate harbor the *ermC*, *mst(A/B)*, *mph(C)* and *linA* genes which confer resistance to macrolides and lincosamides, and the *aac(6')-Ia* which are responsible for the resistance to aminoglycosides. This strain present three virulence genes: *hla*, *hly* and *tst*. Regarding molecular typing, the isolate belongs to ST5, spa type t179, SCC*mec* type II and *agr* type II. After seeded onto congo red agar the strain produced intensive black colonies which is indicative of slime-producing strain. The isolate also presents the following genes: *cna*, *fmbB*, *fib*, *icaB* and *clfB*, related with biofilm production. The strain was grown in brain heart infusion (BHI) agar broth medium (Oxoid, UK) for 24 h at 37 °C.

3.2.5.1 Bacterial Susceptibility Testing

The antibacterial activity of HG and LL18 was determined according to ISO 20776-1⁴⁴. MRSA was grown in BHI (Liofilchem®) broth medium overnight. A small inoculum was added to fresh medium and left growing until reaching the exponential phase. A volume of 50 μL of inoculum intended for a final concentration of 5×10^5 colony forming units (CFU)/mL was added to 96 plate wells, and 50 μL of solutions with different concentrations of peptide were then incubated with the bacteria in each well. After overnight incubation (24 h) at 37 °C, the bacterial growth was evaluated by measuring the optical density at 620 nm in a Microplate Reader (ELX808IU, BioTek). Minimal, and half-minimal, inhibitory concentration (MIC and MIC₅₀, respectively) values were calculated as the concentration required to inhibit bacterial growth by 100 % and 50 %, respectively. Initial bacteria concentration was confirmed by the CFU procedure. **Table 3.4** shows the different concentrations tested for the HG and its degradation products.

Table 3.4 – Concentrations of the HG_{dil} and correspondent concentrations of ODEX and ADH tested for antimicrobial activity. ADH, adipic acid dihydrazide; HG_{dil}, diluted dextrin-based hydrogel; ODEX, oxidized dextrin.

HG_{dil} (mg/mL)	ODEX (mg/mL)	ADH (mg/mL)
2.00	1.90	0.10
3.00	2.85	0.15
4.00	3.80	0.20
6.00	5.69	0.31
8.00	7.59	0.41
10.00	9.49	0.51
12.00	11.39	0.61
15.00	14.23	0.77
22.13	21.00	1.13

3.2.6 Animal Model and *In vivo* General Procedures

In vivo procedures were performed as previously reported ⁴⁵. Animal experiments were performed in conformity with the European norms and recommendations for care and use of laboratory animals (European Directive 2010/63/EU) and National Legislation (Decreto-Lei 113/2013) for animal experimentation and welfare. The experimental procedures were conducted under project license approval by the Organ Responsible for Animal Welfare (ORBEA) at University of Trás-os-Montes and Alto Douro and the Portuguese competent authority Direção Geral de Alimentação e Veterinária (DGAV, Lisbon, Portugal) with reference number 0421/000/000/2017 (**Appendix A**).

Sixty adult male wistar rats (Charles River Laboratories, France), with approximately 400 grams in weight were used in two separate studies (**Table 3.5**). Animals were kept in ventilation-, humidity-, and temperature- controlled rooms with a 12/12 hours light/ dark cycle. The rats were housed in cages (maximum 5 animals per cage) with corn kernels and received food pellets and water *ad libitum*.

In the first study, to select the most efficient concentration of LL18, 40 animals were randomly assigned and blindly equally divided into four groups with 10 animals each. Group I (control) received locally in the left leg none treatment and the right leg HG. Group II received locally in the left leg HG + LL18 C1 and the right leg HG + LL18 C2. Group III received locally in the left leg HG + LL18 C3 and the right leg HG

+ LL18 C4. Group IV received locally in the left leg HG + VH and the right leg HG + VH + LL18 C4. In the second study, to test the efficacy of different concentrations of VH combined with the most efficient concentration of LL18, 20 animals were randomly assigned and blindly equally divided into two groups with 10 animals each. Group I received locally in the left leg HG + LL18 C3 and the right leg HG + LL18 C3 + VH1. Group II received locally in the left leg HG + LL18 C3 + VH2 and the right leg HG + LL18 C3 + VH3. The ratio of LL18 to VH for each condition is shown in **Table 3.5**, where two independent experiments were sequentially performed: A) the first one to select the concentration of LL18, including empty HG and a VH-loaded formulation; and B) then, using a selected LL18 concentration, different concentrations of VH-loaded formulations were tested.

Surgery was performed under general anesthesia by intraperitoneal injection of ketamine (Ketamidor®) (80 mg/kg of body weight) and dexmedetomidine (Dexdomitor®) (0.2 mg/kg of body weight). Both hind legs were shaved and scrubbed with a 4% chlorhexidine solution (Lifo-Scrub®). A 1-2 cm longitudinal skin incision was made over the proximal medial tibial metaphysis and a unicortical hole approximately 6 mm long and 2 mm wide was drilled below the medial collateral ligament insertion. After hemostasis 10 μ L of the MRSA suspension at 1×10^7 cell/mL was injected in the hole to induce OM and after that the formulations were applied as described above (**Figure 3.2**). Skin and soft tissues and skin were sutured with a 5/0 monofilament absorbable suture (Monosyn®). Buprenorphine (Bupaq®) was used for immediate analgesia and postoperative pain control was achieved with buprenorphine (Bupaq®) and meloxicam (Metacam®) for 3 days.

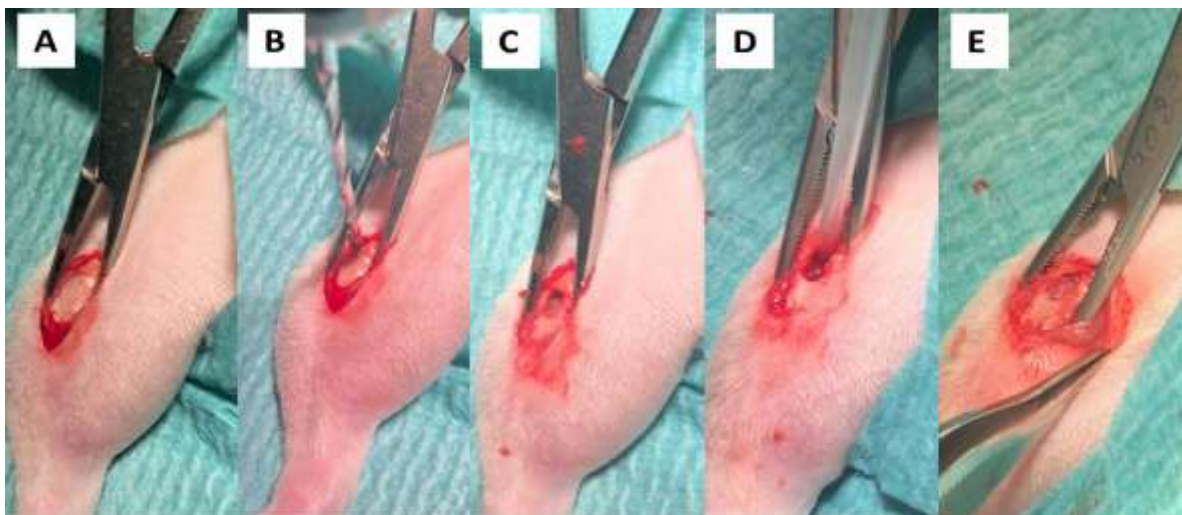


Figure 3.2 – Surgical procedure in rat tibia defects: **(A)** exposed tibia; **(B)** bone drilling; **(C)** bone defect completed; **(D)** application of inoculum and **(E)** defect filled with hydrogel formulations.

Table 3.5 – Concentration of LLKKK18 (LL18) and vancomycin hydrochloride (VH) tested *in vivo*: **(A)** increasing concentrations of LL18, including empty hydrogel (HG) and a VH-loaded formulation; and **(B)** increasing concentrations of VH-loaded formulations in combination with a fixed LL18.

Group	Condition	LL18 (µM)	VH (µM)
A			
I	No treatment	0	0
	HG	0	0
II	HG + LL18 C1	86	0
	HG + LL18 C2	215	0
III	HG + LL18 C3	300	0
	HG + LL18 C4	429	0
IV	HG + VH	0	28 x 10 ³
	HG + VH + LL18 C4	429	28 x 10 ³
B			
V	HG + LL18 C3	300	0
	HG + LL18 C3 + VH1	300	10
VI	HG + LL18 C3 + VH2	300	24
	HG + LL18 C3 + VH3	300	483

3.2.6.1 Sacrifice and Microbiological Evaluation

Animals were sacrificed after 7 days with an application of a lethal dose of pentobarbital (Euthasol®) (80 mg/kg of body weight) under general anesthesia by intracardiac injection and tibias of the right and left hind legs were harvested and weighted in sterile conditions and then immersed in 25 mL of NaCl sterile solution. Tibias were then sonicated for 2 min at 35 kHz to detach bacteria from the bone. Serial dilutions of 100 µL of NaCl solution were performed and the bacterial suspensions were cultured in BHI agar plates and incubated at 37 °C overnight for CFU counting. Tibias were stored in formalin until histological analyses.

3.2.6.2 Bone Histology

For histopathological analysis, after fixation in formaldehyde, tibias were decalcified using a formic acid-sodium citrate (4 %) solution, embedded in paraffin (Shandon), and cut into 4- μ m thick cross-sections. Sections were stained with hematoxylin and eosin (H&E). Histopathological grading was assessed based on intraosseous acute inflammation (IAI), intraosseous chronic inflammation (ICI), periosteal inflammation (PI), and bone necrosis (BN). Each parameter was scored on a 5-point scale (0–4), and a total histological score was calculated by summation of respective histopathological parameters. Histopathological grading is summarized in **Table 3.6** (adapted from⁴⁶).

Table 3.6 – Microscopic histological parameters and scoring system. Adapted from Fukushima *et al.*⁴⁶

Intraosseous acute inflammation (IAI):
0 Not present
1 Minimal to mild inflammation with no intramedullary abscess
2 Moderate to severe inflammation with no intramedullary abscess
3 Minimal to mild inflammation with intramedullary abscess
4 Moderate to severe inflammation with intramedullary abscess
Intraosseous chronic inflammation (ICI):
0 Not present
1 Minimal to mild chronic inflammation with no significant intramedullary fibrosis
2 Moderate to severe chronic inflammation with no significant intramedullary fibrosis
3 Minimal to mild chronic inflammation with significant intramedullary fibrosis
4 Moderate to severe chronic inflammation with significant intramedullary fibrosis
Periosteal inflammation (PI):
0 Not present
1 Minimal to mild inflammation with no subperiosteal abscess formation
2 Moderate to severe inflammation with no subperiosteal abscess formation
3 Minimal to mild inflammation with subperiosteal abscess formation
4 Moderate to severe inflammation with subperiosteal abscess formation
Bone necrosis (BN):
0 No evidence of necrosis
1 Single focus of necrosis without sequestrum formation
2 Multiple foci of necrosis without sequestrum formation
3 Single focus of sequestrum
4 Multiple foci of sequestra

3.2.7 Statistical Analysis

Data was analyzed using GraphPad Prism® 8.02 software (GraphPad Software, La Jolla, CA, USA). Multiple comparisons were performed by using one-way analysis of variance (ANOVA) with Bonferroni's multiple comparison post-test in all cases, and $p < 0.05$ (*) was accepted as denoting significance. Data are presented as mean \pm standard deviation (SD) and the number of replicates is described below each figure.

3.3 Results and Discussion

3.3.1 *In vitro* Biocompatibility

3.3.1.1 Cytotoxicity and Hemolysis

Cytotoxicity was assessed in pre-osteoblastic MC3T3-E1. **Figure 3.3A** shows *in vitro* dose-dependent cytotoxicity of HG_{oxi} and its components, ADH and ODEX, as well as of non-oxidized dextrin. HG_{oxi} exerted cytotoxicity in a concentration-dependent manner, mainly due to ODEX (CC₅₀ of 7.0 ± 0.2 mg/mL and 1.5 ± 0.2 mg/mL, respectively, as shown in **Figure 3.4A and B**), given that dextrin and ADH did not induce significant toxicity at the tested concentrations. HG_{oxi} toxicity is therefore assigned to aldehydes in the ODEX backbone, as previously reported for TK6 human lymphoblastoid cells⁴⁷. The reaction between ODEX and ADH in HG_{oxi} reduces the number of exposed aldehydes, and therefore, potential toxic interactions. **Figure 3.3B** shows dose-dependent cytotoxicity of LL18, with a calculated CC₅₀ of 38.5 ± 0.2 μ M (**Figure 3.4C**). LL18 may thus provide a safer (and cheaper) alternative to LL37, which was shown to be cytotoxic for different human cell types at concentrations ranging from 2 μ M to 13 μ M⁴⁸, with an CC₅₀ of 5 μ M for osteoblasts in particular⁴⁹.

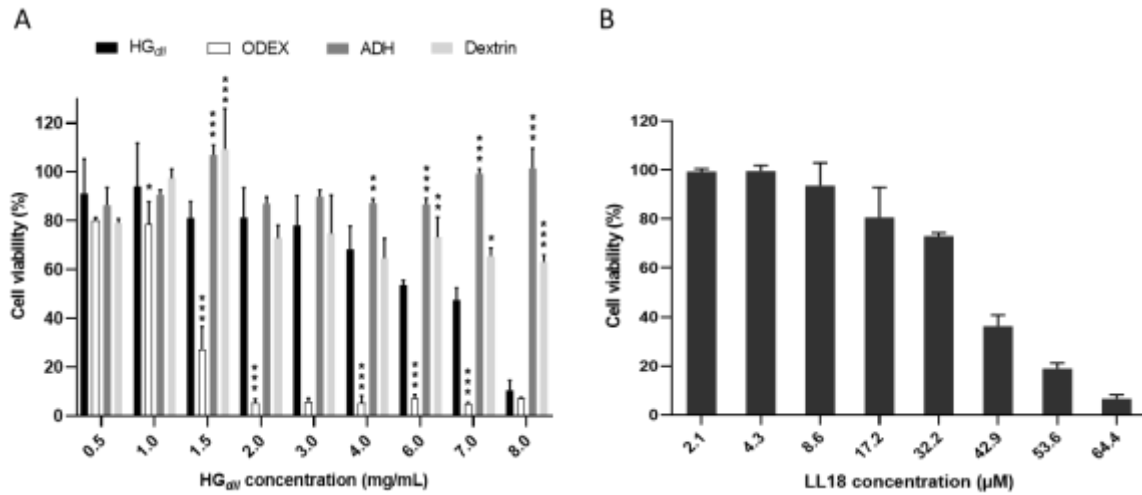


Figure 3.3 – MC3T3-E1 cell viability assessed by the MTT assay: **(A)** Dose-dependent effect of HG_{dil} and its isolated components - ODEX and ADH - and non-oxidized dextrin; **(B)** Dose-dependent effect of LL18. Cells were exposed to different concentrations for 24 h. Results were calculated as percentage of the negative control and data are presented as mean \pm SD (n = 3), * p < 0.05, ** p < 0.01, *** p < 0.001 vs HG_{dil}. ADH, adipic acid dihydrazide; HG_{dil}, diluted hydrogel; ODEX, oxidized dextrin. HG_{dil} refers to the sum of ODEX and ADH concentrations. The concentrations of the pure components, which are the same as in HG_{dil}, can be found in **Table 3.1**.

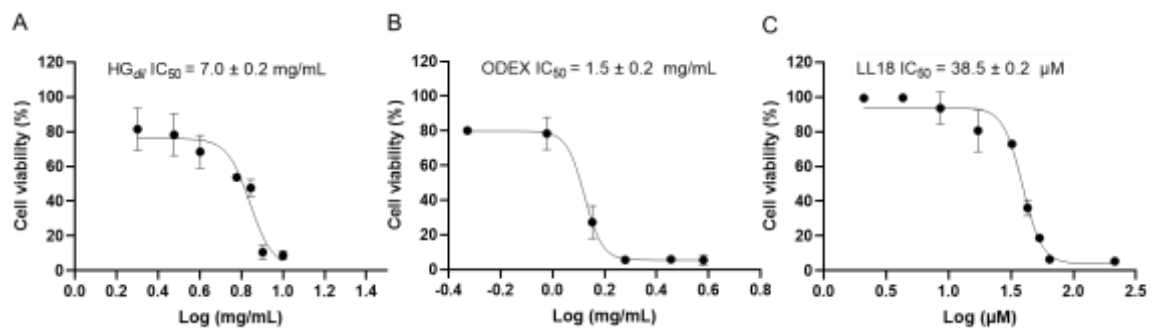


Figure 3.4 – Dose-response (cell viability) curves of MC3T3-E1 cells exposed for 24 h to different concentrations of: **(A)** diluted dextrin-based hydrogel (HG_{dil}); **(B)** oxidized dextrin (ODEX); and **(C)** LLKKK18 (LL18), assessed by the MTT reduction assay, for 50 % cytotoxic concentration (CC₅₀) calculation. Data are presented as mean \pm SD (n = 3).

Given that bone is a highly vascularized tissue, cellular toxicity of HG_{dil} and LL18 were also analyzed using dog RBCs (**Figure 3.5**). Materials used in the fabrication of medical devices are classified as hemolytic when the lysis of blood cells exceeds 5 %, slightly hemolytic when between 2 % and 5 % and non-hemolytic under 2 %⁴². Empty and LL18-loaded HG and its components were analyzed at concentrations

corresponding to HG_{ox} dilution factors of 5- and 10-fold. The most diluted samples were not toxic to erythrocytes. In the case of the most concentrated ones (44.26 mg/mL) only ODEX displayed significant hemolysis of 7.3 % (**Figure 3.5A**). When ODEX and ADH were simultaneously present, hemolysis decreased below 2 % regardless of the tested dilution. In a study using oxidized dextran, cytotoxicity was attributed to the ability of aldehydes to react with free amines⁵⁰. They react with nucleophilic groups in proteins, thereby interfering with cellular processes^{51,52}. However, since hydrazone bonds of crosslinked ODEX are cleaved over a time frame of days or weeks, hydrogels obtained using crosslinked aldehydes do not raise toxicity issues *in vivo*^{35,37,53}. The hemolytic activity of an LL18-loaded HG formulation was then assessed (**Figure 3.5B**). LL18 combined with the HG displayed lytic activity for the concentrations tested (6.1 % to 8.6 %), which is assigned to the presence of the peptide. Hemolysis by LL37 is reported at slightly below 10 % for 40 μM on porcine⁵⁴ and 34.7 % for 3.6 μM, in human erythrocytes⁵⁵. Canine erythrocytes have shown higher sensitivity compared to those from human and rat in hemolytic assessment of several synthetic AMPs⁵⁶, suggesting that LL18 may be less toxic than LL37. Indeed, the C-terminal tails of cathelicidins apparently play a role in the toxicity mechanism, since depletion of nine residues from LL37 C-terminal results in lower hRBC lysis, whereas the antibacterial activity, on the other hand, is not affected^{55,57}. Among other modifications, five amino acids are depleted from the C-terminal end of LL37 to give rise to LL18 (**Figure 3.1**), which may result in reduced peptide-cell membrane interaction and thus lower toxicity.

Interestingly, the lytic effect of combined ODEX and LL18 was lower as compared to the free components, most likely due to crosslinking between the nucleophilic primary amines of the peptide with aldehydes. However, this is a weak and reversible interaction⁵⁸. On the other hand, the reduction in toxicity occurs as well when adding dextrin to LL18, suggesting that the peptide also interacts with ODEX through non-covalent weak forces not dependent on the aldehydes. Indeed, the addition of LL18 to HG did not interfere with the crosslinking reaction time and the LL18 lytic activity is preserved. Thus, the interaction between ODEX and LL18 mutually reduce the toxicity of each component, and may contribute to a controlled release of the peptide.

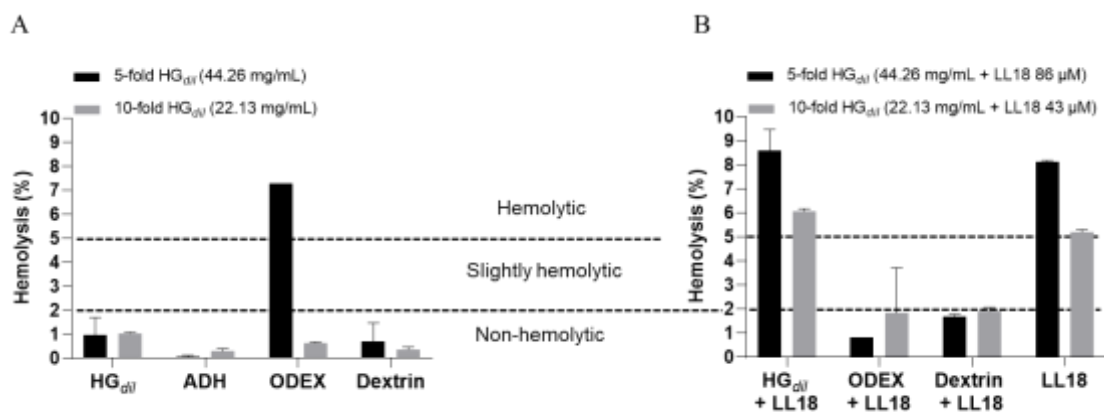


Figure 3.5 – Percentage of hemolysis caused by the hydrogel (HG) and its degradation products at equivalent concentrations, upon their interaction with dog red blood cells for 1 hour: **(A)** empty HG and **(B)** HG loaded with 429 μM of LL18, both 5-fold and 10-fold diluted. Data are expressed as percentage relative to the control and presented as mean \pm SD ($n=3$). Diluted hydrogel (HG_{dil}) refers to the sum of oxidized dextrin (ODEX) and adipic dihydrazide (ADH) concentrations. Tested concentrations refer to HG_{dil}; the concentrations of the pure components can be found in **Table 3.3**.

3.3.2 Hydrogel Degradation and pH Changes

Disc-shaped HG samples were prepared and immersed in PBS (pH 7.4) at 37 °C. The pH decreased from 7.40 to 7.15 in the first 5 h, reaching a final value of 7.04 upon full degradation, after 24 h (**Figure 3.6**). Normal blood pH ranges between 7.35 and 7.45⁵⁹; however, tissue repair has been associated with a lower pH during the early healing phase⁶⁰. The creation of bone defects triggers inflammation and causes the rupture of blood vessels, subsequently causing local acidosis⁶¹. In a sheep model, osteotomy and muscle hematomas yielded a local pH of 7.21 and 7.04 3h-post surgery, respectively, while a rat model showed a variation of 6.62 to 6.74 and 6.76 to 7.02 within 48 hours⁶². Moreover, microenvironment of an infected bone milieu is taken as mildly acidic (pH 5.5 to 6.7)^{63,64}, presumably as a result of production of metabolites by microorganisms. In our work, pH lowering upon HG degradation falls within ranges reported for early healing of tissue repair, thus in this regard it should not give rise to toxicity issues. Moreover, osteoblast proliferation and collagen synthesis were reported to be unaffected by pH in the range 7.4 to 6.9⁶⁵. In previous work we did not find signs of inflammatory cells or necrosis after 3-week implantation of dextrin-based HG in tibia fractures of a goat model³⁷. Hence, the HG formulation is unlikely to cause any harmful reaction under biological conditions due to acidity. Further, in this assay the HG degradation products become fully accumulated in the culture plate wells, while *in vivo* a gradual elimination of products from the implanted site would prevent local pH from lowering.

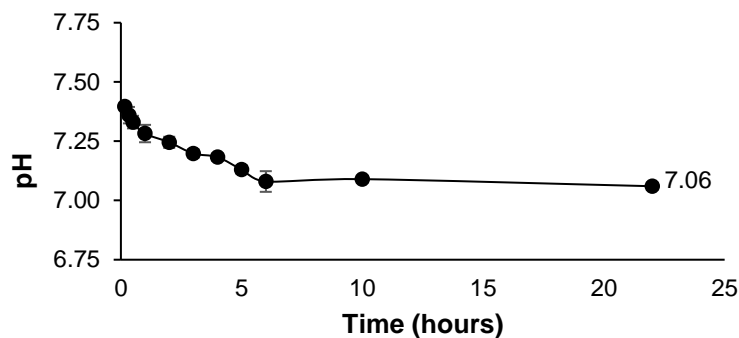


Figure 3.6 – pH changes of the dextrin-based hydrogel until complete degradation in phosphate-buffered saline buffer, pH 7.4. Results expressed as mean \pm SD (n = 3).

3.3.3 Hydrogel Degradation and LL18 Release

Schiff-based crosslinked hydrogels usually degrade fast in water ⁶⁶. However, the *in vitro* conditions, with a large excess of water, are probably quite distinct from the *in vivo* environment. Indeed, we have previously shown that HG fragments are still present 15 days after subcutaneous implantation in a rat model ³⁵, probably due to the less hydrated subcutaneous compartment, retarding hydrolysis of the hydrazone bonds. In this case, plotting the cumulative release of LL18 against the HG mass loss (%) may give us a more insightful view on the peptide release profile, independent of the degradation time (**Figure 3.7**). Since cleavage of hydrazone linkages is a pH dependent event ⁶⁷, we assessed HG mass loss (%) and LL18 release at pH 7.4 and 5.8, to mimic normal blood ⁵⁹ and mildly acidic infected milieu, respectively. The 429 μ M LL18-loaded formulation tested *in vivo* was used. The HG experienced an initial swelling in both conditions, as expected, due to osmotic effects. Most of LL18 is released during this initial swelling phase, particularly at acidic pH, which could favor a suitably rapid response to already established infections. A fairly rapid release was expected, since the peptide is very small as compared to the HG mesh. At pH 7.4, 59 % of the LL18 is released until the end of a 12-hour swelling phase, reaching a maximum of 83 % at complete weight loss. We hypothesize that some of LL18 amines may be linked to ODEX aldehydes (consequently not being detected by the fluorescamine method), at pH 7.4, although this interaction is quite labile ⁶⁸ and should not hamper the release of the bioactive peptide as discussed previously. At pH 5.8, 84 % of the LL18 is released in the swelling phase, being totally released before complete HG degradation, at 88 % weight loss. The lower pH results in a faster peptide release despite slower HG wet weight loss.

Hydrazone linkages have been shown to follow a pH dependent breakdown, being much faster at acidic than physiological pH ⁶⁸⁻⁷⁰. For this reason, hydrazone linkages have been applied in the design of pH-

responsive drug delivery systems ⁷¹. Thus, the faster HG degradation observed at pH 7.4 is an unexpected result. Still, the HG is able to gradually release LL18 until complete degradation, being faster in acidic environment as may be found in infected tissues. As mentioned above, since the degradation occurs *in vivo* in a longer timeframe, the release of the peptide should occur over a period of several days.

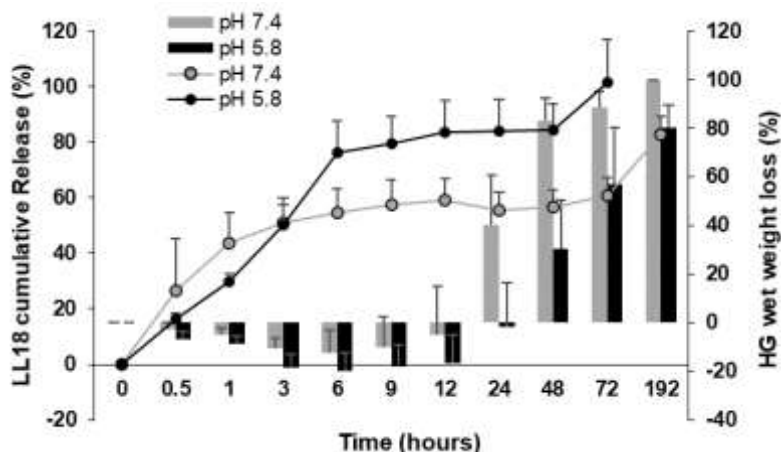


Figure 3.7 – Cumulative release profile of LLKKK18 (LL18)-loaded hydrogel (HG; lines) and HG wet weight loss (bars) calculated in specified time-points within 192 hours, performed at pH 7.4 (grey) and 5.8 (black) at 37 °C. Data are presented as mean ± SD (n=6).

3.3.4 Antibacterial Activity

Given that aldehydes are known for their microbiocidal effect ⁷², we examined *in vitro* the antibacterial activity of the HG. HG_{OH} exerted bactericidal effect owing to ODEX and the reactive aldehydes, with MIC₅₀ values of 18.0 and 10.9 mg/mL, respectively (**Table 3.7**) ⁷². In previous work, a (dialdehyde) dextran-based hydrogel with 80 % oxidation degree exerted anti-staphylococcal activity at 8 mg/mL (MIC), through cell membrane disruption ^{73,74}. Comparatively, in our work, ODEX with an oxidation degree of 40 %, exhibited a MIC₅₀ with a similar value of 10.9 mg/mL, therefore a comparable (or proportional) behavior. Importantly, these findings show the HG can exert antimicrobial effect to some extent at non-hemolytic concentrations (**Figure 3.5A**). On the other hand, it is more toxic towards mouse osteoblastic MC3T3-E1 (**Figure 3.3A**) and human lymphoblastoid TK6 cells ⁴⁷ than against bacteria. However, as demonstrated elsewhere, the HG formulation does not present any signs of toxicity *in vivo* ^{35,37,53}. In this study we selected a clinical MRSA with a vancomycin susceptibility of 1.4 µM. LL18 completely eliminated bacteria at a much higher concentration (150.2 µM).

Table 3.7 – Minimal, and half-minimal, inhibitory concentrations, MIC and MIC₅₀, values of vancomycin hydrochloride (VH), LLKKK18 (LL18), diluted hydrogel (HG_{dil}) and its isolated components, oxidized-dextrin (ODEX) and adipic dihydrazide (ADH).

Sample	MIC (µM)	MIC ₅₀ (mg/mL)
VH	1.4	-
LL18	150.2	-
HG _{dil}	-	18.0
ODEX	-	10.9
ADH	-	-

3.3.5 *In vivo* Study

3.3.5.1 Osteomyelitis Model and Bacterial Load

A process of acute OM was established *in vivo*. At day 7 rats were sacrificed to quantify the remaining bacteria in the tibia. The presence of pus in implanted sites after sacrifice confirms OM establishment (**Figure 3.8**).

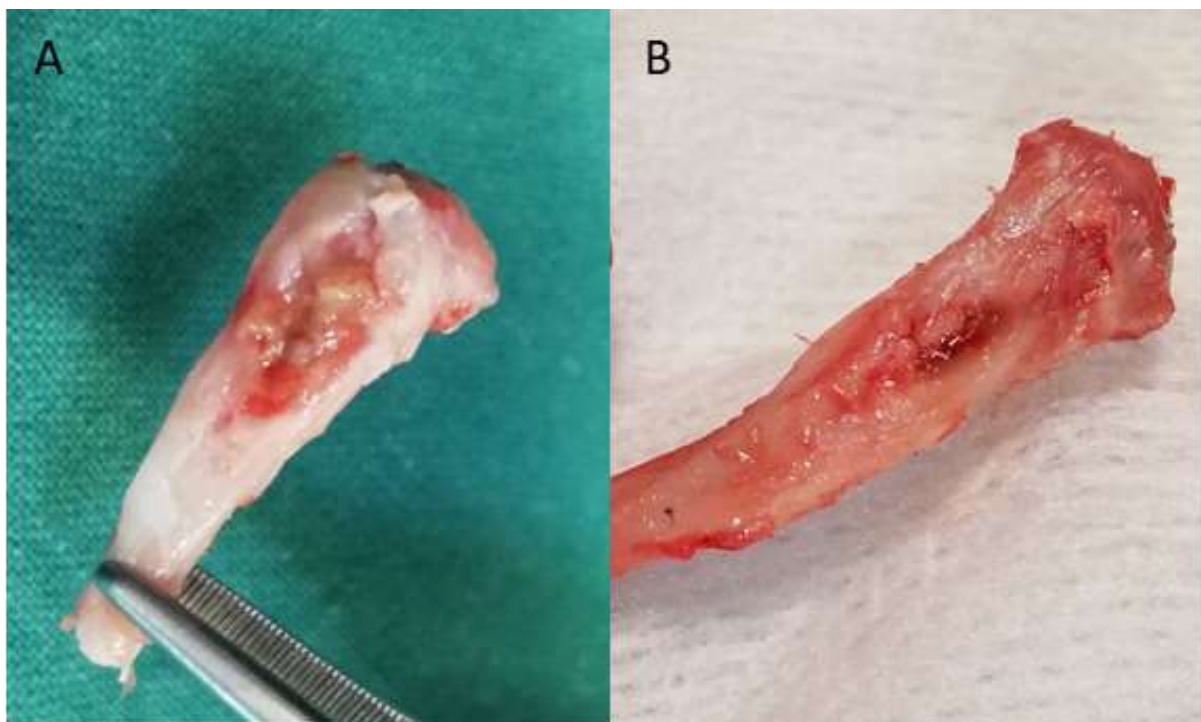


Figure 3.8 – Bone defects of rat tibias after sacrifice, 7 days post-treatment, representative of: **(A)** an infected bone and **(B)** a non-infected bone.

In a first experiment (**Figure 3.9A**), four different concentrations of LL18-loaded HG were tested: 86; 215; 300 and 429 μM (C1, C2, C3 and C4, respectively). In an attempt to analyze tissue damage in the absence of infection, a vancomycin dose previously reported as effective against *S. aureus* in a rat model ⁷, was used alone and in combination with 429 μM of LL18. Empty HG displayed some antimicrobial effect, in accordance to *in vitro* results. LL18 exhibited a dose-dependent antimicrobial effect from 86 to 300 μM , whereas the highest dose of 429 reversed this trend. On the other hand, VH completely eradicated the bacteria at $28 \times 10^3 \mu\text{M}$. Despite eradicating infection at 150 μM *in vitro*, LL18 was much less effective *in vivo* up to 429 μM . Cathelicidin action *in vivo* is hampered by proteolytic degradation, particularly by *S. aureus*-derived proteinases ^{75,76}. Moreover, short cationic AMPs are prone to rapidly binding to serum albumin ⁷⁷. This association has shown to result in a 10-fold increase of the MIC against a *S. aureus* strain ⁷⁸. In this work, the addition of a sustained delivery system delayed the contact between antimicrobial dosage and bacteria. Furthermore, the bacteria inoculated into bone defect, 10^7 CFU/mL, was much higher compared to the one used in the *in vitro* assays (5×10^5 CFU/mL). Taken together, all these factors may have brought LL18 to sub-therapeutic doses.

In a second experiment (**Figure 3.9B**), LL18 at 300 μM (C3) was tested in combination with different low VH concentrations: 10; 24 and 483 μM (VH1; VH2 and VH3, respectively). This combination completely suppressed infection in 10 %, 30 % and 70 % of the individuals as VH concentration increased. When delivered locally, and in combination with the HG and LL18, these results show that concentrations of VH in the range of few mM may suffice to control OM.

Although cytotoxicity and hemolytic effects were observed at much lower concentrations *in vitro* ^{48,54,55}, no safety concerns regarding local or systemic adverse events were detected for up to 712 μM of LL37 topically applied in patients chronic leg ulcers ⁷⁹. Thus, we assumed that intralesional administration of up to 429 μM of the less cytotoxic LL18 into bone defects could be safely applied, to examine the balance between antimicrobial efficacy and tissue damage.

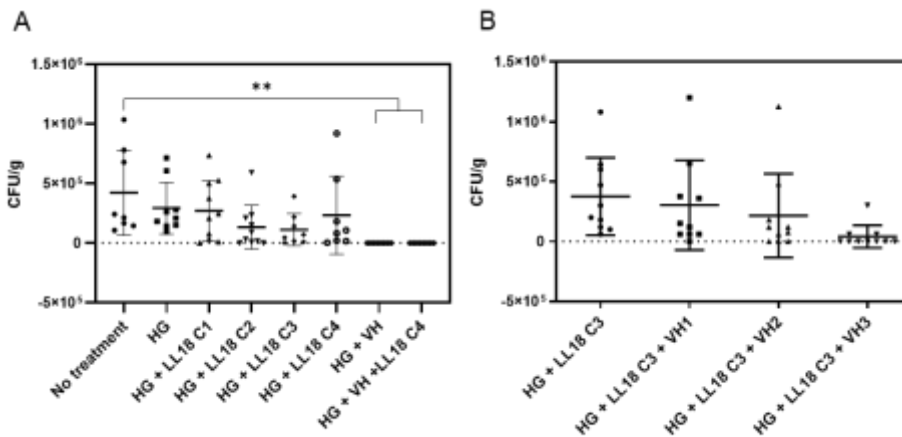


Figure 3.9 – Mean bacterial counts in colony forming units (CFU)/g bone from implanted-site after a 7-day treatment of MRSA-induced osteomyelitis with: **(A)** increasing concentrations of LKKK18 (LL18), including empty hydrogel (HG) and a vancomycin (VH)-loaded formulation; and **(B)** increasing concentrations of VH-loaded formulations in combination with a fixed LL18 concentration. Results are presented as mean \pm SD (n=10), (* p < 0.05, ** p < 0.01, *** p < 0.001). C1, C2, C3 and C4 correspond to 86; 215; 300 and 429 μ M of LL18, respectively. VH1, VH2 and VH3 correspond to 10; 24 and 483 μ M.

3.3.5.2 Histopathological Analysis

Histological analysis performed 7 days after implantation confirmed the presence of infection in animals without treatment, showing bacteria, fibrotic tissue, polymorph nuclear leukocytes infiltration, necrotic cells, multiple foci of sequestrum, severe acute inflammation and some signs of chronic inflammation with significant intramedullary fibrosis (**Figure 3.10** and **Figure 3.11**). Treatment with empty HG showed similar signs to the untreated condition. **Figure 3.12** presents the mean histological parameters. Regarding IAI, PI and BN, the untreated condition showed moderate to severe damage, as previously reported for *S. aureus*-induced OM⁴⁶, similarly to the group that received unloaded HG. Generally, LL18 concentrations C1, C2 and C3 were associated to significantly lower scores of IAI, PI and BN, as compared to C4 (**Figure 3.12A**), and significantly lower PI, as compared to unloaded HG. This suggests that LL18 can exert advantageous immunomodulatory effects from 86 to 300 μ M, but not at 429 μ M. Indeed, significant improvements in wound healing of venous leg ulcers were observed in patients after treatment with 111 or 356 μ M of LL37, whereas 712 μ M did not, further being associated with increased inflammation⁷⁹. Indeed, cathelicidins possess the ability to suppress pro-inflammatory signaling through several and complex mechanisms, including binding to and neutralizing the bacterial toll-like receptor

(TLR) ligands, such as LPS or lipoteichoic acids⁸⁰. They can mediate the generation of both anti-inflammatory and pro-inflammatory mediators depending on peptide concentration and cell type. Reduced inflammation in the presence of the proper concentrations of peptide is of major importance as it can help achieving faster tissue repair. In fact, LL18 was previously shown to reduce oxidative stress and inflammation, promote early M2 macrophage recruitment, and stimulate angiogenesis as concluded by increased microvessel and vascular endothelial growth factor, in the treatment of burn wounds in mice skin, after topically applying 15 µg every 3 days during 9 days³¹. Furthermore, following a C-terminal connection to cell membrane attachment, C-terminal depleted versions of cathelicidins have shown reduced activation of TLR signaling while maintaining bactericidal activity⁵⁵. This may explain why LL18, with 5 amino acids depleted from C-terminal (**Figure 3.1**), may constitute a safer option than LL37. We also show that, despite completely eradicating infection, the histopathological scores of animals treated with 28×10^3 µM VH-loaded HG remained high and similar to untreated and HG conditions, regardless of the presence of 429 µM LL18 C4. This indicates that 28×10^3 µM VH can be toxic, hampering a faster tissue recovery. Most likely, such high dosage is unnecessarily high to eradicate infection.

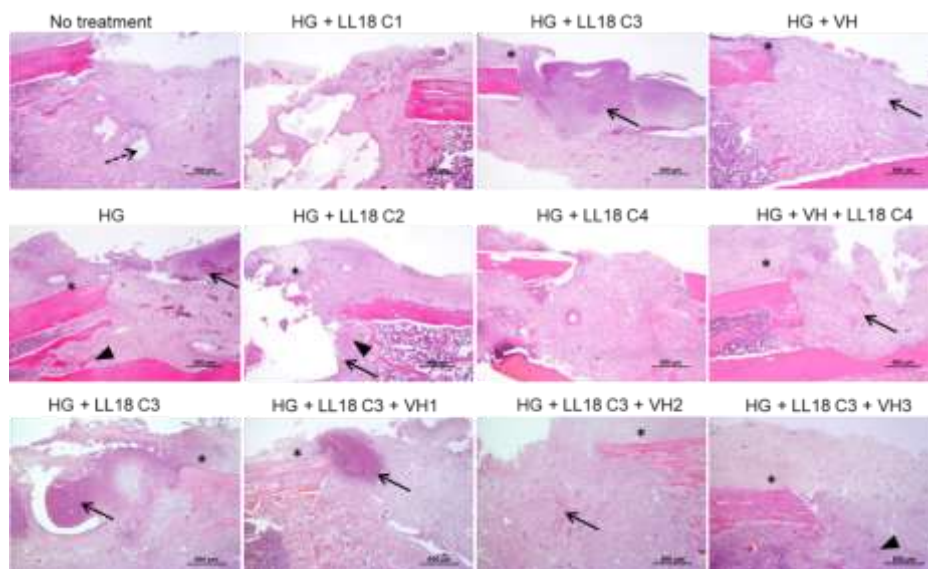


Figure 3.10 – Haematoxylin- and eosin-stained histological sections of the left and right tibias of rats 7 days after surgery (scale bars=500 µm). Periosteal inflammation (asterisk), intraosseous acute inflammation (black arrow), bone necrosis (black arrowhead) and bacteria (dashed arrow). C1, C2, C3 and C4 correspond to 86; 215; 300 and 429 µM of LL18, respectively. VH1, VH2 and VH3 correspond to 10; 24 and 483 µM.

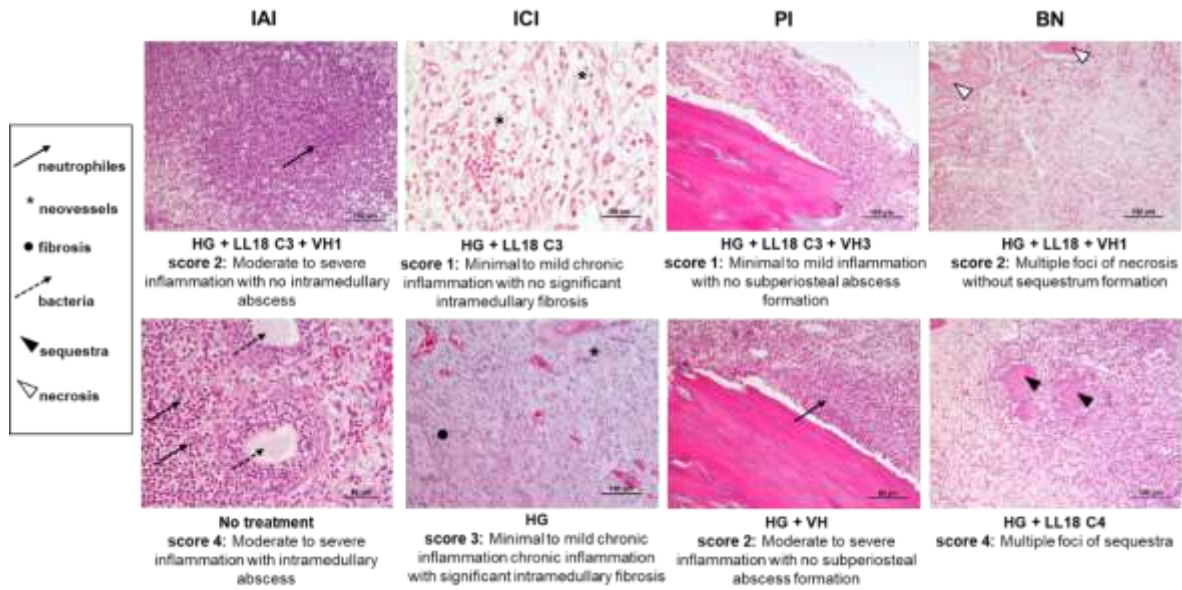


Figure 3.11 – Haematoxylin- and eosin-stained histological sections of tibias, displayed by the four histopathological parameters analyzed. Histological signs described in the scoring system are evidenced with high magnification (scale bars = 50 μm or 100 μm). IAI, Intraosseous acute inflammation; ICI, intraosseous chronic inflammation; PI, periosteal inflammation; BN, bone necrosis; C1, C2, C3 and C4 correspond to 86; 215; 300 and 429 μM of LL18, respectively. VH1, VH2 and VH3 correspond to 10; 24 and 483 μM .

C3 provided a safe option to the follow-up of the study, exhibiting a relevant immunomodulatory activity associated to a contribution to the reduction of the infection burden (**Figure 3.9A**). Combining increasing concentration of VH from 10 to 483 μM with 300 μM of LL18 generally decreased the histopathological scores compared to the untreated condition (**Figure 3.12B**), considerably reducing the tissue damage observed for $28 \times 10^3 \mu\text{M}$ of VH. High VH concentrations are typically used throughout the literature, with negative implications on tissue regeneration⁸⁻¹⁰. Vancomycin concentrations as low as 690 μM and higher reduced alkaline phosphatase activity in osteoblasts, indicating a toxic profile during the process of differentiation⁸. Even for relatively safer concentrations, continuous exposure results in significant reduction of osteoblast survival¹⁰. We show here that $28 \times 10^3 \mu\text{M}$ is unnecessarily harmful, and that much lower and harmless doses slightly above 483 μM (up to few Mm) could be considered, without compromising bacteria eradication, when associated to LL18. This may contribute to a safer and more cost-effective formulation. As far as we are concerned, this is the first time LL18 and such low VH doses are tested in this *in vivo* model of OM. Moreover, since LL37 at 223 μM has been reported to enhance bone regeneration in critical-sized rat calvaria defect²⁵, we envisage LL18 as a regenerating adjuvant in a

chronic OM model. Further investigation is important to find a 100 % bactericidal formulation and to examine its propensity to develop mechanisms of resistance.

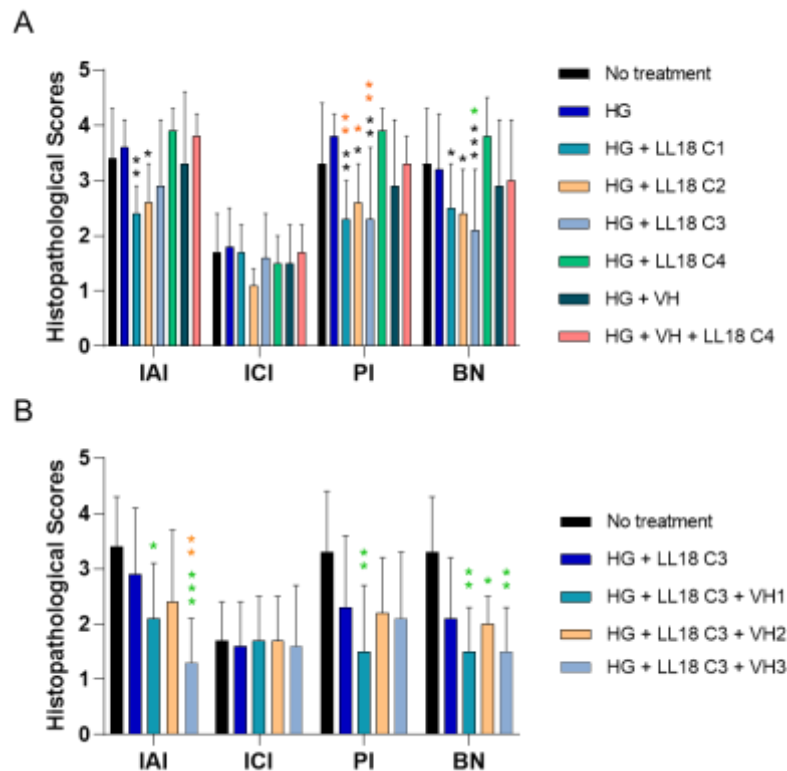


Figure 3.12 – Histopathological scores of: **(A)** increasing concentrations of LLKKK18 (LL18), including empty hydrogel (HG) and a vancomycin hydrochloride (VH)-loaded formulation; and **(B)** increasing concentrations of VH-loaded formulations in combination with a fixed LL18 concentration. Results are presented as mean \pm SD (n=10), (* p < 0.05, ** p < 0.01, *** p < 0.001). Black, green and orange * were compared to HG + LL18 C4, No treatment, and HG **(A)** or HG + LL18 C3 **(B)** conditions, respectively. IAI, intrasosseous acute inflammation; ICI, intrasosseous chronic inflammation; PI, periosteal inflammation; BN, bone necrosis.

In this study, unloaded HG showed tissue damage similar to the untreated condition and enabled a decrease in the histopathological scores by antimicrobial dose-loading variation, suggesting a minimal influence on the outcomes and, therefore, being a suitable carrier. Commercially available products for OM treatment include osteoconductive antibiotic-impregnated bone substitutes such as Osteoset-T®, Herafill® beads and PerOssal®⁸¹. Similar to ODEX-based HG, PerOssal® can be combined with different types of antibiotics at surgeon’s choice. However, despite general recommendations concerning antibiotic loading concentration, evidence-based guidelines are not available. To what extent different concentrations of intra-wound vancomycin damages host tissues and its influence on infection rates and

wound healing *in vivo* are not well explored and, therefore, specific cutoff values are not available to assist surgeons.

3.4 Conclusion

The balance between microbicide effects and host cellular toxicity is critical in OM treatment. We show that combined doses of LL18 and VH can be optimized as to exert potent antimicrobial effect with minimal tissue damage, requiring minimal antibiotic concentrations. LL18 exert immunomodulatory effects in a dose dependent manner - a concentration of 300 μ M combined with 483 μ M of VH eradicated infection in 70 % of the individuals with considerably reduced tissue damage, as compared to using 28 mM of VH. These studies encourage us to further study these formulations for their ability to clear infections while stimulating bone regeneration. We propose dextrin-based HG as a non-invasive delivery system for OM treatment, for its biocompatibility, cost, easy of manufacture and handle properties. The HG works as a sustained drug delivery platform, exhibiting a faster peptide release profile in acidic milieu as typically found in infected environments.

3.5 References

1. Rossel, A. *et al.* Stopping antibiotics after surgical amputation in diabetic foot and ankle infections—A daily practice cohort. *Endocrinol. Diabetes Metab.* 2, e00059 (2019).
2. Metsemakers, W. J., Smeets, B., Nijs, S. & Hoekstra, H. Infection after fracture fixation of the tibia: Analysis of healthcare utilization and related costs. *Injury* 48, 1204–1210 (2017).
3. Fraimow, H. Systemic Antimicrobial Therapy in Osteomyelitis. *Semin. Plast. Surg.* 23, 090–099 (2009).
4. World Health Organization. Prioritization of pathogens to guide discovery, research and development of new antibiotics for drug-resistant bacterial infections, including tuberculosis. World Health Organization. Report <https://apps.who.int/iris/handle/10665/311820>. (2017).
5. van Vugt, T. A. G., Arts, J. J. & Geurts, J. A. P. Antibiotic-Loaded Polymethylmethacrylate Beads and Spacers in Treatment of Orthopedic Infections and the Role of Biofilm Formation. *Front. Microbiol.* 10, 1626 (2019).
6. Haseeb, A., Ajit Singh, V., Teh, C. S. J. & Loke, M. F. Addition of ceftaroline fosamil or vancomycin to PMMA: An *in vitro* comparison of biomechanical properties and anti-MRSA efficacy. *J. Orthop. Surg.* 27, 2309499019850324 (2019).
7. Loc-Carrillo, C., Wang, C., Candan, A., Burr, M. & Agarwal, J. Local Intramedullary Delivery of Vancomycin Can Prevent the Development of Long Bone Staphylococcus aureus Infection. *PLoS One* 11, e0160187 (2016).
8. Braun, J. *et al.* Toxic effect of vancomycin on viability and functionality of different cells involved in tissue regeneration. *Antibiotics* 9, 238 (2020).
9. Röhner, E. *et al.* Vancomycin is toxic to human chondrocytes *in vitro*. *Arch. Orthop. Trauma Surg.* 141, 375–381 (2021).

10. Liu, J. X. *et al.* Topical vancomycin and its effect on survival and migration of osteoblasts, fibroblasts, and myoblasts: An in vitro study. *J. Orthop.* 15, 53–58 (2018).
11. Spohn, R. *et al.* Integrated evolutionary analysis reveals antimicrobial peptides with limited resistance. *Nat. Commun.* 10, 1–13 (2019).
12. Xhindoli, D. *et al.* The human cathelicidin LL-37 - A pore-forming antibacterial peptide and host-cell modulator. *Biochim. Biophys. Acta - Biomembr.* 1858, 546–566 (2016).
13. Kang, J., Dietz, M. J. & Li, B. Antimicrobial peptide LL-37 is bactericidal against *Staphylococcus aureus* biofilms. *PLoS One* 14, e0216676 (2019).
14. Mohamed, M. F., Abdelkhalek, A. & Seleem, M. N. Evaluation of short synthetic antimicrobial peptides for treatment of drug-resistant and intracellular *Staphylococcus aureus*. *Sci. Rep.* 6, 29707 (2016).
15. Tawfik, G. M. *et al.* Concordance of bone and non-bone specimens in microbiological diagnosis of osteomyelitis: A systematic review and meta-analysis. *J. Infect. Public Health* 13, 1682–1693 (2020).
16. Mohamed, W. *et al.* Intracellular proliferation of *S. aureus* in osteoblasts and effects of rifampicin and gentamicin on *S. aureus* intracellular proliferation and survival. *Eur. Cells Mater.* 28, 258–268 (2014).
17. Yu, K. *et al.* Recalcitrant methicillin-resistant *Staphylococcus aureus* infection of bone cells: Intracellular penetration and control strategies. *Bone Jt. Res.* 9, 49–59 (2020).
18. Josse, J., Velard, F. & Gangloff, S. C. *Staphylococcus aureus* vs. Osteoblast: Relationship and Consequences in Osteomyelitis. *Front. Cell. Infect. Microbiol.* 5, 85 (2015).
19. Noore, J., Noore, A. & Li, B. Cationic antimicrobial peptide LL-37 is effective against both extra- and intracellular *Staphylococcus aureus*. *Antimicrob. Agents Chemother.* 57, 1283–90 (2013).
20. Hu, Z. *et al.* Antimicrobial cathelicidin peptide LL-37 inhibits the LPS/ATP-induced pyroptosis of macrophages by dual mechanism. *PLoS One* 9, e85765 (2014).
21. Yu, X. *et al.* LL-37 inhibits LPS-induced inflammation and stimulates the osteogenic differentiation of BMSCs via P2X7 receptor and MAPK signaling pathway. *Exp. Cell Res.* 372, 178–187 (2018).
22. Kittaka, M. *et al.* Antimicrobial peptide LL37 promotes vascular endothelial growth factor-A expression in human periodontal ligament cells. *J. Periodontal Res.* 48, 228–234 (2013).
23. Koczulla, R. *et al.* An angiogenic role for the human peptide antibiotic LL-37/hCAP-18. *J. Clin. Invest.* 111, 1665–1672 (2003).
24. Ramos, R. *et al.* Wound healing activity of the human antimicrobial peptide LL37. *Peptides* 32, 1469–1476 (2011).
25. Kittaka, M. *et al.* The antimicrobial peptide LL37 promotes bone regeneration in a rat calvarial bone defect. *Peptides* 46, 136–142 (2013).
26. Li, L. *et al.* Cathelicidin LL37 Promotes Osteogenic Differentiation in vitro and Bone Regeneration in vivo. *Front. Bioeng. Biotechnol.* 9, 347 (2021).
27. Ramos, R., Domingues, L. & Gama, M. LL37, a human antimicrobial peptide with immunomodulatory properties. in *Science against microbial pathogens: communicating current research and technological advances* (ed. Mendez-Vilas, A.) 915–925 (Formatex Research Center, 2011).
28. Ciornei, C. D., Sigurdardóttir, T., Schmidtchen, A. & Bodelsson, M. Antimicrobial and chemoattractant activity, lipopolysaccharide neutralization, cytotoxicity, and inhibition by serum of analogs of human cathelicidin LL-37. *Antimicrob. Agents Chemother.* 49, 2845–50 (2005).
29. Nagaoka, I., Kuwahara-Arai, K., Tamura, H., Hiramatsu, K. & Hirata, M. Augmentation of the bactericidal activities of human cathelicidin CAP18/LL-37-derived antimicrobial peptides by amino acid substitutions. *Inflamm. Res.* 54, 66–73 (2005).

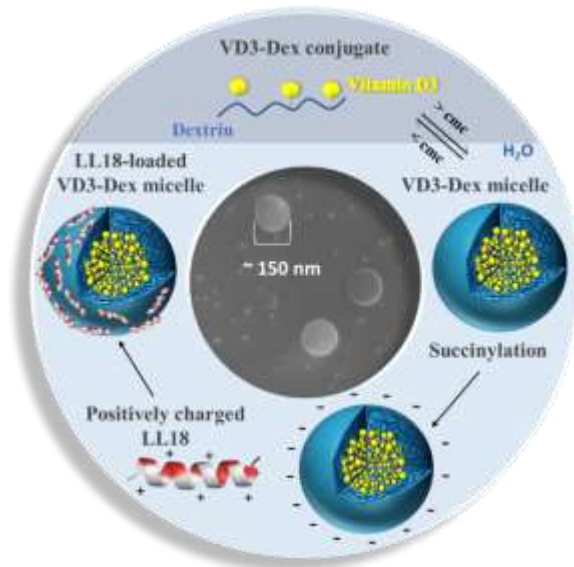
30. Sonawane, A. *et al.* Cathelicidin is involved in the intracellular killing of mycobacteria in macrophages. *Cell Microbiol* 13, 1601–17 (2011).
31. Silva, J. P. *et al.* Improved burn wound healing by the antimicrobial peptide LLKKK18 released from conjugates with dextrin embedded in a carbopol gel. *Acta Biomater.* 26, 249–262 (2015).
32. Pereira, I., Rodrigues, C., Rodrigues, A., Oliveira, M. & Gama, M. 9 - Injectable hydrogels as a delivery system for bone regeneration. in *Bioinspired Materials for Medical Applications* (eds. Rodrigues, L. & Mota, M.) 241–271 (Woodhead Publishing, 2017).
33. Molinos, M., Carvalho, V., Silva, D. M. & Gama, F. M. Development of a hybrid dextrin hydrogel encapsulating dextrin nanogel as protein delivery system. *Biomacromolecules* 13, 517–527 (2012).
34. Silva, D. M. *et al.* Structural analysis of dextrans and characterization of dextrin-based biomedical hydrogels. *Carbohydr. Polym.* 114, 458–466 (2014).
35. Silva, D. M. *et al.* Inflammatory response to dextrin-based hydrogel associated with human mesenchymal stem cells, urinary bladder matrix and Bonelike® granules in rat subcutaneous implants. *Biomed. Mater.* 11, 065004 (2016).
36. Pereira, I., Fraga, S., Silva, S., Teixeira, J. P. & Gama, M. In vitro genotoxicity assessment of an oxidized dextrin-based hydrogel for biomedical applications. *J. Appl. Toxicol.* 39, 639–649 (2019).
37. Pereira, I. *et al.* In vivo systemic toxicity assessment of an oxidized dextrin-based hydrogel and its effectiveness as a carrier and stabilizer of granular synthetic bone substitutes. *J. Biomed. Mater. Res. Part A* 107, 1678–1689 (2019).
38. Gama, M. & Molinos, M. Dextrin hydrogel for biomedical applications. Patent WO/2011/070529A2 (2011).
39. Pizzolato-Cezar, L. R., Okuda-Shinagawa, N. M. & Teresa Machini, M. Combinatory therapy antimicrobial peptide-antibiotic to minimize the ongoing rise of resistance. *Front. Microbiol.* 10, 1703 (2019).
40. Pereira, I. *et al.* Effects of gamma irradiation and periodate oxidation on the structure of dextrin assessed by mass spectrometry. *Eur. Polym. J.* 103, 158–169 (2018).
41. ISO 10993-5. Biological evaluation of medical devices — Part 5: Tests for in vitro cytotoxicity. (2009).
42. ASTM International (F756–13). Standard Practice for Assessment of Hemolytic Properties of Materials. (2013).
43. Ma, J. K. H. & Hadzija, B. Acid–Base Equilibrium and Buffered Solutions. in *Basic physical pharmacy* 32 (Jones & Bartlett Learning, 2013).
44. ISO 20776-1. Clinical laboratory testing and in vitro diagnostic test systems — Susceptibility testing of infectious agents and evaluation of performance of antimicrobial susceptibility test devices — Part 1: Reference method for testing the in vitro activity of antim. (2006).
45. Silva, V. *et al.* Therapeutic potential of dalbavancin in a rat model of methicillin-resistant *Staphylococcus aureus* (MRSA)-osteomyelitis. *Int. J. Antimicrob. Agents* 56, 106021 (2020).
46. Fukushima, N., Yokoyama, K., Sasahara, T., Dobashi, Y. & Itoman, M. Establishment of rat model of acute staphylococcal osteomyelitis: Relationship between inoculation dose and development of osteomyelitis. *Arch. Orthop. Trauma Surg.* 125, 169–176 (2005).
47. Pereira, I., Fraga, S., Silva, S., Teixeira, J. P. & Gama, M. In vitro genotoxicity assessment of an oxidized dextrin-based hydrogel for biomedical applications. *J. Appl. Toxicol.* 39, 639–649 (2019).
48. Nilsson, B. O. What can we learn about functional importance of human antimicrobial peptide LL-37 in the oral environment from severe congenital neutropenia (Kostmann disease)? *Peptides* 128 170311 (2020).
49. Säll, J. *et al.* The antimicrobial peptide LL-37 alters human osteoblast Ca handling and induces Ca²⁺-independent apoptosis. *J. Innate Immun.* 5, 290–300 (2013).

50. Aziz, M. A. *et al.* In vitro biocompatibility and cellular interactions of a chitosan/ dextran-based hydrogel for postsurgical adhesion prevention. *J. Biomed. Mater. Res. - Part B Appl. Biomater.* 103, 332–341 (2015).
51. Voulgaridou, G. P., Anestopoulos, I., Franco, R., Panayiotidis, M. I. & Pappa, A. DNA damage induced by endogenous aldehydes: Current state of knowledge. *Mutat. Res. - Fundam. Mol. Mech. Mutagen.* 711, 13–27 (2011).
52. Lopachin, R. M. & Gavin, T. Molecular mechanisms of aldehyde toxicity: A chemical perspective. *Chem. Res. Toxicol.* 27, 1081–1091 (2014).
53. Pereira, I. *et al.* Regeneration of critical-sized defects, in a goat model, using a dextrin-based hydrogel associated with granular synthetic bone substitute. *Regen. Biomater.* 8, 1–10 (2021).
54. Scheenstra, M. R. *et al.* Cathelicidins PMAP-36, LL-37 and CATH-2 are similar peptides with different modes of action. *Sci. Rep.* 9, 1–12 (2019).
55. Kao, C. *et al.* Cathelicidin Antimicrobial Peptides with Reduced Activation of Toll-Like Receptor Signaling Have Potent Bactericidal Activity against Colistin-Resistant Bacteria. *MBio* 7, e01418-16 (2016).
56. Greco, I. *et al.* Correlation between hemolytic activity, cytotoxicity and systemic in vivo toxicity of synthetic antimicrobial peptides. *Sci. Reports* 2020 101 10, 1–13 (2020).
57. De Miguel Catalina, A. *et al.* The C-Terminal VPRTES Tail of LL-37 Influences the Mode of Attachment to a Lipid Bilayer and Antimicrobial Activity. *Biochemistry* 58, 2447–2462 (2019).
58. Kalia, J. & Raines, R. T. Hydrolytic stability of hydrazones and oximes. *Angew. Chem. Int. Ed. Engl.* 47, 7523–7526 (2008).
59. Shock, N. W. & Hastings, A. B. Studies of the acid-base balance of the blood in normal individuals. *J. Biol. Chem.* 104, 585–600 (1934).
60. Chakkalakal, D. A., Mashoof, A. A., Novak, J., Strates, B. S. & McGuire, M. H. Mineralization and pH relationships in healing skeletal defects grafted with demineralized bone matrix. *J. Biomed. Mater. Res.* 28, 1439–1443 (1994).
61. Walters, G., Pountos, I. & Giannoudis, P. V. The cytokines and micro-environment of fracture haematoma: Current evidence. *J. Tissue Eng. Regen. Med.* 12, e1662–e1677 (2018).
62. Berkmann, J. C. *et al.* Early pH changes in musculoskeletal tissues upon injury—aerobic catabolic pathway activity linked to inter-individual differences in local pH. *Int. J. Mol. Sci.* 21, 2513 (2020).
63. Chen, Z. *et al.* Construction of injectable, pH sensitive, antibacterial, mineralized amino acid yolk-shell microspheres for potential minimally invasive treatment of bone infection. *Int. J. Nanomedicine* 13, 3493–3506 (2018).
64. Cicuéndez, M. *et al.* Multifunctional pH sensitive 3D scaffolds for treatment and prevention of bone infection. *Acta Biomater.* 65, 450–461 (2018).
65. Arnett, T. R. Extracellular pH regulates bone cell function. in *Journal of Nutrition* vol. 138 415–418 (American Society for Nutrition, 2008).
66. Weis, M. *et al.* Evaluation of Hydrogels Based on Oxidized Hyaluronic Acid for Bioprinting. *Gels* 4, 82 (2018).
67. Su, H. *et al.* Schiff base-containing dextran nanogel as pH-sensitive drug delivery system of doxorubicin: Synthesis and characterization: *J Biomater Appl* 33, 170–181 (2018).
68. Zhang, Z., He, C. & Chen, X. Hydrogels based on pH-responsive reversible carbon–nitrogen double-bond linkages for biomedical applications. *Mater. Chem. Front.* 2, 1765–1778 (2018).
69. Prabakaran, M., Grailer, J. J., Pilla, S., Steeber, D. A. & Gong, S. Amphiphilic multi-arm-block copolymer conjugated with doxorubicin via pH-sensitive hydrazone bond for tumor-targeted drug delivery. *Biomaterials* 30, 5757–5766 (2009).
70. Yu, J. *et al.* The potential of pH-responsive PEG-hyperbranched polyacylhydrazone micelles for cancer therapy. *Biomaterials* 35, 3132–3144 (2014).

71. Sonawane, S. J., Kalhapure, R. S. & Govender, T. Hydrazone linkages in pH responsive drug delivery systems. *European Journal of Pharmaceutical Sciences* vol. 99 45–65 (2017).
72. Paulus, W. Aldehydes. in *Directory of Microbicides for the Protection of Materials* 459–474 (Springer Netherlands, 2004). doi:10.1007/1-4020-2818-0_25.
73. Chan, M., Brooks, H. J. L., Moratti, S. C., Hanton, L. R. & Cabral, J. D. Reducing the oxidation level of dextran aldehyde in a chitosan/dextran-based surgical hydrogel increases biocompatibility and decreases antimicrobial efficacy. *Int. J. Mol. Sci.* 16, 13798–13841 (2015).
74. Hyon, S. H., Nakajima, N., Sugai, H. & Matsumura, K. Low cytotoxic tissue adhesive based on oxidized dextran and epsilon-poly- l-lysine. *J. Biomed. Mater. Res. - Part A* 102, 2511–2520 (2014).
75. Moncla, B. J., Pryke, K., Rohan, L. C. & Graebing, P. W. Degradation of naturally occurring and engineered antimicrobial peptides by proteases. *Adv. Biosci. Biotechnol.* 02, 404–408 (2011).
76. Sieprawska-Lupa, M. et al. Degradation of human antimicrobial peptide LL-37 by *Staphylococcus aureus*-derived proteinases. *Antimicrob. Agents Chemother.* 48, 4673–9 (2004).
77. Sivertsen, A. et al. Synthetic cationic antimicrobial peptides bind with their hydrophobic parts to drug site II of human serum albumin. *BMC Struct. Biol.* 14, 4 (2014).
78. Svenson, J., Brandsdal, B. O., Stensen, W. & Svendsen, J. S. Albumin binding of short cationic antimicrobial micropeptides and its influence on the in vitro bactericidal effect. *J. Med. Chem.* 50, 3334–3339 (2007).
79. Grönberg, A., Mahlapuu, M., Ståhle, M., Whately-Smith, C. & Rollman, O. Treatment with LL-37 is safe and effective in enhancing healing of hard-to-heal venous leg ulcers: a randomized, placebo-controlled clinical trial. *Wound Repair Regen.* 22, 613–621 (2014).
80. Alford, M. A., Baquir, B., Santana, F. L., Haney, E. F. & Hancock, R. E. W. Cathelicidin Host Defense Peptides and Inflammatory Signaling: Striking a Balance. *Front. Microbiol.* 11, 1902 (2020).
81. Van Vugt, T. A. G., Geurts, J. & Arts, J. J. Clinical Application of Antimicrobial Bone Graft Substitute in Osteomyelitis Treatment: A Systematic Review of Different Bone Graft Substitutes Available in Clinical Treatment of Osteomyelitis. *BioMed Research International* vol. 2016

CHAPTER 4

4. THERAPEUTIC PARTNERSHIP OF LLKKK18 AND VITAMIN D3 LOADED INTO DEXTRIN-BASED MICELLES TAILORED FOR BONE INFECTIONS



In this work, we aimed at developing a novel self-assembled nanoplatform to treat bone infection, incorporating vitamin D3 (VD3) and the antimicrobial LLKKK18 (LL18) peptide. A micelle system was developed by conjugation of succinylated VD3 to dextrin (VD3-Dex). Then, negative superficial charges were incorporated into VD3-Dex conjugate by succinylation to benefit from the electrostatic association of cationic LL18.

VD3-Dex yielded self-assembled homogeneous-in-size micelles with ~ 160 nm diameter, stable in solution for at least 4 months. The VD3-Dex micelles exhibited erythrocyte (≤ 2.5 mg/mL) and cell biocompatibility (≤ 3 mg/mL), and antimicrobial activity (≥ 0.5 mg/mL). Association of LL18 with micelles resulted in improved biocompatibility, faster cell uptake, and wound healing potential (≤ 0.125 mg/mL). Importantly, the antimicrobial profile of the VD3-Dex-LL18 micelles was highly improved, reaching 93.1 % bacteria killing at 0.15 mg/mL:15 μ g/mL of micelle:peptide ratio, and 100 % at 0.175 mg/mL:17.5 μ g/mL. Peptide association with VD3-Dex micelles also abrogated LL18-induced hemolysis, and drastically reduced albumin denaturation as an indication of an anti-inflammatory action. Through confocal microscopy, LL18 was traced in the perinuclear region of osteoblasts, and both in lysosomes and perinuclear area of macrophages. In contrast, micelle-loaded LL18 was fully concentrated in the lysosomes of both osteoblasts and macrophages.

We developed a dual delivery system for non-antibiotic VD3 and LL18 with tissue healing and synergistic antimicrobial properties, overcoming recurrent limitations of VD3 solubility and diminishing LL18 toxicity. Dextrin provided a safe and resourceful platform for drug delivery design.

4.1 Introduction

Hard-to-treat bone infections are a serious burden in modern society. Rapidly evolving microbe resistance and impaired bone healing, resulting from persistent infection, represent a dual challenge impairing patient recovery^{1,2}. Bone infections are still a common event reporting incidences as, for instance, 11.1 % after surgical debridement of open tibial fractures, 34.6 % in patients with open tibial fractures who underwent separate operations, reaching 50 % in diabetic foot infections³⁻⁵. If not properly treated, bone infections can result in frequent therapeutic relapse with diminished quality of life, occasionally leading to amputation. The treatment of fracture-related infections is a substantial financial burden for the health systems – 6.5 times higher compared to non-infected fractures⁶.

Antimicrobial peptides (AMPs) are naturally occurring molecules of the primary host defense against microbial invasion. AMPs-based therapeutics meets a recent trend that advocates the importance of designing new materials allying a high spectrum of antimicrobial activity to a low propensity for the development of microbe resistance⁷. LL37 is a cationic peptide with 37 amino acid residues derived from the single human cathelicidin, hCAP18. LL37, attaches to the pathogen membrane through electrostatic forces, disrupting the membrane surface by creating pores⁸. Cathelicidin is proposed as a smart option for bone infections therapy for reasons such as: i) potent anti-staphylococcal activity^{9,10}, the most common species causing bone infections¹¹⁻¹⁴, ii) inhibition of biofilm formation^{9,15} and lipopolysaccharide (LPS) activity¹⁶; iii) pro-angiogenic activity¹⁷⁻¹⁹; iv) promotion of wound healing^{18,19}; v) enhancement of bone regeneration^{20,21}; and vi) clinical safety and remarkable healing rates as demonstrated in the treatment of chronic leg ulcers by topical administration²². Exogenous administration of LL37 (NH₂-LLGDFFRKSKEKIGKEFKRIVQRIKDFLRNLPRTES-COOH) is discouraged by the cost of the long peptide, toxicity issues and rapid protease degradation. LLKKK18 (LL18) is an 18-length amino acid peptide (NH₂-KEFKRIVKRIKKFLRKLV-COOH) designed from LL37 but displaying higher cationicity and hydrophobicity than LL37, which results in higher attachment to pathogen membrane (i.e. higher antimicrobial activity). LL18 is three-fold more effective in killing mycobacteria than LL37²³, displays higher chemoattractant activity, decreased toxicity and binding to plasma proteins²⁴. The angiogenic and chemoattractant potential of LL18 was demonstrated *in vivo*, resulting in improved burn wound healing in a rat model²⁵. However, LL18 showed no improvements in a goat model of cranial bone regeneration²⁶, and increased tissue damage as a function of concentration in an osteomyelitis (OM) rat model²⁷. LL18 remains mostly unexplored. While manufacturing costs can be reduced by shorter derivatives, toxicity and early degradation may be circumvented by sustained delivery platforms.

Once regarded as mostly regulating calcium and bone homeostasis, vitamin D3 (VD3) has currently become a worldwide hot topic for its role in fighting infections. Its active metabolite, $1\alpha,25$ -dihydroxyvitamin D3 ($1,25[\text{OH}]_2\text{D}_3$), interacts with a nuclear vitamin D3 receptor (VDR), a ligand-activated transcription factor that controls gene expression through activation of gene transcription at specific deoxyribonucleic acid (DNA) sequences – vitamin D3 response elements (VDRE)²⁸. Cathelicidin can be up-regulated by a VD3-dependent mechanism, through VDR, acting as a secondary messenger driving VD3-mediated host response to infection^{29,30}. Additional VD3-associated effects include promotion of cell proliferation and differentiation, oxidative stress reduction, immunoregulation and anti-inflammatory/anticancer actions³¹. As the VDR has been found in most cell types, VD3 is itself a pleiotropic, repair and maintenance agent acting as a molecular switch targeting hundreds of known human genes across a wide variety of tissues.

VD3 is produced by the skin upon exposure to ultraviolet (UV) radiation, and undergoes a two-step enzymatic activation in the liver and kidneys. However, local activation of VD3 in osteoblasts seems to exert effects on cell differentiation similar to those induced by the biologically active form³². Since the active metabolite has been associated to complications, the use of VD3 becomes essential. The activation machinery at a cellular level endows VD3 with the capability of acting in an autocrine manner in the local environment, supporting the use of this safer and affordable form – cholecalciferol – in the design of advanced therapeutic systems. Enhanced levels of angiogenesis, vascularization, osteogenesis and bone structure differentiation were achieved by VD3 enriched delivery system, successfully reconstructing artificial bone defects in rat mandible³³. Clinically, antibiotic-associated VD3 granules were successfully applied as a topical treatment for infected open wounds³⁴, including diabetic foot ulcer with OM, with minimum systemic side effects³⁵. Overall, VD3 is evolving as both a booster of immunity and an inexpensive tissue healing adjuvant for bone infection therapy. The limitations on the direct use of VD3 as a therapeutic agent are low bioavailability, due to its hydrophobic nature, and low solubility and cytotoxicity issues, which can be alleviated by a sustained delivery platform.

Dextrin is a natural glucose polymer produced by partial hydrolysis of starch. The α -(1→4) glycosidic bonds connecting the glucose units are susceptible to cleavage by blood α -amylases³⁶, being cleared by renal elimination thus avoiding tissue accumulation^{36,37}. The biodegradability of a dextrin-growth factor conjugate was demonstrated under amylase blood levels of 188 and 52 units per liter (U/L) in acute and chronic wound patient-derived fluids, respectively³⁸. Dextrin is an affordable, biocompatible and non-immunogenic raw material generally recognized as safe (GRAS) ingredient³⁹. A high density of hydroxyl groups, suitable for bioconjugation, endows the dextrin backbone with excellent tunability for sustained

drug delivery applications^{25,40}. The biocompatibility of dextrin, as a bone filling material or granules carrier in the form of hydrogel (HG) formulations, was reported recently^{26,41}. Importantly, it was recently shown that dextrin not only promotes proliferation but also enhances alkaline phosphatase activity of osteoblast-like cells, showing stimulating effects on cell differentiation and calcification⁴². Dextrin could further work as a source of energy to osteoblasts in oxygen depleted conditions⁴³, as it is the avascular critical defect. Microbe resistance to antibiotics is a serious threat to human health⁴⁴, severely hampering the treatment of bone infections. In this study dextrin works as a biodegradable carrier to solubilize hydrophobic VD3 and simultaneously entrap LL18, shielding both compounds from the immune system and combining bone repairing properties and antibacterial activity without resorting to conventional antibiotics. While LL18 provides an exogenous source of an optimized LL37 version, with pro-angiogenic and antimicrobial actions, VD3 may constitute a cost-effective, natural, safe and pleiotropic adjuvant for tissue healing and provide additional stimulation of endogenous LL37. This formulation is designed for local or intralesional administration scenarios.

4.2 Materials and Methods

4.2.1 Materials and Reagents

All reagents used were of the highest analytical grade available. Dextrin (MW ~ 2000 g/mol) was from Tackidex® B 167 (Batch E 8747, dextrin from potato starch) kindly provided by Roquette (Lestrem, France). LL18 (KEFKRIVKRIKKFLRKLV-OH, 95 % purity, MW = 2330 g/mol) and carboxytetramethyl-rhodamine (TAMRA)-labeled LL18 (TAMRA-KEFKRIVKRIKKFLRKLV-OH >90 % purity, MW = 2741.5 g/mol) were purchased from Schafer-N (Copenhagen, Denmark). Cholecalciferol (vitamin D3, CAS no. 67-97-0), 4-dimethylaminopyridine (DMAP; CAS no. 1122-58-3), fluorescamine (CAS no. 38183-12-9), and Mitomycin C (CAS no. 50-07-7) were purchased from Fisher Scientific (New Jersey, USA). Succinic anhydride (CAS no. 108-30-5), 1-ethyl-3-(3-dimethylaminopropyl) carbodiimide hydrochloride (EDC, CAS no. 25952-53-8), phosphate-buffered saline (PBS, CAS no. 10049-21-5), pyrene (CAS no. 129-00-0), 3-[4,5-Dimethylthiazole-2-yl]-2,5-diphenyl tetrazolium bromide (MTT, CAS no. 298-93-1), Triton X-100 (CAS no. 9036-19-5) and paraformaldehyde (CAS no. 30525-89-4), were supplied by Sigma-Aldrich (Missouri, USA). All other reagents including dimethylsulfoxide (DMSO), dichloromethane (DCM), extra-dry pyridine, petroleum ether, ethyl acetate and hydrochloric acid (HCl) were of analytical grade. Dialysis tubing with a molecular weight cut-off of 1000 Da was obtained from Orange Scientific (Braine-l'Alleud, Belgium). Dulbecco's Modified Eagle Medium (DMEM), fetal bovine serum (FBS) and penicillin-streptomycin were obtained from Merck Millipore (Massachusetts, USA). Hoechst 33342 (CAS no. 23491-52-3) was

purchased from Santa Cruz Biotechnology, Inc. (Texas, USA), BioTracker™ 540 Red lysosome dye and fluorescein isothiocyanate (FITC, CAS no. 3326-32-7) from Merck KGaA (Darmstadt, Germany), and LysoSensor™ Green DND-189 from Thermo Fisher Scientific (Massachusetts, USA). Albumin, human serum, fraction V, was purchased from calbiochem (California, USA) and Brain Heart Infusion (BHI) for microbiology from PanReac AppliChem (Darmstadt, Germany).

4.2.2 Production of Micelles

4.2.2.1 Succinylation of Vitamin D3

VD3 (1 g), succinic anhydride (2 g) and DMAP (0.020 g) were dissolved in 5 mL of extra-dry pyridine. The solution was left to stir under nitrogen atmosphere for 24 h in the dark. The mixture was then poured in DCM (50 ml) and washed with HCl 0.1 M (3 x 20 ml) by liquid-liquid extraction. The organic DCM phase was dried with anhydrous MgSO₄, and evaporated under vacuum to afford the succinylated VD3 (SucVD3) as a yellow oil. The oil was purified by dry flash chromatography using stepwise elution with petroleum ether:ethyl acetate mixtures (50 ml; 100 % petroleum ether – petroleum ether:ethyl acetate 1:1 v/v) of increasing polarity. The purification progress was monitored by thin-layer chromatography (silica gel 60; elution with petroleum ether:ethyl acetate and (1:1, v/v) with visualization under UV irradiation (265 nm) and revelation with iodine vapor. The relevant fractions were pooled and the solvent was removed under vacuum to obtain the SucVD3 as a colorless oil. SucVD3 was characterized by infrared spectroscopy, and stored protected from light at 4 °C until use.

4.2.2.2 Synthesis of Conjugates

The polymerization degree of dextrin (Tackidex® B 167) was reported to range from 6 to 17 glucose (MW = 162 g/mol) units⁴⁵, with an average MW of ~2000 g/mol and a maximum of ~2800 g/mol. In order to obtain a more homogeneous < 1000 Da material for all experiments described in this study, dextrin was previously dissolved in dH₂O and dialyzed with a 1000 Da cut-off membrane, freeze-dried and stored in a desiccator until use.

SucVD3 and dextrin were dissolved separately in DMSO and then mixed at 1:4 or 1:8 molar ratio. EDC (3 molar eq. in relation to SucVD3) and DMAP (3 mol eq. in relation to SucVD3) were added to the mixture and left stirring for 24 h at room temperature. Then, succinic anhydride (3 mol eq. in relation to SucVD3) was added and the reaction mixture was left stirring at room temperature for another 24 h period. The reaction mixture was poured into water and dialyzed in a 1000 Da pore size membrane against 5 L of

distilled water (dH₂O) with a total of 9 water changes during 72 h. The final product was freeze-dried for 5 days. **Figure 4.1** depicts the overall reactions. Unbound SucVD3 was separated from Vitamin D3-dextrin (VD3-Dex) conjugates by an ethanol extraction method. Briefly, ethanol was added to the freeze-dried product and agitated, followed by centrifugation at 7,000 g for 5 min. The unbound SucVD3 in the ethanol supernatant was discarded and VD3-Dex was collected in the pellet and dried under nitrogen stream to obtain a light-yellow solid. Conjugates were then dissolved in H₂O and extruded through a 200-nm pore size filter. The micelles were freeze-dried and stored in the desiccator at 4 °C protected from light. This step was conducted in aseptic conditions on every occasion requiring sterilized material, then freeze-dried in sterile and gauze-covered glass tubes, and weighed under aseptic conditions before use.

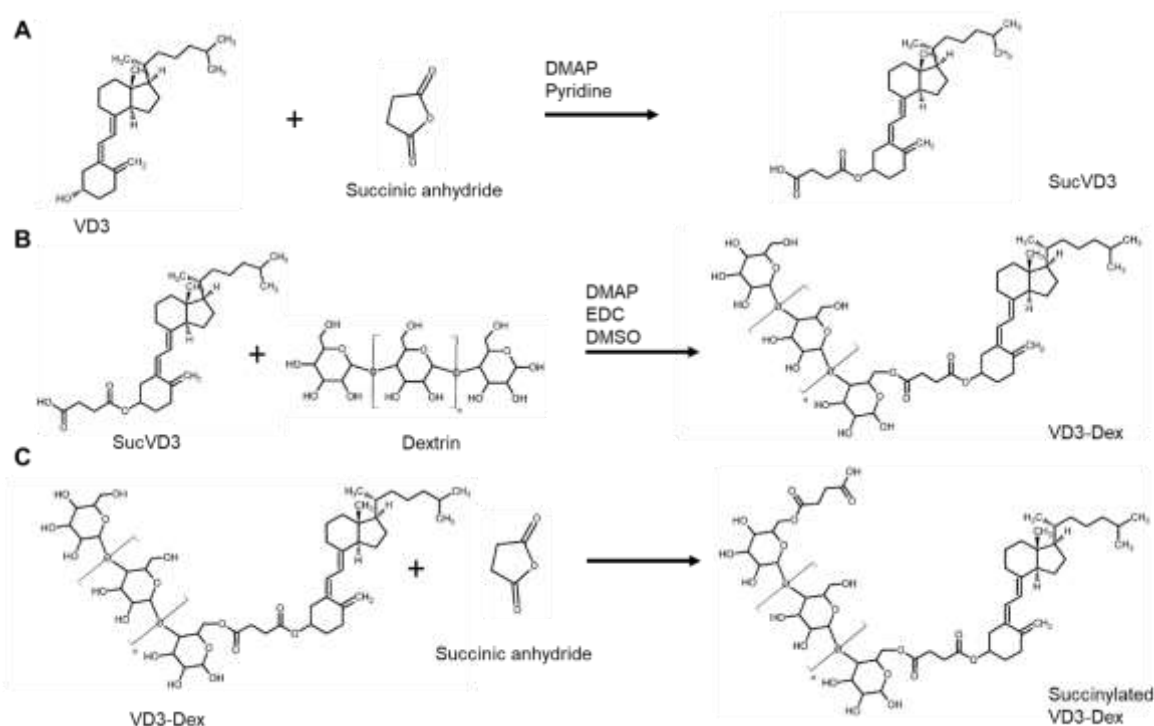


Figure 4.1 – Synthesis of vitamin D3-Dextrin (VD3-Dex) conjugates. **(A)** Vitamin D3 (VD3) was succinylated (SucVD3) by reaction with succinic anhydride in pyridine solvent using a catalytic amount of dimethylaminopyridine (DMAP) as nucleophilic catalyst. **(B)** VD3-Dex was prepared by a two-step procedure: first, SucVD3 was conjugated to dextrin polymer via ester bonding under carbodiimide (EDC) activation in the presence of DMAP catalyst, in dimethyl sulfoxide (DMSO) as solvent; next **(C)** the SucVD3-dextrin conjugate was allowed to react *in situ* with succinic anhydride under DMAP catalysis; the final conjugate was purified by dialysis against water and freeze-dried, then unreacted SucVD3 was eliminated by ethanol extraction.

4.2.3 Peptide Loading

Micelles were prepared by dissolving VD3-Dex (1 mg/mL) in phosphate-buffered saline (PBS) buffer (pH = 7.4). For the preparation of loaded micelles, LL18 was previously dissolved in PBS buffer before dissolving micelles, then left stirring for 15 minutes. LL18 loading was quantified without requiring previous separation of unloaded peptide, using the fluorescamine method. Briefly, LL18 standard solutions with concentrations ranging between 5 µg/mL to 100 µg/mL were prepared in PBS. Afterwards, 200 µL of these standards, empty and loaded micelles, were mixed with 50 µL of fluorescamine solution (at 0.3 mg/mL in acetone) in microplate wells and left to incubate for 15 minutes in the dark. The fluorescence was measured (λ_{ex} 385/ λ_{em} 480), with 20 nm bandwidth and 5 s shake, in a Cytation™ 3 (BioTek Instruments, Inc., Vermont, USA). Loaded (associated with the micelles) LL18 is not detected, whereas free LL18 can interact with fluorescamine, emitting a fluorescent signal. The peptide association efficiency (AE) % and drug loading (DL) % were deduced from the standard curve, and calculated using the **Equation 1** and **Equation 2** below:

$$AE (\%) = \frac{\text{Total LL18} - \text{free LL18}}{\text{Total LL18}} \times 100 \quad (1)$$

$$DL (\%) = \frac{\text{Total LL18} - \text{free LL18}}{\text{Total LL18} + \text{Total conjugate}} \times 100 \quad (2)$$

For the sterility-requiring experiments, empty micelles were sterilized as described above (section 4.2.2.2), dissolved in a filtered LL18 PBS (0.1×) solution, freeze-dried, and finally dissolved in the desired medium.

4.2.4 Characterization of Conjugates and Micelles

4.2.4.1 Infrared Spectroscopy

Attenuated total reflectance Fourier transform infrared spectroscopy (ATR-FTIR) in the absorbance mode (ABB Bomem FLTA2000-160 spectrophotometer, Québec, Canada) was used to confirm VD3 succinylation and subsequent conjugation to dextrin. The infrared spectra were collected at 4 cm⁻¹

resolution in the frequency range between 500 cm^{-1} and 4000 cm^{-1} , each spectrum accumulating 64 scans.

4.2.4.2 Thermogravimetric Analysis

Thermal decomposition behaviors were investigated through thermogravimetric analysis (TGA) using a PerkinElmer TGA 4000 system (Massachusetts, USA). 20 to 15 mg of each sample was weighted in ceramic pan and heated at heating rate of 5 $^{\circ}\text{C}/\text{min}$ from 30 $^{\circ}\text{C}$ to 700 $^{\circ}\text{C}$ under nitrogen gas.

4.2.4.3 Differential Scanning Calorimetry

Differential scanning calorimetry (DSC) thermograms were obtained by using PerkinElmer DSC 600 (Massachusetts, USA). The measurements were carried out with samples hermetically sealed in aluminum pans. Under a nitrogen atmosphere, samples were first cooled from 25 $^{\circ}\text{C}$ to 10 $^{\circ}\text{C}$ at 5 $^{\circ}\text{C}/\text{min}$ and equilibrated for 5 min. Samples were then heated from 10 to 250 $^{\circ}\text{C}$ at a heating rate of 5 $^{\circ}\text{C}/\text{min}$.

4.2.4.4 Critical Micellar Concentration

The critical micellar concentration (CMC) of VD3-Dex micelles was determined by fluorescence spectroscopy using pyrene as the hydrophobic probe by an adapted version of a previously described procedure⁴⁶. Briefly, about 20 μL of a stock solution of pyrene (0.1 mM) in acetone was transferred into different glass vials and the solvent was removed with a nitrogen stream. Varying volumes of VD3-Dex micelle solution in PBS buffer were added to each vial and the final volume was adjusted with same solvent, obtaining a series of solutions with constant pyrene concentration (1×10^{-6} M) and varying amounts of VD3-Dex ranging from 0.001 to 0.75 mg/mL. The solutions were allowed to equilibrate for 24 h at room temperature under agitation, after which the emission spectra were recorded from 350 to 450 nm wavelength at an excitation wavelength of 338 nm, using a fluorescence spectrophotometer (HORIBA Aqualog 800 spectrofluorometer, Kyoto, Japan). The ratio of the emission intensities at 372 and 391 nm (I_{391}/I_{372}) was plotted against SucVD3 concentrations (Log C), and CMC was obtained from an inflection point in the plot.

4.2.4.5 Size and Zeta Potential

The mean particle size of the micelles was measured by Dynamic Light Scattering (DLS) using a Zetasizer NanoZS, (Malvern Instruments Ltd., Worcestershire, UK). Micelles were prepared in PBS buffer (0.1× concentration) and 3 sets of at least 10 measurements each were performed at a 90-degree scattering angle to get the average particle size. The zeta potential of micelles was also analyzed.

4.2.4.6 Morphology

Morphology of the micelles was observed by scanning electron cryo-microscopy (Cryo-SEM). Micelles were dispersed in PBS at a concentration of 1 mg/mL and rapidly cooled plunging it into sub-cooled nitrogen. The sample was transferred under vacuum to the cryo stage (Gatan, Alto 2500, UK) and then fractured and sublimated for 120 seconds at -90 °C to remove the superficial ice layer and allow the exposure of the micelles. Then, the samples were sputter-coated with gold and palladium for 45 seconds and transferred to the observation chamber of an electron microscope (SEM/EDS: JEOL JSM 6301F/Oxford Inca Energy 350 from the Laboratory for Scanning Electron Microscopy and X-ray Microanalysis at Materials Centre of the University of Porto. The observation was operated at -150 °C and 15 kV.

4.2.5 Biocompatibility

4.2.5.1 Cell Culture Conditions

Mouse calvaria-derived pre-osteoblast MC3T3-E1 was acquired from RIKEN BioResource Center Cell Bank (RIKEN BRC, Tsukuba, Ibaraki, Japan) and maintained in DMEM with 1.0 g/L glucose supplemented with 10 % (v/v) heat-inactivated FBS and 1 % (v/v) Penicillin (10,000 U/mL)-Streptomycin (10,000 µg/mL) at 37 °C and 5 % CO₂, all obtained from Merck Millipore (Massachusetts, USA). Supplemented medium was termed as complete-DMEM. Cells were detached using a 0.02 % EDTA-0.05 % trypsin solution and sub-cultured when they were 70 % confluent.

Bone marrow-derived macrophages (BMMΦ) were differentiated as previously described⁴⁷. C57BL/6 mice of 6 to 8 weeks of age were anesthetized using a CO₂ chamber and euthanized by cervical dislocation. Under aseptic conditions, skin was peeled off from the top of hind legs, then tibiae and femurs were removed and cleaned. Bones were disjointed, extremities were cut off, a needle was inserted, and then bone was flushed using complete-DMEM medium. Cell suspension was then centrifuged (300 × g, 10 min.) and the pellet re-suspended in 15 mL of complete-DMEM further supplemented with 20 % (v/v) L929-cell conditioned medium – termed macrophage-medium – as source of macrophage colony-

stimulating factor. Cell suspension was cultured overnight in an incubator at 37 °C and 5% CO₂ atmosphere, after which the non-adherent cells (undifferentiated macrophage) were harvested with macrophage-medium, plated at a confluent monolayer-seeding density and incubated again as mentioned. Medium was replaced every 3 days until full differentiation into macrophage at day 10. All the following experiments with BMM Φ were performed at day 10. Mice were provided from the Animal Facility of the Life and Health Sciences Research Institute, ICVS (Braga, Portugal). Animals were handled in strict accordance with good animal practice as defined by national authorities (DGV, Law nu1005/92 October 23) and European legislation (EEC/86/609).

4.2.5.2 Cell Viability Assay

Cytotoxicity evaluation was performed in MC3T3-E1 and BMM Φ cells by MTT assay, according to ISO 10993-5-2009 (Biological evaluation of medical devices - Part 5: Tests for *in vitro* cytotoxicity). Briefly, 100 μ L of cell suspension, at 1×10^5 cells/mL for MC3T3-E1 and 2×10^5 cells/well for BMM Φ , were seeded in 96-well plates at 37 °C and 5 % CO₂. After 24 h, culture medium was replaced by 100 μ L of testing samples (free VD3 was dissolved in DMSO and diluted in the medium). After another 24 h, medium was discarded and 50 μ L of MTT solution (1.0 mg mL^{-1}) were added and incubated at 37 °C for 2 h. MTT medium was discarded and 100 μ L of DMSO was added. The optical density value was measured by a microplate reader Cytation™ 3 (BioTek Instruments, Inc., Vermont, USA) at 570 nm (reference wavelength 650 nm). Cell viability was calculated and expressed as the mean percentage \pm standard deviation (SD) of viable cells relative to the negative control – the untreated cells (considered as 100 % viability). The concentration of a drug that kills half the cells, the 50 % cytotoxic concentration (CC₅₀), was calculated by nonlinear regression analysis using GraphPad Prism software. Cells without treatment were used as negative control, wells with medium without cells were used as blanks, and cells treated with DMSO (20% v/v) were used as positive control. In all *in vitro* cellular tests, micelles were previously sterilized by filtration using 0.22 μ m PES filter in a flow chamber, freeze-dried in sterile and gauze-covered glass tubes, and weighed under aseptic conditions before use. Peptide-loaded micelles were also prepared aseptically at a known concentration, using those previously sterilized micelles dissolved in a filtered LL18 PBS solution, then freeze-dried.

4.2.5.3 Hemolysis Assay

Blood was obtained from a healthy dog after owners' agreement and collected to an EDTA tube. Whole blood was centrifuged (10 min. at $1200 \times g$, $4 \text{ }^\circ\text{C}$) and the supernatant and buffy coat were discarded. Red blood cells (RBCs) were resuspended in isotonic PBS pH = 7.4. The purified RBCs were counted using a Neubauer chamber and diluted to a concentration of 1×10^8 cells/mL. Afterwards, $450 \text{ }\mu\text{L}$ of RBCs were placed in a 48-well plate containing $50 \text{ }\mu\text{L}$ of test samples dissolved in PBS buffer, $10\times$ concentrated compared to the final desired concentrations. Plates were incubated for 5 h at $37 \text{ }^\circ\text{C}$ under agitation (150 rpm) after which solutions were collected to micro tubes and centrifuged (10 min at $1200 \times g$, $4 \text{ }^\circ\text{C}$). The supernatants were collected for analysis of the extent of hemolysis by measuring the absorption of hemoglobin at 540 nm. Results were expressed as a percentage of hemolysis with respect to the amount of hemoglobin released in the presence of 1 % of triton X-100, which was taken as measure of complete (100 %) lysis, using the **Equation 3**:

$$\text{Hemolysis (\%)} = \frac{\text{AbsS} - \text{AbsNC}}{\text{AbsLys} - \text{AbsNC}} \times 100 \quad (3)$$

where AbsS is the absorbance of the sample, AbsNC is the average absorbance of the negative control (PBS buffer), and AbsLys is the average absorbance of the triton X-100 lysed samples.

4.2.6 Cell Internalization

4.2.6.1 Fluorescently labeled Conjugates

Micelles were fluorescently labeled by conjugation with FITC to achieve a bio-imaging material. The reactive group of FITC can covalently attach to the hydroxyl groups of dextrin. Briefly, different ratios of FITC:VD3-Dex (mg:mg) micelles were co-dissolved in anhydrous DMSO and left overnight in agitation under a nitrogen atmosphere at room temperature, protected from light. To remove DMSO, the mixture was dialyzed against 2 L of dH_2O using a 1000 Da pore size membrane, with water being replaced every 2 h up to a total of 8 water changes. The solution was freeze-dried and then unbound FITC was separated by ethanol extraction: the material was vigorously vortexed in ethanol and after 5 minutes. centrifugation at $7000 \text{ }g$, unbound FITC in the supernatant was separated from the pellet containing insoluble FITC-VD3-Dex micelles. After five cycles, ethanol remains were evaporated from the pellet under a nitrogen

stream. The clearance of unbound FITC from the supernatant in the successive wash cycles was monitored by fluorescence spectroscopy at $\lambda_{ex}477/\lambda_{em}517$ (HORIBA Aqualog 800 spectrofluorimeter, Kyoto, Japan). Conjugated FITC content was inferred from plotted fluorescent intensities against free FITC concentrations ranging from 0.03 to 0.47 $\mu\text{g}/\text{mL}$. Concentrated stock solutions of pure FITC and FITC-micelles were prepared in DMSO and then diluted in PBS solution up to a fluorescent signal that could fit within the calibration curve range.

4.2.6.2 Subcellular Localization and Cell Uptake

Cells were seeded in 24-well plates on spherical coverslips. MC3T3-E1 cells ($2.5 \times 10^5/\text{mL}$) were cultured for 48 h in complete-DMEM, whereas BMM Φ ($1.5 \times 10^6/\text{mL}$) were cultured in macrophage-medium for 10 days, changing medium every 3 days. Then, test samples were incubated for 1 h or 24 h. Wells were washed with PBS, fresh medium was added and incubated with nuclei stainer Hoechst 33342 (blue; 1 % v/v) and lysosome stainer Biotracker red 540 (red; 3 % v/v) for 15 minutes, for FITC-micelle tracking. Hoechst 33342 and LysoSensorGreen DND-189 (green; 1 % v/v) were used for LL18-TAMRA tracking. Micelles were incubated at 0.5 mg/mL and LL18-loaded micelles prepared at a 25 μg :1 mg peptide:micelle ratio. Cells were analyzed by confocal laser scanning microscope, CLSM (BX61, Model FluoView 1000, Olympus, Tokyo, Japan). The image analysis was performed using the FV10-Ver 4.1.1.5 (Olympus), at 60x and 100x magnifications. Considering stainers were suitable for live cells, analysis was performed immediately upon cell staining, without any fixation steps.

Cell uptake studies were performed in a fluorescence microscope Olympus BX51, 20x magnification. Concentration-dependent uptake was studied at 0.1, 0.5 and 1 mg/mL of FITC-micelles and LL18-loaded FITC-micelles, (100 μg :1 mg peptide:micelle ratio) after 1 h incubation (n=3). Uptake was quantified using Image J: pixel density (integrated optical density) of each image was normalized to the number of nuclei in the same image (Hoechst 33342).

4.2.7 Functionality

4.2.7.1 Bacterial Susceptibility Test

The antibacterial activity was determined according to ISO 20776-1.44. *Staphylococcus aureus* (*S. aureus*) ATCC 25923, was thawed and grown in agar BHI medium overnight at 37 °C. A small inoculum was collected and left growing for 3 h in fresh BHI broth medium, then few μL were transferred to fresh medium again and left growing until reaching the exponential phase. A volume of 50 μl of inoculum

intended for a final concentration of 5×10^5 colony forming units/ml was added to 96 plate wells, and incubated with 50 μ l of test solutions. After overnight incubation (24 h) at 37 °C, the bacterial growth was evaluated by measuring the optical density at 620 nm in a microplate reader Cytation™ 3 (BioTek Instruments, Inc., Vermont, USA). Minimal inhibitory concentration (MIC) was calculated as the minimal concentration required to inhibit bacterial growth by 100 %.

4.2.7.2 Inhibition of Albumin Denaturation

The anti-inflammatory potential of micelles was analyzed through heat-induced albumin denaturation assay. Micelles ranging from 0.5 to 10 mg/mL were dissolved in PBS solution containing 1 % human serum albumin. Equivalent amounts of dextrin, LL18-loaded micelles (100 μ g:1 mg, peptide:micelle ratio) and LL18 were prepared, accordingly. All samples were adjusted to pH = 7.4 and 1 % albumin in PBS was used as untreated condition. Replicates were prepared in PBS solution without albumin to subtract any possible background. Samples were transferred to 96 well plates, sealed and protected from the dark, incubated at 37 °C for 15 minutes and then heated in a water bath at 70 °C for 3h. After cooling at room temperature, the turbidity was measured spectrophotometrically at 660 nm.

4.2.7.3 Migration Assay

The effect of micelles and LL18 on migration of MC3T3-E1 cells was analyzed by the scratch assay. Cells were seeded at a density of 7×10^4 cell/mL into a 24-well plate containing complete-DMEM culture medium and incubated overnight at 37 °C, in a humidified 5 % CO₂ atmosphere until 95 % confluency. The adherent cell layer was scratched with a sterile yellow pipette tip and cellular debris was washed with PBS. The cells were treated with empty and LL18-loaded micelles, free LL18 and dextrin. Mitomycin C at 0.05 μ g/mL, a proliferation inhibitor, was added to all treatment conditions and to untreated condition (control) as well, so that results strictly reflect cells migration capacity. MTT assay was performed and a concentration of 0.05 μ g/mL was shown to inhibit cell proliferation whilst maintaining viability, as also reported elsewhere⁴⁸. The cells were incubated at 37 °C in humidified 5 % CO₂ atmosphere and at defined time-points of samples incubation of 0 h (immediately after scratching cells) and 24 h, multiple images of the scratch areas were recorded using a manual inverted microscope Leica DMI3000 B (20x magnification). Images were processed using ImageJ. The width of the scratch was determined to calculate the open wound area within cells by the following **Equation 4**:

$$\text{Open wound area (\%)} = \frac{\text{wound area at 24 h}}{\text{wound area 0 h}} \times 100 \quad (4)$$

4.2.8 Statistical Analysis

Statistical analysis was performed by one-way analysis of variance (ANOVA) and Tukey's post-hoc correction, excepting for AE and cell uptake quantification, in which a paired Student's t-test was used (GraphPad Prism® 8.02 software, La Jolla, CA). A **p* value < 0.05 was considered to be statistically significant. Results are presented as mean ± SD.

4.3 Results and Discussion

4.3.1 Characterization of Vitamin D3-Dextrin Conjugates

The synthesis of SucVD3 and VD3-Dex is shown in **Figure 4.1**. The addition of a reactive carboxylic acid group to VD3 by esterification with succinic anhydride, enabled its subsequent conjugation via ester linkage to the hydroxyl groups of dextrin, by carbodiimide chemistry. This two-step reaction was confirmed by ATR-FTIR (**Figure 4.2A**). According to previous reports⁴⁹, VD3 displayed the hydroxyl group O–H bond stretching at 3290 cm⁻¹ and alkyl C–H stretches at 2930 cm⁻¹ and 2860 cm⁻¹. Succinylation of VD3 resulted in the appearance of two peaks at 1731 cm⁻¹ and 1713 cm⁻¹, attributed to stretching vibrations of carbonyl groups of ester and carboxylic acid groups, respectively. This is an unambiguous confirmation of esterification of the hydroxyl group of vitamin D3 with a succinic acid moiety, as reported by other authors for the functionalization of VD3 using succinic⁵⁰, or glutaric acid⁴⁶. These two peaks were replaced by a single peak at 1725 cm⁻¹, assigned to the ester bonds, in the VD3-Dex conjugates. The disappearance of the carboxylic acid vibration at 1731 cm⁻¹, together with an intensity reduction of the characteristic peak of native dextrin⁴⁷ at 3389 cm⁻¹, assigned to sugar hydroxyl –OH stretching vibrations, confirms their involvement in the formation of the ester bond between the VD3-appended succinic acid carboxylic acid group and the sugar hydroxyl groups, as reported for similar systems where VD3 is appended to polymers^{46,50,51}.

DSC and TGA are two widely used thermal analysis techniques in the characterization of crystalline and amorphous drugs physically or chemically entrapped within nano-sized materials. These techniques allow to establish a connection between temperature variations and specific physical properties of substances. Crystallization affects properties such as solubility, stability, and pharmacokinetics. DSC measures the

quantity of excessively radiated or adsorbed heat by a sample, in response to changes in temperature. Dextrin curves displayed broad endotherm glass transition at the vicinity of 75 °C and 215 °C with maximum peak at 163 °C, and a narrower endotherm melting transition starting at 220 °C, with a maximum peak at 237 °C (**Figure 4.2B**). Although displaying a similar pattern, both glass and melting transitions were shifted to lower temperatures in VD3-Dex conjugates, exhibiting maximum peaks at 126 °C (glass transition) and 198 °C (melting transition), suggesting higher amorphous regions. After VD3-Dex conjugation reaction, carboxyl groups were introduced in micelles by succinylation. Consistently with other reports^{52,53}, the thermogram of pure VD3 exhibits a sharp endothermic peak at 84 °C, assigned to the melting point of VD3 crystal, therefore indicating the crystalline nature of the compound (**Figure 4.2B**). The absence of a comparable peak in VD3-Dex indicates that the VD3 moieties are in an amorphous state inside the polymer complex. From a therapeutical point-of-view, the amorphous state provides higher solubility and, subsequently, higher bioavailability.

TGA moisture loss and decomposition on the basis of mass change analysis, provides information related to the thermal stability of compounds. Dextrin mass loss, about 11 % weight from 30 °C to 100 °C, corresponds to the loss of adsorbed water (**Figure 4.2C**). In a second stage of weigh decrease, a 50 % rapid loss of mass from 250 °C to 303 °C, corresponds to the cleavage of glycosidic bonds and thermal decomposition of the sugar polymer⁵⁴. Dextrin remains are then gradually decomposed up to 12 % weigh at 650 °C. Thermal degradation of VD3 occurs around 200 °C, following an abrupt decay up to 0 % weight from 300 °C to 400 °C, as previously reported⁵². Water loss was not observed for VD3, presumably owing to its high hydrophobicity. When dextrin is conjugated to VD3, the complex exhibits a pattern similar to dextrin, except for four major differences: i) initial water loss is less pronounced, representing only about 4 % of weigh from 30 °C to 75 °C, consistent with a more hydrophobic material; ii) breakdown of bonds starts at lower temperatures around 170 °C; iii) decomposition occurs at a slower rate up to 50 % weight loss, and iv) the temperature at which dextrin and micelles reach 50 % mass loss, 313 °C, is slightly higher than that of dextrin, 300 °C. From this point on, the decomposition pattern up to at 650 °C is fairly the same, ending with 14 % weight compared to 12 % in dextrin. The lower decomposition temperature of VD3-Dex, can be assigned to the onset of the decomposition of the ester groups. The functionalization of dextrin with SucVD3 and its further succinylation reduced the thermodynamic stability of the conjugate compared to dextrin. The decoration with the SucVD3 moiety alters both the hydrophobicity as well as the hydrogen bonding pattern of the dextrin polymer as reported for other ester-functionalized starches⁵⁵ and after incorporation of curcumin (hydrophobic) in octenyl

succinic anhydride–short glucan chains-based nanoparticles⁵⁶. The decomposition pattern, however, occurs over a wider temperature range, meeting dextrin's at 65 % weight (280 °C).

The conjugate is able to self-assemble in water into a micelle-like structure consisting of a hydrophobic interior core provided by VD3, and an outer hydrophilic region provided by dextrin and the pendant succinic acid moieties. Hydrophobic pyrene has low solubility in water, with negligible fluorescence intensity. In the presence of micelles, pyrene solubilizes into their hydrophobic core, substantially increasing its fluorescence emission (**Figure 4.2D**). A sharp inflection point, identified as the CMC, can be observed in the signal (ratio between peaks I_{391}/I_{372}), below which pyrene is not able to solubilize due to micelle disassembly (**Figure 4.2E**). CMC is an important indicator of micelle stability upon blood dilution, expressing the minimum concentration of material at which the micelles remain self-assembled. A low CMC endows micelle carriers with higher stability during circulation, enhancing the delivery of drug cargoes to the target site. VD3-dex micelles exhibited a CMC value (0.08 mg/ml) comparable to that reported for other VD3-polyethylene glycol (PEG) conjugate-based micelles, 0.08 mg/mL⁵⁰ and 0.089 mg/mL⁴⁶. Given that this construct is intended for intralesional rather than systemic administration, disassembly of micelles due to dilution is less probable.

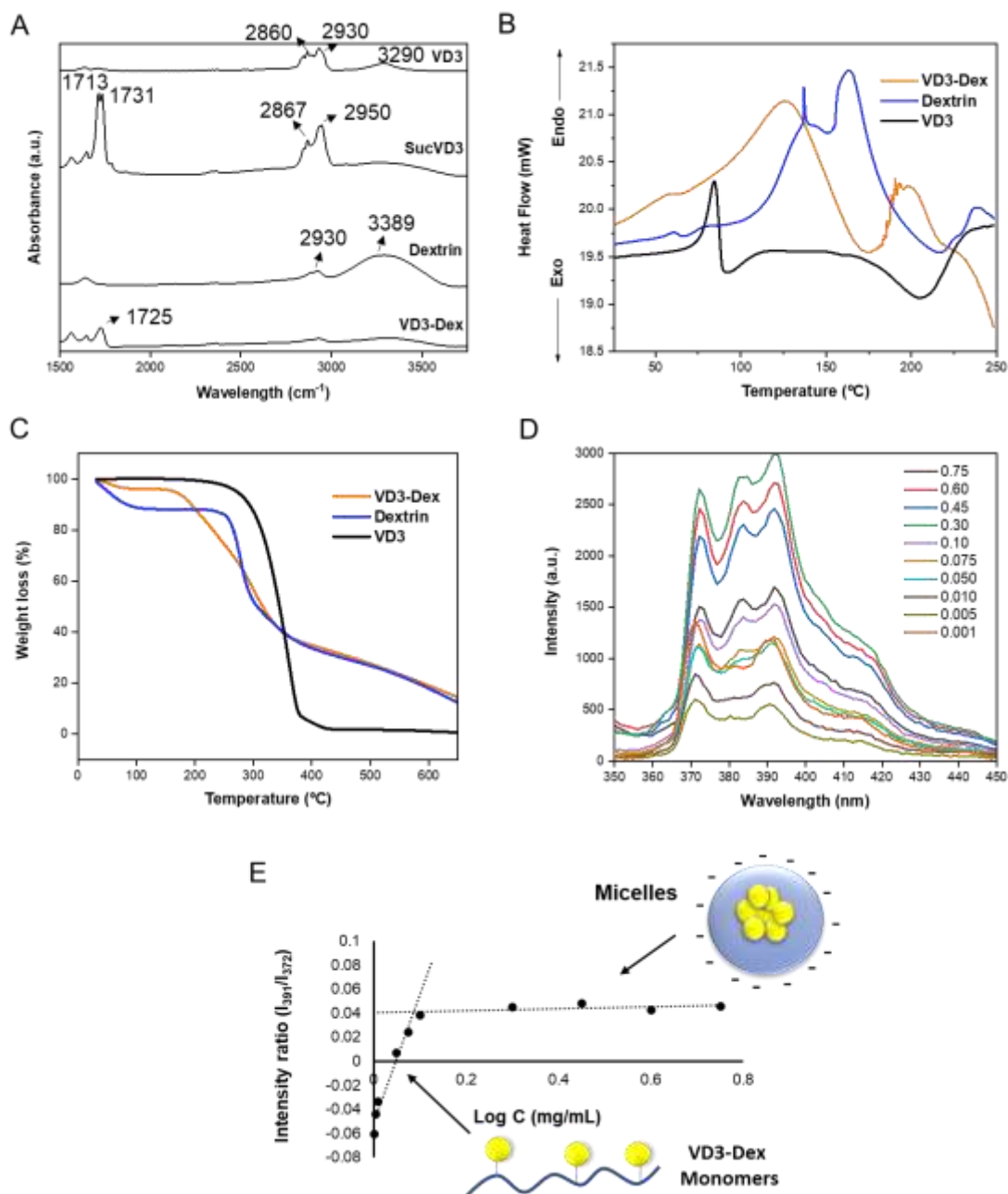


Figure 4.2 – **(A)** ATR-Fourier-transform infrared spectroscopy (ATR-FTIR) studies; **(B)** Differential scanning calorimetry (DSC) thermograms; **(C)** thermogravimetric analysis (TGA) curves; **(D)** excitation spectra of pyrene as a function of VD3-Dex concentration and **(E)** plot of intensity peak ratios (I_{391}/I_{372}) versus log C, to determine critical micellar concentration (CMC). VD3, Vitamin D3; SucVD3, succinylated vitamin D3, VD3-Dex, vitamin D3-dextrin conjugate.

4.3.2 LL18 Association Efficiency

LL18-loaded micelles were efficiently produced by direct co-dissolution. To have an insight into the mechanism of peptide association with micelles, two preparations with different molar ratios VD3:dextrin, 1:4 and 1:8, and a non-succinylated VD3-dex 1:4, were compared in terms of AE (**Figure 4.3**). Micelle concentration was kept constant at 1 mg/mL and the peptide mass varied from 25 to 150 µg/mL, in PBS. Excepting for the non-succinylated VD3-Dex (1:4) micelles, AE (%) decreased as a function of the initial peptide increase, as could be expected. The highest AE (%) of the succinylated VD3-Dex (1:4) micelles comparing to the non-succinylated micelles indicates that the binding behavior is, at least in part, strongly dependent on succinylation (i.e. introduction of -COOH groups), confirming that peptide adsorption is strongly driven by electrostatic interactions. The carboxylic acid group is a weak acid with a typical pKa $\sim 4.5 - 5.0$, thus in PBS (pH 7.4) this group is ionized (RCOO⁻) and available to associate with the positively charged LL18 peptide. LL18, displays an isoelectric point of 12.3 and a net charge of +8 at pH 7. Peptide disassociation at low pH values (protonated RCOOH) may occur in infected milieu, typically acidic in nature. Interestingly, hydrophobic interactions also seem to play an important role in peptide adsorption, which may be explained considering the mostly non-polar character of VD3 and that 44 % of LL18 amino acids are hydrophobic. In fact, VD3-Dex (1:8) displayed a drastically lower AE (%) compared to VD3-Dex (1:4) despite being succinylated. Moreover, non-succinylated micelles at 1:4 (mol) of VD3:dextrin were capable of loading significantly more LL18 than the succinylated micelles with less VD3 (1:8), at least for the highest peptide concentrations.

VD3-Dex at 1:4 molar ratio was selected for the follow up work, being hereafter referred as VD3-Dex. Freeze-dry is an expedite process for the development of nano-entrapped drugs at the pilot scale. **Figure 4.3** shows that AE (%) is not compromised by freeze-drying, even presenting a smooth increase for formulations bearing the highest peptide concentrations.

Succinylated VD3-Dex 1:4 micelles allowed the best DL (10.77 ± 0.05), whereas non-succinylated reached 5.37 ± 0.38 , for the highest initial peptide tested of 150 µg/mL (**Table 4.1**). Micelles with the lowest VD3 content reached its best DL of 0.95 ± 0.09 with 25 µg of initial peptide.

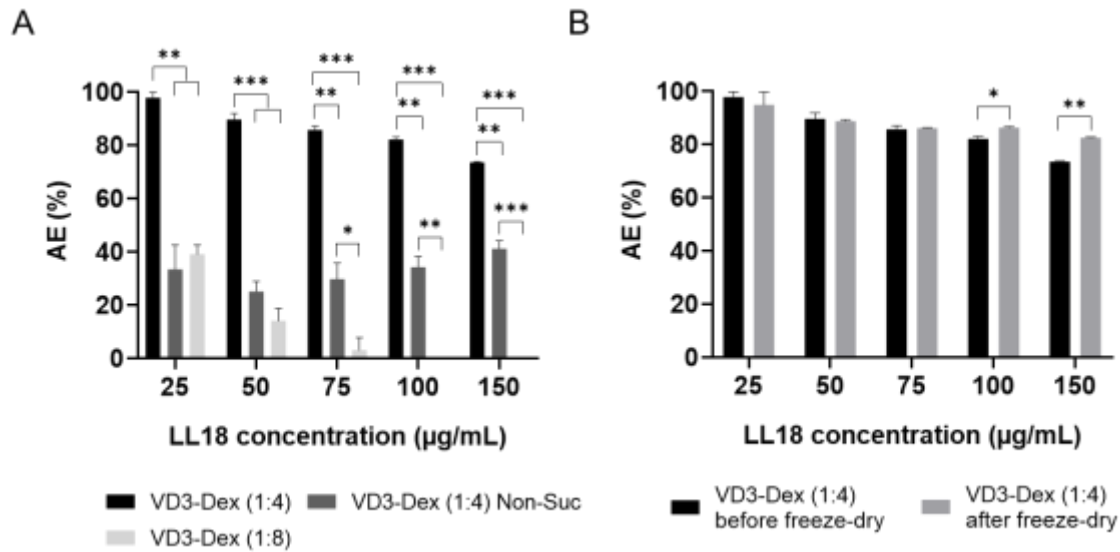


Figure 4.3 – Influence of negative surface charge, VD3:dextrin preparation ratio, and freeze-drying process in the association efficiency (AE) of LL18 with micelles: **(A)** 1:4 vs 1:8 molar ratio of succinylated VD3-Dex vs 1:4 non-succinylated micelles, and **(B)**: before and after freeze-dry for 1:4 ratio succinylated VD3-Dex micelles. Micelles were prepared at 1 mg/mL in LL18-dissolved PBS solution. Results presented as mean \pm SD, $n=3$, ($*p < 0.05$, $**p < 0.01$, $***p < 0.001$).

Table 4.1 – Drug loading (DL) efficiency % for different formulations with initial peptide concentration varying from 25 to 150 $\mu\text{g/mL}$.

LL18 concentration	25	50	75	100	150
VD3-Dex 1:4	2.39 ± 0.05	4.27 ± 0.11	5.98 ± 0.1	7.47 ± 0.08	9.58 ± 0.04
VD3-Dex 1:4 after freeze-dry	2.31 ± 0.12	4.23 ± 0.03	6.00 ± 0.02	7.84 ± 0.03	10.77 ± 0.05
VD3-Dex 1:4 Non-Suc	0.82 ± 0.22	1.19 ± 0.19	2.07 ± 0.42	3.11 ± 0.37	5.37 ± 0.38
VD3-Dex 1:8	0.95 ± 0.09	0.68 ± 0.22	0.21 ± 0.33	0	0

Non-Suc, non-succinylated.

4.3.3 Morphology and Stability

Succinylated VD3-Dex at 1:4 VD3:dextrin molar ratio, and a formulation consisting of 1 mg:100 µg (micelle:peptide) ratio, were selected to the follow up of this study. The analysis of the morphological properties of micelles was performed by Cryo-SEM (**Figure 4.4**).

Cryo-SEM images of freshly prepared micelles show that samples were generally homogeneous and spherical in shape, perfectly individualized with no signs of aggregation. Loading with LL18 does not significantly changes micelle structure or size. DLS measurements over 4 months suggest that empty micelles undergo a decrease in average size, from 162.4 ± 8.9 to 130 ± 1.9 nm, a slight increase in PDI, from 0.17 ± 0.02 to 0.22 ± 0.01 , though maintaining a similar ζ -potential around -30 mV, which is indicative of colloidal stability. Differently, LL18-loaded micelles experience an increase in average size, from 143.1 ± 4.6 to 181.1 ± 14.7 nm, an increase in PDI from 0.21 ± 0.01 to 0.39 ± 0.05 , and a drastic decrease (in modulus) of the ζ -potential.

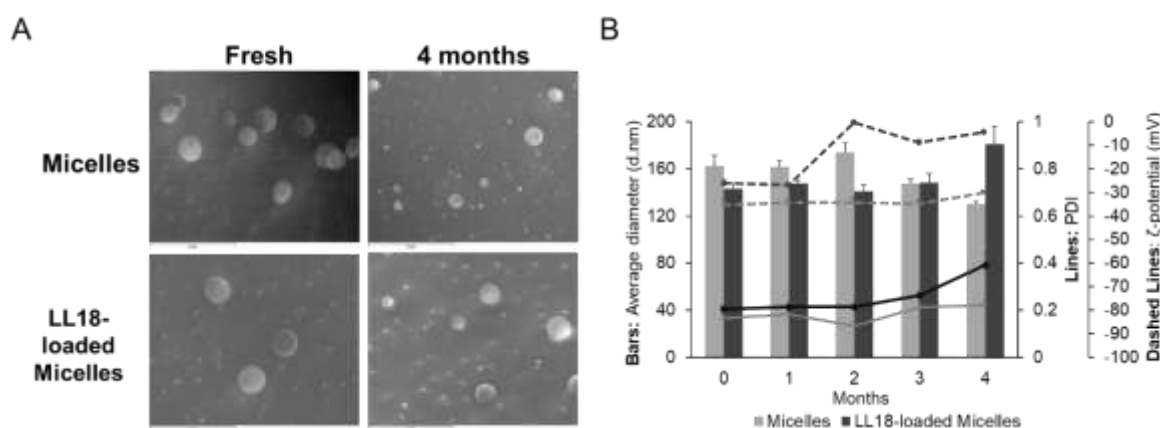


Figure 4.4 – (A) Representative Cryo-SEM microphotographs of unloaded and LL18-loaded VD3-Dex micelles before and after a four-month storage in phosphate-buffered saline solution at 4 °C (magnification of 50,000×, scale bars = 1 µm). (B) Stability studies: dynamic light scattering measurements performed each month, from day 0 to 4 months. Formulation of 100µg:1mg peptide:micelle ratio, dissolved at 1 mg/mL of micelle.

Accordingly, Cryo-SEM images show slightly more heterogeneous micelles in both cases, being apparently larger when LL18 is loaded. Despite, the significant reduction of ζ -potential observed for the LL18 loaded micelles over time, Cryo-SEM provided no evidence of major aggregation/instability.

4.3.4 Cytotoxicity and Hemolysis

Cytotoxicity was evaluated in bone-forming pre-osteoblasts and pathogen phagocytosis-specialized macrophages (**Figure 4.5**). With respect to osteoblasts (**Figure 4.5A**), the CC_{50} of free LL18, 103.5 $\mu\text{g}/\text{mL}$ (confidence interval, CI, 91.7 to 118.3), was increased when loaded into VD3-Dex micelles to 153.4 $\mu\text{g}/\text{mL}$ (CI 132.9 to 191.0), demonstrating the protecting effect of the carrier (**Figure 4.6A**). Macrophages (**Figure 4.5B**) exhibited a slightly higher sensitivity, although a similar shielding effect was observed, where the CC_{50} of free LL18, 91.4 $\mu\text{g}/\text{mL}$ (CI 83.8 to 100.0), was increased by micelles to 123.4 $\mu\text{g}/\text{mL}$ (CI 116.5 to 130.7) (**Figure 4.6B**). LL18-loaded micelles displayed a CC_{50} of 1.54 mg/mL (CI 1.33 to 1.91) in osteoblasts, and a lower 1.23 mg/mL (CI 1.17 to 1.31) in macrophages. This can be mostly attributed to the presence of the peptide, whose cytotoxicity has been previously observed against both cell lines^{27,57}. Human cathelicidin has been reported to accumulate in osteoblast-like MG63 cells mitochondria, triggering the release of the mitochondrial protein apoptosis-inducing factor to the cytosol, directly affecting mitochondrial membrane structural properties⁵⁸.

In osteoblasts, unloaded VD3-Dex micelles displayed a safe profile up to 2 mg/mL , reducing cell viability up to a minimum of $59.6 \pm 6.2\%$ at the higher tested concentration, being comparable to dextrin. In contrast, in macrophages, micelles were not only safe but even stimulated mitochondrial metabolism, reaching around 120% in most concentrations, even at the highest one tested. The same behavior was noted for LL18-loaded micelles, though only up to 0.75 mg/mL . This stimulatory effect, not shared by dextrin, was also observed for free VD3 exclusively in macrophages as well (**Figure 4.5C** and **Figure 4.5D**). Although VD3 concentration within micelles was not determined, this is a clear indication of its presence with intact biological activity. Increased mitochondrial metabolism upon treatment with the active VD3 metabolite, (1,25[OH]2D3), was recently described in more detail in human macrophages⁵⁹. Among other relevant features concerning the macrophage antimicrobial activity, it was found to induce expression of the vacuolar-type ATPase (V-ATPase) responsible for acidification of phagosomes – a pivotal event not only for bactericidal function but also for cytokine production. V-ATPase activity is energy consuming, requiring adenosine triphosphate (ATP), primarily produced by mitochondria. The induction of V-ATPase by active VD3 was also reported in osteoclasts⁶⁰. Taking into account the presence of VDR and activation machinery in macrophages, we assume the same mechanism could occur with VD3.

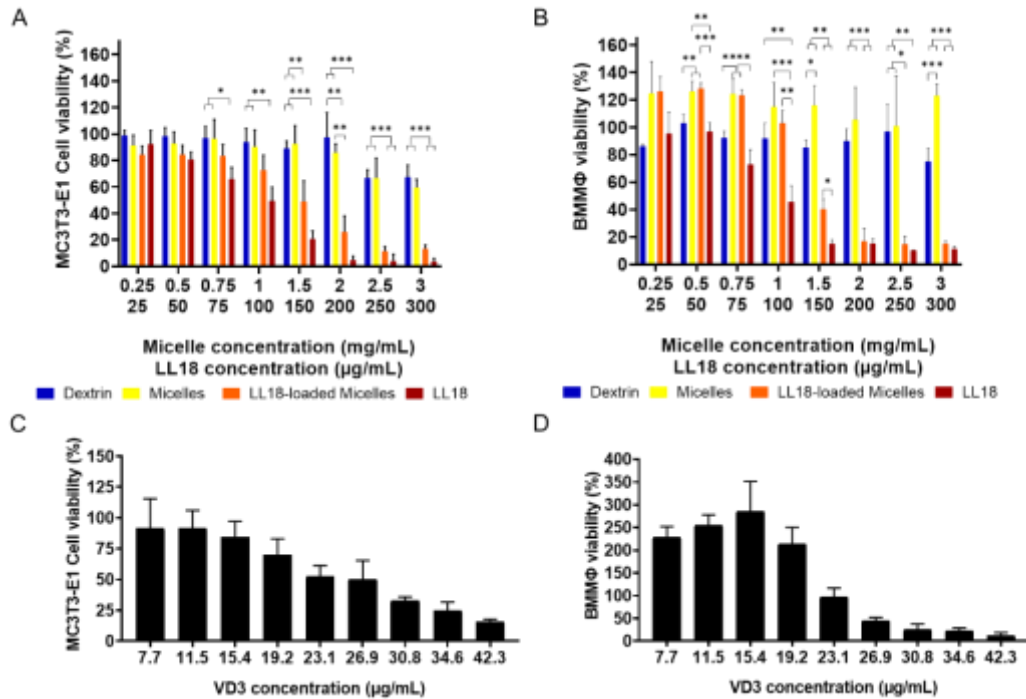


Figure 4.5 – Dose-dependent effect assessed by the MTT assay in **(A and C)** MC3T3-E1 and **(B and D)** BMMΦ. Cells were exposed to different concentrations for 24 h. Results calculated as percentage of the negative control and presented as mean ± SD, n = 3, (**p* < 0.05, ***p* < 0.01, ****p* < 0.001). Formulation of 100μg:1mg peptide:micelle ratio.

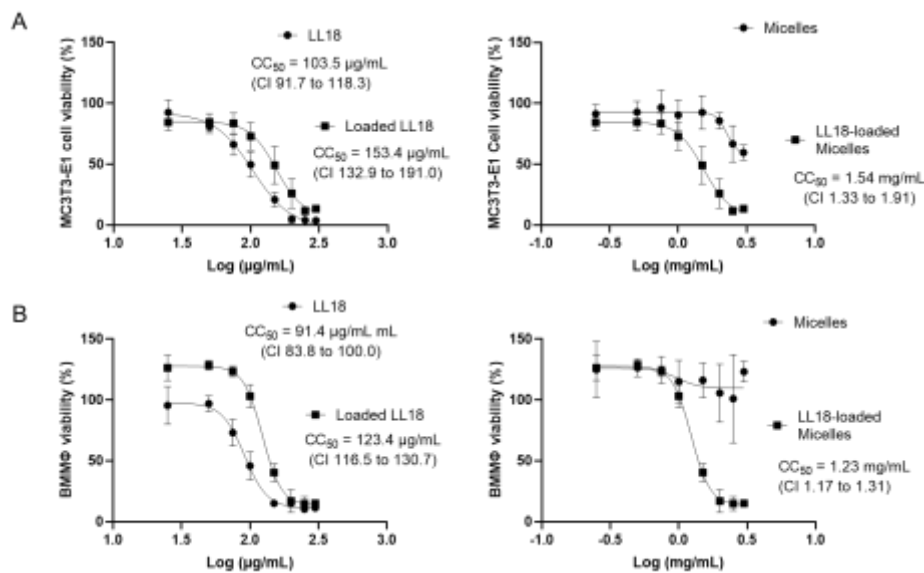


Figure 4.6 – Dose-response (cell viability) curves of cells exposed for 24 h to different concentrations of LLKKK18 (LL18) and loaded-LL18 (left), micelles and LL18-loaded micelles (right) in: **(A)** MC3T3-E1 and **(B)** BMMΦ. Results assessed by the cytotoxicity assay, for 50 % cytotoxic concentration (CC_{50}) calculation (n = 3).

The hemolytic activity of AMPs is a matter of concern for clinical translation. Despite potent antibacterial activity, the use of cathelicidin as antibacterial agent is limited by its hemolytic profile, encouraging the design of derivatives and carriers with reduced toxicity⁶¹. Given that bone is a highly vascularized tissue, cellular toxicity was assessed in dog RBCs (**Figure 4.7**). Materials used in the fabrication of medical devices are classified as hemolytic when the lysis of blood cells exceeds 5%⁶². We have previously shown LL18 induced hemolytic activity up to 8.6% at 200 µg/mL for a 1 h incubation, when incorporated into a HG²⁷. In this study, with an extended incubation period of 5h, LL18 in the concentration range 50 – 250 µg/mL displayed a dose-dependent hemolysis from 3.4 ± 0.2% to 25.1 ± 0.8%. This toxic effect was completely abrogated by VD3-Dex micelles, displaying no hemolytic activity up to 250 µg/mL of loaded LL18 and 2.5 mg/mL of micelles, behaving comparably to the unloaded carrier and to dextrin. The endocytic pathway is a common mechanism of micelle internalization. However, whether RBCs possess an endocytic mechanism is a matter of debate. Endocytosis of nanoparticles by RBCs has been shown to be inhibited by the spectrin-actin network coupled to their membrane bilayer⁶³. However, nanoparticles internalization into RBCs via endocytosis is also possible⁶⁴. Thus, although a diminished endocytic mechanism could explain the lack of toxicity, micelle internalization should not be excluded. Overall, the LL18-loaded micelles provide a wide safe range of LL18 concentrations for blood-contacting therapeutics.

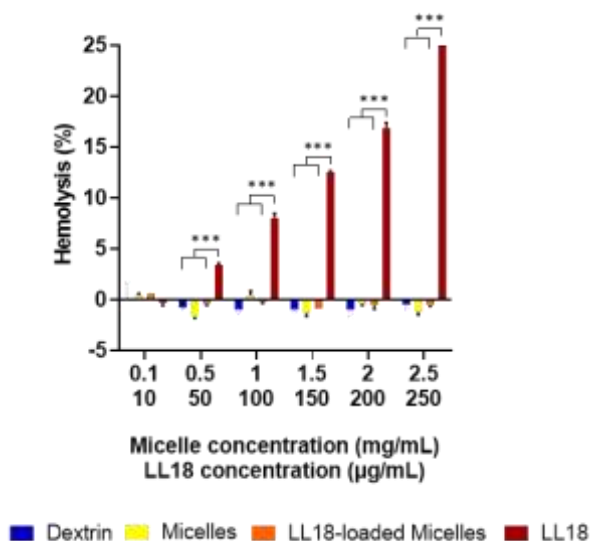


Figure 4.7 – Percentage of hemolysis upon 5h incubation. Data are expressed as percentage relative to the control and presented as mean ± SD, n = 3, (**p* < 0.05, ***p* < 0.01, ****p* < 0.001).

4.3.5 Fluorescently Labeled Micelles

The isothiocyanate group of FITC can react with the dextrin hydroxyls via stable thiocarbamoyl linkage. Different ratios of FITC:VD3-Dex were prepared. A FITC:VD3-Dex ratio (mg:mg) of 1:40, with physical-chemical properties similar to the non-labeled micelles, with an average size of 124.7 ± 2.7 nm, a PDI of 0.18 ± 0.03 and -19.7 ± 1.8 mV of surface charge, was selected to follow up studies (**Table 4.2**). This formulation was tested for LL18 AE (%) using 25 and 100 μ g peptide per mg of micelle, resulting in 100 % and 89.7 %, respectively. LL18 encapsulation resulted in higher size and PDI and lower surface charge. The size increase was corroborated by Cryo-SEM (**Figure 4.8**). The 1:40 FITC:VD3-Dex ratio formulation entrapping 25 μ g of LL18 per mg of micelle (100 % AE) was selected to the following cell tracking studies, whereas micelles entrapping 89.7 % of 100 μ g LL18 were selected for cell uptake studies.

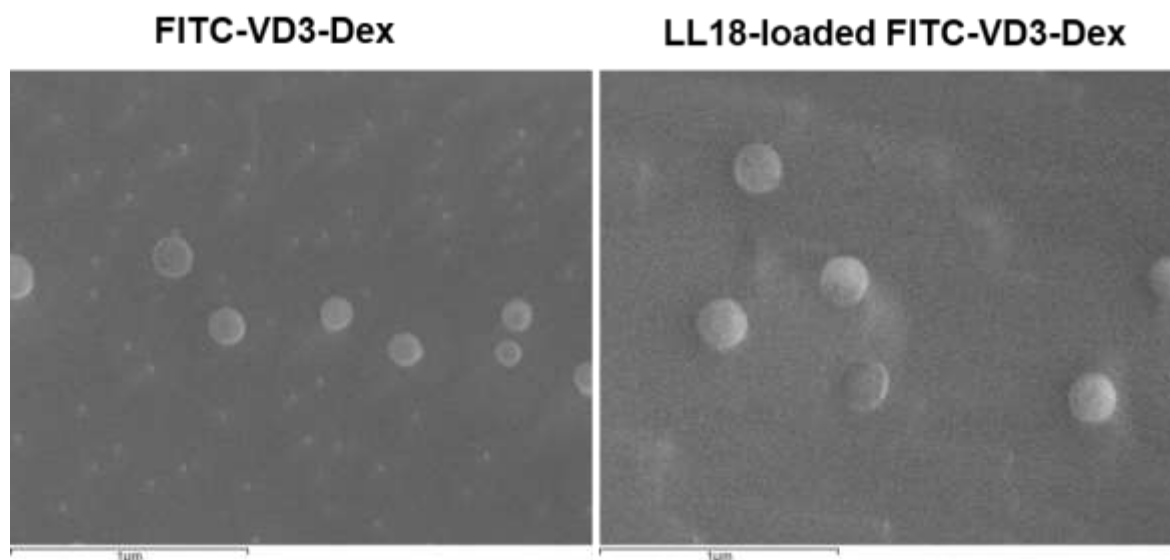


Figure 4.8 – Representative scanning electron cryo-microscopy microphotographs of **(A)** FITC-VD3-Dex (1:40 mass ratio) and **(B)** LL18 (100 μ g/mL)-loaded FITC-VD3-Dex, in phosphate-buffered saline solution at 1 mg/mL (magnification of 50,000 \times . Scale bars = 1 μ m).

Table 4.2 – Dynamic light scattering measurements of unlabeled and FITC-VD3-Dex micelles, dissolved in phosphate-buffered saline solution at a constant concentration of 1 mg/mL, and quantification of conjugated FITC by fluorescence spectroscopy (λ_{ex} 477/ λ_{em} 517). Results for LL18 or LL18-TAMRA-loaded micelles are also shown. Results are expressed as mean \pm SD (n=3).

FITC:VD3-Dex initial ratio (mg:mg)	Average size (nm)	PDI	ζ -potential (mV)	FITC (μ g)/mg of micelle	Initial LL18 (μ g/mL)	LL18 AE (%)
Unlabeled	162.4 \pm 8.9	0.17 \pm 0.02	-35.2 \pm 2.5			
1:40	124.7 \pm 2.7	0.18 \pm 0.03	-19.7 \pm 1.8	1.90 \pm 0.08		
Unlabeled	143.1 \pm 4.6	0.21 \pm 0.01	-26.1 \pm 1.5		100	86.3 \pm 0.4
1:40	147.8 \pm 8.7	0.22 \pm 0.01	-3.9 \pm 0.1		25	100.0 \pm 0.0
1:40	204.3 \pm 10.9	0.41 \pm 0.02	-8.9 \pm 0.3		100	89.7 \pm 0.1
Unlabeled	142.5 \pm 8.5	0.15 \pm 0.03	-25.8 \pm 2.1		25*	
1:40	96.8 \pm 4.2	0.12 \pm 0.01	-14.8 \pm 0.1		25*	

LL18, LLKKK18; FITC, fluorescein isothiocyanate; PDI, polydispersity index; AE, association efficiency.

*LL18-TAMRA (based on LL18 AE % results, loading of LL18-TAMRA is assumed as 90 to 100 %).

4.3.6 Subcellular Localization and Cell Uptake

Fluorescently labelled VD3-Dex micelles were used for cell uptake and subcellular localization studies. In addition to unmodified LL18, a TAMRA-conjugated LL18 was also used for more detailed analysis. TAMRA has been reported as a suitable fluorophore, with strong fluorescent signal and no membrane binding, although increased cytotoxicity, when conjugated to cell-penetrating peptides⁶⁵. Formulations containing 25 μ g of TAMRA-conjugated LL18, per mg of micelles, were produced for CLSM analysis (**Table 4.2**).

FITC-VD3-Dex micelles were localized in the lysosome compartment both in BMM Φ and MC3T3-E1, given the co-localization of FITC-labelled micelles and the lysosome-specific BioTracker (**Figure 4.9**). Loaded LL18 does not change the intracellular distribution of the micelles. In a similar study performed with VD3-PEG based micelles, these were also internalized into lysosomes in HeLa cells⁶⁶.

Differently, free TAMRA-labeled LL18 was localized in the perinuclear region of MC3T3-E1, as showed in other studies for LL37 uptake in A549 epithelial cells⁶⁷, and in osteoblast-like MG63, particularly localizing in mitochondria within the perinuclear region⁶⁸ (**Figure 4.11**). In A549 cells, the internalization process was correlated with elements involved in endocytosis, and trafficking to the perinuclear region was reliant on microtubules integrity. In MG63 cells, inhibition of clathrin-mediated endocytosis reduced the cellular uptake of LL37 by about 30 %, whereas an inhibitor of caveolin-mediated endocytosis had no effect⁶⁸. In

contrast, in BMM Φ , a considerable fraction of free LL18 TAMRA seems to co-localize with lysosomes. LL18 has been previously tracked in the lysosomes of infected BMM Φ , co-localizing with mycobacteria, resulting in a significant reduction of the mycobacterial burden in macrophages⁵⁷. LL37-TAMRA has also been observed in the membrane of early endosomes and lysosomes of human macrophages, in which a direct interaction with mycobacteria was revealed in detail by super-resolution microscopy⁶⁹.

S. aureus has been tracked in late endosomal/lysosomal osteoblast compartments⁷⁰, and a study of the internalization (low) and survival (high) of bacteria in osteoblasts, demonstrate the inability of osteoblasts to clear the bacteria after internalization⁷¹. The complete absence of LL18 inside lysosomes of MC3T3-E1 (likely occurring with LL37 as well), may provide another explanation for the less effective antimicrobial defense mechanism of osteoblasts compared to macrophages. This is of major importance when designing antimicrobial systems relying on endogenous production of cathelicidin by VD3 stimulation, as endogenous LL37 is unable to reach the lysosomes in particular cell lines. In the present work, we demonstrate that antimicrobial VD3-Dex micelles can shift the internalization mechanism of free LL18, and promote the accumulation of loaded peptide within the lysosomes, where *S. aureus* is known to be internalized.

Regarding the fate of the micelles, **Figure 4.11** (left) shows that loaded LL18-TAMRA and FITC-VD3-Dex are still co-localized in lysosomes after a 24 h incubation period (since the micelles are colocalized with lysosomes, LL18-TAMRA is also in the lysosomes). In another experimental setup, cells were incubated with free LL18-TAMRA, washed, and then incubated with unloaded FITC-VD3-Dex before analysis **Figure 4.11** (right). Comparing the sequential incubation of the two materials (right) with that observed with LL18-TAMRA-loaded FITC-VD3-Dex (left), it is noticeable that in BMM Φ , although large portion of free LL18 is co-localized with unloaded micelles, co-localization is much more intensified the when LL18 is loaded in the micelles. It is also much clearer that free LL18 does not co-localize with the FICT-VD3-Dex micelles in osteoblasts, though the peptide entrapped in the LL18-TAMRA-loaded FITC-VD3-Dex co-localizes mainly with the micelles in the lysosomal compartment.

FITC-VD3-Dex micelle tracking after 1 h

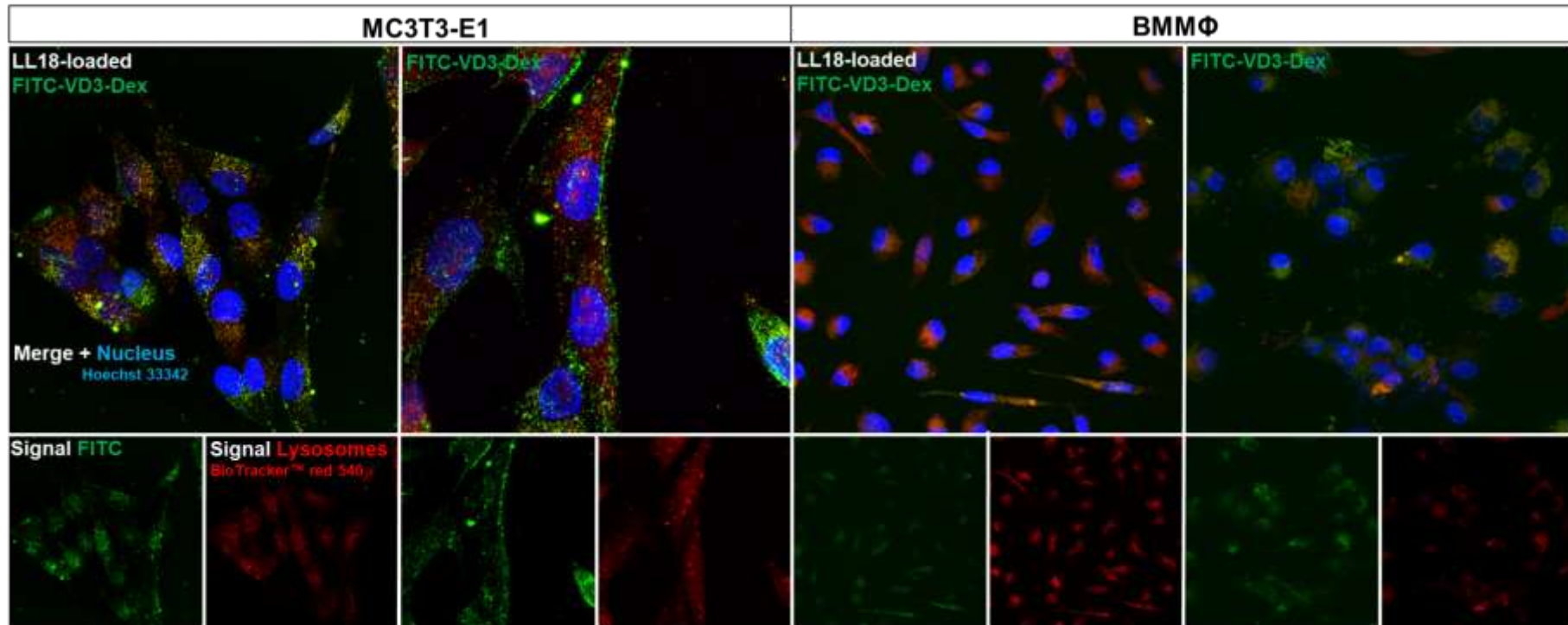


Figure 4.9 – Subcellular localization analysis by a confocal laser scanning microscope (CLSM) of unloaded and LL18-loaded FITC-VD3-Dex, after 1 h incubation, in MC3T3-E1 (60× magnification) and BMMΦ (100× magnification). Formulation of 25 µg:1 mg peptide:micelle ratio, incubated at 0.5 mg/mL. Green signal refers to FITC, and red signal to the lysosome probe.

LL18-TAMRA tracking after 1 h

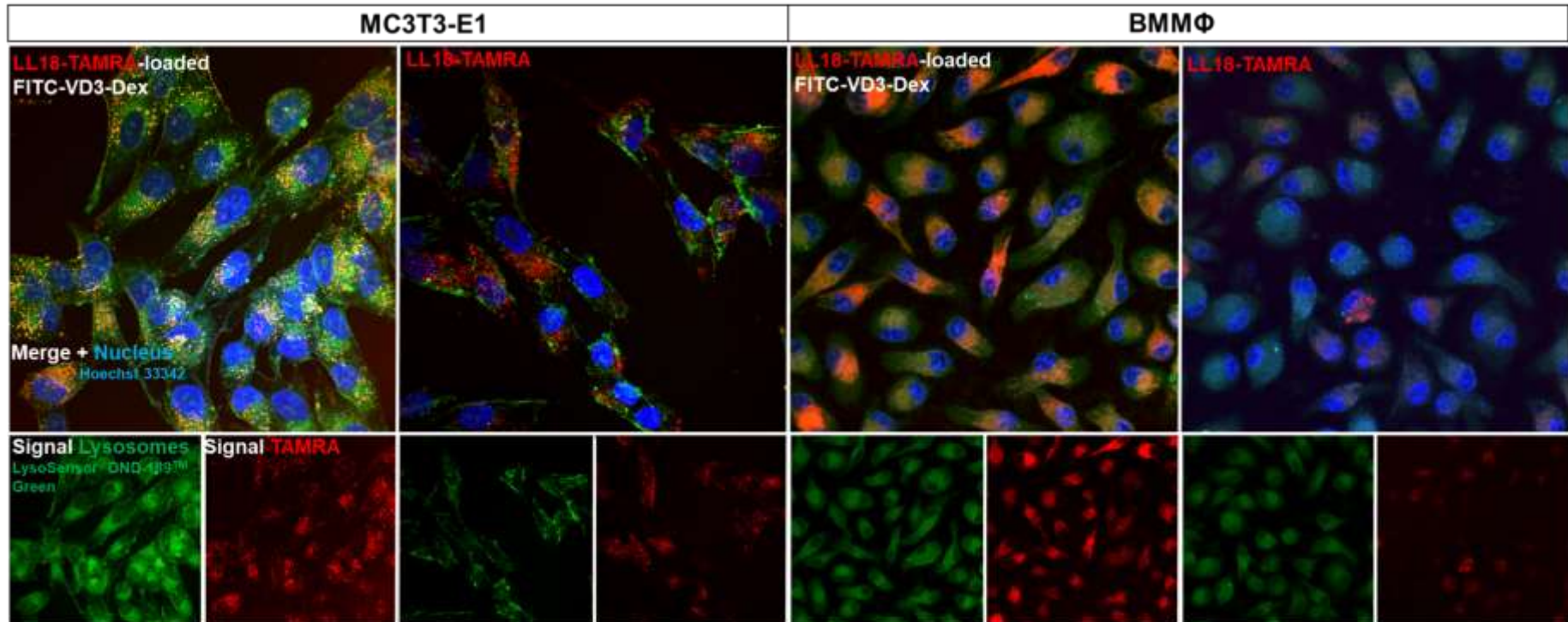


Figure 4.10 – Subcellular localization analysis using a confocal laser scanning microscope (CLSM) of free and micelle-loaded LL18-TAMRA after 1 h incubation MC3T3-E1 (60× magnification) and BMMΦ (100× magnification). Formulation of 25 µg:1 mg peptide:micelle ratio, incubated at 0.5 mg/mL. Green signal refers to lysosome probe, red signal to TAMRA.

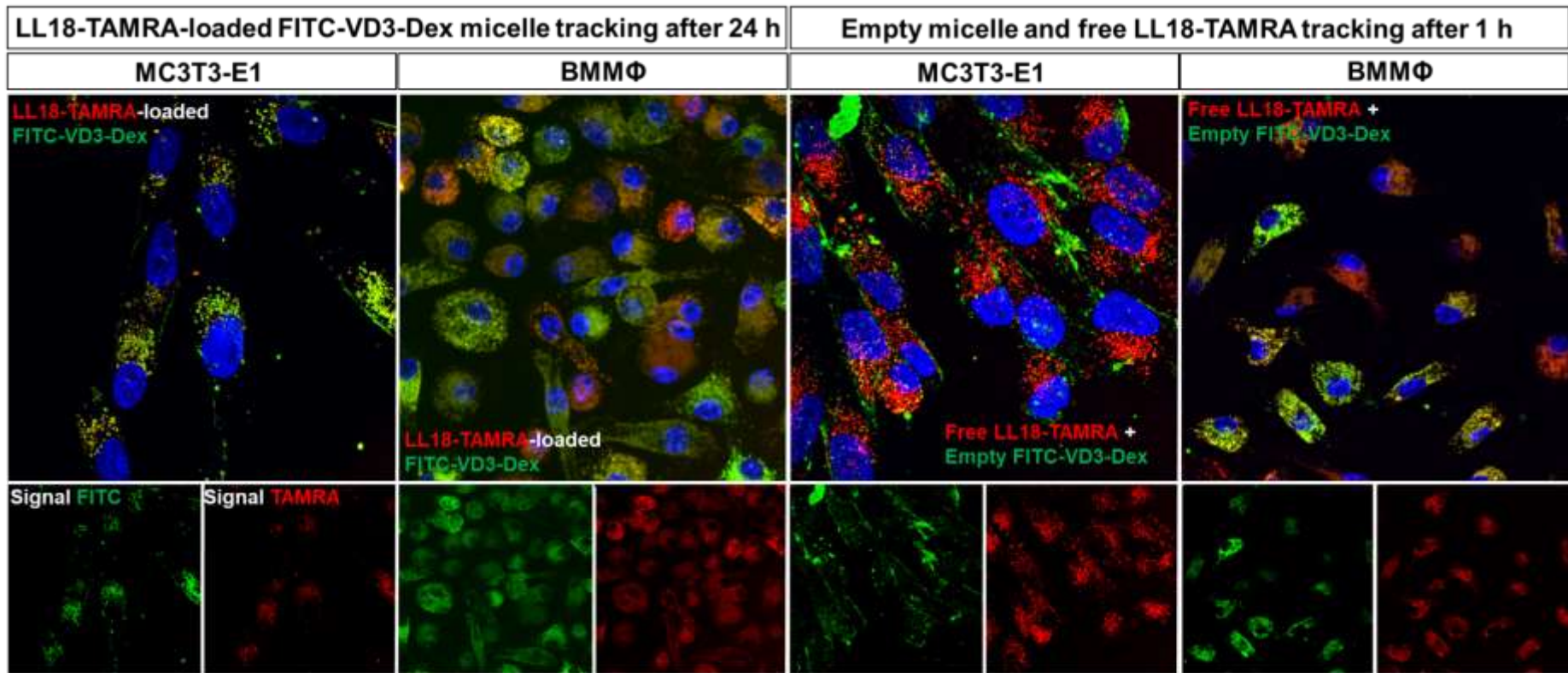


Figure 4.11 – Subcellular localization analysis using a confocal laser scanning microscope (CLSM) of: (left) LL18-TAMRA-loaded FITC-VD3-Dex micelles after a 24 h incubation; and (right) free LL18-TAMRA and empty FITC-VD3-Dex micelles after 1 h incubation each, separately, in MC3T3-E1 (60× magnification) and BMMΦ (100× magnification). Formulation of 25 µg:1 mg peptide:micelle ratio, incubated at 0.5 mg/mL. Lysosomes are not marked, green signal refers to FITC, red signal to TAMRA.

This reinforces the LL18-loaded VD3-Dex micelles potential in improving infection eradication from osteoblasts, and to a lesser extent from BMM Φ , by shifting the internalization mechanism of the peptide to an endocytosis mechanism through lysosomal compartments.

Although LL18 encapsulation had no apparent influence on the intracellular distribution of the micelles, uptake by BMM Φ cells was considerably increased both at 0.5 mg/mL ($*p < 0.05$) and 1 mg/mL ($***p < 0.001$) during 1 h incubation, in a dose-dependent manner (**Figure 4.12**). The loading of LL18 resulted in a lower surface charge and higher average size for the FITC-VD3-Dex micelles (**Table 4.2**), which may have contributed to the higher intake. This faster uptake when LL18 is present may lead to cytotoxicity, the micelles being unable to effectively provide a peptide shielding effect. The null hemolytic activity of both unloaded and loaded micelles – where uptake by endocytosis may be diminished – reinforces this uptake-dependent toxicity effect.

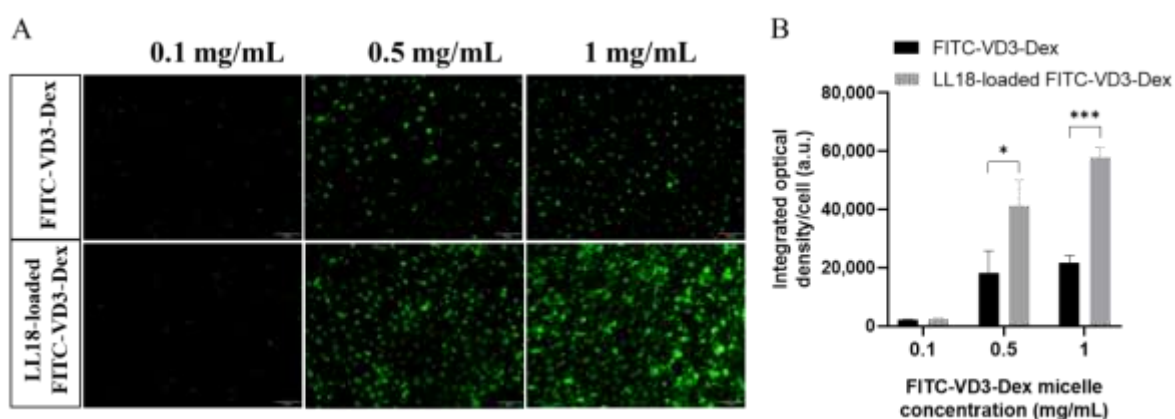


Figure 4.12 – Concentration dependence of the intracellular uptake of FITC-VD3-Dex and LL18-loaded FITC-VD3-Dex by BMM Φ cells, after 1 h incubation: **(A)** electronic microscope observation (20 \times magnification), and **(B)** uptake quantification. Results presented as mean \pm SD, n = 3, ($*p < 0.05$, $**p < 0.01$, $***p < 0.001$). Formulation of 100 μ g:1 mg peptide:micelle ratio.

4.3.7 Functionality

Bacterial bone infections induce a massive inflammatory response as a defense mechanism against tissue damage. Inflammation is a complex combination of events, including increase in protein denaturation. Non-steroidal anti-inflammatory drugs are widely used to reduce inflammation generally through blocking prostaglandins production, however, their anti-inflammatory activity is also closely related to their anti-denaturation ability^{72,73}. Inhibition of heat-induced albumin denaturation is a well-established assay for the screening of anti-inflammatory substances.

In our work, LL18 in the concentration range 50 – 500 µg/mL induced an overwhelming dose-dependent enhancing effect on albumin denaturation, which was drastically reduced by incorporation into VD3-Dex micelles (**Figure 4.13A**). As heat-induced denaturation is also time-dependent, significant albumin denaturation was also demonstrated for lower LL18 concentrations upon extended incubation periods. LL18 has recently been shown to induce concentration-dependent tissue damage in a rat model of OM²⁷. Our results suggest that LL18-induced protein denaturation may also play an important role in increased inflammation *in vivo*.

LL18-loaded micelles revealed also a dose-dependent enhancing effect on albumin denaturation, though much less pronounced. Empty micelles revealed a dose dependent protective effect, reducing albumin denaturation compared to untreated condition. The protective effect could be ascribed to VD3 (probably the micellar structure being required as well for this effect) as dextrin *per se* seems to have a neutral effect on albumin denaturation. Albumin shares a considerable amino acid homology and structural similarity with Vitamin D3-binding protein (DBP). DBP, and to a lesser extent albumin, bind with high affinity to circulating, otherwise insoluble, VD3 metabolites through a specific protein binding site composed of hydrophobic residues⁷⁴. The stability of DBP at 60 °C was markedly enhanced in the presence of 25-hydroxyvitamin D3⁷⁵. Negatively-charged serum albumin displays a binding affinity for short cationic AMPs, a process exclusively driven by interactions with peptides' hydrophobic residues rather than the (antimicrobial relevant) cationic residues⁷⁶.

Overall, we propose that VD3-Dex micelles prevent LL18-induced albumin denaturation at high temperatures by means of a shield effect, leaving no free peptide molecules for albumin binding, and possibly also by a stabilizing effect provided by hydrophobic interaction with conjugated VD3, by a process requiring further investigation.

Cell migration is essential for bone formation. In a bone fracture of zebrafish model, osteoblasts were shown to move to the site of injury to replace damaged tissue, particularly by active migration rather than passive displacement caused by cell proliferation⁷⁷. Up-regulation of MC3T3-E1 migration *in vitro* was associated to accelerated fracture healing in a rat femur⁷⁸. In this work, cell migration capacity was studied (**Figure 4.13B**) in the presence of mitomycin C, to exclude cell proliferation (**Figure 4.14**). The peptide significantly stimulated MC3T3-E1 migration after 24 h, resulting in lower open wound areas at the lowest concentrations tested of 6.25 (43.7 %) and 12.5 µg/mL (41.5 %) comparing to 25 (53.7 %) and 50 µg/mL (55.7 %). LL18 has previously demonstrated angiogenic and chemoattractant potential, improving burn wound healing in a rat model²⁵. VD3-Dex micelles also reduced open wound area compared to the control from as low as 0.06 (59.5 %) and 0.125 mg/mL (57.4 %), but not from 0.25

mg/mL upwards. It is interesting to note that 0.0625 mg/mL is below VD3-Dex calculated CMC (0.08 mg/mL), evidencing that the process of disassembly somehow does not abrogate the biological function. Considering the apparent null effect of dextrin, this outcome may be attributed to conjugated VD3.

Loading LL18 into micelles resulted in an intermediate effect between empty micelles and free LL18, reaching 52.9 % and 51.1 % at 0.065 and 0.125 mg/mL, respectively. Although peptide shielding seems to slightly diminish LL18 performance, this is counterbalanced by the positive stimulation of VD3 in the nanocarrier. As shown in our subcellular localization results, micelles changed the biodistribution of the peptide from the perinuclear region to lysosomes. The lower propensity for accelerated wound healing provided by loaded LL18 suggests that the presence of free peptide in the perinuclear region of osteoblasts is somehow required for the migration process. Thus, in this particular cell line, providing cathelicidin through lysosomes (where *S. aureus* has been traced) and perinuclear region simultaneously seems important to enhance both antimicrobial and tissue repair capabilities. LL18-loaded VD3-Dex may offer the targeting of exogenous cathelicidin to lysosomes allied to endogenous production of cathelicidin via VDR activation ^{32,79}.

Antimicrobial activity of LL18 against *S. aureus* reduced viability, at best, to 23.9 ± 5.0 % at 200 $\mu\text{g/mL}$, without further improvement up to 500 $\mu\text{g/mL}$ (**Figure 4.13C**). LL18-loaded micelles, with LL18 concentrations of 15 and 17.5 $\mu\text{g/mL}$, reduced bacterial viability by 93.1 % and 100%, respectively. Whereas dextrin displayed no activity, VD3-Dex micelles eradicated bacteria at 0.5 mg/mL concentration, an effect that may be assigned to VD3. The anti-microbial action of VD3 is drawing great attention, mostly on the basis of induced expression of cathelicidin via VDR-VDRE gene activation ^{29,30}. Compelling evidence of antimicrobial action of VD3 by direct contact is scarce in literature, with most studies reporting bactericidal improvements only by concomitant administration with antibiotics ^{80,81}. The underlying VD3 antimicrobial mechanism is likely to be related to its high lipophilicity ⁸⁰⁻⁸², solubility in the bacterial membrane and binding to efflux transporters, thus avoiding resistance mechanisms. It can alter the structure of the bacterial lipoprotein membrane, resulting in damage to components that are essential for the membrane integrity, thereby enhancing antibiotic uptake. Indeed, a study reported enhanced antibiotic activity by VD3 against resistant strains of *S. aureus* by affecting the bacterial of efflux systems

⁸⁰.

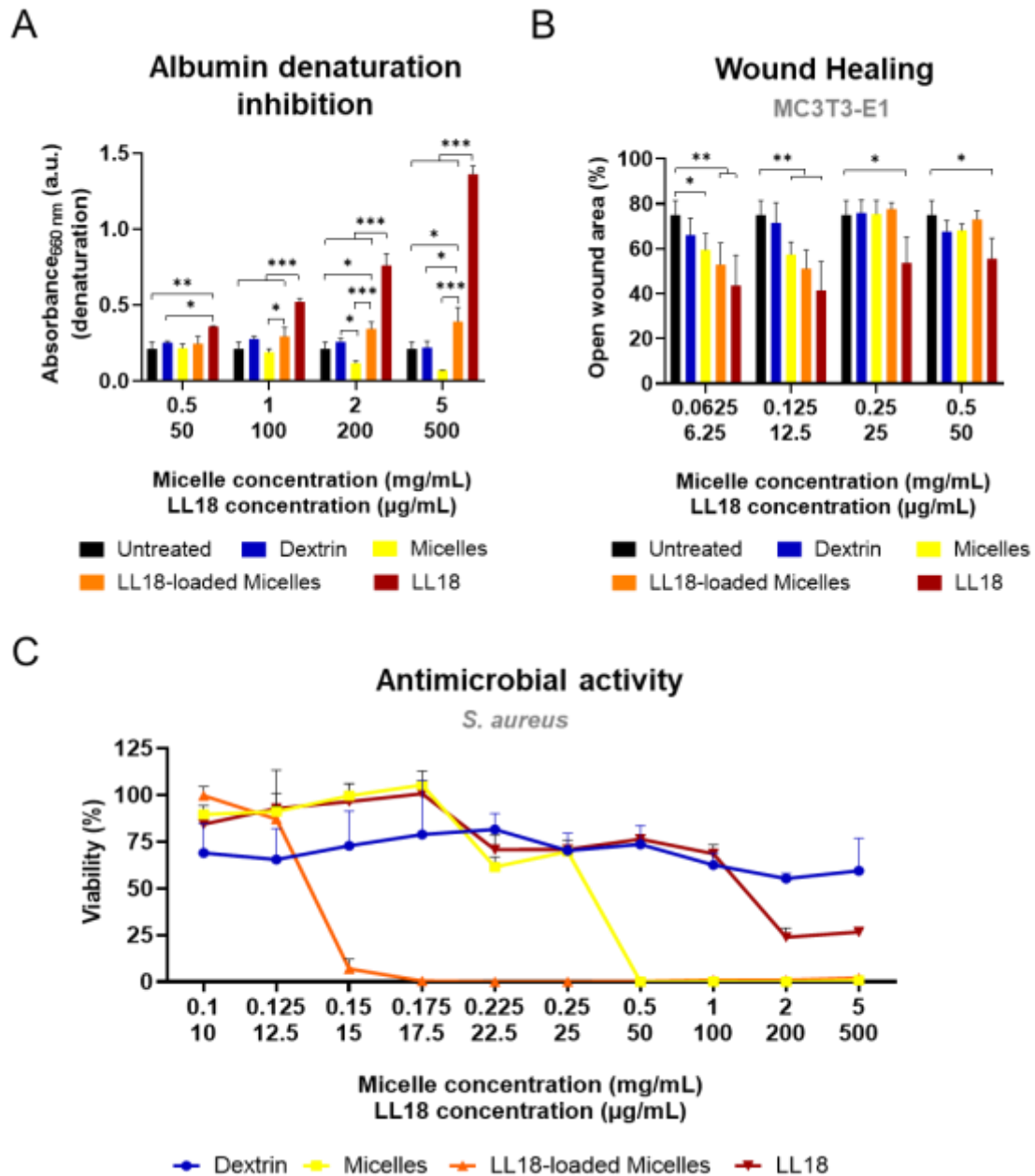


Figure 4.13 – (A) Albumin (1 % w/v) denaturation after 3h at 70 °C (n=3), (B) quantification (%) of open wound area in MC3T3-E1 cells after 24 h (n=6), and (C) antimicrobial activity against *S. aureus* after 24 h (n=4). Results presented as mean ± SD (* $p < 0.05$, ** $p < 0.01$, *** $p < 0.001$). Formulation of 100 µg:1 mg peptide:micelle ratio.

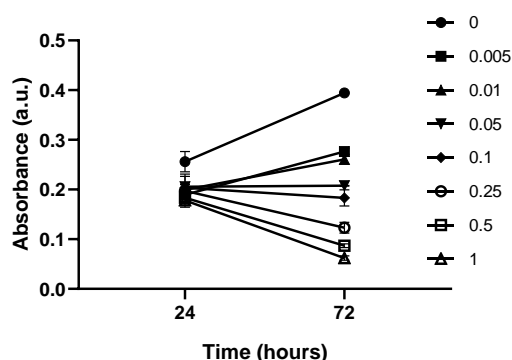


Figure 4.14 – Dose ($\mu\text{g}/\text{mL}$)-response results for MC3T3-E1 cells exposed up to 72 h to different concentrations of mitomycin C, assessed by the MTT reduction assay. Results are expressed in absorbance values. Data are presented as mean \pm SD ($n = 3$).

Drug-shielding is usually accompanied by diminished drug performance. The advantage relies in the balance between cytotoxicity and function. **Table 4.3** shows a summary of the balance between cell toxicity and antimicrobial activity attained by LL18-loaded micelles. The association between LL18 and VD3-Dex resulted in a synergistic partnership with highly improved MIC, absence of hemolysis, approximating antibacterial concentrations ($\geq 0.15 \text{ mg}/\text{ml}$) towards formulations with accelerated cell migration ($\leq 0.125 \text{ mg}/\text{mL}$). Since a functional concentration range is far below CC_{50} , an increase in peptide loading could be considered to achieve an optimized formulation in the future.

Table 4.3 – Summary balance of cytotoxicity and antimicrobial activity.

Sample	LL18	Loaded LL18	LL18-Loaded Micelles	Unloaded Micelles	Dextrin
BMMΦ CC_{50}	91.4 $\mu\text{g}/\text{mL}$ (CI 83.8 - 100.0)	123.4 $\mu\text{g}/\text{mL}$ (CI 116.5 - 130.7)	1.23 mg/mL (CI 1.17 - 1.31)	Cell viability > 50% up to 3 mg/mL	
MC3T3-E1 CC_{50}	103.5 $\mu\text{g}/\text{mL}$ (CI 91.7 - 118.3)	153.4 $\mu\text{g}/\text{mL}$ (CI 132.9 - 191.0)	1.53 mg/mL (CI 1.33 - 1.91)		
MIC <i>S. aureus</i>	> 500 $\mu\text{g}/\text{mL}$	17.5 $\mu\text{g}/\text{mL}$	0.175 mg/mL	0.5 mg/mL	-
BMMΦ SI	-	7.05	7.05	-	-
MC3T3-E1 SI	-	8.77	8.77	-	-
Hemolysis	Hemolytic	Non-hemolytic	Non-hemolytic	Non-hemolytic	Non-hemolytic

CC_{50} , 50 % cytotoxic concentration; CI, confidence interval ($n=3$); MIC, minimal inhibitory concentration; SI, *Staphylococcus aureus*, *S. aureus*; Selectivity Index = $\text{CC}_{50}/\text{MIC}$.

4.4 Conclusion

We developed a micelle-like delivery system based on dextrin and VD3, further engineered to work as a vehicle for LL18, culminating in a dual delivery system with antimicrobial and tissue healing properties. The construct overcomes recurrent limitations of drug (VD3) solubility, diminishes cytotoxicity and hemolysis, improves antibacterial activity, reduces heat-induced albumin denaturation and holds wound healing capacity. LL18 encapsulation did not change the intracellular distribution of the micelles and promoted a significantly faster cell uptake, advantageous to rapidly address intracellular bacteria. Importantly, unlike the free peptide, loaded LL18 internalizes in osteoblasts through the lysosomal compartments - the same compartment where *S. aureus* is internalized.

Micelles can be extruded to yield homogeneous-in-size particles under 200 nm. Micelles provide protection, solubility (and thereby bioavailability) and transport of VD3 into cells, where local activation and subsequent endogenous cathelicidin stimulation is likely to occur. Owing to dextrin tunability, VD3-Dex micelles still have much room for improvement, given that different VD3-dextrin proportions (molar ratios) can be precisely manipulated to adjust the balance between the micelles physical-chemical properties (size, charge), toxicity and solubility and biological properties. Overall, VD3 may constitute a prophylactic option and therapeutic product to traditional antimicrobial and bone healing agents, even disregarding the endogenous stimulation cathelicidin.

4.5 References

1. Gimza, B. D. & Cassat, J. E. Mechanisms of Antibiotic Failure During Staphylococcus aureus Osteomyelitis. *Front. Immunol.* 0, 303 (2021).
2. Li, B. & Webster, T. J. Bacteria antibiotic resistance: New challenges and opportunities for implant-associated orthopedic infections. *J. Orthop. Res.* 36, 22–32 (2018).
3. Li, J. et al. Relationship Between Time to Surgical Debridement and the Incidence of Infection in Patients with Open Tibial Fractures. *Orthop. Surg.* 12, 524–532 (2020).
4. Mathews, J. A., Ward, J., Chapman, T. W., Khan, U. M. & Kelly, M. B. Single-stage orthoplastic reconstruction of Gustilo–Anderson Grade III open tibial fractures greatly reduces infection rates. *Injury* 46, 2263–2266 (2015).
5. Rossel, A. et al. Stopping antibiotics after surgical amputation in diabetic foot and ankle infections—A daily practice cohort. *Endocrinol. Diabetes Metab.* 2, e00059 (2019).
6. Metsemakers, W. J., Smeets, B., Nijs, S. & Hoekstra, H. Infection after fracture fixation of the tibia: Analysis of healthcare utilization and related costs. *Injury* 48, 1204–1210 (2017).
7. Spohn, R. et al. Integrated evolutionary analysis reveals antimicrobial peptides with limited resistance. *Nat. Commun.* 10, 1–13 (2019).

8. Sancho-Vaello, E. *et al.* The structure of the antimicrobial human cathelicidin LL-37 shows oligomerization and channel formation in the presence of membrane mimics. *Sci. Rep.* 10, 1–16 (2020).
9. Boix-Lemonche, G., Guillem-Marti, J., D'Este, F., Manero, J. M. & Skerlavaj, B. Covalent grafting of titanium with a cathelicidin peptide produces an osteoblast compatible surface with anti-staphylococcal activity. *Colloids Surfaces B Biointerfaces* 185, 110586 (2020).
10. Noore, J., Noore, A. & Li, B. Cationic antimicrobial peptide LL-37 is effective against both extra- and intracellular *Staphylococcus aureus*. *Antimicrob. Agents Chemother.* 57, 1283–90 (2013).
11. Zhang, X., Lu, Q., Liu, T., Li, Z. & Cai, W. Bacterial resistance trends among intraoperative bone culture of chronic osteomyelitis in an affiliated hospital of South China for twelve years. *BMC Infect. Dis.* 19, 1–8 (2019).
12. Kavanagh, N. *et al.* Staphylococcal Osteomyelitis: Disease Progression, Treatment Challenges, and Future Directions. *Clin. Microbiol. Rev.* 31, e00084-17 (2018).
13. Pozo, E. G. del, Collazos, J., Carton, J. A., Camporro, D. & Asensi, V. Factors predictive of relapse in adult bacterial osteomyelitis of long bones. *BMC Infect. Dis.* 18, 1–11 (2018).
14. Tawfik, G. M. *et al.* Concordance of bone and non-bone specimens in microbiological diagnosis of osteomyelitis: A systematic review and meta-analysis. *J. Infect. Public Health* 13, 1682–1693 (2020).
15. Kang, J., Dietz, M. J. & Li, B. Antimicrobial peptide LL-37 is bactericidal against *Staphylococcus aureus* biofilms. *PLoS One* 14, e0216676 (2019).
16. Yu, X. *et al.* LL-37 inhibits LPS-induced inflammation and stimulates the osteogenic differentiation of BMSCs via P2X7 receptor and MAPK signaling pathway. *Exp. Cell Res.* 372, 178–187 (2018).
17. Koczulla, R. *et al.* An angiogenic role for the human peptide antibiotic LL-37/hCAP-18. *J. Clin. Invest.* 111, 1665–1672 (2003).
18. Yang, X. *et al.* Chitosan hydrogel encapsulated with LL-37 peptide promotes deep tissue injury healing in a mouse model. *Mil. Med. Res.* 7, 1–10 (2020).
19. Garcia-Orue, I. *et al.* LL37 loaded nanostructured lipid carriers (NLC): A new strategy for the topical treatment of chronic wounds. *Eur. J. Pharm. Biopharm.* 108, 310–316 (2016).
20. Kittaka, M. *et al.* The antimicrobial peptide LL37 promotes bone regeneration in a rat calvarial bone defect. *Peptides* 46, 136–142 (2013).
21. Li, L. *et al.* Cathelicidin LL37 Promotes Osteogenic Differentiation in vitro and Bone Regeneration in vivo. *Front. Bioeng. Biotechnol.* 9, 347 (2021).
22. Grönberg, A., Mahlapuu, M., Stähle, M., Whately-Smith, C. & Rollman, O. Treatment with LL-37 is safe and effective in enhancing healing of hard-to-heal venous leg ulcers: a randomized, placebo-controlled clinical trial. *Wound Repair Regen.* 22, 613–621 (2014).
23. Sonawane, A. *et al.* Cathelicidin is involved in the intracellular killing of mycobacteria in macrophages. *Cell Microbiol* 13, 1601–17 (2011).
24. Ciornei, C. D., Sigurdardóttir, T., Schmidtchen, A. & Bodelsson, M. Antimicrobial and chemoattractant activity, lipopolysaccharide neutralization, cytotoxicity, and inhibition by serum of analogs of human cathelicidin LL-37. *Antimicrob. Agents Chemother.* 49, 2845–50 (2005).
25. Silva, J. P. *et al.* Improved burn wound healing by the antimicrobial peptide LLKKK18 released from conjugates with dextrin embedded in a carbopol gel. *Acta Biomater.* 26, 249–262 (2015).
26. Pereira, I. *et al.* Regeneration of critical-sized defects, in a goat model, using a dextrin-based hydrogel associated with granular synthetic bone substitute. *Regen. Biomater.* 8, 1–10 (2021).
27. Machado, A. *et al.* Injectable hydrogel as a carrier of vancomycin and a cathelicidin-derived peptide for osteomyelitis treatment. *J. Biomed. Mater. Res. Part A* 110, 1786–1800 (2022).
28. Essen, M. R. von & Geisler, C. VDR, the Vitamin D Receptor. in Choi S. *Encyclopedia of Signaling Molecules* 5907–5914 (Springer, Cham, 2018).

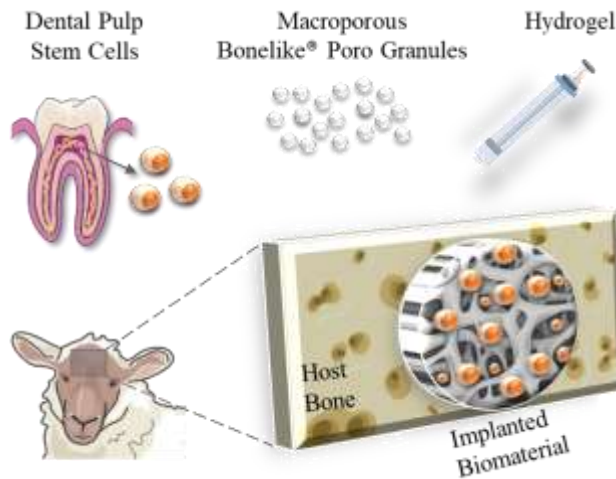
29. Chung, C., Silwal, P., Kim, I., Modlin, R. L. & Jo, E.-K. Vitamin D-Cathelicidin Axis: at the Crossroads between Protective Immunity and Pathological Inflammation during Infection. *Immune Netw.* 20, (2020).
30. Gombart, A. F., Borregaard, N. & Koeffler, H. P. Human cathelicidin antimicrobial peptide (CAMP) gene is a direct target of the vitamin D receptor and is strongly up-regulated in myeloid cells by 1,25-dihydroxyvitamin D3. *FASEB J.* 19, 1067–1077 (2005).
31. Gil, Á., Plaza-Diaz, J. & Mesa, M. D. Vitamin D: Classic and Novel Actions. *Ann. Nutr. Metab.* 72, 87–95 (2018).
32. Mason, S. S., Kohles, S. S., Winn, S. R. & Zelick, R. D. Extrahepatic 25-Hydroxylation of Vitamin D3 in an Engineered Osteoblast Precursor Cell Line Exploring the Influence on Cellular Proliferation and Matrix Maturation during Bone Development. *ISRN Biomed. Eng.* 2013, 956362 (2013).
33. Ignjatović, N., Uskoković, V., Ajduković, Z. & Uskoković, D. Multifunctional hydroxyapatite and poly(D,L-lactide-co-glycolide) nanoparticles for the local delivery of cholecalciferol. *Mater. Sci. Eng. C. Mater. Biol. Appl.* 33, 943–50 (2013).
34. Shekhar, C. An Innovative Technique in Local Antibiotic Delivery Method in Open Infected Wounds of the Musculoskeletal System. *Int. J. Low. Extrem. Wounds* 18, 153–160 (2019).
35. Shekhar, C. et al. Role of topical cholecalciferol granules for antimicrobial drug delivery in diabetic foot ulcers. *Indian J. Orthop. Surg.* 5, 165–167 (2019).
36. Hreczuk-Hirst, D., Chicco, D., German, L. & Duncan, R. Dextrins as potential carriers for drug targeting: tailored rates of dextrin degradation by introduction of pendant groups. *Int. J. Pharm.* 230, 57–66 (2001).
37. Kaneo, Y., Uemura, T., Tanaka, T. & Kanoh, S. Polysaccharides as drug carriers: biodisposition of fluorescein-labeled dextrans in mice. *Biol. Pharm. Bull.* 20, 181–187 (1997).
38. Hardwicke, J. et al. Bioresponsive Dextrin–rhEGF Conjugates: In Vitro Evaluation in Models Relevant to Its Proposed Use as a Treatment for Chronic Wounds. *Mol. Pharm.* 7, 699–707 (2010).
39. “Food And Drugs.” Code of Federal Regulations, title 21 (2021), Chapter I, Subchapter B, Part 184, Subpart B §184.1277.
40. Varache, M. et al. Polymer Masked–Unmasked Protein Therapy: Identification of the Active Species after Amylase Activation of Dextrin–Colistin Conjugates. *Mol. Pharm.* 16, 3199–3207 (2019).
41. Pereira, I. et al. In vivo systemic toxicity assessment of an oxidized dextrin-based hydrogel and its effectiveness as a carrier and stabilizer of granular synthetic bone substitutes. *J. Biomed. Mater. Res. Part A* 107, 1678–1689 (2019).
42. Asai, T. et al. Dextrin Promotes Proliferation of Cultured MC3T3-E1 Mouse Osteoblast-like Cells and Their Alkaline Phosphatase Activity: Implications for Potential Application of Dextrin as a Binder of Bone Filling Material. *J. Hard Tissue Biol.* 27, 65–68 (2018).
43. Cui, Y. C. et al. Metabolic utilization of human osteoblast cell line hFOB 1.19 under normoxic and hypoxic conditions: A phenotypic microarray analysis. *Exp. Biol. Med.* 246, 1177–1183 (2021).
44. World Health Organization. Prioritization of pathogens to guide discovery, research and development of new antibiotics for drug-resistant bacterial infections, including tuberculosis. World Health Organization. Report <https://apps.who.int/iris/handle/10665/311820>. (2017).
45. Silva, D. M. et al. Structural analysis of dextrans and characterization of dextrin-based biomedical hydrogels. *Carbohydr. Polym.* 114, 458–466 (2014).
46. Kutlehria, S. et al. Cholecalciferol-PEG Conjugate Based Nanomicelles of Doxorubicin for Treatment of Triple-Negative Breast Cancer. *AAPS PharmSciTech* 19, 792–802 (2018).
47. Silva-Carvalho, R. et al. Development of dextrin-amphotericin B formulations for the treatment of Leishmaniasis. *Int. J. Biol. Macromol.* 153, 276–288 (2020).

48. Man, J., Shelton, R. M., Cooper, P. R., Landini, G. & Scheven, B. A. Low intensity ultrasound stimulates osteoblast migration at different frequencies. *J. Bone Miner. Metab.* 30, 602–607 (2012).
49. Kiani, A., Fathi, M. & Ghasemi, S. M. Production of novel vitamin D3 loaded lipid nanocapsules for milk fortification. *Int. J. Food Prop.* 20, 2466–2476 (2017).
50. Zhao, H. Z., Tan, E. C. & Yung, L. Y. L. Potential use of cholecalciferol polyethylene glycol succinate as a novel pharmaceutical additive. *J. Biomed. Mater. Res. Part A* 84A, 954–964 (2008).
51. Kotlehria, S. *et al.* Tacrolimus Loaded PEG-Cholecalciferol Based Micelles for Treatment of *Ocular Inflammation*. *Pharm. Res.* 35, 1–12 (2018).
52. Rabelo, R. S., Oliveira, I. F., da Silva, V. M., Prata, A. S. & Hubinger, M. D. Chitosan coated nanostructured lipid carriers (NLCs) for loading Vitamin D: A physical stability study. *Int. J. Biol. Macromol.* 119, 902–912 (2018).
53. Hasanvand, E., Fathi, M. & Bassiri, A. Production and characterization of vitamin D3 loaded starch nanoparticles: effect of amylose to amylopectin ratio and sonication parameters. *J. Food Sci. Technol.* 55, 1314 (2018).
54. Sun, B., Tian, Y., Chen, L. & Jin, Z. Linear dextrin as curcumin delivery system: Effect of degree of polymerization on the functional stability of curcumin. *Food Hydrocoll.* 77, 911–920 (2018).
55. Datta, D. & Halder, G. Blending of phthalated starch and surface functionalized rice husk extracted nanosilica with LDPE towards developing an efficient packaging substitute. *Environ. Sci. Pollut. Res.* 27, 1533–1557 (2020).
56. Hu, Z. *et al.* Structural Characterization and Digestibility of Curcumin Loaded Octenyl Succinic Nanoparticles. *Nanomater. (Basel)* 9, 1073 (2019).
57. Silva, J. P. *et al.* Delivery of LLKKK18 loaded into self-assembling hyaluronic acid nanogel for tuberculosis treatment. *J. Control. Release* 235, 112–124 (2016).
58. Bankell, E. *et al.* The antimicrobial peptide LL-37 triggers release of apoptosis-inducing factor and shows direct effects on mitochondria. *Biochem. Biophys. Reports* 29, 101192–101192 (2021).
59. Bergandi, L., Apprato, G. & Silvagno, F. Vitamin d and beta-glucans synergically stimulate human macrophage activity. *Int. J. Mol. Sci.* 22, (2021).
60. Lee, B. S., Holliday, L. S., Krits, I. & Gluck, S. L. Vacuolar H⁺-ATPase activity and expression in mouse bone marrow cultures. *J. Bone Miner. Res.* 14, 2127–2136 (1999).
61. Kao, C. *et al.* Cathelicidin Antimicrobial Peptides with Reduced Activation of Toll-Like Receptor Signaling Have Potent Bactericidal Activity against Colistin-Resistant Bacteria. *MBio* 7, e01418-16 (2016).
62. ASTM International (F756–13). Standard Practice for Assessment of Hemolytic Properties of Materials. (2013).
63. Gao, X., Yue, T., Tian, F., Liu, Z. & Zhang, X. Erythrocyte membrane skeleton inhibits nanoparticle endocytosis. *AIP Adv.* 7, 065303 (2017).
64. Wadhwa, R. *et al.* Red blood cells as an efficient in vitro model for evaluating the efficacy of metallic nanoparticles. *3 Biotech* 9, 279 (2019).
65. Birch, D., Christensen, M. V., Staerk, D., Franzyk, H. & Nielsen, H. M. Fluorophore labeling of a cell-penetrating peptide induces differential effects on its cellular distribution and affects cell viability. *Biochim. Biophys. Acta - Biomembr.* 1859, 2483–2494 (2017).
66. Patil, S., Gawali, S., Patil, S. & Basu, S. Synthesis, characterization and in vitro evaluation of novel vitamin D3 nanoparticles as a versatile platform for drug delivery in cancer therapy. *J. Mater. Chem. B* 1, 5742–5750 (2013).
67. Lau, Y. E. *et al.* Interaction and Cellular Localization of the Human Host Defense Peptide LL-37 with Lung Epithelial Cells. *Infect. Immun.* 73, 583 (2005).

68. Anders, E., Dahl, S., Svensson, D. & Nilsson, B. O. LL-37-induced human osteoblast cytotoxicity and permeability occurs independently of cellular LL-37 uptake through clathrin-mediated endocytosis. *Biochem. Biophys. Res. Commun.* 501, 280–285 (2018).
69. Deshpande, D. *et al.* Super-Resolution Microscopy Reveals a Direct Interaction of Intracellular Mycobacterium tuberculosis with the Antimicrobial Peptide LL-37. *Int. J. Mol. Sci.* 21, 1–16 (2020).
70. Jauregui, C. E., Mansell, J. P., Jepson, M. A. & Jenkinson, H. F. Differential interactions of Streptococcus gordonii and Staphylococcus aureus with cultured osteoblasts. *Mol. Oral Microbiol.* 28, 250–266 (2013).
71. Hamza, T. & Li, B. Differential responses of osteoblasts and macrophages upon Staphylococcus aureus infection. *BMC Microbiol.* 14, 1–11 (2014).
72. Saso, L. *et al.* Inhibition of heat-induced denaturation of albumin by nonsteroidal antiinflammatory drugs (NSAIDs): pharmacological implications. *Arch. Pharm. Res.* 24, 150–158 (2001).
73. Leelaprakash, G. & Dass, S. M. Invitro Antiinflammatory activity of Methanol extract of Eriostemma Axillare. *Int. J. Drug Dev. Res* 3, 189–196 (2011).
74. Delanghe, J. R., Speeckaert, R. & Speeckaert, M. M. Behind the scenes of vitamin D binding protein: More than vitamin D binding. *Best Pract. Res. Clin. Endocrinol. Metab.* 29, 773–786 (2015).
75. Bouillon, R., Van Baelen, H., Rombatus, W. & De Moor, P. The Purification and Characterisation of the Human-Serum Binding Protein for the 25-Hydroxycholecalciferol (Transcalciferin) Identity with Group-Specific Component. *Eur. J. Biochem.* 66, 285–291 (1976).
76. Sivertsen, A. *et al.* Synthetic cationic antimicrobial peptides bind with their hydrophobic parts to drug site II of human serum albumin. *BMC Struct. Biol.* 14, 4 (2014).
77. Geurtzen, K. *et al.* Mature osteoblasts dedifferentiate in response to traumatic bone injury in the zebrafish fin and skull. *Development* 141, 2225–2234 (2014).
78. Zhang, Z., Hu, P., Wang, Z., Qiu, X. & Chen, Y. BDNF promoted osteoblast migration and fracture healing by up-regulating integrin β 1 via TrkB-mediated ERK1/2 and AKT signalling. *J. Cell. Mol. Med.* 24, 10792–10802 (2020).
79. Yagi, H. *et al.* Antimicrobial activity of mesenchymal stem cells against Staphylococcus aureus. *Stem Cell Res. Ther.* 11, 1–12 (2020).
80. Tintino, S. R. *et al.* Action of cholecalciferol and alpha-tocopherol on Staphylococcus aureus efflux pumps. *EXCLI J.* 15, 315–22 (2016).
81. Andrade, J. C. *et al.* Cholecalciferol, Ergosterol, and Cholesterol Enhance the Antibiotic Activity of Drugs. *Int. J. Vitam. Nutr. Res.* 88, 244–250 (2018).
82. Gibbons, S. Anti-staphylococcal plant natural products. *Nat. Prod. Rep.* 21, 263 (2004).

CHAPTER 5

5. DEXTRIN HYDROGEL LOADED WITH A MACROPOROUS BONELIKE® SCAFFOLD AND DENTAL PULP STEM CELLS FOR CRITICAL-SIZED DEFECT REPAIR



Regeneration of severe bone defects remains a challenge. A formulation of synthetic glass-reinforced hydroxyapatite bone substitute, Bonelike® Poro (BL®P), 250 - 500 μ m-diameter, with a dextrin-based hydrogel (HG), further loaded with human dental pulp stem cells (hDPSCs) with osteogenic differentiation ability, was tested for the management of critical-sized defects in an ovine model.

Morphology, calcium release, and mechanical strength of HG + BL®P were analyzed. Then, BL®P, HG + BL®P, and 10^6 hDPSCs-loaded HG + BL®P were implanted in ovine critical-sized 14 mm-diameter calvaria defects. Bone samples were collected after 3 and 6 weeks for histological and micro-computed tomography analysis.

BL®P exhibits a suitable porous size for cell ingrowth, from the nm (>200 nm) to the μ m (5 μ m) range. The addition of BL®P granules to the HG resulted in increased compressive elastic modulus and ultimate tensile strength. The mildly acidic nature of the HG contributed to a faster dissolution of granules. *In vivo* results confirmed the HG suitability as a carrier, providing better defect filling, easy handling, and injectability of BL®P without compromising new bone formation nor biocompatibility. The HG + BL®P formulations can successfully regenerate critical-sized defects; however, addition of hDPSCs did not significantly enhance new bone formation under these conditions.

Granular BL®P provides an effective alternative to autologous grafts. The HG acts as a biocompatible carrier of granular bone substitutes and cells, conferring injectability and cohesivity.

5.1. Introduction

Bone substitutes can substantially improve life quality by repairing damaged bone, accelerating healing, avoiding complications, and improving outcomes, but they become absolutely indispensable in cases of critical-sized defects, defined as defects incapable of complete spontaneous regeneration during the entire lifetime ¹. A study report shows the global bone graft and substitutes market size was valued at USD 2.78 billion in 2020, being expected to grow at a rate of 5.8 % from 2021 to 2028 ². Indeed, bone defect is a common event that may arise from numerous clinical circumstances related to, for instance, fractures, traumas, tumors, infections, and other disorders ³. Incidence of these scenarios will likely be aggravated as a consequence of the increasing human life span. World Health Organization foresees the proportion of the world's population over 60 years to double from 12 % to 22 % between 2015 and 2050 ⁴.

In the management of bone defects, grafts have long been used to support bone deposition at the early stages of osteointegration, providing mechanical support, and a tuned resorption rate as synchronized as possible with new host bone replacement, being osteoconductive, osteoinductive and osteogenic so that new bone can grow within the biomaterial ³. Hydroxyapatite (HA) is a bioactive ceramic, one of the most effective calcium phosphates used for the development of synthetic grafts for bone repair. This mineral mimics the composition of natural bone, is porous, osteoconductive, resorbable, biocompatible and shows good osseointegration, providing excellent conditions for tissue ingrowth ⁵. We have been applying a glass-reinforced HA bone substitute of different granulometries, Bonelike®, for regenerative purposes ⁶⁻¹³. Bonelike® Poro (B®LP) is a biomaterial with micro and macroporous interconnected architecture ¹⁴. Contrasting with micropores which are an important factor for cell adhesion, macroporosity is defined as possessing pores with one of its dimensions larger than 10 µm ¹⁵ which, together with interconnectivity, favors vessel infiltration for blood supply, cell colonization, communication, migration and proliferation, exchange of water and nutrients ¹⁶. Consequently, macroporosity also favors cell-mediated biomaterial resorption which, ideally, should not occur faster than new bone ingrow. Additionally, osteoblasts (sized 10 - 50 µm) show preference for >100 µm pores ^{16,17}. BL®P production method generates granules of sizes between 150 µm and 6 mm (approximately), being convenient for various clinical applications, from smaller to larger defects in dentistry and orthopedics. Recently, BL®P from 2000 to 5600 µm in diameter, with pore sizes ranging from 200 to 600 µm, enabled the regeneration of 17 mm diameter critical-sized lesions over 5 months of recovery, in an ovine model of iliac crest ¹⁴, performing comparably to the autograph technique parallelly tested. Synthetic grafts emerge to overcome limited sources, morbidity, and rejections associated with autographs or allografts.

Grafts can be associated with other bioactive agents to modulate or boost the regenerative process. Human dental pulp stem cells (hDPSCs), present inside the dental pulp, are a type of self-renewing, multipotent mesenchymal stem cells (MSCs) with easy accessibility and suitable for cryopreservation, being attractive for clinical application. hDPSCs have low immunogenicity, and lack expression of human leucocyte antigen (HLA-DR) surface molecules¹⁸, diminishing the risk of transplant rejection between species¹⁹. hDPSCs are auspicious for bone repair owing to their osteodifferentiation potential and secretion of important pro-regenerative biomolecules. They can generate osteoblasts²⁰, produce extracellular and mineralized matrix²¹, and have shown higher proliferative capacity and alkaline phosphatase activity compared to the popularly used bone marrow-derived MSCs²². Although several critical-sized pre-clinical models have been used to demonstrate the regenerative potential of hDPSCs associated with synthetic scaffolds, they have been mainly performed in rats, whereas other close-to-human models, such as goats, sheep, or swine are still rare²³. Sheep is a suitable pre-clinical model of novel osteogenic technologies for reasons such as ease of housing, compliance, docility, availability, life-span for long-term treatment processes, and sufficiently large bones to allow testing multiple conditions simultaneously. Bodyweight, the macrostructure and the turnover and bone modeling rate are similar to those of humans^{24,25}.

Currently, there are many clinical cases requiring bone filling materials but most commercially available grafts display limited handling properties. The combination of hydrogels with bone substitutes is a well-established trend that can not only confer injectability, moldability, non-invasive techniques and avoid early evasion of particles, but also act as a platform for cell colonization and as a carrier of bioactive molecules and cells, which can considerably improve the healing process. Dextrin ((C₆H₁₀O₅)_n) is a glucose polymer predominately composed of α-(1→4) glycosidic bonds, derived from starch by partial hydrolysis - a natural, broadly available, renewable source. Dextrin is a smart option for therapy design for several reasons, for instance: i) non-toxic, accepted as a generally recognized as safe food (GRAS) ingredient²⁶⁻³⁰, and available in medical grade; ii) low molecular weight (< 2800 g/mol)³¹ below the renal filtration limit range (~30–50 kDa)^{32,33}, avoiding tissue accumulation; iii) biodegradable, as it can be enzymatically decomposed into glucose monosaccharides by blood α-amylases; iv) holds multiple reactive primary and secondary hydroxyl groups, suitable for conjugations or grafting strategies and other chemical reactions; and vi) low viscosity, which can be adjustable, to improve quality of shape-filling materials³⁴. In this work, aldehyde-bearing dextrin spontaneously cross-linked with adipic acid dihydrazide (ADH) amine groups by Schiff base reaction, without any chemical initiator, was used³⁵. An injectable *in situ* hydrogel (HG) is so obtained, capable of complete filling and molding to irregular defects. This network is gradually dismantled

owing to the reversible nature of hydrazone bonds in water³⁶. We have previously reported HG's suitability as a carrier of nanogels, cells, biomolecules, and granular ceramics^{31,35,37-39} and also demonstrated the *in vitro* cyto- and genocompatibility^{35,40}.

In a previous study, microporous BL®P (250 – 500 µm) associated with hDPSCs improved bone regeneration in a non-critical ovine model⁴¹. In this work, the same macroporous BL®P associated with HG will be used as a transplantation-based strategy for hDPSCs and tested in ovine critical-sized calvaria defects. Bone formation and biomaterial resorption will be analyzed at weeks 3 and 6 post-treatment through histologic and micro-CT processing.

5.2. Materials and Methods

5.2.1. Materials and Reagents

Dextrin used in this study was Tackidex B 167 (Batch E 1445), was kindly provided by Roquette (Lestrem, France). Sodium *m*-periodate, diethylene glycol, ADH, silver nitrate, sodium thiosulfate, dexamethasone, ascorbic acid-2-phosphate, β-glycerophosphate, Alcian Blue, acetic acid, sodium carbonate (Na₂CO₃), calcium fluoride (CaF₂), calcium hydrogen phosphate (CaHPO₄), di-phosphorus pentoxide (P₂O₅) and polyvinyl alcohol (PVA), formaldehyde, pepsin and hydrochloric acid (HCl) were purchased from Sigma-Aldrich (St. Louis, MO, USA). Dulbecco's phosphate-buffered saline (DPBS), αMEM, fetal bovine serum (FBS), streptomycin, penicillin, and amphotericin B were obtained from Gibco® (Waltham, MA, USA). BL®P granules (250 - 500 µm) were provided by Biosskin – Molecular and Cell Therapies, S.A. Trypan Blue™ exclusion assay was purchased from Invitrogen™, for use with the Countess™ Automated Cell Counter Invitrogen™.

5.2.2. Preparation of Dextrin-based Hydrogel

First, dextrin was oxidized as previously described by our group³⁸. Briefly, sodium *m*-periodate (NaIO₄), was added to dextrin solution (2 % w/v), at an equivalent theoretical degree of oxidation of 40 % (mol). The reaction was left stirring for 20h at room temperature, protected from light, until stopped with a NaIO₄-equimolar amount of diethylene glycol. NaIO₄ and diethylene glycol were removed by dialysis (1000 Da cut-off membrane from Merck Millipore, USA) over 48h with, and the dialyzed product, oxidized-dextrin (ODEX) was freeze-dried. Then, dextrin-based HG was prepared as described by Pereira et al. (Pereira, Fraga, Silva, et al., 2019). ODEX solution was prepared in phosphate-buffered saline (PBS) buffer (30%

w/v) and sterilized by gamma irradiation (20 kGy; 2 kGy/h), by IONISOS (Dagneux, France). ADH solution was prepared in phosphate-buffered saline (PBS) buffer as well (3.76 % w/v) and sterilized by filtration with a 0.22 µm pore filter membrane (Pall Corporation, USA). ODEX and ADH solutions were used in a volume ratio of 7:3 to prepare *in vivo* formulations.

5.2.3. Preparation of Bonelike® Poro

BL®P was prepared as previously reported^{42,43}. Briefly, HA powder and P₂O₅-CaO-based glass were individually prepared and mixed. To prepare P₂O₅-CaO phase, appropriate quantities of Na₂CO₃, CaHPO₄, CaF₂, and P₂O₅ were mixed and heated up to 1450 °C, for 90 min, in a glass furnace and poured into deionized water, then crushed in an agate mortar and sieved to obtain a fine glass powder with a particle size below 50 µm. BL®P was obtained by mixing 2.5 wt% of this glass powder with 97.5 wt% of HA, and then further mixed with pore-forming agents, microcrystalline cellulose and PVA, to obtain the micro and macroporous structure. The resulting mixture was dried at 60 °C for two days and samples were sintered at 1300 °C for 1 h, using a heating rate of 4 °C/min, then milled to the desired granule size. BL®P of 250 - 500 µm granule size was obtained, displaying a macroporous structure with interconnective porosity. **Table 5.1** shows BL®P composition and properties were characterized by chemical analysis, X-ray diffraction (phases quantification), scanning electron microscopy (morphology), and mercury porosimetry (porosity).

Table 5.1 – Composition and properties of BL®P.

Material	Ca/P ratio	HA (%)	α-TCP (%)	β-TCP (%)	Ions	Granules Size (µm)	Surface Area (m²/g)	Porosity (%)
BL®P	1.70	75 ± 2	15 ± 2	8.0 ± 1.1	Ca ²⁺ , PO ₄ ³⁻ , F ⁻	250 - 500	7.237	65

HA, Hydroxyapatite; BL®P, Bonelike® Poro; TCP, Tricalcium phosphate.

5.2.4. Bonelike® Poro Dissolution Behaviour

The dissolution behaviour of BL®P was determined by measuring the concentration of calcium (Ca²⁺) ions released into solution, using inductively coupled plasma optical emission spectroscopy, ICP-OES (Optima 8000, PerkinElmer). In short, the dissolution rate was measured by immersing BL®P (30 ± 0.2 mg) in

PBS buffer (without Ca²⁺ and Mg²⁺, BioConcept Ltd.) pH 7.2, and in ODEX solution (30 % p/v) with PBS in a 7:3 ratio at pH 5.2, i.e., using the HG components without ADH, to prevent gelling, at 37 °C, under mild agitation. Samples (n = 5) were collected at defined time-points, then diluted with ultra-pure water, filtered through a membrane with a 0.22 µm pore size and a few drops of nitric acid, HNO₃, (Fisher, Loughborough, UK, 69%) were added before analysis. A standard curve between 0.05 mg/L and 40 mg/L was prepared in nitric acid (5 %) and plotted before analyzing samples. The operating conditions of ICP-OES were as follows: RF (radio frequency) power: 1400 W, argon plasma flow: 12 L/min, auxiliary gas flow: 0.2 L/min, nebulizer gas flow: 0.7 L/min. The plasma view was axial and the wavelength used for Ca²⁺ analysis was 317.933nm.

5.2.5. Mechanical Test

Mechanical properties of empty or BL®P loaded HG samples were analyzed by uniaxial compression measurements on a TA HD Plus Texture Analyzer (Stable Micro Systems, UK), using a 25 mm aluminum probe. Test samples (5 mm thickness × 12 mm diameter) were poured into cylindrical molds and left crosslinking for 30 minutes before analysis. The force used to compress 70 % of the initial height was measured at a speed rate of 0.5 mm/s. A trigger force of 1 g was used. The rupture point was evaluated by the maximum peak of the stress–strain curve, and Young's modulus (E) was determined as the average of the slopes of the first linear interval in the range between 2–7 % deformation of the stress–strain curve. Tests were performed in triplicate.

5.2.6. Scanning Electron Microscopy

Dried BL®P granules before and after 15 days of immersion in PBS or ODEX were added to aluminum pin stubs with electrically conductive carbon adhesive tape (PELCO Tabs™) and 25 angstroms Au coated. The coated samples were then placed on a Phenom Standard Sample Holder and characterized using a desktop scanning electron microscope (SEM) (Phenom ProX, Netherlands) at 15Kv. Resulting images were acquired using ProSuite software v.3.0.

5.2.7. Human Dental Pulp Stem Cells Culture and Characterization

Cells were obtained from AllCell, LLC (Cat. DP0037F, Lot No. DPSC090411-01) and cultured under standard conditions (37°C, 95 % humidified atmosphere and 5 % CO₂) with αMem (32561029, Gibco®), supplemented with 10 % FBS (A31608-02, Gibco®) and 100 IU/ml penicillin, 0.1 mg/ml streptomycin

(15140122, Gibco®), 2.05 mg/ml amphotericin B (15290026, Gibco®). We have previously shown hDPSCs differentiation ability towards the osteogenic, chondrogenic and adipogenic cell lineages, and further MSCs' phenotype identification, assessed by flow cytometry and real-time polymerase chain reaction (RT-PCR)⁴⁴.

Each cell dosage was composed of 10⁶ viable hDPSCs at passage 4, suspended in 0.05 mL DPBS (14190144, Gibco®). Cell viability was assessed using the Trypan Blue™ exclusion assay, after trypsinization of the cells at passage 3. Cell population presented approximately 98% viability after trypsinization. Cell dosages of 10⁶ viable hDPSCs were prepared in DPBS, immediately prior to *in vivo* application. The use of hDPSCs was authorized by Direção-Geral da Saúde, DGS (**Appendix B**).

5.2.8. Preparation of Formulations for *In vivo* Implantation

To reach a final HG volume of 500 µL, 150 µL of ADH (3.76 %, w/v) and 350 µL of ODEX (30 %, w/v) were aliquoted separately. BL®P granules (0.29 g) were distributed in microtubes, representing 60% (w/v) of the HG (W_{BL}/V_{HG}). A dose of 10⁶ of hDPSCs were used per formulation. Cells were thawed and washed by centrifugation (270 g, 7 min) with culture medium to eliminate the cryoprotectant, dimethyl sulfoxide, and then washed with PBS to eliminate fetal bovine serum present in the culture medium, to avoid any undesired reaction. The final pellet was resuspended in 50 µL PBS. Formulations were prepared according to **Table 5.2**. When used without HG, BL®P granules were mixed with autologous blood prior to application. For injectable samples, BL®P granules were poured into ODEX solution and 50 µL of cell suspension in PBS were then added. ADH was mixed for crosslinking reaction, which took 20 to 30 min until a properly gelled and mouldable paste was achieved. For HG + BL®P formulation, 50 µL of empty PBS was added in substitution of cell suspension. The preparation and handling details are represented in **Figure 5.1**.

Table 5.2 – Composition of formulations applied *in vivo*.

Formulation	BL®P (60% W_{BL}/V_{HG})	hDPSCS	ODEX (30% W/V)	ADH (3.76 W/V)
BL®P	0.29 g	-	Autologous blood	
HG + BL®P	0.29 g	50 µL PBS	350 µL	150 µL
HG + BL®P + hDPSCS	0.29 g	10 ⁶ cells in 50 µL PBS	350 µL	150 µL

BL®P, Bonelike Poro; HG, hydrogel; hDPSCs, human dental pulp stem cells; ODEX, oxidized-dextrin; ADH, adipic acid dihydrazide.

5.2.9. Surgical Procedure

All procedures were in conformity with the Directive 2010/63/EU of the European Parliament and Portuguese legislation (Portaria 1005/92), and with the approval of the Portuguese Veterinary Authorities (Direção-Geral de Alimentação e Veterinária, DGAV – see **Appendix A**). *Ovis aries* (churra da terra quente sheep) were included this study: 10 healthy nonpregnant adult female individuals, with an average weight of ~40 kg and aged between 7 and 8 years. Animals were randomly sacrificed at weeks 3 and 6, 5 animals per time-point for bone deposition analysis. In each animal, four identical defects were performed in the calvaria and randomly filled with different formulations, as follows: i) no treatment (control); ii) BL®P; iii) HG + BL®P and iv) HG + BL®P + hDPSCs (**Figure 5.1**). The animals were pre-medicated with 0.1 mg/kg acepromazine and 0.01 mg/kg buprenorphine, with anaesthesia induction performed with 0.25 mg/kg diazepam, 5 mg/kg ketamine and 4 mg/kg propofol. Endotracheal intubation was performed by direct visualization using a rigid endoscope placed inside the endotracheal tube. Surgeries were conducted under inhaled general anaesthesia using isoflurane and intravenous fluid was provided at maintenance rate (NaCl 0,9% B Braun®). The skin was prepared by performing wool shaving and antiseptis with chlorhexidine 4 % and an incision was made along the sagittal plan from the base of the horns until the middle of the nasal bone, so that defects could be made in the calvaria. The periosteum was opened and full thickness critical-sized bone defects were performed in the frontal bone with a trephine (outer Ø 14 mm) overlying the frontal sinus, leaving the sinus mucosa and its fibrous connections intact. During this procedure, the bone was continuously irrigated with saline solution in order to avoid overheating and consequent bone necrosis. HG formulations were then placed in the defect with a syringe, excepting for the HG-depleted BL®P sample that was mixed with autologous blood. All treatments were sculpted within the defect with a spatula. Periosteum and soft tissues were closed in layers with resorbable sutures in a continuous pattern and the skin with an intradermic suture. The animals were set free and received analgesic medication for 4 days, with flunixin meglumine and antibiotic treatment for 7 days with amoxicilin. Animals were sacrificed with a lethal intravenous injection of 40% sodium pentobarbital (Euthasol®). The frontal bones were removed from the head using an oscillating saw, a hammer and an osteotome and then fixed in 4% formaldehyde solution and X-ray images were obtained. Then, each bone defect was sectioned using an oscillating saw and maintained in formaldehyde until analysis.

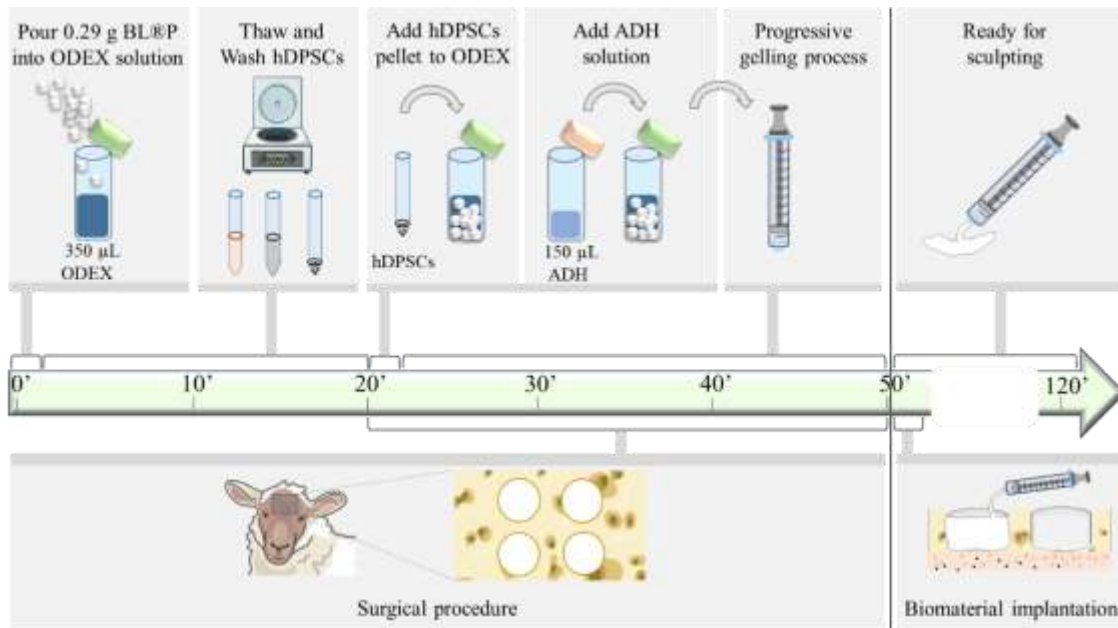


Figure 5.1 – Sequence of events demonstrating preparation and handling of hydrogel formulations, accompanying the surgical procedure time length. BL®P, Bonelike® Poro; ODEX, oxidized-dextrin; ADH, adipic dihydrazide; hDPSCs, human dental pulp stem cells.

5.2.10. Micro-computed Tomography Analysis

The micro-computed tomography (CT) images of the collected samples were obtained using SkyScan 1275 equipment (source voltage 80 kV and source current 125 μ A and with an acquisition time of 45 min) (Bruker, Karlsruhe, Germany). The images were reconstructed using Nrecon 1.7.5.0 software. For data analysis, samples were first aligned perpendicular to the skull surface and a volume of interest (VOI) with 300 slices was defined using DataViewer 1.5.6.3 software. Then, using CTanalyser 1.18.10.0 software, a circular region of interest (ROI) with a diameter of 13.9 mm was determined (**Figure 5.2**). The cut to start the data analysis was determined by the first lower cut that presented a closed bone circle. In order to characterize the different types of components existing in the samples three thresholds were defined: the one characterizing the ceramic granules (170 / 255); the one characterizing the previously existing bone (110 / 160) and the one characterizing the newly formed bone (85 / 255). The data analysis was performed firstly by subtracting in the ROI the existing bone with the 110 / 160 threshold and then determining the presence of granules with the 170 / 255 threshold and the formation of new bone with the 85 / 255 threshold.

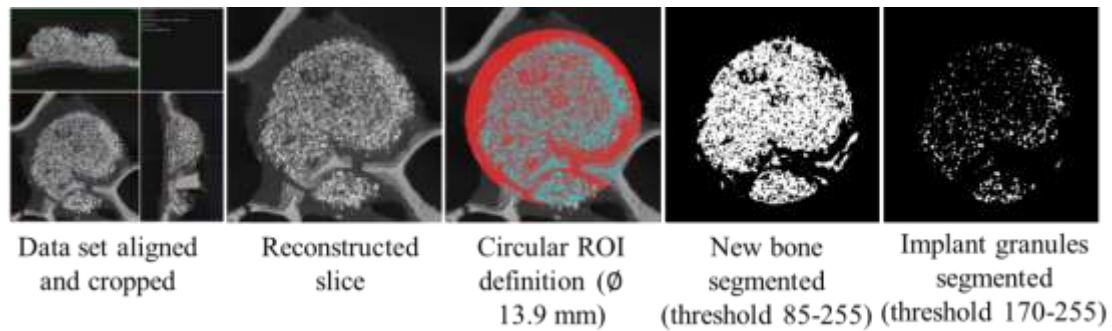


Figure 5.2 – Micro-computed tomography protocol visually exemplified. ROI, region of interest.

5.2.11. Histological Analysis

Bone samples kept in formaldehyde solution were decalcified with Surgipath decalcifier II (Leica Biosystems, USA), for at least 5 days, dehydrated and embedded in paraffin wax, in an automatic tissue processor Hypercenter XP (Shandon®, GMI Trusted Laboratory Solutions, USA). Consecutive 3 μ m sections were cut and stained with haematoxylin and eosin (H&E) and Masson's trichrome. Images were acquired using a Nikon VR microscope connected to a Nikon VR digital camera DXM1200.

5.2.12. Statistical Analysis

Experimental data were presented as mean \pm standard deviation (SD). Statistical analysis of data was performed by one-way analysis of variance (ANOVA) followed by the Tukey's post-test, a value of $p < 0.05$ (*) was considered to be significant. The analysis was performed using Prism Graph Pad 8.0.2 software® (Graph Pad Software, La Jolla, CA, USA).

5.3 Results

5.3.1 Human Dental Pulp Stem Cells Characterization

hDPSCs used in this experiment were previously characterized and published by Campos *et al*, 2019 ⁴¹.

Figure 5.3 shows hDPSCs morphology cultured at passage 3. Briefly, hDPSCs were demonstrated to present characteristic hMSCs' markers, as assessed through flow cytometry. Over 90% of the population was positive for CD90, CD105 and CD44, and $\leq 2\%$ were negative for CD34, CD11b, CD19, CD45 and MHC II. Gene expression was performed through RT-qPCR analysis. Total ribonucleic acid (RNA) was successfully extracted from cultured hDPSCs and specific gene expression was assessed. CD34 was not detected, as expected for hDPSCs. CD105, CD73 and CD90 were highly expressed; CD166, MHC I and

CD117 showed strong to moderate expression. Multipotency genes as Nanog, Oct4, Sox2, were also weakly expressed (Delta threshold cycle value >35). Moreover, weak expression of MHC class II was detected in hDPSCs by RT-qPCR analysis, however, membrane expression demonstrated by flow cytometry, was not detected. Tri-lineage differentiation was quantitatively evaluated through Oil Red O, Alizarin Red S and Sulphated Glycosaminoglycans protocols, to evaluate adipogenic, osteogenic and chondrogenic differentiation, respectively. Results demonstrated successful differentiation towards the three lineages, with significant differences from undifferentiated controls.

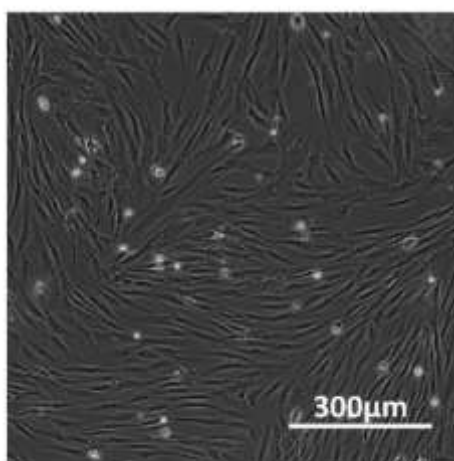


Figure 5.3 – Human dental pulp stem cells (hDPSCs) cultured at passage 3, with a ~90% confluency, prior to trypsinization, cell viability assessment by the Trypan Blue™ exclusion assay, and dosage preparation.

5.3.2 Dissolution Rate, Morphology and Mechanical Behaviour

Despite being mostly composed of HA, BL®P also possesses α -TCP and β -TCP phases (**Table 5.1**) which are much more soluble than HA. The dissolution rates of BL®P at different pH are summarized in **Figure 5.4**. In the weak acidic ODEX solution (pH 5.2), simulating the HG pH environment, BLP released Ca^{2+} ions at a faster rate compared to PBS (pH 7.2). **Figure 5.5** shows the BL®P morphology, exhibiting irregular structure with interconnected macropores from the nm (>200 nm) to the μm range at 4,500 \times magnification. No significant morphological differences were seen after 15 days of dissolution.

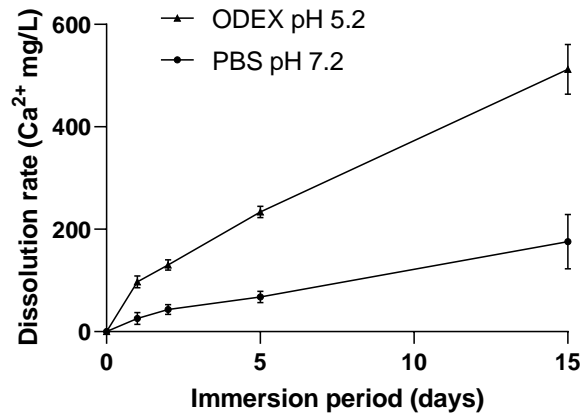


Figure 5.4 – Dissolution of Bonelike® Poro, expressed as the amount of calcium ions (Ca²⁺) release as a function of time in oxidized-dextrin (ODEX) solution pH 5.2, and phosphate-buffered saline (PBS) buffer pH 7.2, up to day 15. Data are presented as mean ± SD (n=5).

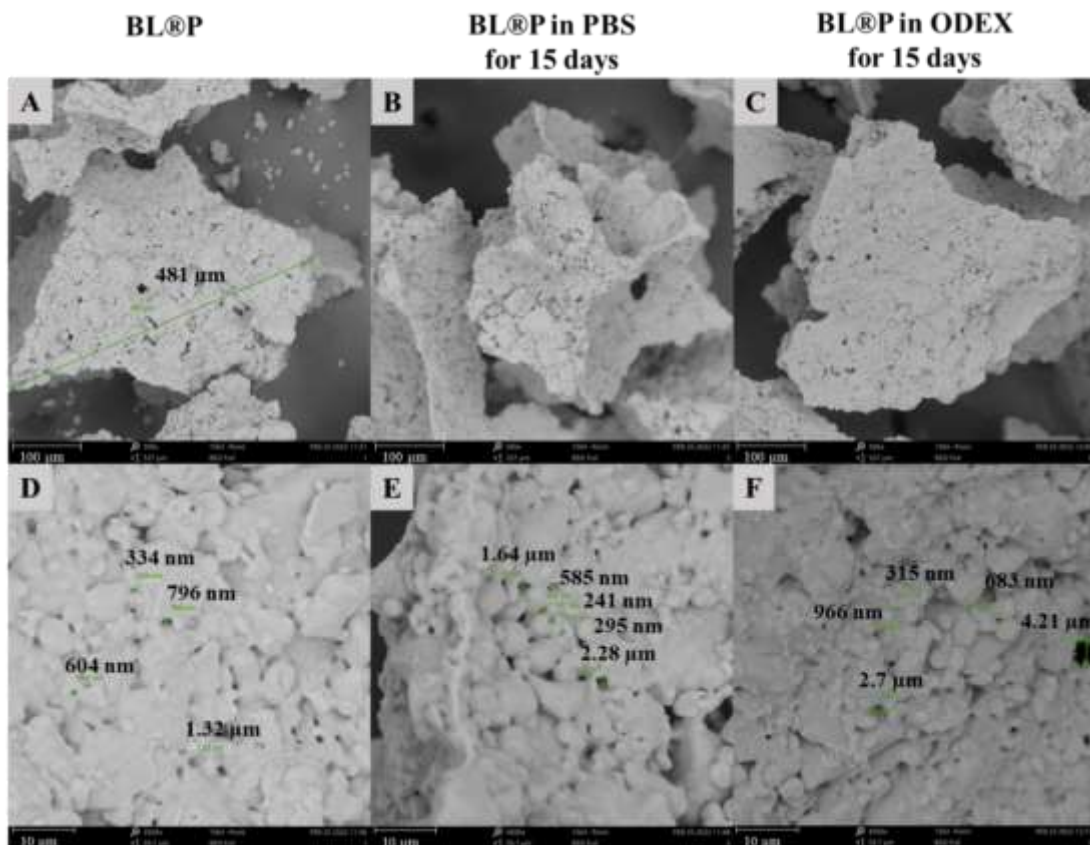


Figure 5.5 – SEM images of (A and D) Bonelike® Poro (BL®P) granules before immersion, (B and E) BL®P after 15 days of immersion in phosphate-buffered saline (PBS) solution and (C and F) in oxidized-dextrin (ODEX) solution. Macropores of BL®P are indicated by green arrows (A to C: 500× magnification, scale bars=100 μm, E to G: 4500× magnification, scale bars=10 μm).

A compressive test was performed on HG and HG + BL®P formulations with 5 mm thickness and 12 mm in diameter (**Figure 5.6**). The addition of BL®P to the HG increased its Young’s modulus and maximum compressive strength, from 0.163 ± 0.040 kPa to 0.400 ± 0.137 kPa and from 66.8 ± 6.5 kPa to 163.3 ± 13.2 kPa, respectively (**Table 5.3**). The HG + BL®P presents better mechanical properties, but insufficient to confer relevant load bearing ability to the composite.

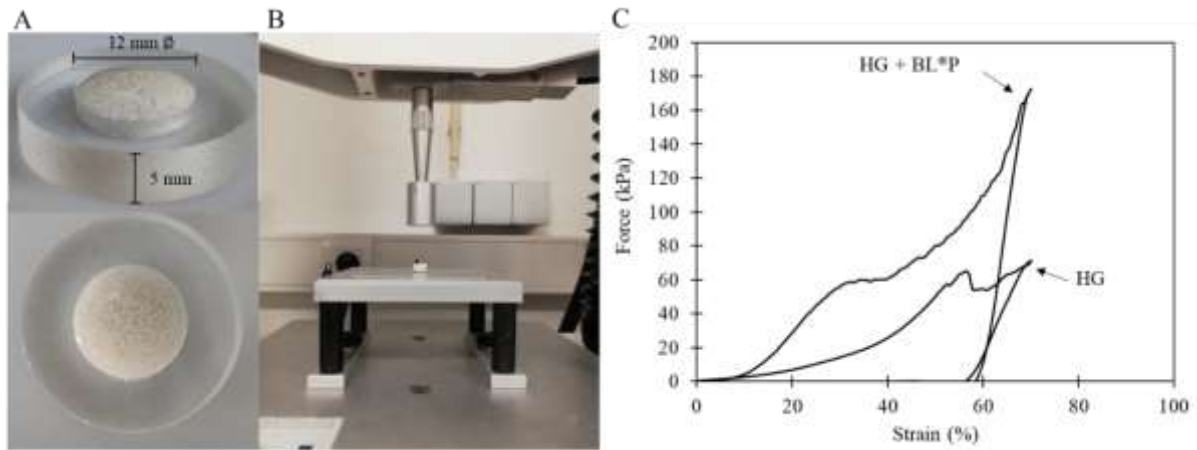


Figure 5.6 – Compressive test: preparation of (A) disc-form HG + BL®P material in 12-diameter molds before (B) positioned under the probe, and (C) stress–strain curves for HG and HG + BL®P formulations. Data are presented as mean \pm SD (n=3). HG, hydrogel; BL®P, Bonelike® Poro.

Table 5.3 – Compressive modulus, stress (at 70 % strain) for HG and HG + BL®P formulations. Data are presented as mean \pm SD (n=3).

Sample	Young’s modulus (<i>E</i>) [kPa]	Maximum compressive strength [kPa]
HG	0.163 ± 0.040	66.8 ± 6.5
HG + BL®P	0.400 ± 0.137	163.3 ± 13.2

HG, hydrogel; BL®P, Bonelike® Poro.

5.3.3 Surgical Analysis

The surgical procedure was simple and well tolerated by the animals. The HG formulations were convenient to handle and administered in one step, perfectly shaping to the defects up to the edges, without leaking granules. On the contrary, BL®P previously mixed with autologous blood, was implanted with a surgical spatula little by little, until complete defect filling, each time gently compressing in an attempt to stick the material together and prevent leakage out of the defect. Gelling time refers to the moment when samples become sticky enough as to properly being implanted without leakage. The more time, the stickier or harder the sample becomes. The addition of hDPSCs pellet (or empty PBS) to the pre-established 7:3 (v/v) (ODEX:ADH) HG formulation, diluting the sample, culminated in a gelling time around ~25 to 30 minutes, with no influence on handling, sculpting, cohesivity, injectability or any other formulation feature. A representative final aspect of the implantation sites is shown in **Figure 5.7A** and that of the harvested bone after the fixation process in **Figure 5.7B**. The post-surgery period was free of any complications (infections, abscesses or allergic reactions), and the surgical skin incision healed as expected. Also, no evidence of adverse tissue reaction nor infection were detected during bone sample harvesting.

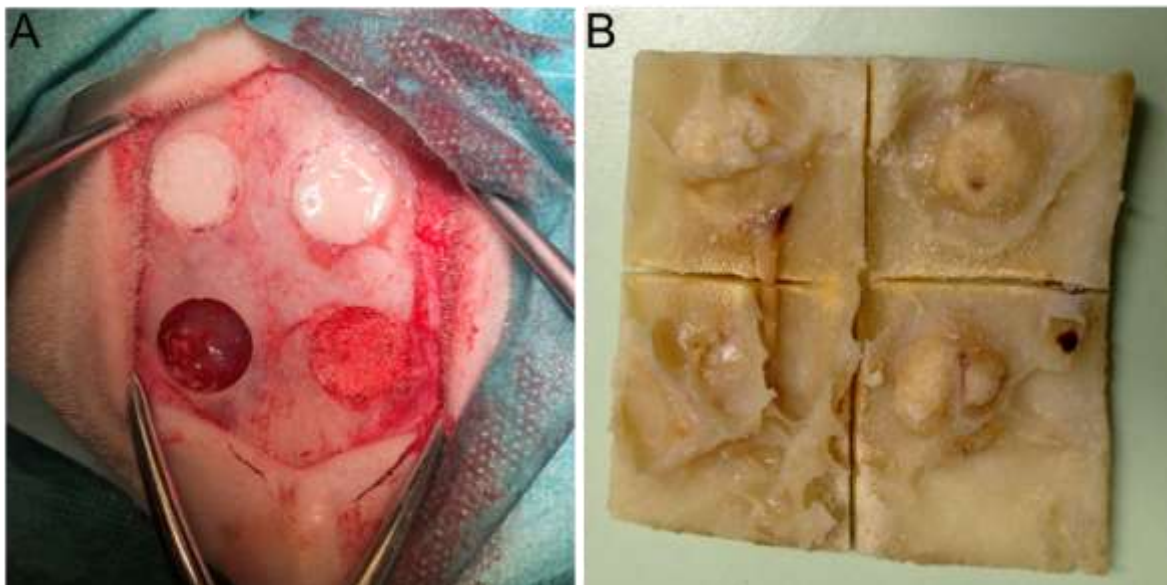


Figure 5.7 – **(A)** Frontal bone critical-sized defects performed in sheep, fulfilled with formulations: control (left-bottom); BL®P mixed with autologous blood (right-bottom); dextrin-based hydrogel (HG) + BL®P + hDPSCs (left-upper) and HG + BL®P (right-upper). **(B)** Harvested frontal bone after fixation. BL®P, Bonelike® Poro; HG, hydrogel; hDPSCs, human dental pulp stem cells.

5.3.4 Bone Regeneration of Critical-sized Defects

5.3.4.1 Micro-computed Tomography Analysis

Implantation sites were examined 3- and 6-weeks post-treatment. Micro-CT analysis provided visual proof of bone deposition in the whole implanted area in each time-point, further enabling the distinction between new bone and remaining granules (**Figure 5.8**). Control condition was not able to regenerate over time, presenting scarce and small ossification focus, whereas all the three BL®P treatments displayed considerable bone deposition. These conditions achieved an almost complete osteointegration up to week 6, excepting for the peripheral area and, in the case of HG formulations, few interspersed empty areas. The effect of the addition of the HG or hDPSCs to BL®P formulations can be more precisely distinguished in **Figure 5.9A** and **B**, where the volume of new bone, granules and total bone were quantified in mm³ (n=5). New bone and total bone volumes were not significantly different among treatments with and without HG, for both time-points, which demonstrates that the HG does not compromise the formation of new bone. These results also show that hDPSCs loaded into the HG and BL®P did not significantly enhance new bone formation for the specific conditions used and up to week 6 of tissue repair, though a tendency for more bone ingrowth may be denoted at early stage compared to the HG + BL®P formulation. At week 3, the remaining amount of granules was higher in the BL®P condition, as compared to the HG formulations (although not statistically significant - **Figure 5.9C**), which suggests a faster resorption in the presence of the HG, as shown previously in **Figure 5.4**. At week 6, the remaining granules are present in similar amounts for all formulations; although a trend towards lower amount of granules over time (week 6 versus week 3) is apparent, the difference is not significant, due to the low absorption rate of the biomaterial.

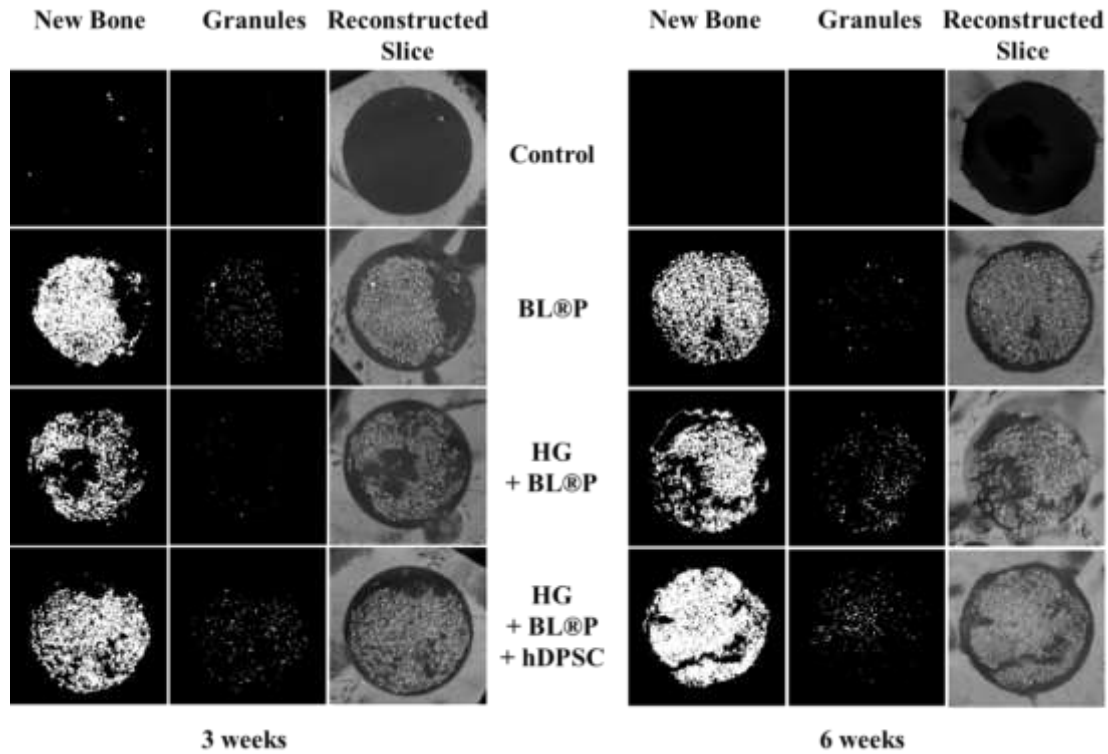


Figure 5.8 – Representative micro-computed tomography (CT) slice images of the implantation sites after 3 and 6 weeks of treatment with different formulations. BL®P, Bonelike® Poro; HG, hydrogel; hDPSCs, human dental pulp stem cells.

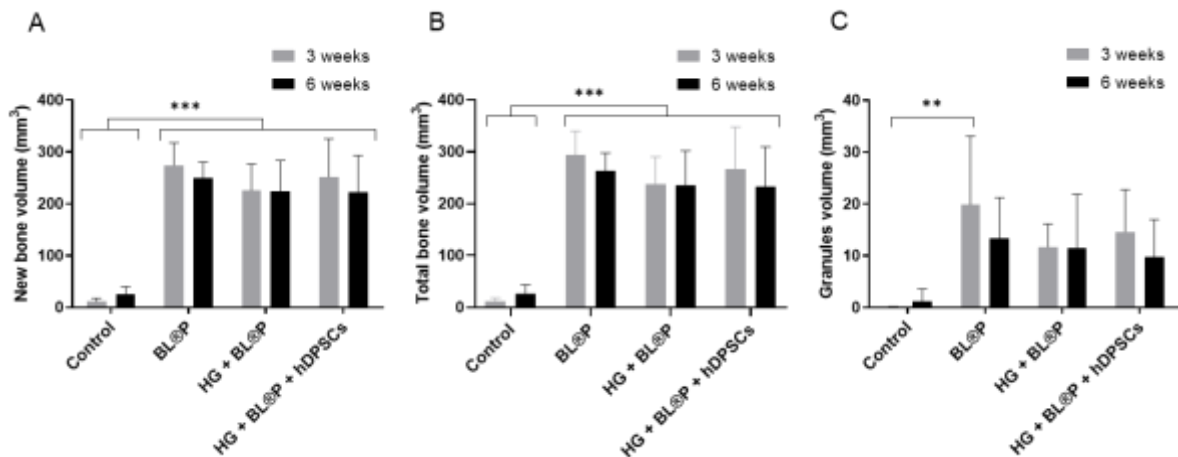


Figure 5.9 – Quantification of the new bone (A), total bone (B) and granules (C) volumes in implanted sites after 3 and 6 weeks of treatment. Total bone refers to the sum of new bone with granules. Statistical analysis was performed within each time-point using one-way analysis of variance (ANOVA) followed by the post-hoc Tukey test (** $p < 0.01$ and *** $p < 0.001$). Results are shown as mean values \pm SD ($n = 5$). BL®P, Bonelike® Poro; HG, hydrogel; hDPSCs, human dental pulp stem cells.

5.3.4.2 Histological Analysis

The tissue obtained after regeneration was further analysed histologically. **Figure 5.10** and **Figure 5.11** show H&E and Masson´s trichome staining, respectively. Three weeks post-surgery, defects without treatment (control) show dense connective tissue with scattered inflammatory cells and no signs of bone formation. Usually, all treatments presented new trabecular bone interspersed with connective tissue circling the granules, evidencing the presence of osteoblasts, osteoclasts and vessels. BL®P group induced a faster regenerative process, evidencing notorious mature bone with well differentiated osteocytes. Both the addition of HG and hDPSCs to BL®P granules showed no benefit in terms of bone formation at week 3, according to micro-CT analysis (**Figure 5.9**). Macrophage activity was detected around a material suspected being HG remains.

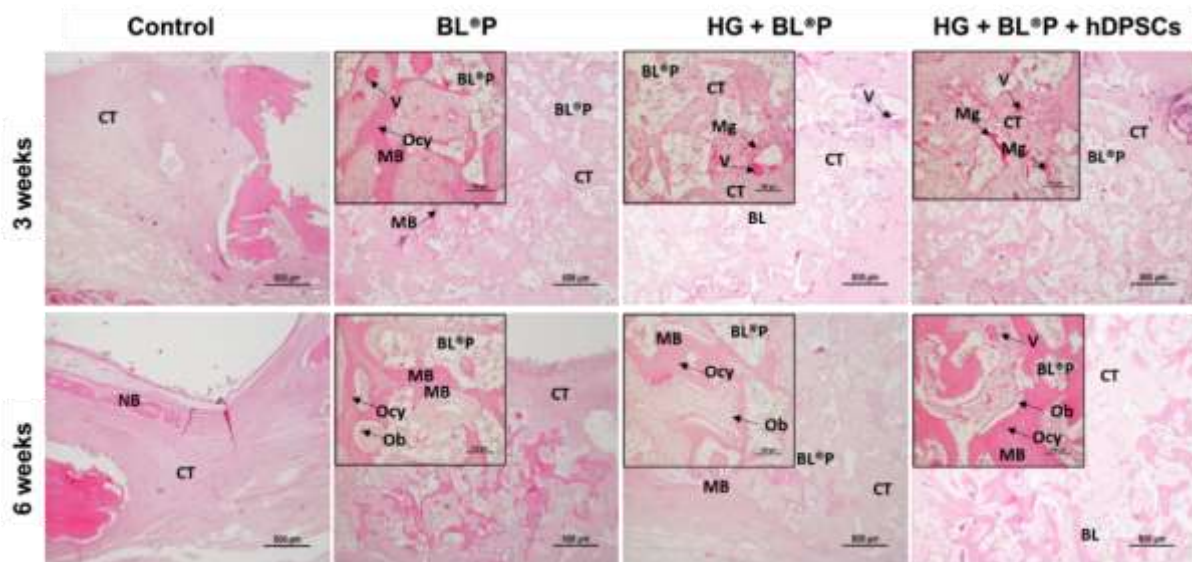


Figure 5.10 – Haematoxylin- and eosin-stained histological sections from implanted sites after 3 and 6 weeks of treatment. HG, hydrogel; hDPSCs, human dental pulp stem cells; BL®P, Bonelike® Poro granules; CT, connective tissue; NB, new bone; V, vessel; Ob, osteoblasts; Ocy, osteocytes; MB, mature bone; Mg, macrophage. Scale bar 500 µm (larger images) and 100 µm (smaller images).

At week 6, non-treated group confirmed the difficulty on developing new bone as expected for a critical-sized defect, showing dense connective tissue with few minor focus of ossification. Groups with HG+BL®P and HG + BL®P + hDPSCs evidenced the presence of larger amounts of mineralized bone (magenta color on Masson´s trichome stain) spread throughout almost the entire defect, engulfing granules of smaller size, accompanied by a decrease in fibrous tissue, as compared to week 3. The groups treated with BL®P granules presented several new vessels circling the biomaterial. No signs of HG remains was

noticed at this stage. Overall, the addition of HG and cells did not compromise nor accelerate bone formation, respectively.

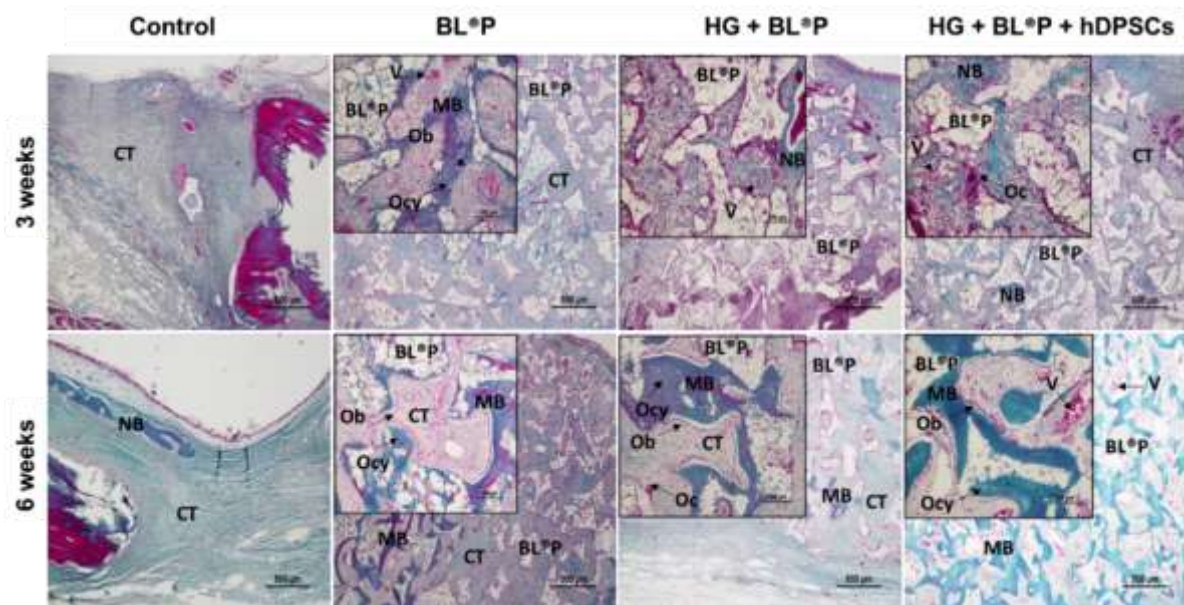


Figure 5.11 – Masson's trichrome-stained histological sections from implanted sites after 3 and 6 weeks of treatment. HG, hydrogel; hDPSCs, human dental pulp stem cells; BL®P, Bonelike® Poro granules; CT, connective tissue; NB, new bone; V, vessel; Ob, osteoblasts; Oc, osteoclasts; Ocy, osteocytes; MB, mature bone. Scale bar 500 µm (larger images) and 100 µm (smaller images).

5.4 Discussion

We hereby show the regeneration of full-thickness 14 mm Ø critical-sized defects performed in the calvaria of an ovine model, using a synthetic glass-reinforced HA bioceramic associated to an HG, further loaded with hDPSCs. Main features of the formulation include ease of preparation and administration, safety validation and bone deposition after 3 and 6 weeks of treatment.

Calcium ions release was nearly 3 times higher in acidic ODEX solution than in PBS at day 15, therefore expected to result in a faster BL®P dissolution rate *in vivo*. We have previously observed this outcome in other dextrin-based HG reinforced Bonelike® formulations applied *in vivo*⁶⁸. Indeed, the dissolution behavior of HA and TCP-based bone substitutes in weak acidic solution, mimicking Howship's lacunae, has been shown to be faster compared to physiological solution, mostly owing to the TCP phase⁴⁵. Though, significant morphological differences could not be noticed microscopically for up to 15 days of immersion. The HG exhibits a soft structure, and the incorporation of ceramic granules increased the stiffness of the material, providing a more stable 3D shape where granules are homogeneously distributed

within the bone defect. Stability of the 3D shape can be important to avoid defect collapse. Young's modulus and maximum compression strength increased by nearly 2.5 times by adding the mineral phase to the HG, though the material is still soft and moldable enough to fit non-regular shapes. Indeed, the addition of ceramic particles to hydrogels has been reported to reinforce mechanical properties simultaneously exhibiting moldability¹⁷. HG stiffness has been shown to have major impact on MSCs differentiation and fate⁴⁶⁻⁴⁸, playing a major role in fracture healing. The spreading capacity of umbilical cord MSCs and expression of osteoblastic makers were shown to be stronger as the stiffness of polyacrylamide gels increased (Young's modulus: 13-16, 35-38, 48-53, and 62-68 kPa)⁴⁷. The interplay between biomaterial composition, stiffness and cellular response should therefore be customized. Since this matter is highly target-specific, comparisons with data from the literature is not straightforward. In our case, ODEX HG may be customized by adjusting the HG to BL®P ratio or degree of crosslinking.

The surgical process was free of any complications. The administration of BL®P was more convenient when associated to the HG, which molded granules (250 – 500 µm) into a cohesive paste-like material suitable for injectability, within 25 to 30 minutes. The HG formulations were applied in one step without granules leakage, while granules embedded in blood required a multiple step administration-and-sculpt process. The addition of cells (or PBS) to the BL®P and HG components slightly delayed the gelling time by around ~10 min. The HG formulation is, therefore, suitable for holding small volumes of water-based bioactive agents, particularly those requiring immediate administration upon preparation, whereas autologous blood would not serve this purpose. In an attempt to deliver and retain Bonelike® granules and hDPSCs, fibrinogen and thrombin-based TISSEEL Lyo® glue of human origin was used in another work, evidencing the need for a vehicle or handling tool for this type of grafts⁴¹. Although generally safe, products derived from human blood cannot exclude the possibility of transmitting infections, or generate allergic or hypersensitivity reactions as with any protein-containing products. TISSEEL Lyo® mimics physiological clot and can only be applied topically or epilesionally as a thin layer, to maintain efficacy and avoid interference with the healing process, being also inadequate for injecting, as stated in the product's data sheet.

A 14 mm diameter defect was not able to regenerate up to week 6 without treatment. BL®P was an effective biomaterial for this critical-sized repair and the addition of HG did not compromise bone regeneration. The addition of hDPSCs at these specific conditions did not improve outcomes at weeks 3 and 6. As histologically observed, all treatments were free of any adverse reaction to the biomaterials used, providing safety validation of all intervening components: BL®P, HG an hDPSCs. Generally, granules were surrounded by new bone and connective tissue, evidencing the presence of osteoblasts,

osteoclasts and vessels, reflecting a good osseointegration and osteoconduction, as previously reported for other Bonelike® granules^{14,38}. At week 3, the presence of the HG formulations, irrespective of cells presence, exhibited a slight apparent delay on bone mineralization compared to BL®P granules, but later converged to much similar values at week 6, being indicative of HG degradation during the first weeks. Despite the higher BL®P dissolution rate observed *in vitro* in the presence of ODEX, granule degradation was not faster than that of bone formation *in vivo*, therefore still providing an adequate scaffold.

This work shows evidence that allogenic transplantation of hDPSCs is a safe therapeutic strategy for the repair of bone defects, although significant improvements on bone deposition could not be perceived. This may be explained by inadequacy of time-points or cell dose, for instance. In another work, a hDPSCs dose of 10^5 cells per 5 mm Ø defect (non-critical) was able to improve bone regeneration in an ovine model after 60 and 120 days, i.e. week 8 and 16. Therefore, a positive effect at later stages should not be excluded in this work, along with different cell dose. Moreover, large animals present large variability between individuals. With a limited number of animals, due to costs and ethical issues, a single cell dose of 10^6 was tested. Other doses should be addressed, together with different time-points. Yet, preliminary outcomes could be attained, such adding pre-clinical data on safety validation on host tissue-biomaterial interaction and cell transplantation methodology that can help designing future experimental set-ups. The conditions towards effective stem cell transplantation treatments in critical-sized defects needs more investigation for clinical translation.

5.5 Conclusion

The addition of HG to BL®P performed comparably to BL®P granules, enabling the regeneration of critical-sized bone defects and, therefore, validating its potential for clinical application as a tool to confer easy handling, injectability and moldability, while simultaneously acting as a carrier of cells for bone regeneration purposes. The HG is an advanced 3D carrier instead of a simple sticky binder. However, the presence of hDPSCs did not accelerate bone formation until week 6, although a positive effect at latter stages or with a different cell dose should not be excluded.

5.6 References

1. Schemitsch, E. H. Size Matters: Defining Critical in Bone Defect Size! *J. Orthop. Trauma* 31, S20–S22 (2017).
2. Bone Graft And Substitutes Market Size, Share & Trends Analysis Report By Material Type (Allograft, Synthetic), By Application (Craniofacial, Dental, Foot & Ankle), By Region, And Segment Forecasts, 2021 - 2028. Report GVR-1-68038-154-2. (Grand View Research, Inc. 2021).

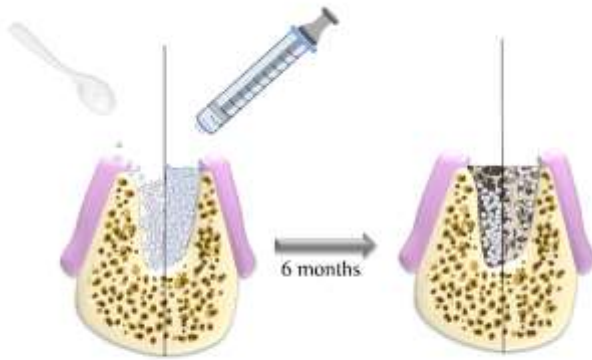
3. Gillman, C. E. & Jayasuriya, A. C. FDA-approved bone grafts and bone graft substitute devices in bone regeneration. *Mater. Sci. Eng. C* 130, 112466 (2021).
4. World Health Organization. Ageing and health. Date Accessed 2022-08-14. <https://www.who.int/news-room/fact-sheets/detail/ageing-and-health> (2021).
5. Fiume, E., Magnaterra, G., Rahdar, A., Verné, E. & Baino, F. Hydroxyapatite for Biomedical Applications: A Short Overview. *Ceramics* 4, 542–563 (2021).
6. Duarte, F., Santos, J. D. & Afonso, A. Medical Applications of Bonelike® in Maxillofacial Surgery. *Mater. Sci. Forum* 455–456, 370–373 (2004).
7. Gutierrez, M. *et al.* Biological Behaviour of Bonelike® Graft Implanted in the Tibia of Humans. *Key Eng. Mater.* 284–286, 1041–1044 (2005).
8. Gutierrez, M. *et al.* Histological and scanning electron microscopy analyses of bone/implant interface using the novel Bonelike® synthetic bone graft. *J. Orthop. Res.* 24, 953–958 (2006).
9. Lobato, J. V. *et al.* Titanium dental implants coated with Bonelike®: Clinical case report. *Thin Solid Films* 515, 279–284 (2006).
10. Lobato, J. V. *et al.* Clinical applications of titanium dental implants coated with glass-reinforced hydroxyapatite composite (Bonelike®). *Int. J. Nanomanuf.* 2, 135–148 (2008).
11. Gutierrez, M. *et al.* Opening wedge high tibial osteotomy using 3D biomodelling Bonelike® macroporous structures: Case report. *J. Mater. Sci. Mater. Med.* 18, 2377–2382 (2007).
12. Gutierrez, M. *et al.* Bone ingrowth in macroporous Bonelike® for orthopaedic applications. *Acta Biomater.* 4, 370–377 (2008).
13. Sousa, R. C. *et al.* A clinical report of bone regeneration in maxillofacial surgery using bonelike® synthetic bone graft. *J. Biomater. Appl.* 22, 373–385 (2008).
14. Pinto, P. O. *et al.* The application of Bonelike® Poro as a synthetic bone substitute for the management of critical-sized bone defects - A comparative approach to the autograft technique - A preliminary study. *Bone reports* 14, 101064 (2021).
15. ISO 13175-3. Implants for surgery – Calcium phosphates – Part 3: Hydroxyapatite and beta-tricalcium phosphate bone substitutes. (2012).
16. Abbasi, N., Hamlet, S., Love, R. M. & Nguyen, N. T. Porous scaffolds for bone regeneration. *J. Sci. Adv. Mater. Devices* 5, 1–9 (2020).
17. Iviglia, G. *et al.* Novel bioceramic-reinforced hydrogel for alveolar bone regeneration. *Acta Biomater.* 44, 97–109 (2016).
18. Patil, V. R., Kharat, A. H., Kulkarni, D. G., Kheur, S. M. & Bhonde, R. R. Long term explant culture for harvesting homogeneous population of human dental pulp stem cells. *Cell Biol. Int.* 42, 1602–1610 (2018).
19. Kot, M. *et al.* The Importance of HLA Assessment in “Off-the-Shelf” Allogeneic Mesenchymal Stem Cells Based-Therapies. *Int. J. Mol. Sci.* 20, 5680 (2019).
20. Awais, S., Balouch, S. S., Riaz, N. & Choudhery, M. S. Human Dental Pulp Stem Cells Exhibit Osteogenic Differentiation Potential. *Open Life Sci.* 15, 229 (2020).
21. Riccio, M. *et al.* Human dental pulp stem cells produce mineralized matrix in 2D and 3D cultures. *Eur. J. Histochem.* 54, 205–213 (2010).
22. Alge, D. L. *et al.* Donor-matched comparison of dental pulp stem cells and bone marrow-derived mesenchymal stem cells in a rat model. *J. Tissue Eng. Regen. Med.* 4, 73–81 (2010).
23. Lorusso, F. *et al.* Synthetic Scaffold/Dental Pulp Stem Cell (DPSC) Tissue Engineering Constructs for Bone Defect Treatment: An Animal Studies Literature Review. *Int. J. Mol. Sci.* 21, 9765 (2020).
24. Zhang, Z., Gan, Y., Guo, Y., Lu, X. & Li, X. Animal models of vertical bone augmentation (Review). *Exp. Ther. Med.* 22, 1–13 (2021).

25. Alvites, R. D. *et al.* Small Ruminants and Its Use in Regenerative Medicine: Recent Works and Future Perspectives. *Biol.* 10, 249 (2021).
26. Gómez-Mascaraque, L. G., Méndez, J. A., Fernández-Gutiérrez, M., Vázquez, B. & San Román, J. Oxidized dextrans as alternative crosslinking agents for polysaccharides: Application to hydrogels of agarose–chitosan. *Acta Biomater.* 10, 798–811 (2014).
27. Li, S., Xia, Y., Qiu, Y., Chen, X. & Shi, S. Preparation and property of starch nanoparticles reinforced aldehyde–hydrazide covalently crosslinked PNIPAM hydrogels. *J. Appl. Polym. Sci.* 135, 45761 (2018).
28. Wang, D. *et al.* Hydrogen-Bonding Reinforced Injectable Hydrogels: Application As a Thermo-Triggered Drug Controlled-Release System. *ACS Appl. Polym. Mater.* 2, 1587–1596 (2020).
29. Priya *et al.* Synthesis of dextrin-polyacrylamide and boric acid based tough and transparent, self-healing, superabsorbent film. *Int. J. Biol. Macromol.* 182, 712–721 (2021).
30. “Food And Drugs.” Code of Federal Regulations, title 21 (2021), Chapter I, Subchapter B, Part 184, Subpart B §184.1277.
31. Silva, D. M. *et al.* Structural analysis of dextrans and characterization of dextrin-based biomedical hydrogels. *Carbohydr. Polym.* 114, 458–466 (2014).
32. Hreczuk-Hirst, D., Chicco, D., German, L. & Duncan, R. Dextrans as potential carriers for drug targeting: tailored rates of dextrin degradation by introduction of pendant groups. *Int. J. Pharm.* 230, 57–66 (2001).
33. Kaneo, Y., Uemura, T., Tanaka, T. & Kanoh, S. Polysaccharides as drug carriers: biodisposition of fluorescein-labeled dextrans in mice. *Biol. Pharm. Bull.* 20, 181–187 (1997).
34. Asai, T. & Kawai, T. Bone filling material comprising sintered titanium dioxide and dextrin and method for reconstructing bone defects using the same. Patent US20120064172A1 (2010).
35. Molinos, M., Carvalho, V., Silva, D. M. & Gama, F. M. Development of a hybrid dextrin hydrogel encapsulating dextrin nanogel as protein delivery system. *Biomacromolecules* 13, 517–527 (2012).
36. Zhang, Z., He, C. & Chen, X. Hydrogels based on pH-responsive reversible carbon–nitrogen double-bond linkages for biomedical applications. *Mater. Chem. Front.* 2, 1765–1778 (2018).
37. Silva, D. M. *et al.* Inflammatory response to dextrin-based hydrogel associated with human mesenchymal stem cells, urinary bladder matrix and Bonelike® granules in rat subcutaneous implants. *Biomed. Mater.* 11, 065004 (2016).
38. Pereira, I. *et al.* Regeneration of critical-sized defects, in a goat model, using a dextrin-based hydrogel associated with granular synthetic bone substitute. *Regen. Biomater.* 8, 1–10 (2021).
39. Pereira, I. *et al.* In vivo systemic toxicity assessment of an oxidized dextrin-based hydrogel and its effectiveness as a carrier and stabilizer of granular synthetic bone substitutes. *J. Biomed. Mater. Res. Part A* 107, 1678–1689 (2019).
40. Pereira, I., Fraga, S., Silva, S., Teixeira, J. P. & Gama, M. In vitro genotoxicity assessment of an oxidized dextrin-based hydrogel for biomedical applications. *J. Appl. Toxicol.* 39, 639–649 (2019).
41. Campos, J. M. *et al.* Dental pulp stem cells and Bonelike® for bone regeneration in ovine model. *Regen. Biomater.* 6, 49–59 (2019).
42. Torres, J. *et al.* The benefit of bone marrow concentrate in addition to a glass-reinforced hydroxyapatite for bone regeneration: An in vivo ovine study. *J. Orthop. Res.* 35, 1176–1182 (2017).
43. Atayde, L. M. *et al.* Morphology effect of bioglass-reinforced hydroxyapatite (Bonelike®) on osteoregeneration. *J. Biomed. Mater. Res. Part B Appl. Biomater.* 103, 292–304 (2015).

44. Caseiro, A. R. *et al.* Mesenchymal Stem/ Stromal Cells metabolomic and bioactive factors profiles: A comparative analysis on the umbilical cord and dental pulp derived Stem/ Stromal Cells secretome. *PLoS One* 14, e0221378 (2019).
45. Ishikawa, K. *et al.* Physical and histological comparison of hydroxyapatite, carbonate apatite, and β -tricalcium phosphate bone substitutes. *Materials (Basel)*. 11, 1993 (2018).
46. Liu, Y. *et al.* Stiffness-mediated mesenchymal stem cell fate decision in 3D-bioprinted hydrogels. *Burn. trauma* 8, tkaa029 (2020).
47. Xu, J. *et al.* Effect of matrix stiffness on the proliferation and differentiation of umbilical cord mesenchymal stem cells. *Differentiation*. 96, 30–39 (2017).
48. Maia, F. R., Fonseca, K. B., Rodrigues, G., Granja, P. L. & Barrias, C. C. Matrix-driven formation of mesenchymal stem cell-extracellular matrix microtissues on soft alginate hydrogels. *Acta Biomater.* 10, 3197–3208 (2014).

CHAPTER 6

6. RANDOMIZED CLINICAL STUDY OF INJECTABLE DEXTRIN-BASED HYDROGEL AS A CARRIER OF A SYNTHETIC BONE SUBSTITUTE



This study aimed to improve the performance and mode of administration of a glass-reinforced hydroxyapatite synthetic bone substitute, Bonelike by Biosckin® (BL®), by association with a dextrin-based hydrogel, DEXGEL, to achieve an injectable and moldable device named DEXGEL Bone.

Twelve participants requiring pre-molar tooth extraction and implant placement were enrolled in this study. BL® granules (250-500 μm) were administered to 6 randomized participants whereas the other 6 received DEXGEL Bone. After 6 months, a bone biopsy of the grafted area was collected for histological and histomorphometric evaluation, prior to implant placement. The performance of DEXGEL Bone and BL® treatments on alveolar preservation were further analyzed by computed tomography and Hounsfield density analysis. Primary implant stability was analyzed by implant stability coefficient technique.

The healing of defects was free of any local or systemic complications. Both treatments showed good osseointegration with no signs of adverse reaction. DEXGEL Bone exhibited increased granules resorption ($p = 0.029$) accompanied by a tendency for more new bone ingrowth (although not statistically significant) compared to BL® group. The addition of DEXGEL to BL® granules did not compromise bone volume or density, being even beneficial for implant primary stability ($p = 0.017$). The hydrogel-reinforced biomaterial exhibited an easier handling, a better defect filling, and benefits in implant stability. This study validates DEXGEL Bone safety and performance as an injectable carrier of granular bone substitutes for alveolar ridge preservation.

Adapted from: *Clinical Oral Investigations*, (2022).

6.1 Introduction

Post-extraction bone remodeling is an inevitable natural phenomenon and can lead to significant ridge dimensional changes with loss of height and width of the alveolar bone ¹. Placing space-maintaining grafts in the edentulous site at the time of extraction is a common approach to prevent or minimize impairment of the supporting structures of an implant ². Bone regeneration procedures are essential to successfully settle an implant afterwards, restoring the site with satisfactory functionality and aesthetics. The design of shape fitting hydrogels (HGs) is a recent trend intended to circumvent the poor cohesivity and injectability that restrain bone substitutes use as bone fillers ³⁻⁵, conferring suitability for minimal invasive procedures.

DEXGEL is an *in situ* gelling hydrogel (WO/2011/070529A2) ⁶ with oxidized dextrin as the base component. Dextrin is a low cost, broadly available raw material derived from starch, widely used in many industrial applications and accepted as a generally recognized as safe (GRAS) food ingredient ⁷. Dextrin is available in medical grade, has high solubility in water and DMSO and holds hydroxyl groups suitable for bioconjugation, which has prompted this glucose polymer for several biomedical applications ⁸, including as hydrogels ⁹⁻¹¹. In this work, dextrin was firstly oxidized (ODEX) with sodium periodate to bear aldehyde groups suitable to cross-link with adipic acid dihydrazide (ADH) amine groups, without any chemical initiator that could be potentially harmful for any agents to be embedded within it ¹². ODEX and ADH are spontaneously stitched together upon contact by Schiff base reaction, creating hydrazone bonds ($R_2C=NNR_2$) ¹³. Hydrazone linkages are reversible in water ¹⁴, gradually dismantling the hydrogel network as the free and bound polymer chains reach for constant equilibrium. These dynamic covalent bonds endow HGs with injectability and moldability, acquiring a versatile array of shapes for a better defect filling.

The polysaccharide nature of DEXGEL mimics the extracellular matrix of native bone, offering excellent biocompatibility. We have previously reported DEXGEL suitability as a carrier of nanogels, cells, biomolecules and granular ceramics ^{12,15-18}. Moreover, biocompatibility, safety and effectiveness were assessed through a battery and a combination of *in vitro* and *in vivo* approaches. DEXGEL has demonstrated *in vitro* cyto- and genocompatibility ^{12,19}. *In vivo* biocompatibility and safety was demonstrated through the assessment of the inflammatory response in rat subcutaneous implants ¹⁶, subacute systemic toxicity and skin sensitization using rodent models ¹⁸. The effectiveness of the DEXGEL combined with BL® granules was demonstrated in two different bone defects: in goat critical-sized bone

defects¹⁷ and tibial fractures¹⁸. After extensive pre-clinic evaluation and formulation design, DEXGEL is ready for the first clinical assessment as an injectable and moldable carrier of BL® granules.

Bone graft synthetic substitutes are desired to overcome the limited source and significant morbidity associated with the harvesting of autologous bone grafts^{20,21}. BL®, property of Biosckin, Molecular and Cell Therapies, S.A. (WO2010021559A1)²², is a synthetic bone graft designed to mimic the inorganic composition of bone. It has been subject of extensive characterization and clinical evaluation, which provided the conformity of the material for human use²³⁻³⁰. Particularly, BL® granules (250 µm to 500 µm) have been used successfully in maxillofacial surgery to repair bone defects caused by removal of cysts and elevation of the maxillary sinus, resulting in partial regeneration of the bone defect with no adverse reaction³⁰ and recently functioned as a space filler in appendicular bone defects and maxillary / mandibular bone defects, promoting a faster bone fusion in 14 animals³¹. Although currently unavailable, this study intends to accelerate BL® (250 µm to 500 µm) market re-entry, now as an innovative injectable device.

This clinical study aimed to improve the performance and mode of administration of the glass-reinforced hydroxyapatite (HA) synthetic bone substitute, BL®, by association with dextrin-based hydrogel, DEXGEL, in the management of alveolar bone. Biocompatibility and bone ingrowth are crucial parameters to be examined for clinical acceptability. Herein, we report a study that aims to validate the clinical safety and efficacy of DEXGEL Bone (DEXGEL + BL®) for the treatment of bone defects through the following analysis: a) assess the capacity and performance of DEXGEL both as a bioceramic vehicle and an adjuvant matrix in the bone regeneration process; b) assess the volume and quality of regenerated bone; c) assess the primary stability of the dental implant; and d) assess granule stabilization and ease of clinical use. DEXGEL Bone will be applied as an intermediate alveolar regeneration procedure from tooth extraction moment to implant placement, aiming at achieving a volume of bone formed after 6 months equal to the initial post-extraction alveolar volume – primary endpoint.

6.2 Materials and methods

6.2.1 Study Design and Overall Clinical Procedures

G*Power 3.1.9.2 software was used a priori to define sample size (**Figure 6.1**). This pilot study was designed for a two-tailed analysis with Student's t-test or Wilcoxon signed rank test (depending on the normality of the results), with a confidence interval (statistical power) of 95% ($1-\beta=0.95$), with a probability of occurrence of a type 1 error of 5% ($\alpha=0.05$) and assuming an *effect size* *dz* of 2. The analysis

determined a total of 6 participants for each group were needed to meet aforementioned parameters for the primary endpoint of this study: the volume of bone formed after 6 months equals to the initial post-extraction alveolar volume. All of the participants underwent tooth extraction and socket preservation, with test and control group materials (parallel group design), for 6 months before implant placement.

The overall clinical study involved seven visits to the study facilities by each patient, as listed in **Table 6.1**. Postoperative clinical evaluations were performed after three, ten, and twenty-four days to determine the presence of any complications such as infection, inflammation, wound dehiscence or loss of graft material. After 6 months, clinical examinations were performed following implant placement. Afterwards, patients were still closely followed by the dentist over an extended period, however, with no relevance to this paper.

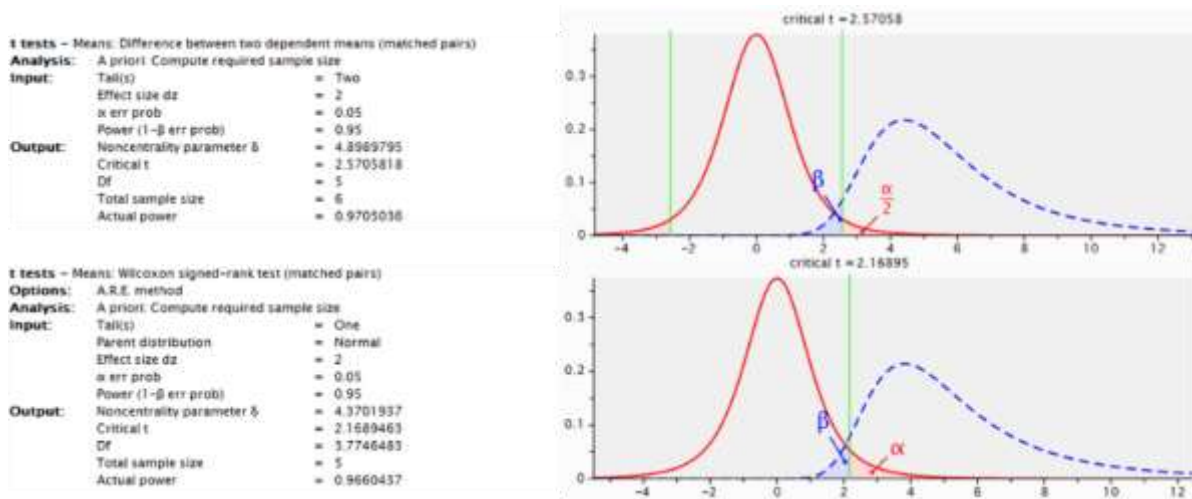


Figure 6.1 – Study designed for a two-tailed analysis with Student's t-test or Wilcoxon signed rank test (depending on the normality of the results), with a confidence interval (statistical power) of 95% (1-β=0.95). G*Power 3.1.9.2 software was used to define sample size.

Table 6.1 – Overall study procedures listed by order of accomplishment.

Medical visit	Main procedures
1st Recruitment interview	The candidate is invited to participate in the study, the anamnesis, inclusion and exclusion criteria are reviewed, and if the candidate is eligible to participate, the information leaflet and declaration of consent are signed.
2nd Pre-surgical visit	Computed tomography (CT). This visit could be done on the same day as the candidate's recruitment interview or the same day as the surgical visit).
3rd Surgical intervention	Surgery for tooth extraction, fill the alveolar socket with medical device and closure of the surgical wound.
4th First Check-up visit	3 days post-surgery: check-up for visual examination of the extraction site and tissue condition.
5th Second Check-up visit	1 week after first check-up visit: check-up for visual examination of the extraction site and tissue condition, and for suture removal.
6th Third Check-up visit	2 weeks after second check-up visit: check-up for visual examination of the extraction site and tissue condition.
7th Pre-surgical visit	6 months post-surgery: CT examination. This visit could be done few days before or on the same day as the surgical re-entry.
8th Surgical re-entry	6 months post-surgery: collect bone sample and evaluate tissue condition, following implant placement.

6.2.2 Recruitment

The recruitment process began with the dissemination of the clinical study within the Hospital da Luz, Coimbra. The selection of potential candidates was carried out based on patients with teeth with surgical indication for orthodontic treatment or with unviable teeth for recovery or reconstruction, or patients wishing to rehabilitate a lost dental piece by placing an implant in the upper premolars area. Patients who meet these criteria were informed about the clinical study. Those who showed interest in participating in the study were redirected to a recruitment interview. During the interview, disease diagnosis, inclusion and exclusion criteria were reviewed, and if the participant was eligible to participate, the information leaflet and the declaration of consent were signed. Specific inclusion and exclusion criteria are listed in **Table 6.2**. Twelve male and female adults (above 18 years), were assigned into two groups (**Table 6.3**), randomly allocated 6 to each group through a simple randomization methodology, according to the date of acceptance of the patients informed declaration of consent.

Table 6.2 – Inclusion and exclusion criteria.

Inclusion Criteria	Exclusion Criteria
<ul style="list-style-type: none"> ✓ Individuals requiring tooth extraction and dental implant replacement, in the upper premolars area. ✓ Skeletally mature individuals, aged between 18 and 65. ✓ Good general health. 	<ul style="list-style-type: none"> ✗ Individuals with premolars diagnosed with pulp necrosis and chronic endodontic and / or periodontal pathology involving changes in the alveolar bone (except teeth with endodontic pathology without symptoms of inflammatory and / or bacterial origin). ✗ Accidental avulsion. ✗ Individuals with acute or chronic infections, local or distant from the area to be submitted to surgery. ✗ Women who are pregnant, breastfeeding or intending to become pregnant during the study. ✗ Individuals with smoking, alcoholic habits or consumption of illegal substances. ✗ Individuals with medical contraindications (severe kidney disease, malignant tumors, uncontrolled diabetes, vascular or neurological damage, bone or metabolic diseases, patients with prosthetic valves and immunocompromised individuals). ✗ Individuals who are engaged to other clinical study or are still covered by a clinical study insurance. ✗ Individuals who demonstrate inability to follow up during the clinical study period.

Table 6.3 – List of participants.

Patient	1	2	3	4	5	6	7	8	9	10	11	12
Sex	M	F	F	F	F	M	M	M	F	F	F	M
Age	40★	41◆	66●	43★	40◆	48◆	41◆	48◆	51◆	47★	41◆	48◆
Tooth	24	24	14	25	14	15	14	14	24	14	24	25
Group	DEXGEL Bone (test)						BL® (control)					

● Extraction due to periodontal reason; ★Caries; ◆ Tooth/root fracture; F: female; M: male; BL®: Bonelike by Biosskin®.

6.2.3 Materials

All reagents used were of the highest degree of purity commercially available, suitable for biopharmaceutical production. Dextrin from Tackidex B 167 (Batch E8747) was kindly provided by Roquette (Lestrem, France), sodium *m*-periodate (CAS no. 7790-28-5) and diethylene glycol (CAS no. 111-46-6) were purchased from BIOCHEM Chemopharma (Cosne sur Loire, France). Adipic acid dihydrazide (ADH; CAS no. 1071-93-8) was supplied by Merck KGaA (Darmstadt, Germany) and endotoxin free phosphate-buffered saline (PBS; CAS no. 10049-21-5) by BioConcept (Allschwil, Switzerland). BL® was provided by Biosskin, Molecular and Cell Therapies, S.A. (Maia, Portugal).

6.2.4. Preparation of DEXGEL

Dextrin oxidation was performed as previously described³². Briefly, aqueous solutions of dextrin (2 % w/v) were oxidized with sodium *m*-periodate (NaIO₄), to yield the theoretical degree of oxidation of 40 %, at room temperature, with stirring, in the dark. The oxidation reaction was stopped after 20 hours by dropwise addition of an equimolar amount of diethylene glycol to reduce any unreacted periodate. Sodium *m*-periodate and diethylene glycol were removed by dialysis, using a 1000 Da cut-off membrane (Merck Millipore, Billerica, MA, USA), and then freeze-dried. ODEX was dissolved in phosphate-buffered saline (PBS) solution (30 % w/v) and sterilized by gamma irradiation (IONISOS, Dagneux, France), using a ⁶⁰Co source, at 20 kGy (2 kGy/h), at room temperature. ADH was also dissolved in PBS solution (3.76 % w/v) and sterilized by filtration, using a 0.22 µm pore filter membrane (Pall Corporation, Ann Arbor, MI, USA). For the crosslinking reaction, ODEX and ADH solutions were mixed in a 7:3 volume ratio, respectively. ODEX and ADH were packaged in separate microtubes, vacuum sealed and stored at 4 °C. Three samples of each were analyzed for endotoxin content by Biogerm, S.A. (Moreira, Portugal) and sterility by Sagilab Laboratório de Análises Técnicas, S.A. Heat-resistant laboratory materials were sterilized by autoclave, heat-sensitive materials were sterilized by ethylene oxide. Sterilization process and subsequent sterility validation were performed according to ISO 11137:2006³³ and ISO 11737: 2009³⁴ requirements, respectively.

6.2.5. Preparation of BL® Granules

BL® was ready in previous commercially available packages. The production procedure has been reported^{22,35}. Briefly, phase pure HA was prepared by the precipitation between calcium hydroxide

[Ca(OH)₂] (Prolabo, Paris, France) and orthophosphoric acid 85 wt % [H₃PO₄] (Merck, Darmstadt, Germany). Filtered and dried HA precipitate was ground into a fine powder, with a granulometry less than 75 μm. A P₂O₅-CaO-based glass with the composition of 65P₂O₅-15CaO-10CaF₂10Na₂O (mol%) was obtained by mixing the following reagent-grade chemicals: calcium hydrogen phosphate dehydrate (CaHPO₄ · 2H₂O; Sigma, St. Louis), disodium carbonate (Na₂CO₃; Panreac, Spain), calcium fluoride (CaF₂; Merck, Darmstadt, Germany) and phosphorus pentoxide (P₂O₅; Panreac, Spain). A frit was obtained at 1450 °C for 30min in a platinum crucible. Spherical granules were obtained by mixing 2.5 wt% of glass HA with a pore forming agent, via a dry process, at a rate up to 100 rpm. Then, the mixture was hydrated with purified water and submitted to malaxation. The resulting moist paste was extruded with an extrusion screen of 1 mm (Caleva Extruder 20, Caleva Process Solutions, Blandford, UK) and spheronized (Caleva Spheronizer 120, Caleva Process Solutions, Blandford, UK), and the pellets were then sintered at 1300 °C. Standard sieving techniques were used to obtain the 250–500 μm particle size ranges, displaying an interconnective microporosity structure. BL® was sterilized by gamma irradiation at 25 kGy in Centro de Higienização por Ionização de Produtos S.A., Instituto Tecnológico e Nuclear. (Lisboa, Portugal). **Table 6.4** shows a summary of BL® composition.

Table 6.4 – Composition of BL®.

Material	Ca/P ratio	HA (%)	α-TCP (%)	β-TCP (%)	Ions	Granules Size (μm)	Surface Area (m²/g)	Porous Size (μm)
BL®	1.70	81	17	<2	Ca ²⁺ ; PO ₄ ³⁻	250 - 500	0.368	0.7402 - 100.35

Ca/P, Calcium/Phosphate; HA, Hydroxyapatite; TCP, Tricalcium phosphate; Ca, calcium; BL®, Bonelike by Biosskin®.

6.2.6. DEXGEL Bone kit

DEXGEL Bone is an injectable, porous and osteoconductive bone substitute composed of two phases: (i) dextrin hydrogel matrix, DEXGEL - polymeric phase and (ii) BL®, composed mostly of HA, having a percentage of tricalcium phosphate - ceramic phase. DEXGEL Bone kit is composed of (i) four vials: one with the ODEX solution, another with ADH (both dissolved in PBS) and 2 vials of BL® with 0.5 g each;

(ii) a syringe with needle, to transfer ADH solution and subsequent mixing of all components; and (iii) a second syringe to apply the final formulation into the alveolar socket. Components must be mixed at the time of surgery by the medical team, according to a specific protocol (**Figure 6.2**). Each device was prepared for a final volume of 2 cm³, including 0.4 mL of ADH, 0.933 mL of ODEX and 1 g of BL®. BL® granules, 50 % v/v of the total volume of the final formulation (HG), were mixed with the ODEX solution and the reticulation was achieved adding the ADH solution prior to surgery, in a proportion of 7:3 (ODEX:ADH) volume ratio. DEXGEL Bone was ready for administration in a pre-gelled moldable form 5 minutes upon ADH addition.



Figure 6.2 – DEXGEL Bone preparation procedure.

Figure 6.3 shows the necessary time for device handling at the time of surgery, from components mixing to implantation. The preparation was performed by a technician the moment surgeon began the extraction process. Exodontia generally took five to ten minutes, which matched the time needed for device preparation. After properly gelled in the form of a moldable paste, DEXGEL Bone could be readily implanted or either rest for an extended period of two hours before implantation, as most convenient to the surgeon. Within this period the hydrogel matrix did not dehydrate, thus not compromising granules stabilization. Sculpting could be performed from one to two minutes. There was no need for a set time within the defect as in other grafting materials, the gum tissue can therefore be closed right after sculpting.

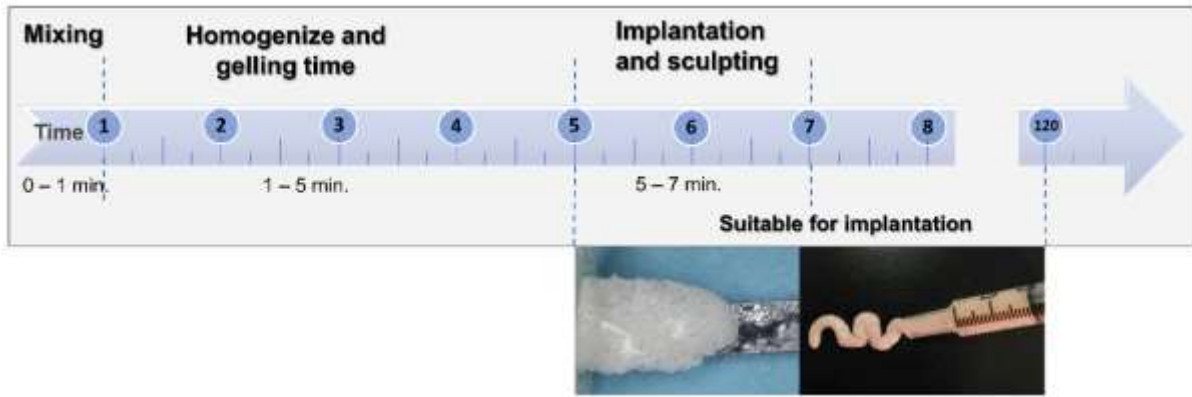


Figure 6.3 – Time-line for DEXGEL Bone preparation and handling.

6.2.7. Ethical Considerations

iBone Therapies (European Databank on Medical Devices, EUDAMED, No.: CIV-PT-18-01-02705; Protocol No.: EC.01.01.17), was previously approved by the Portuguese National Authority of Medicines and Health Products, I.P. (INFARMED), after submitted in National Registry of Clinical Studies (RNEC, No.: 30122), by National Ethics Commission for Clinical Research (CEIC, RNEC No.: 30121) and National Commission for the Protection of Data (CNPD). The production of DEXGEL was carried out in a cleanroom with ISO class 4 classification, suitable for the production of medical devices, at the facilities of RESDEVMED Unipessoal Lda (Ovar, Portugal). Qualified candidates were provided all the necessary clarifications so that they could make an informed consciousness decision. Twelve participants provided written informed consent. All participants were covered by a civil liability insurance from Haftpflichtverband der Deutschen Industrie (HDI) company. This study followed CONSORT (consolidated standards of reporting trials) 2010 statement guidelines for reporting parallel group randomized trials.

6.2.8. Surgical Procedure

6.2.8.1. Tooth Extraction and Biomaterial Implantation

The surgical intervention was performed by a dentist with experience in oral surgery and implantology at Hospital da Luz Coimbra (Coimbra, Portugal). After CT and X-ray examination, the patient was anesthetized with Artinibsa (Articaine + Epinephrine at a dosage of 72 mg/1.8 mL + 0.009 mg/1.8 mL, Inibsa Laboratories, Barcelona, Spain). The indicated tooth was extracted and alveolar curettage was performed for complete removal of injured tissue and tooth remains. DEXGEL Bone was applied using a syringe and sculpted with a spatula, filling the alveolar socket without exceeding alveolar crest. BL® was

mixed with autologous blood previously extracted from the alveolar defect, and applied with a spatula. Gum tissue was then sutured to end the process. Volunteers were prescribed with ibuprofen 600 mg (Brufen 600, Mylan, LDa., Lisboa, Portugal) from 12h to 12h for three days and amoxicillin 1 g (Cipamox, Laboratórios Vitória, Amadora, Portugal) from 12 h to 12 h for 8 days. In the case of allergy, azithromycin 500 mg (Zithromax, Pfizer, NY, USA) was prescribed once daily for three days.

6.2.8.2. Sample Collection and Implant Placement

Six months after the extraction, another CT and X-ray were performed to compare with the initial ones. The patient was anesthetized and the crestal incision was made. A bone sample for histologic analysis purpose was taken with a surgical trephine drill of 3 mm diameter and 10 mm length used vertically in occlusal- apical direction. After this step, titanium implants were finally placed according to the manufacturer (conical dental implant C1, MIS Implants Technologies Ltd., NC, United States.). The wound was closed with a pedicle rotated soft tissue graft from the palate, sutured with a 4-0 thickness PROLENE™ polypropylene suture (Ethicon®, Johnson & Johnson, NJ, USA), and another radiograph was performed. The sequence of major events for a DEXGEL Bone group volunteer is depicted in **Figure 6.4**.

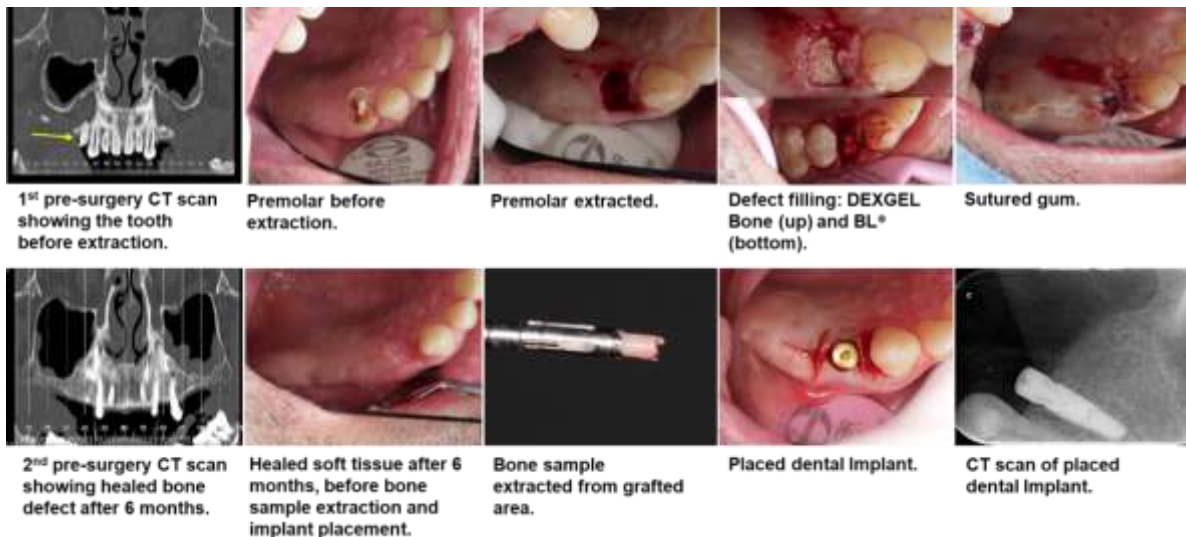


Figure 6.4 – Clinical images illustrating the procedures sequentially ordered from tooth extraction to dental implant placement.

6.2.9. Histological Analysis

Histomorphometric analysis were performed at the Hard Tissue Laboratory, Faculty of Medicine, University of Coimbra, Portugal. Bone biopsy samples measuring 6 to 8 mm in length were fixed with 10% formaldehyde (Panreac, Barcelona, Spain) solution buffered at pH 7.4 and stored at 4°C, until histology analysis of non-decalcified hard tissues with the high-precision Exakt® system (Exakt Technologies, OK, USA). The blocks were sectioned longitudinally in 50-100 µm thick slices, then stained with toluidine blue and examined with a light microscope (Nikon® Eclipse E600, Tokyo, Japan). The new bone formation, the remaining biomaterial and marrow space were quantified in percentages using Bioquant® (Image Analysis Corporation, Nashville, TN).

6.2.10. Computed Tomography

To examine alveolar preservation, CT scans were performed at two time-points: 1) previous to extraction), and 2) after 6 months of biomaterial implantation. Based on an axial section of the upper jaw, the respective curvature was traced, over which radial sections perpendicular to it were obtained, with 1 mm thick and 1 mm intervals. Also, 1 mm thick panoramic representations were obtained, one according to the curve mentioned above and also in the palatal and in the vestibular direction with 2 mm intervals.

6.2.11. Implant Stability Quotient

Implant Stability Quotient (ISQ) measurement unit was obtained by an advanced non-invasive technique based on resonance frequency analysis, RFA (Penguin^{RFA}, Göteborg, Sweden), commonly used to monitor implant stability. Briefly, a disposable Multipeg™ (metal transducer with a magnet top) was attached to the implant and magnetically stimulated to vibrate at a micro scale by a hand-held probe put closer by 2-4 mm towards the Multipeg™ top. Then the resonance frequency, i.e. the frequency with the strongest vibration, is measured in a few seconds. Readings were performed from the buccal-lingual and mesial-distal directions. This way, the stiffness of the implant-bone interface was measured and expressed as an ISQ dimensionless value within a scale from 1-100, in which the higher the ISQ, the lower the micromotion and the more stable the implant is. Degree of stability can be classified as low for an ISQ <60, high for an ISQ >70, and as medium for values in between. ISQ is an objective standard measure reflecting the degree of stability.

6.2.12. Statistical Analysis

In this study, histomorphometry, bone density, bone volume and primary stability of the implant were compared between test and control groups. Statistical differences in the percentage were assessed by unpaired Student's t-test and a value of $p < 0.05$ (*) was considered to be significant. Data are presented as mean \pm standard deviation (SD) ($n = 6$). The normal distribution of the data was assessed by Shapiro-Wilk test. The analysis was performed using Prism Graph Pad 8.02 software® (Graph Pad Software, La Jolla, CA, USA). Effect size was measured using Hedges's g formula ³⁶.

6.3 Results

From a commercial point-of-view, an extended shelf-life is important for any product. However, extended stability studies on hydrogels for biomedical applications are scarce in literature. The reticulation of DEXGEL is driven by covalent interactions between ODEX aldehydes and ADH amines and gelation time can be manipulated to vary between few seconds to several hours, depending on ODEX and ADH concentration or on the oxidation degree ¹². Thus, reduction on the content of reactive groups induced by any structural modifications, such as degradation, would interfere with the gelation period. We performed a gelation study using sterilized ODEX and ADH solutions stored at 4 °C for up to 3 years (**Table 6.5**). The term “gelation” here refers to the moment when it was no longer possible to pipette the hydrogel – which is the relevant form for clinical handling – irrespective of crosslinking extent reactions.

Table 6.5 – Gelation time of HG upon mixture of ODEX and ADH, expressed in seconds ($n = 3$). After production and sterilization, ODEX (30 % w/v) and ADH (3.76 % w/v) solutions were separately kept at 4 °C and a gelling test was performed at different time-points by mixing both in a proportion of 7:3 volume, respectively. Freshly prepared ADH was also used for crosslinking in each time-point with the ODEX stored over time.

Mixture (7:3 ratio)	Initial	3 months	1 year	3 years
ODEX + ADH	30 \pm 2 sec	30 \pm 2 sec	30 \pm 2 sec	-
ODEX + fresh ADH	30 \pm 2 sec	30 \pm 2 sec	30 \pm 2 sec	30 \pm 2 sec

ODEX, oxidized dextrin; ADH, Adipic dihydrazide.

ODEX was stable up to 3 years, whereas ADH solution was stable up to 1 year. Freshly prepared ADH enabled the demonstration of ODEX stability up to 3 years, inducing no changes in the gelation time.

6.3.1 Clinical Analysis

The CONSORT flow diagram is shown in **Figure 6.5**. One of the aims of this study included evaluating the capability of DEXGEL Bone to mold into the defect and stabilize BL® granules within it. The device fitted and completely filled the alveolar socket, without leakage of the granules. DEXGEL Bone displayed improved handling compared to BL® free granules, both during insertion into alveolus and sculpting, operations that were simple to perform and well tolerated by volunteers.

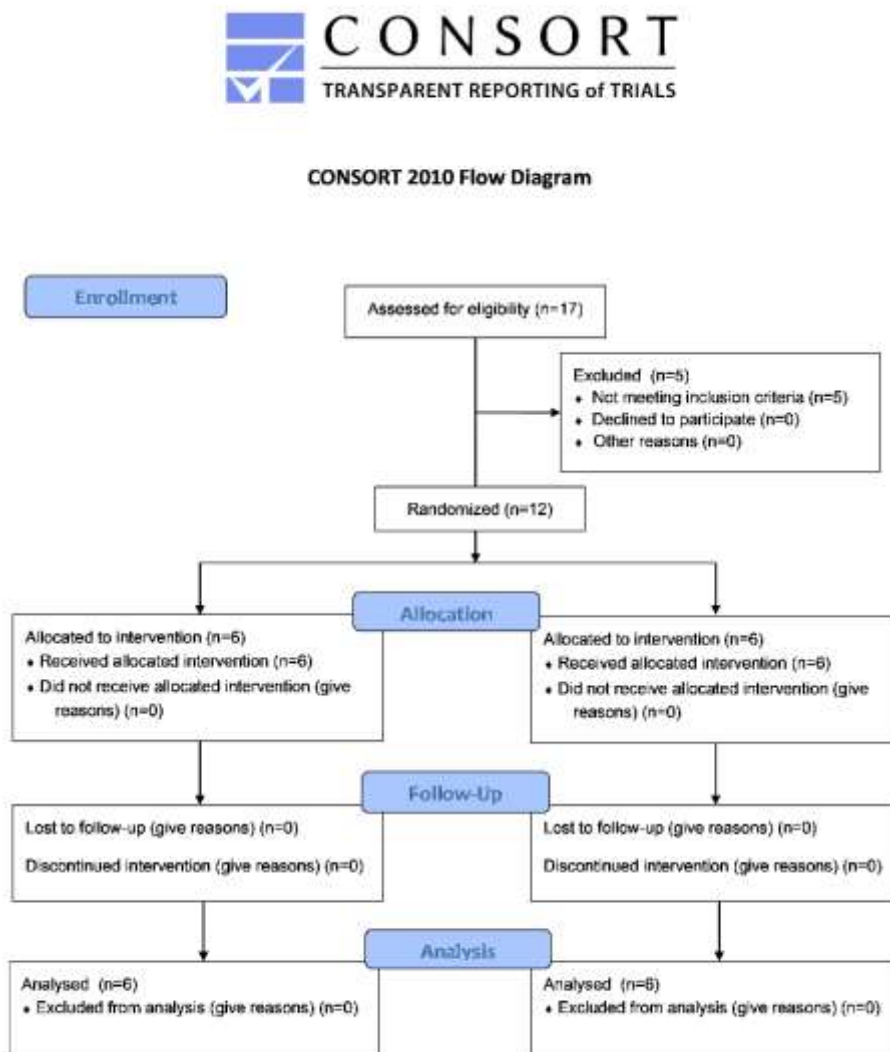


Figure 6.5 – CONSORT flow diagram of this study.

This study was carried out with no signs of local nor systemic complications or infection to any volunteer. Patients experienced the usual discomfort associated with oral surgery, with no correlation with grafting material. The sequence of events from exodontia to dental implant placement is shown in **Figure 6.4**. Six months post-grafting, a 2 mm x 10 mm bone sample was collected, and both DEXGEL Bone and BL® groups exhibited suitable bone density for dental implant placement in alveolus. At this stage, the polymeric matrix had already been reabsorbed and only BL® particulate remains were visible.

6.3.2 Histological and Histomorphometric Analysis

A qualitative evaluation of the bone tissue collected six months after implantation was performed by observation of toluidine blue stained slides. **Figure 6.6** shows the representative photomicrographs of the samples collected from each group.

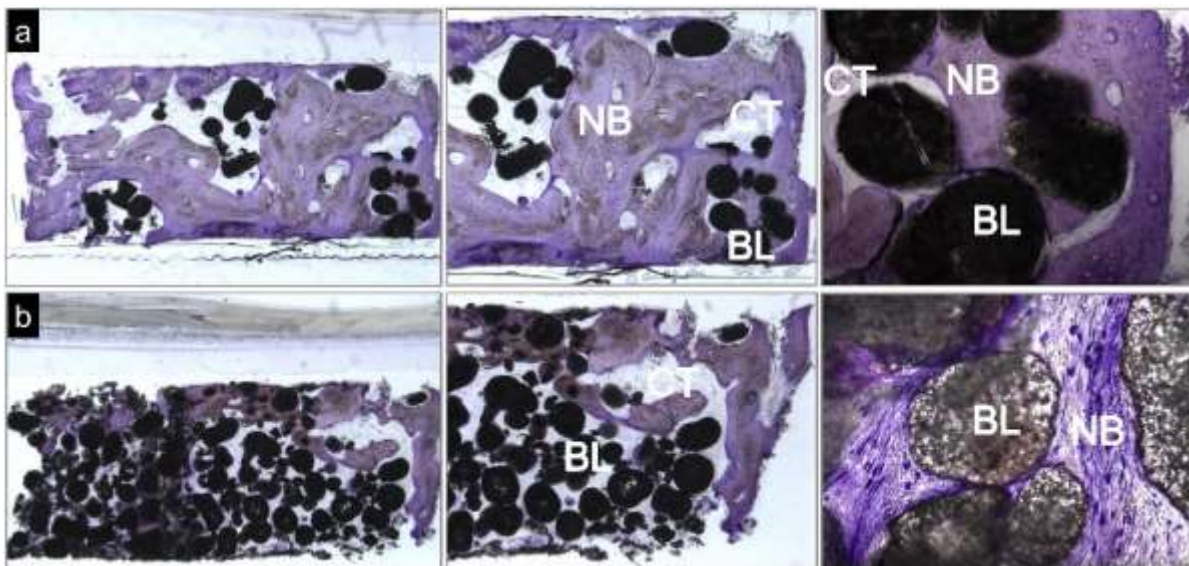


Figure 6.6 – Toluidine blue-stained representative photomicrographs of the grafted site 6 months post-implantation: **(a)** DEXGEL Bone group and **(b)** BL® group. New bone (NB), BL® remains (BL) and connective tissue (CT). Magnification from left to right: **(a)** 1×, 3× and 10×; **(b)** 1×, 3× and 20×.

Remains of the bone substitute were found in both conditions, in higher amounts in the BL® group. There were no signs of hydrogel after 6 months. New bone was formed on the surfaces and within granules, interspersed with connective tissue. The amount of new bone is notoriously higher in the DEXGEL Bone group. As an important indicator of biocompatibility, no signs of adverse inflammatory reaction were

evidenced in both groups. DEXGEL Bone seems to induce a faster new bone regeneration, less unfilled areas being noticed in the histological analysis.

The collected bone sample was also analyzed quantitatively with respect to new bone formation, biomaterial remains, and connective tissue (**Figure 6.7**). The use of DEXGEL Bone is considered effective since the total bone volume was similar to that of BL® group (**Figure 6.7a**). DEXGEL Bone might even be beneficial for bone regeneration since a mean of 49.7 % of new bone was reached compared to 32.4 % in BL® group, although the difference is not statistically significant (**Figure 6.7b**). Higher new bone ingrowth was accompanied by more extensive granule resorption (**Figure 6.7c**). Connective tissue ingrowth was similar in both groups, 34.0 % and 35.6 %, respectively (**Figure 6.7d**). Overall, DEXGEL accelerated BL® reabsorption without compromising (or even stimulating) faster bone growth.

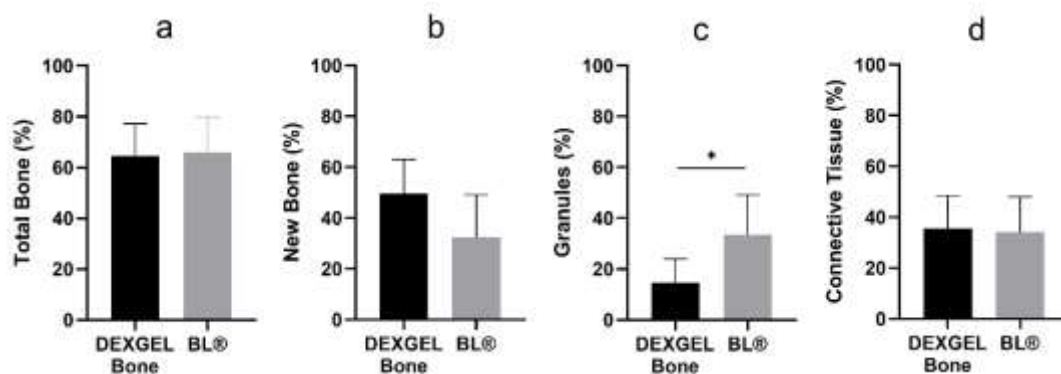


Figure 6.7 – Quantitative histomorphometric results of DEXGEL Bone and Bonelike by Bioskin® (BL®) conditions: total bone (**a**), new bone formation (**b**), reminiscent BL® granules (**c**), and connective tissue (**d**) 6 months after implantation. Statistical analysis was performed using Student’s t-test ($*p < 0.05$). Results are shown as mean percentages \pm SD ($n = 6$). Total bone refers to the sum of new bone with granules.

6.3.3 Bone Density and Volume

The main application of CT is the preoperative assessment of bone volume and density, providing an important tool for decision-making. Bone density is an important indicator of bone quality for a proper mechanical implant anchorage. Density (HU, Hounsfield units) was analyzed 6 months after biomaterial implantation, prior to implant placement. Five grades were established by Misch³⁷ to classify and distinguish bone from the highest to the lowest density: D1 (> 1250 HU); D2 (850 to 1250 HU); D3 (350 to 850 HU); D4 (150 to 350 HU); and D5 (< 150 HU) (**Table 6.6**). DEXGEL Bone group resulted in a

slightly lower density (924), compared to BL® (1114), although with no statistical significance for a $p < 0.05$ (**Table 6.7**). The mean value of both groups falls into D2 grade, characterized by porous cortical bone with coarse trabeculae, typically found in the anterior maxilla and the midpalatal region, consistent with the pre-molar area³⁸. D2 classification is indicative of a high strength bone.

Table 6.6 – Bone density classification by Misch³⁷.

Classification	Hounsfield Units	Description	Typical Anatomical location
D1	>1250	Dense cortical	Anterior mandible
D2	850-1250	Thick dense to porous cortical and coarse trabecular	Anterior and posterior mandible, anterior maxilla
D3	350-850	Thin porous cortical and fine trabecular	Posterior mandible, anterior and posterior maxilla
D4	150-350	Fine trabecular bone	Posterior maxilla
D5	<150	Poorly mineralized bone	

Table 6.7 – Bone density (HU) of DEXGEL Bone and BL® groups, for clinician interpretation. Results are shown as mean \pm SD (n = 6). The differences in bone volume and time-point between DEXGEL Bone (test) and Bonelike by Biosskin®, BL®, (control) groups were analyzed using Student's t-test ($p < 0.05$).

	DEXGEL Bone	BL®
Mean (HU)	924	1114
Standard deviation	168.44	125.00
Range	721 - 1145	997 - 1267
Bone quality (Misch³⁷)	D2	D2
p value	0.0516	

BL®, Bonelike by Biosskin®; HU, Hounsfield Units

To examine alveolar preservation, initial (post-extraction) bone volume was compared by CT scan to that obtained 6 months after implantation (**Figure 6.8**). Both groups showed a reduction after 6 months, from $7.73 \pm 2.99 \text{ cm}^3$ to $7.13 \pm 2.76 \text{ cm}^3$ in DEXGEL Bone, and from $5.32 \pm 2.84 \text{ cm}^3$ to $4.89 \pm 2.91 \text{ cm}^3$ in BL® group, corresponding to a variation mean of -7.91 % and -9.84 % respectively, although

without statistical significance. Nevertheless, results were more favorable to the DEXGEL Bone group. The addition of hydrogel, therefore, did not compromise bone volume formation.

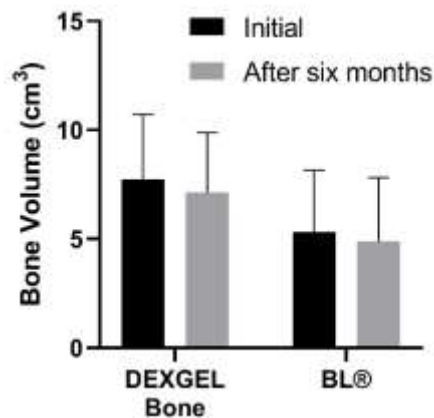


Figure 6.8 – Quantitative bone volume results (cm³) obtained from computer tomography (CT) analysis, at the implantation time and after 6 months. Results are shown as mean percentages \pm SD (n = 6). The differences in bone volume and time-point between DEXGEL Bone (test) and Bonelike by Biosskin®, BL®, (control) groups were analyzed using Student’s t-test ($*p < 0.05$).

6.3.4 Primary Stability of the Implant

ISQ analysis was used to evaluate primary stability, upon implant placement. The mean ISQ value for the DEXGEL Bone group was 79.7 ± 7.3 and 70.8 ± 2.0 for BL® group (**Figure 6.9**). Though the mean values obtained for both groups fall into a high stability classification (ISQ >70), the DEXGEL Bone group showed statistically superior stability ($p = 0.017$). In the DEXGEL Bone group, three out of 6 patients exhibited individual ISQ values from 82 to 90 and none below 70, while in BL® group no value above 74 was recorded, one individual presenting a value of 68. Therefore, the addition of the hydrogel matrix to BL® granules did not compromise bone quality in terms of stability, apparently being even beneficial for the subsequent restoration. Nevertheless, immediate implant loading with provisional prostheses was not performed in both groups to avoid mechanical pressure. Ten weeks post-implantation silicon impressions were taken and at week thirteen implants were loaded with the final restoration. No complications were detected during follow-up.

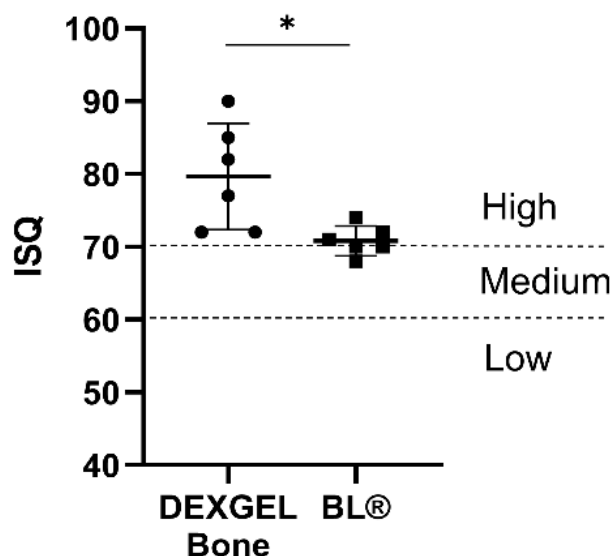


Figure 6.9 – Implant Stability Quotient (ISQ) results of DEXGEL Bone and Bonelike® (BL®) groups, upon dental implant placement. Statistical analysis was performed using Student’s t-test ($p < 0.05$). Results are shown as mean values \pm SD (n = 6).

Effect size is a quantitative measure of the magnitude of the experimental effect. A measure of 0.2, 0.5 and 0.8 are considered small, medium and large effect sizes, respectively. Effect size measures below 0.2 may express a negligible difference between two groups, even if statistically significant. **Table 6.8** displays the effect size values that show if the treatment as had a small, medium or large effect on the designated outcomes. Compared to BL® group, DEXGEL Bone exhibited a lost associated to a small effect size in total bone ($g = -0.11$) and large in granules ($g = -1.36$) and density ($g = -1.18$) outcomes, as expressed by the negative Hedges’ g value. Effect size measures were also small in the primary outcome for DEXGEL Bone ($g = -0.21$) and for BL® ($g = -0.15$), suggesting that the difference between initial bone volume and the same after 6 months is unimportant, as also indicated by a $p > 0.05$. Positive Hedges’ g expresses a gain associated with large effect size in respect to new bone ($g = 1.05$) and ISQ ($g = 1.52$) analysis, whereas small in connective tissue ($g = 0.11$).

Despite a non-significant p value, new bone and density outcomes show large effect sizes, being indicative of an advantageous stimulus to the regenerative process provided by DEXGEL Bone. The significant p value of granules quantification and ISQ are reinforced by large effect sizes, and non-significant p values are reinforced by a low effect size for total bone, connective tissue, and bone volume after 6 months.

Table 6.8 – Summary of mean and p value results, assessing the effect size of each outcome by Hedges' g calculations.

Outcome	Mean DEXGEL Bone (test)	Mean BL® (control)	p Value^b	Hedges' g^a
Total Bone (%)	64.4	66.0	0.847	-0.11
New Bone (%)	49.7	32.4	0.076	1.05
Granules (%)	14.7	33.6	0.029	-1.36
Connective Tissue (%)	35.6	34.0	0.847	0.11
Density (HU)	924	1114	0.052	-1.18
ISQ	79.7	70.8	0.017	1.52
	Mean (after 6 months)	Mean (initial)	p Value^b	Hedges' g^c
Bone volume (cm ³) for DEXGEL Bone	7.13	7.73	0.722	0.19
Bone volume (cm ³) for BL®	4.89	5.32	0.803	0.14

a The effect size was estimated by the difference (test – control) in mean change in the specified outcome measurement and represents the gain associated with treatment. **b** Significance probability associated with the Student's t-test performed to compare the means of test and control * $p < 0.05$). **c** The effect size was estimated by the difference (after – initial) in mean change in the specified outcome measurement and represents the gain associated with the 6 months' time-point.

6.4 Discussion

This is the first-in-human study of DEXGEL Bone on safety and efficacy. No local nor systemic complications or infections were identified and none of the participants were excluded from the study. A synthetic bone substitute, BL® (control) was compared to its hydrogel-reinforced version, DEXGEL Bone (test), in the preservation of the alveolar ridge dimensions following tooth extraction. Six months after exodonty and grafting, CT scans showed healed bone defects in both groups, suitable for bone sample collection and dental implant placement. The implants were eventually loaded with prostheses, generally 13 weeks post-implantation. Major outcomes of this study include handling properties, safety validation, assessment of bone quantity and quality, and primary stability of implant.

From a commercial point-of-view, an extended shelf-life is important for any product. However, extended stability studies on hydrogels for biomedical applications are scarce in literature. The reticulation of

DEXGEL is driven by covalent interactions between ODEX aldehydes and ADH amines and gelation time can be manipulated to vary between few seconds to several hours, depending on ODEX and ADH concentration or on the oxidation degree¹². Thus, reduction on the content of reactive groups induced by any structural modifications, such as degradation, would interfere with the gelation period. We performed a gelation study using sterilized ODEX and ADH solutions stored at 4 °C for up to 3 years. The term “gelation” here refers to the moment when it was no longer possible to pipette the hydrogel – which is the relevant form for clinical handling – irrespective of crosslinking extent reactions. The gelling time (30 seconds) of an ODEX mixture, prepared with fresh ADH, did not suffer any changes up to 3 years, demonstrating an excellent stability.

Stability and conformability are of particular importance, to avoid the release or migration of particles, assess difficult sites, mold to the defect and provide a reproducible and homogeneous mixing procedure convenient to the surgeon. Synthetic bone substitutes are now available in different forms, though with some shortcomings on handling properties. For instance, granules can migrate out of the defect during and after surgery; microporous blocks may be difficult to fit within the defect; cement paste might set too fast and, similar to putty, can be poorly injectable³⁹. The addition of DEXGEL to BL® improved granules cohesivity, by turning it into a moldable paste-like material, easy to administer with a syringe in the maxillary alveolar socket of the pre-molar area, avoiding granules leakage until wound closure. DEXGEL Bone is neither too liquid nor too viscous, therefore extrusion force was suitable as to provide an easy control of biomaterial outflow from the syringe opening¹⁸. BL® granules (mixed with autologous blood), on the other hand, had to be administered with a spatula and were prone to leakage during socket loading. Since DEXGEL is produced in separate from the bone substitute, combinations with other commercially available grafting materials can be considered. DEXGEL is able to pass through a needle (injectability), being the diameter of the opening limited by the size of the particles to which is combined. The association of this HG to a particulate bone substitute would enable further loading of molecules with bone healing or antimicrobial properties.

Clinically, no complications were observed and all participants healed normally. Histologically, both test and control groups showed good integration of grafting material into newly formed bone and were biologically compatible with the host tissues, showing no signs of adverse reaction. Photomicrographs confirmed the formation of vascularized mature bone and soft tissue matrix, confirming the osteoconductive character of both test and control groups. A considerably lower number of granules were visible in test group, interspaced by a thicker new bone formation, as compared to the control group. In accordance with histologic observations, histomorphometric examination showed DEXGEL accelerated

BL® reabsorption without compromising total bone growth, as we previously shown in the regeneration of critical-sized defects in a goat model ¹⁷. The higher rate of BL® granules resorption may have opened up space for more new bone ingrowth in the DEXGEL Bone group. The balance between resorption of a scaffold and its replacement by new bone formation is a key factor to shorten bone healing time. The addition of DEXGEL to BL® apparently optimized this balance. This higher resorption effect may be explained by the acidic character provided by aldehyde-bearing ODEX. The pH of ODEX solution around 3.0 increases to 4.7 after adding BL® granules in the first step of biomaterial preparation. The subsequent addition of ADH solution (pH=7.4) further increases pH of the final formulation to 5.2. After implantation, the more soluble TCP phase is prone to a faster resorption rate than HA ⁴⁰, which can be considerably accelerated by pH acidification ⁴¹.

Ideally, scaffold materials should degrade synchronously as new bone ingrowth takes place, without loss of mechanical support. As the bone regeneration process takes place, BL® is also resorbed in a slow and controlled manner, contributing to the natural remodeling of the bone ⁴². BL® is composed by modified HA ($\geq 50\%$) matrix, TCP and ionic species commonly found in human bone, i.e. magnesium, sodium and fluor ($\leq 50\%$). The addition of TCP phase confers a degradability character to the non-degradable HA ^{40,43}. TCP resorption mechanism is essentially cell-mediated ^{39,44}: bone remodeling cells, osteoclasts, release hydrochloric acid at the material surface, inducing calcium phosphate dissolution by acidification ⁴⁵. Polymer-based bone graft substitutes are resorbed by hydrolysis ³⁹. The reversibility nature of ADH and ODEX crosslinking ¹⁴ gradually releases 1-4 α -linked glucose dextrin, which can be enzymatically decomposed by blood α -amylases ⁴⁶. Dextrin and its degradation products can be metabolized or undergo renal elimination, owing to its low molecular weight (~ 2 kDa for Tackidex® B 167) below the renal filtration limit range (~ 30 – 50 kDa) ^{46,47}. Overall, DEXGEL Bone resorption can occur by several ways such as dissolution, cell-mediated dissolution, hydrolysis and enzymatic decomposition. Despite the favorable biodegradability, the use of polymeric bone grafters is restricted by limitations related to acidic degradation products that may accelerate implant deterioration and induce inflammatory reactions with negative implications for tissue repair ^{48,49}. In this study, DEXGEL was not detected 6 months post-treatment prior to implant placement, neither has ever been detected in previous pre-clinical studies from three weeks on ¹⁶⁻¹⁸. Interference with implants would not therefore be a concern. The HG improved the granules cohesivity and ease of handling at the time of administration, as intended (injectability and mouldability), then being fully resorbed rapidly, opening space for more new bone growth.

The success of dental implant placement relies on both the alveolar bone volume and density. The first may allow implant placement in the three-dimensionally correct position or, on the contrary, prevent its

placement due to inadequate bone dimensions. In this last case, a second regeneration treatment simultaneously with implant placement may be considered. The second may essentially influence the primary stability of the implant, its osseointegration and the timing of prostheses loading. Human studies on dimensional changes of undisturbed alveolar natural healing have reported horizontal bone loss of 29–63% and vertical bone loss of 11–22% at 6 months post-extraction⁵⁰. In this work, we report bone volume variation means of -7.91% and -9.84% for test and control group, respectively. The addition of HG showed no constraints on this parameter. Bone density could be defined as the amount of bone filling within a certain bone volume, being indicative of bone ability to ensure proper mechanical attachment of an implant⁵¹. Indeed, primary retention is achieved by mechanical means rather than through osseointegration. Implants on low density bone are more likely to fail⁵². In our study, DEXGEL Bone did not compromise the regeneration process, evidencing a good quality bone with a density classification of D2 (Misch³⁷), the typical structural conformation of a common pre-molar tooth region³⁸. With respect to strength, D1 and D4 bones are spaced by a 10-fold difference, which if converted to a scale of 1 to 10 from the least to the greatest strength, D1 could be seen as a 9 or 10, D2 a 7 or 8, D3 a 3 or 4 and D4 a 1 or 2³⁷. Implant failure has been reported as 5% in D1 bone, 2.2% in D2, 13.6% in D3 and 19.2% in D4⁵³. While a healing period of 3 to 4 months would be adequate for D1 and D2 before implant loading, 5 to 6 months would be required for D3 and D4.

ISQ can ultimately determine whether or not the implant will withstand the impact of a provisional or a final restoration, and the subsequent mechanical impact from masticatory forces when integrated in the overall dentition. ISQ is, therefore, important for decision-making during implant treatment and follow-up⁵⁴. Although both conditions occasioned an excellent ISQ mean (>70) at implant placement, administration of DEXGEL Bone generally resulted in a higher primary stability of dental implant, indicating that the presence of DEXGEL did not compromise immediate osseointegration, being even advantageous. In these cases, immediate implant loading is accepted. Higher ISQ may be explained by the higher tendency for more new bone ingrowth, as a positive linear correlation between both has been reported⁵¹. ISQ values were high even for HA grafted sites⁵⁵. ISQ changes over time are reported in many studies, describing an initial decline lasting from up to the first two weeks to three months, followed by gradual increase up to higher or similar values to the original one⁵⁶. Therefore, although ISQ evaluation taken later at restoration placement (secondary stability) seems more important for success predictability than at implant placement (primary stability)^{57,58}, initial ISQ values of this study may nevertheless be indicative of implant clinical success. These results further indicate that DEXGEL Bone would possibly enable the earlier placement of a final prosthesis, shortening the conventional period of 3 to 6 months, improving life quality

of the patient. This study also confirms that changing the physicochemical properties of a bone substitute material can influence implant stability.

In this study, we used the 250 - 500 μm spherical BL® which has shown to induce a slightly faster bone regeneration than 500 - 1000 μm ⁴². The presence of adequate pore dimension in BL® favors osteointegration, osteoconduction and degradation, allowing bone ingrowth in the interspaces, as it enables blood vessels and cell infiltration, exchange of proteins and nutrients and waste clearance. Overall, BL® provides an ideal environment for bone adhesion, cell proliferation and differentiation, has a slow and controlled resorption and contributes to natural bone remodeling. DEXGEL provides an easy and effective filling of bone defects according to its irregularities, given its excellent handling and molding properties. It was rapidly resorbed and accelerated BL® resorption as well, freeing up space that favored new bone ingrowth, without compromising mechanical support. The small population size is a limitation of this study, which however was adequate to prove the safety of this HG in its first contact with humans. Larger samples can now be considered in future studies. The present study validates DEXGEL Bone suitability for oral rehabilitation with endosseous implants, although other clinical scenarios may be considered.

6.5 Conclusion

DEXGEL Bone is a moldable, easy-to-apply bone regeneration optimized technology that naturally stimulates bone formation. The addition of DEXGEL to BL® granules provided the biomaterial with injectability without compromising bone volume nor density. DEXGEL Bone even showed a tendency for more new bone formation and maximized primary stability of the dental implant, which have reportedly a positive correlation. A clinical benefit is therefore achieved: improved granules cohesivity, easier handling, delivering (injectability) and sculpting of the biomaterial within the alveolar socket. DEXGEL Bone did not cause pain, discomfort or infections, being effective in alveolar ridge preservation. DEXGEL is easy to produce, cost-effective, has a long-shelf life and can provide benefits to commercially available grafting materials in terms of injectability, moldability and clinical performance. This *in situ* gelling HG further provides a platform for the entrapment of specific therapeutic agents to meet other clinical scenarios.

ETHICS APPROVAL

All procedures performed in this study involving human participants were in accordance with the ethical standards of the Portuguese INFARMED and with the 1964 Helsinki Declaration or comparable ethical standards. iBone Therapies (EUDAMED, No.: CIV-PT-18-01-02705; Protocol No.: EC.01.01.17, RNEC,

No.: 30122), was previously approved by INFARMED, CEIC and CNPD. All authorizations are shown in

Appendix C.

CONSENT TO PARTICIPATE AND TO PUBLISH

Informed consent was obtained from all individual participants included in the study. Research participants also provided informed consent regarding the publication of every information included in the present document.

6.6 References

1. Couso-Queiruga, E., Stuhr, S., Tattan, M., Chambrone, L. & Avila-Ortiz, G. Post-extraction dimensional changes: A systematic review and meta-analysis. *J. Clin. Periodontol.* 48, 127–145 (2021).
2. Khojasteh, A., Kheiri, L., Motamedian, S. R. & Khoshkam, V. Guided bone regeneration for the reconstruction of alveolar bone defects. *Ann. Maxillofac. Surg.* 7, 263 (2017).
3. Iviglia, G. *et al.* Novel bioceramic-reinforced hydrogel for alveolar bone regeneration. *Acta Biomater.* 44, 97–109 (2016).
4. Barbeck, M. *et al.* Implantation of an injectable bone substitute material enables integration following the principles of guided bone regeneration. *In Vivo* 34, 557–568 (2020).
5. Flegeau, K. *et al.* Injectable silanized hyaluronic acid hydrogel/biphasic calcium phosphate granule composites with improved handling and biodegradability promote bone regeneration in rabbits. *Biomater. Sci.* 9, 5640–5651 (2021).
6. Gama, M. & Molinos, M. Dextrin hydrogel for biomedical applications. Patent WO/2011/070529A2. (2011).
7. “Food And Drugs.” Code of Federal Regulations, title 21 (2021), Chapter I, Subchapter B, Part 184, Subpart B §184.1277.
8. Gonçalves, C., Moreira, S. M., Carvalho, V., Silva, D. M. & Gama, M. Dextrin. in *Encyclopedia of Biomedical Polymers and Polymeric Biomaterials* (ed. Mishra, M.) 2634–2649 (CRC Press, 2016).
9. Carvalho, J., Moreira, S., Maia, J. & Gama, F. M. Characterization of dextrin-based hydrogels: rheology, biocompatibility, and degradation. *J. Biomed. Mater. Res. A* 93, 389–399 (2010).
10. Carvalho, J., Gonçalves, C., Gil, A. M. & Gama, F. M. Production and characterization of a new dextrin based hydrogel. *Eur. Polym. J.* 43, 3050–3059 (2007).
11. Das, D. & Pal, S. Modified biopolymer-dextrin based crosslinked hydrogels: application in controlled drug delivery. *RSC Adv.* 5, 25014–25050 (2015).
12. Molinos, M., Carvalho, V., Silva, D. M. & Gama, F. M. Development of a hybrid dextrin hydrogel encapsulating dextrin nanogel as protein delivery system. *Biomacromolecules* 13, 517–527 (2012).
13. Xu, J., Liu, Y. & Hsu, S. Hydrogels based on schiff base linkages for biomedical applications. *Molecules* 24, 3005 (2019).
14. Zhang, Z., He, C. & Chen, X. Hydrogels based on pH-responsive reversible carbon–nitrogen double-bond linkages for biomedical applications. *Mater. Chem. Front.* 2, 1765–1778 (2018).
15. Silva, D. M. *et al.* Structural analysis of dextrans and characterization of dextrin-based biomedical hydrogels. *Carbohydr. Polym.* 114, 458–466 (2014).

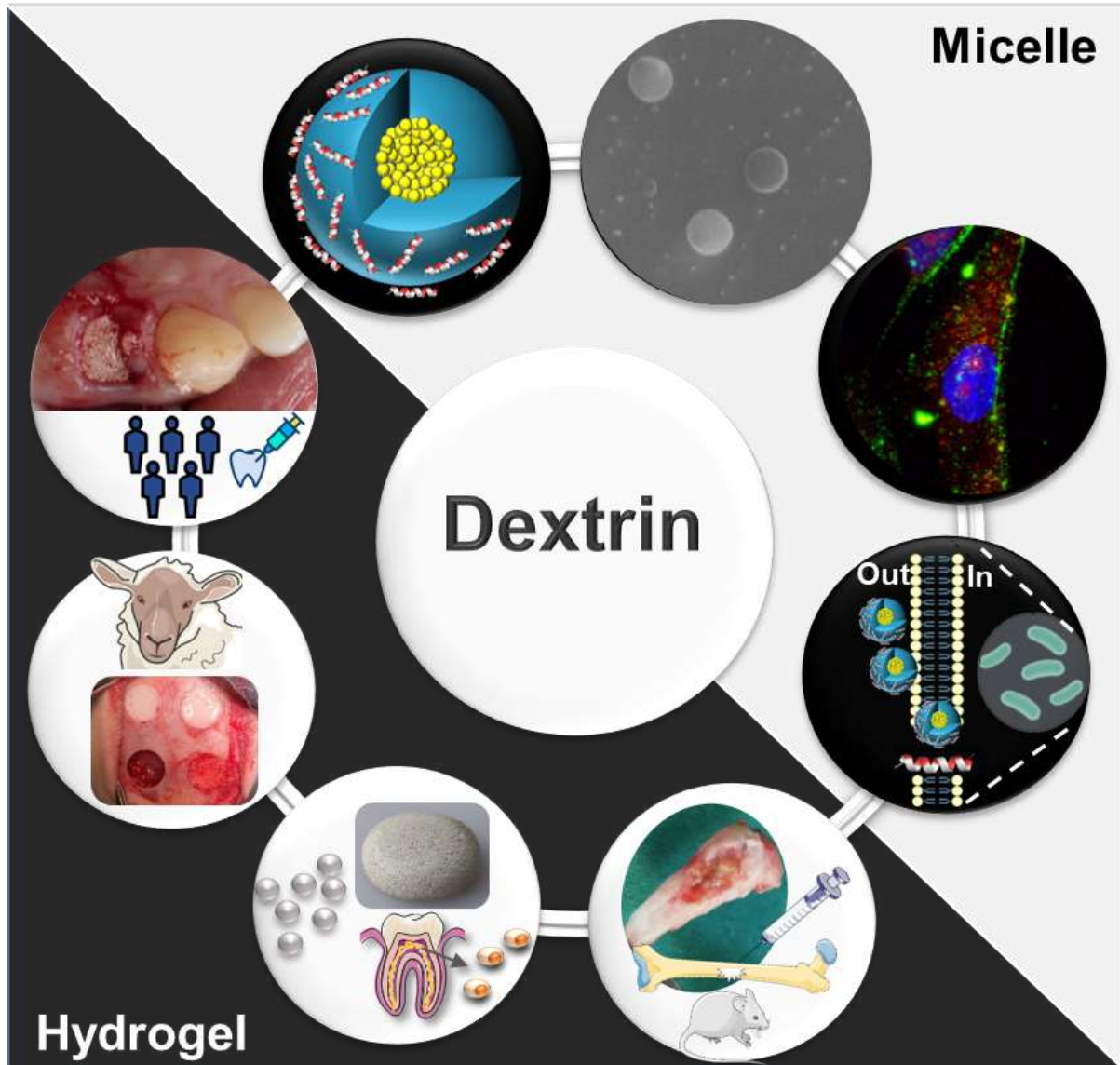
16. Silva, D. M. *et al.* Inflammatory response to dextrin-based hydrogel associated with human mesenchymal stem cells, urinary bladder matrix and Bonelike® granules in rat subcutaneous implants. *Biomed. Mater.* 11, 065004 (2016).
17. Pereira, I. *et al.* Regeneration of critical-sized defects, in a goat model, using a dextrin-based hydrogel associated with granular synthetic bone substitute. *Regen. Biomater.* 8, 1–10 (2021).
18. Pereira, I. *et al.* In vivo systemic toxicity assessment of an oxidized dextrin-based hydrogel and its effectiveness as a carrier and stabilizer of granular synthetic bone substitutes. *J. Biomed. Mater. Res. Part A* 107, 1678–1689 (2019).
19. Pereira, I., Fraga, S., Silva, S., Teixeira, J. P. & Gama, M. In vitro genotoxicity assessment of an oxidized dextrin-based hydrogel for biomedical applications. *J. Appl. Toxicol.* 39, 639–649 (2019).
20. Wang, W. & Yeung, K. W. K. Bone grafts and biomaterials substitutes for bone defect repair: A review. *Bioact. Mater.* 2, 224–247 (2017).
21. Papageorgiou, S. N., Papageorgiou, P. N., Deschner, J. & Götz, W. Comparative effectiveness of natural and synthetic bone grafts in oral and maxillofacial surgery prior to insertion of dental implants: Systematic review and network meta-analysis of parallel and cluster randomized controlled trials. *J. Dent.* 48, 1–8 (2016).
22. Santos, J. D., Lopes, M. A. & Silva, M. A. Hydroxyapatite and bioglass-based pellets, production process and applications of thereof. Patent EP2349361A1 (2008).
23. Duarte, F., Santos, J. D. & Afonso, A. Medical Applications of Bonelike® in Maxillofacial Surgery. *Mater. Sci. Forum* 455–456, 370–373 (2004).
24. Gutierrez, M. *et al.* Biological Behaviour of Bonelike® Graft Implanted in the Tibia of Humans. *Key Eng. Mater.* 284–286, 1041–1044 (2005).
25. Gutierrez, M. *et al.* Histological and scanning electron microscopy analyses of bone/implant interface using the novel Bonelike® synthetic bone graft. *J. Orthop. Res.* 24, 953–958 (2006).
26. Lobato, J. V. *et al.* Titanium dental implants coated with Bonelike®: Clinical case report. *Thin Solid Films* 515, 279–284 (2006).
27. Lobato, J. V. *et al.* Clinical applications of titanium dental implants coated with glass-reinforced hydroxyapatite composite (Bonelike®). *Int. J. Nanomanuf.* 2, 135–148 (2008).
28. Gutierrez, M. *et al.* Opening wedge high tibial osteotomy using 3D biomodelling Bonelike® macroporous structures: Case report. *J. Mater. Sci. Mater. Med.* 18, 2377–2382 (2007).
29. Gutierrez, M. *et al.* Bone ingrowth in macroporous Bonelike® for orthopaedic applications. *Acta Biomater.* 4, 370–377 (2008).
30. Sousa, R. C. *et al.* A clinical report of bone regeneration in maxillofacial surgery using bonelike® synthetic bone graft. *J. Biomater. Appl.* 22, 373–385 (2008).
31. Campos, J. M. *et al.* Application of Bonelike® as synthetic bone graft in orthopaedic and oral surgery in veterinary clinical cases. *Biomater. Res.* 22, 38 (2018).
32. Pereira, I. *et al.* Effects of gamma irradiation and periodate oxidation on the structure of dextrin assessed by mass spectrometry. *Eur. Polym. J.* 103, 158–169 (2018).
33. ISO 11137-1. Sterilization of health care products – Radiation – Part 1: Requirements for development, validation and routine control of a sterilization process for medical devices. (2006).
34. ISO 11737-2. Sterilization of medical devices – Microbiological methods – Part 2: Tests of sterility performed in the definition, validation and maintenance of a sterilization process. (2009).
35. Cortez, P. P. *et al.* Characterization and preliminary in vivo evaluation of a novel modified hydroxyapatite produced by extrusion and spheronization techniques. *J. Biomed. Mater. Res. B. Appl. Biomater.* 99, 170–179 (2011).
36. Lakens, D. Calculating and reporting effect sizes to facilitate cumulative science: A practical primer for t-tests and ANOVAs. *Front Psychol* 4, 863 (2013).

37. Misch, C. E. Bone Density: A Key Determinant for Treatment Planning. in *Dental Implant Prosthetics* (ed. Misch, C. E.) 237–252 (Mosby, 2015).
38. Kravitz, N. D., Kusnoto, B., Tsay, T. P. & Hohlt, W. F. The use of temporary anchorage devices for molar intrusion. *J. Am. Dent. Assoc.* 138, 56–64 (2007).
39. Bohner, M. Resorbable biomaterials as bone graft substitutes. *Mater. Today* 13, 24–30 (2010).
40. Daculsi, G., Legeros, R. Z., Nery, E., Lynch, K. & Kerebel, B. Transformation of biphasic calcium phosphate ceramics in vivo: Ultrastructural and physicochemical characterization. *J. Biomed. Mater. Res.* 23, 883–894 (1989).
41. Ishikawa, K. *et al.* Physical and histological comparison of hydroxyapatite, carbonate apatite, and β -tricalcium phosphate bone substitutes. *Materials (Basel)*. 11, 1993 (2018).
42. Atayde, L. M. *et al.* Morphology effect of bioglass-reinforced hydroxyapatite (Bonelike®) on osteoregeneration. *J. Biomed. Mater. Res. Part B Appl. Biomater.* 103, 292–304 (2015).
43. Pinto, P. O. *et al.* Therapeutic Strategies for Bone Regeneration: The Importance of Biomaterials Testing in Adequate Animal Models. in *Advanced Composite Materials* (eds. Tiwari, A., Alenezi, M. R. & Jun, S. C.) 275–319 (John Wiley & Sons, Ltd, 2016).
44. Sheikh, Z. *et al.* Mechanisms of in vivo degradation and resorption of calcium phosphate based biomaterials. *Materials (Basel)*. 8, 7913 (2015).
45. Heymann, D., Pradal, G. & Benahmed, M. Cellular mechanisms of calcium phosphate ceramic degradation. *Histol. Histopathol.* 14, 871–877 (1999).
46. Hreczuk-Hirst, D., Chicco, D., German, L. & Duncan, R. Dextrins as potential carriers for drug targeting: tailored rates of dextrin degradation by introduction of pendant groups. *Int. J. Pharm.* 230, 57–66 (2001).
47. Kaneo, Y., Uemura, T., Tanaka, T. & Kanoh, S. Polysaccharides as drug carriers: biodisposition of fluorescein-labeled dextrans in mice. *Biol. Pharm. Bull.* 20, 181–187 (1997).
48. Wei, S., Ma, J. X., Xu, L., Gu, X. S. & Ma, X. L. Biodegradable materials for bone defect repair. *Mil. Med. Res.* 7, 54 (2020).
49. Zhao, R. *et al.* Bone grafts and substitutes in dentistry: A review of current trends and developments. *Molecules* 26, 3007 (2021).
50. Tan, W. L., Wong, T. L. T., Wong, M. C. M. & Lang, N. P. A systematic review of post-extraction alveolar hard and soft tissue dimensional changes in humans. *Clin. Oral Implants Res.* 23, 1–21 (2012).
51. Ivanova, V., Chanchev, I., Zlatev, S. & Mijiritsky, E. Correlation between primary, secondary stability, bone density, percentage of vital bone formation and implant size. *Int. J. Environ. Res. Public Health* 18, 6994 (2021).
52. Goiato, M. C., Dos Santos, D. M., Santiago, J. F., Moreno, A. & Pellizzer, E. P. Longevity of dental implants in type IV bone: a systematic review. *Int. J. Oral Maxillofac. Surg.* 43, 1108–1116 (2014).
53. Mohajerani, H., Roozbayani, R., Taherian, S. & Tabrizi, R. The Risk Factors in Early Failure of Dental Implants: a Retrospective Study. *J. Dent.* 18, 298–303 (2017).
54. Huang, H., Wu, G. & Hunziker, E. The clinical significance of implant stability quotient (ISQ) measurements: A literature review. *J. Oral Biol. Craniofacial Res.* 10, 629 (2020).
55. Fernández, M. P. R., Gehrke, S. A., Mazón, P., Calvo-Guirado, J. L. & De Aza, P. N. Implant stability of biological hydroxyapatites used in dentistry. *Materials (Basel)*. 10, 644 (2017).
56. Chen, M., Lyons, K., Tawse-Smith, A. & Ma, S. Clinical significance of the use of resonance frequency analysis in assessing implant stability: A systematic review. *Int. J. Prosthodont.* 32, 51–58 (2019).
57. Rodrigo, D., Aracil, L., Martin, C. & Sanz, M. Diagnosis of implant stability and its impact on implant survival: a prospective case series study. *Clin. Oral Implants Res.* 21, 255–261 (2010).

58. Monje, A., Ravidà, A., Wang, H.-L., Helms, J. & Brunski, J. Relationship between primary/mechanical and secondary/biological implant stability. *Int. J. Oral Maxillofac. Implants* 34, s7–s23 (2019).

CHAPTER 7

7. FINAL REMARKS



This final chapter presents the main conclusions resulting from this doctoral thesis. Finally, suggestions for future work are also proposed.

7.1 General Conclusions

Previous to this work, oxidized-dextrin-based (ODEX) hydrogel (HG) has been thoroughly investigated by our group, in the scope of two research projects across the past 10 years, which included the development and comprehensive characterization of the biomaterial and preclinical studies. This thesis describes the ultimate work that culminated in its first clinical usage.

At the pre-clinical stage, ODEX was tested for two novel purposes, by different approaches: i) as a carrier of antimicrobials, LLKKK18 (LL18) and vancomycin hydrochloride (VH), in a rat model of osteomyelitis, and ii) as a carrier of a macroporous, granular bone substitute, Bonelike® Poro, and human dental pulp stem cells (hDPSCs), in an ovine model of critical-sized calvaria defects. In the first case, main and novel achievements included the assessment of the *in vivo* antimicrobial efficacy and toxicity of LL18, together with a potent antibacterial efficacy by adding a very low VH concentration, compared to the typically used ones, culminating in an antimicrobial formulation with 70 % infection eradication success and minimal tissue damage. Although still requiring optimization, this result evidenced that local release provides a way to substantially reduce the dosages commonly used in antibiotherapy. This work also provided the first drug release profile as a function of HG degradation, at physiological and acidic pH, demonstrating its potential as a sustained release system. In the second case, the HG + BL®P formulations could successfully regenerate critical-sized defects without compromising new bone formation or biocompatibility. This work also provided *in vitro* demonstration that ODEX accelerates the degradation of BL®P granules, as suggested in previous *in vivo* experiments, though without supporting evidence at that time.

This thesis reports the first-in-human study of dextrin-based HG as a carrier of Bonelike® by Biosskin, in the management of alveolar ridge preservation following a tooth extraction, culminating in dental implant placement 6-months post-treatment. This study had the purpose of obtaining CE, *Conformité Européenne*, market approval for Bonelike® by Biosskin, simultaneously developing an innovative and competitive material. DEXGEL Bone is a moldable, minimally-invasive, easy-to-apply bone regeneration device that naturally stimulated bone formation, without compromising bone volume or density (as compared to the formulation without DEXGEL). The presence of the HG actually resulted in maximized primary stability of the dental implant, and exhibited a tendency for more new bone formation which, we believe, would have been statistically relevant if the population size could have been higher. Therefore, population size is identified as a limitation of the study. Nevertheless, clinical validation was achieved as intended and, now, other clinical scenarios with a higher number of volunteers can be safely designed. Importantly, ODEX

displayed a long shelf life of up to 3 years which, together with the aforementioned benefits, gives rise to a competitive biomaterial within other commercially available grafting materials. The preparation of this HG in a certified clean room, properly designed for the manufacturing and packaging of medical devices, implied a meticulous effort to organize all required reagents and materials, rigorously sterilized, and careful conduction of the biofabrication in compliance with the respective standards.

Taking advantage of the hydrophilicity and multifunctional groups present in the dextrin backbone, we developed a micelle-like delivery system by means of conjugation to hydrophobic vitamin D3 (VD3), further engineered to work as a vehicle for LL18, culminating in a dual delivery system with antimicrobial and tissue healing properties. The construct overcomes recurrent limitations of drug solubility, diminishes drug cytotoxicity and hemolysis, improves antibacterial activity, reduces heat-induced albumin denaturation, and holds wound healing capacity. Unlike the free peptide, loaded LL18 was directed to lysosomes of bone cells known for its reduced phagocytic capacity and subsequent vulnerability to persistent infection. Free LL18 was traced in the perinuclear region of osteoblasts and associated with significant accelerated wound healing, given that loaded LL18, present in lysosomes, displayed a less pronounced effect. Thus, whereas intracellular bacteria could be rapidly addressed by lysosomal LL18, additional cathelicidin directed to the perinuclear region would be important for regenerative purposes. This is a key-aspect arising from this work, with crucial importance for therapeutic design. Instead of merely shielding agents from the immune system and increasing solubility, we attempted to design a construct based on electrostatically (and more labile) bounded antimicrobial peptide located at the surface of micelles to make it readily available for bacteria binding, whereas chemically bounded VD3 can be more sustained to keep up with the long-term regeneration process, possibly providing a stimulus for endogenous production of cathelicidin at later stages. In terms of production feasibility, micelles can be extruded to yield homogeneous-in-size particles under 200 nm, a process simultaneously working as a sterilization method. Lower pore sizes can be applied if desired. Dried vitamin D-Dextrin (VD3-Dex) micelles can then be easily and rapidly prepared by direct dissolution in H₂O or in LL18-dissolved solution. The VD3-Dex formulation still has much room for improvement, given that different bounded VD3 ratios can be precisely manipulated to adjust a balance between biological effect, toxicity and solubility. Overall, naturally occurring dextrin and VD3 may constitute a prophylactic option and therapeutic product to traditional antimicrobial and bone healing agents, even disregarding the endogenous stimulation of cathelicidin – a mechanism currently lacking suitable *in vivo* models.

7.2 Suggestions for Future Work

In this work, ODEX HG, an injectable/moldable carrier for a granular ceramic-based bone substitute, was validated for human use. Although DEXGEL Bone may be ready for clinical practice in terms of safety, further investigation is required to achieve a final commercially available product, with competitive features against other market products, for instance:

- i) Develop a customized syringe to mix granules with HG and use to administer the formulation, without compromising homogeneity and sterility before administration, ensuring an easy perception of the preparation procedure to the surgeon;
- ii) Test the formulation in other clinical scenarios of bone repair, with a large number of volunteers.

LL18 holds promise in pathogen defense and bone repair *in vitro*. However, its performance can be critically and rapidly inhibited by salts, early degradation, or binding to molecules present in body fluids. This is a major issue for *in vivo* or clinical translation, particularly in the case of prolonged healing scenarios, as it occurs in bone tissue. The association with dextrin-based micelles bearing conjugated VD3 provides a shield effect whilst improving antimicrobial efficacy. Considering that we have shown ODEX HG suitability for the incorporation and release of LL18 in an OM context, conditions are gathered to merge all the different works developed in all chapters of this thesis:

- i) Test different concentrations of LL18-loaded VD3-Dex micelles in the chick embryo *in vivo* model, (reduced ethical and financial issues) to further explore its pro-angiogenic capabilities;
- ii) Test different concentrations of pro-angiogenic LL18-loaded VD3-Dex micelles incorporated into ODEX HG, in rat models of acute and chronic OM to find the most antibacterial and least toxic formulation;
- iii) Test the best formulations developed in the previous point, incorporated into HG + BL®P, in a rat or ovine model of bone regeneration.

VD3-cathelicidin therapeutic partnership has much more to offer. Future advances in the study of VD3-Dex micelles should include:

- i) Demonstration of the conversion of inactive into active VD3, and subsequent endogenous cathelicidin expression, *in vitro*;
- ii) Test LL18-loaded VD3-Dex in an *in vitro* model of infection in osteoblasts and macrophages;
- iii) lipopolysaccharide (LPS) neutralization;

- iv) Anti-oxidant activity;
- v) Quantify VD3 content within micelles, possibly by acid hydrolysis;
- vi) Access thermal and light stability of micelle-incorporated VD3 as compared to the free form;
- vii) Analyze stimulation of osteoblast differentiation (alkaline phosphatase activity) and mineralization.

Considering the multifunctional uses of dextrin, other interesting research lines may arise from this thesis, for instance:

- i) Succinylated VD3 (-COOH) could be conjugated to the remaining multiple -OH groups present in ODEX backbone, then reacted with ADH, culminating in a hydrogel bearing soluble VD3, with a release profile proportional to the HG degradation behavior;
- ii) Conjugate succinylated VD3 to FITC, to track intracellular free VD3 in relevant cell lines;
- iii) Owing to its hydrophobic core, these VD3-Dex micelles can also work as a delivery system for hydrophobic drugs by non-covalent interaction, offering plenty of drug-delivery designs. Some work has already been developed with curcumin, known for its anti-inflammatory and antioxidant properties, and coumarin-6 (C6), with fluorescence-tracking utility.
- iv) Due to its amphiphilic nature, VD3-Dex potential as an emulsifier can also be considered, comparably to a previously reported VD3-poly(ethylene glycol) (PEG) conjugate used to increase encapsulation efficiency and stabilize a poly(lactic-co-glycolic acid) (PLGA)-based drug delivery formulation;
- v) Develop LL18(-COOH)-VD3(-OH) conjugates and explore their antimicrobial activity and propensity to resistance mechanisms;
- vi) Given the safe and wide use of dextrans in the food industry and high-water solubility, micelle-solubilized VD3 could also be applied to the development of value-added food products;
- vii) Given the antitumor effects of VD3, the presence of vitamin D3 receptor, VDR, and the overexpression of esterase in tumor cells as a target for esterase-responsive nanocarriers, VD3-Dex could be explored for its antitumor properties. VD3-Dex is linked by ester bonds, therefore, possibly being sensitive to esterase activity.

7.3 References

1. Zhao, H.Z., Tan, E.C., Yung, L.Y.L. Potential use of cholecalciferol polyethylene glycol succinate as a novel pharmaceutical additive. *J Biomed Mater Res Part A* 84A:954-964 (2008).

APPENDIX A

DGAV Licence



REPÚBLICA
PORTUGUESA

AGRICULTURA, FLORESTAS
E DESENVOLVIMENTO RURAL



2017-06-30 015191

Ex^{mo} Senhor
Professor José Eduardo Teixeira Pereira
Departamento de Ciências Veterinárias da
Universidade de Trás-os-Montes e Alto Douro
Quinta dos Prados
5000 – 801 VILA REAL

Nossa referência
0421/000/000
/2017

Vossa referência

Vossa data

Assunto:

PROTEÇÃO DOS ANIMAIS UTILIZADOS PARA FINS EXPERIMENTAIS E/OU OUTROS FINS CIENTÍFICOS – PEDIDO DE AUTORIZAÇÃO PARA REALIZAÇÃO DE PROJECTO DE EXPERIMENTAÇÃO ANIMAL

Na sequência do pedido efetuado por V. Ex^a no sentido de poder ser autorizada a realização do projeto experimental designado “**iBone Therapies – Terapias inovadoras para a regeneração óssea**”, de que é o investigador aresponsável, cabe-me informar que o mesmo foi avaliado de acordo com o Artigo 44º do Decreto-Lei nº 113/2013, de 7 de Agosto, relativo à “proteção dos animais utilizados para fins científicos”.

Mais se informa V. Ex^a que, depois de esclarecidas as dúvidas que a sua análise nos levantou, o projeto em apreço recebeu uma **avaliação favorável** e foi **autorizado** de acordo com o nº 1, do Artigo 42º do mesmo diploma legislativo.

No entanto, deverá fazer-se para cada um dos procedimentos a realizar, - independentemente de aos mesmos ter sido atribuída classificações de severidade prospetiva **Ligeira e Moderada**-, uma adequada monitorização dos sinais de dor, sofrimento ou angústia dos animais neles envolvidos, por forma a poder fazer-se uma adequada atualização sobre o nível de dor efetiva a que os mesmos possam vir a ficar sujeitos.

Para além disso, e no caso de virem a ser detetados sinais de dor, sofrimento ou angústia dos animais submetidos aos procedimentos enquadráveis na categoria de severidade **Severo** o projeto terá que ser submetido a uma avaliação retrospectiva, de acordo com o ponto 3, do artigo 45º, do documento legislativo acima referido.

Finalmente, resta-me especificar, de acordo com o discriminado no nº 2, do Artigo 46º, do atrás referido Decreto-Lei, o seguinte:

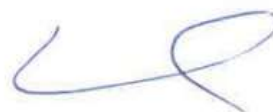
- **O utilizador que realiza o projeto:** Diretor do Departamento de Ciências Veterinárias da Universidade de Trás-os-Montes e Alto Douro;

- **A pessoa responsável pela execução global do projeto e pela sua conformidade com a autorização do mesmo:** Professor José Eduardo Teixeira Pereira;
- **O estabelecimento onde o projeto vai ser realizado:** Biotério de pequenos roedores e Hospital Veterinário do Departamento de Ciências Veterinárias da Universidade de Trás-os-Montes e Alto Douro;

Com os melhores cumprimentos,

 O Diretor Geral

Fernando Bernardo



GRAÇA MARIANO
SUBDIRETORA-GERAL
Por Delegação de Competências n.º 12801/2016
Publicado na DR n.º 201 de 19 de outubro de 2016

APPENDIX B

DGS Licence

DGS
Departamento da Qualidade na Saúde

CERTIFICADO DE AUTORIZAÇÃO

REPÚBLICA PORTUGUESA
SAÚDE

Biosckin, Molecular And Cell Therapies, S.A.
Parque da Ciência e de Tecnologia
Rua Engenheiro Frederico Ulrich, 2650
4470-605 Moreira da Maia - Porto

A Direção-Geral da Saúde autoriza a Biosckin, Molecular And Cell Therapies, S.A., nos termos do disposto na Lei nº 12/2009, de 26 de março, alterada pela Lei nº 1/2015, de 8 de janeiro, em cumprimento da alínea i) do nº 2 do artº. 2º do Decreto-Regulamentar nº 14/2013, de 26 de janeiro a exercer as seguintes atividades:

Polpa Dentária:
Análise
Processamento
Armazenamento

O Certificado de Autorização emitido fundamenta-se no processo de avaliação da qualidade e segurança concluído em 08-07-2016.

O Diretor do Departamento da Qualidade na Saúde

J. Alexandre Diniz

DATA de Emissão: 08-07-2016

APPENDIX C

Ethics Approval

		
---	---	--

Exmo.(a). Senhor(a)

Bioskin, Molecular and Cell Therapies S.A.
Parque de Ciência e Tecnologia da Maia,
Rua Eng. Frederico Ulrich
2650 - Moreira da Maia

Carta Registada com Aviso de Receção

Nossa ref.: DPS/DM/450.10.053/2019/0065

Assunto: **AUTORIZAÇÃO CONDICIONAL DE ESTUDO CLÍNICO COM INTERVENÇÃO DE DISPOSITIVOS MÉDICOS**

N.º Infarmed: EC/001/2018

Estudo Clínico com intervenção de dispositivos médicos: *"iBone Therapies: Terapias inovadoras para regeneração óssea"*

Promotor: Bioskin, Molecular and Cell Therapies S.A.

Tipo de pedido: Autorização de Estudo Clínico com intervenção de dispositivos médicos

Notifica-se V. Exa. que a realização do Estudo Clínico com intervenção de dispositivos médicos mencionado em epígrafe foi Autorizada Condicionalmente, conforme o Despacho superior de 02-04-2019 (cópia em anexo).


Com os melhores cumprimentos,


A Diretora da Direção de Produtos de Saúde


Maria Judite Neves

Em caso de resposta solicita-se que seja incluída a referência a este documento.
In case of reply please indicate the reference document.

LWL ☎ (+351) 21 798.72.35



INFARMED - Autoridade Nacional do Medicamento e Produtos de Saúde, I.P.
Parque de Saúde de Lisboa - Av. do Brasil, 53
1500-084 Lisboa
TEL: +351 217 987 380 Fax: +351 217 983 316 Website: www.infarmed.pt Email: informacao@infarmed.pt

1/1



Exma. Sra.
Raquel Peixoto
RESDEVMED, Unipessoal Lda
Travessa do navega, 436 C
Arada
3885-183 Ovar

Vosso ref.: EC.01.01.17

Data: 07-02-2018

Nosso ref.: YAP 1802FG116

Assunto: **Estudo Clínico com Intervenção de Dispositivo Médico com o N.º de Protocolo EC.01.01.17 e Código CEIC 1802FG116**

Exmos. Senhores,

Em resposta ao V. pedido de parecer para realização do Estudo Clínico com Intervenção de Dispositivo Médico supramencionado, informa-se que o mesmo foi considerado válido pelo que o prazo para a emissão do parecer deverá ser contado nos termos do n.º 1, do artigo 16.º da Lei n.º 21/2014 de 16 de abril.

Com os melhores cumprimentos,

O GABINETE DE APOIO DA COMISSÃO DE ÉTICA PARA A INVESTIGAÇÃO CLÍNICA

Lénia Costa
Gestora de processos



N/Ref. 02.02
Proc. n.º 18285 / 2017
Of. n.º 34814
Data: 2017-11-07

Assunto: Notificação de tratamento de dados de investigação clínica

Com referência ao assunto em epígrafe, ficam V. Exas. notificados de todo o conteúdo da decisão desta CNPD n.º 12504/ 2017 proferido em 07-11-2017, cuja cópia se anexa.

Com os melhores cumprimentos.

A Secretária da CNPD

(Isabel Cristina Cruz)



Autorização n.º 12504/ 2017

RESDEVMED Unipessoal Lda , NIPC 510683290, notificou à Comissão Nacional de Protecção de Dados (CNPD) um tratamento de dados pessoais com a finalidade de realizar um Estudo Clínico de Dispositivo Médico, denominado iBone Therapies: Terapias inovadoras para regeneração óssea , com o Protocolo n.º EC.01.01.17.

O participante é identificado por um código especificamente criado para este estudo, constituído de modo a não permitir a imediata identificação do titular dos dados; designadamente, não são utilizados códigos que coincidam com os números de identificação, iniciais do nome, data de nascimento, número de telefone, ou resultem de uma composição simples desse tipo de dados. A chave da codificação só é conhecida do(s) investigador(es).

É recolhido o consentimento expresso do participante ou do seu representante legal.

A informação é recolhida diretamente do titular.

As eventuais transmissões de informação são efetuadas por referência ao código do participante, sendo, nessa medida, anónimas para o destinatário.

A CNPD já se pronunciou na Deliberação n.º 1704/2015 sobre o enquadramento legal, os fundamentos de legitimidade, os princípios aplicáveis para o correto cumprimento da Lei n.º 67/98, de 26 de outubro, alterada pela Lei n.º 103/2015, de 24 de agosto, doravante LPD, bem como sobre as condições e limites aplicáveis ao tratamento de dados efetuados para a finalidade de investigação clínica.

No caso em apreço, o tratamento objeto da notificação enquadra-se no âmbito daquela deliberação e o responsável declara expressamente que cumpre os limites e condições aplicáveis por força da LPD e da Lei n.º 21/2014, de 16 de abril, alterada pela Lei n.º 73/2015, de 27 de junho – Lei da Investigação Clínica –, explicitados na Deliberação n.º 1704/2015.

O fundamento de legitimidade é o consentimento do titular.

A informação tratada é recolhida de forma lícita, para finalidade determinada, explícita e legítima e não é excessiva – cf. alíneas a), b) e c) do n.º 1 do artigo 5.º da LPD.



Assim, nos termos das disposições conjugadas do n.º 2 do artigo 7.º, da alínea a) do n.º 1 do artigo 28.º e do artigo 30.º da LPD, bem como do n.º 3 do artigo 1.º e do n.º 9 do artigo 16.º ambos da Lei de Investigação Clínica, com as condições e limites explicitados na Deliberação da CNPD n.º 1704/2015, que aqui se dão por reproduzidos, autoriza-se o presente tratamento de dados pessoais nos seguintes termos:

Responsável – RESDEVMED Unipessoal Lda

Finalidade – Estudo Clínico de Dispositivo Médico, denominado iBone Therapies: Terapias inovadoras para regeneração óssea , com o Protocolo n.º EC.01.01.17

Categoria de dados pessoais tratados – Código do participante; idade/data de nascimento; género; dados da história clínica; dados de meios complementares de diagnóstico; medicação prévia concomitante; eventos adversos

Exercício do direito de acesso – Através dos investigadores, presencialmente

Comunicações, Interconexões e fluxos transfronteiriços de dados pessoais identificáveis no destinatário – Não existem

Prazo máximo de conservação dos dados – A chave que produziu o código que permite a identificação indireta do titular dos dados deve ser eliminada No prazo máximo de 15 anos para os estudos com dispositivos médicos implantáveis e 5 anos para os restantes dispositivos médicos, nos termos do disposto no Decreto-Lei n.º 145/2009, de 17 de junho.

Da LPD e da Lei de Investigação Clínica, nos termos e condições fixados na presente Autorização e desenvolvidos na Deliberação da CNPD n.º 1704/2015, resultam obrigações que o responsável tem de cumprir. Destas deve dar conhecimento a todos os que intervenham no tratamento de dados pessoais.

Lisboa, 07-11-2017

A Presidente